NASA Technical Memorandum 79729

Reports of Planetary Geology Program, 1977-1978

MAY 1978

NASA

NASA Technical Memorandum 79729

Reports of Planetary Geology Program, 1977-1978

Compiled by Robert Strom and Joseph Boyce
Office of Space Science
Washington, D.C.

National Aeronautics
and Space Administration

Scientific and Technical Information Office

1978

Page intentionally left blank

Page intentionally left blank

FOREWORD

This is a compilation of abstracts of reports from Principal Investigators of NASA's Office of Space Science, Division of Lunar and Planetary Programs Planetary Geology Program.

The purpose is to provide a document which succinctly summarizes work conducted in this program. Each report reflects significant accomplishments within the area of the author's funded grant or contract.

No attempt has been made to introduce editorial or stylistic uniformity; on the contrary, the style of each report is that of the Principal Investigator and may best portray his research. Bibliography information will be included in a separately published document.

Full reports of selected abstracts were presented to the annual meeting of Planetary Geology Principal Investigators at The University of Arizona, Tucson, Arizona, May 30, 31, and June 1, 1978.

S. E. Dwornik
Discipline Scientist
Planetary Geology Program

J. M. Boyce
Staff Scientist
Planetary Geology Program

Page intentionally left blank

Page intentionally left blank

CONTENTS

CHAPTER 1 - CONSTRAINTS ON SOLAR SYSTEM FORMATION

Nonaxisymmetric Models of Collapsing, Rotating Protostars,
A. P. Boss and S. J. Peale, Univ. of California, Santa Barbara Ca. 93106

The problem of the origin of the solar system and of planetary systems in general is intimately connected to the question of the distribution of angular momentum in collapsing gas clouds. As previous numerical work has shown (Larson, 1969, 1972; Black and Bodenheimer, 1976) it appears that a full three spatial dimension gravitational hydrodynamical calculation is needed to determine the dynamical evolution of a rotating, non-uniform, collapsing protostellar gas cloud. Indeed there is even a question as to whether or not a ring or a disk forms in the restricted axially symmetric calculation (Kamiya, 1977). A comprehensive theory of planetary formation is dependent upon the results of these calculations of the formation of rings/disks and of their subsequent fragmentation to provide a realistic estimate of the initial conditions in the solar nebula.

A three spatial dimension hydrodynamical code has been developed to follow the early stages of protostellar collapse. The code employs explicit time differencing on an Eulerian spherical coordinate grid, based on the two-step Lax-Wendroff hydrodynamics scheme. A tensor artificial viscosity is included, and the usual viscous terms may be included as well, though they are negligible unless a turbulent viscosity is assumed. The difference formula are written for a non-uniform grid and the grid itself can be adjusted in the radial direction in order to follow the collapse. The Poisson equation for the gravitational potential is solved using an expansion in spherical harmonics. An A.D.I. (Alternating Direction Implicit) method for solving the Poisson equation is under development and may be employed in the future. Radiative transfer is at present handled by the diffusion approximation. Eventually a more exact treatment of radiation involving the equation of transfer in the Eddington approximation is planned, though radiative transfer is probably not of great importance during the initial, nearly isothermal phases of protostar collapse. Subroutines for the opacity at low temperatures ($10^{\circ}K \rightarrow 10,000^{\circ}K$), the equation of state, and the internal energy have also been constructed.

The Poisson solver has been checked on various test mass distributions such as centrally condensed spherically symmetric objects and constant density oblate spheroids in different orientations. With a coarse grid involving twenty radial points, eleven in declination (north-south hemisphere symmetry is assumed) and twenty in azimuth, accuracy of the gradients of the gravitational potential of the order of one percent or better is indicated.

The hydrodynamics code has been run for one, two, and three dimensional test cases and analysis of the results is in progress. The code so far has succeeded in matching previous results (Bodenheimer and Sweigart, 1968) for isothermal dynamic collapse of spherically symmetric stars, as well as passing an equilibrium test of the isothermal Bonnor-Ebert sphere. With an adiabatic pressure law the cloud collapses down and then bounces back and forth indefinitely, indicating that the scheme has very little implicit viscosity. The sensitivity of the hydrodynamic scheme to the initial conditions is studied by varying the initial temperature (T) of a given uniform density (ρ) configuration of fixed radius (R). This amounts to varying the critical Jean's radius (Bonnor, 1956)

$$R_J = \alpha kT/(G\rho m_{gas}) , \quad \alpha=0.89 \text{ (for spherical geometry)}.$$

A collapsing cloud must have its radius $R>R_J$. It is found that for a $1M_\odot$ cloud of radius 1.63×10^{17}cm the cloud collapses for $T_i \lesssim 10.7\ ^oK$ and oscillates for higher temperatures, indicating an α of 0.73 (Larson (1969) obtained $\alpha=0.72$).

The choice of treatment of the energy equation and radiative transfer was found to have important effects on the dynamics of the collapse in the nonisothermal regime. When the energy equation without radiative transfer is advanced explicitly while the radiative transfer terms are separated out and treated implicitly (Black and Bodenheimer, 1975) the temperature-density response of the code is close to that of Black and Bodenheimer (1975) but the first bounce does not occur. When the energy equation, including radiative transfer, is treated fully implicitly, the collapse is halted at central densities and temperature roughly equal to those found by Black and Bodenheimer (1975) and Larson (1969) for spherically symmetric collapse of $2M_\odot$ and $1M_\odot$ clouds respectively. The velocity and density profiles compare favorably throughout the cloud at the time of the "bounce".

For the case of isothermal axially symmetric collapse calculations there remains a controversy over the eventual formation of a ringlike or disklike structure in the inner regions. Larson (1972) and Black and Bodenheimer (1976) always obtain rings, while Nakazawa et al. (1976) obtain rings for low temperature models and disks for high temperature models. Tscharnuter (1975) did not obtain rings until he changed his difference scheme to conserve angular (CAM) momentum instead of angular velocity (CAV) (Black, private communication). Kamiya (1977), using the only Lagrangian hydrodynamics code employed so far, did not obtain rings, and claims that this is due to the superior ability of a Lagrangian code to conserve angular momentum. The Santa Barbara code was run with Black and Bodenheimer's (1976) case 1A initial conditions to test how well the code

conserves angular momentum. In this slow rotation case the central region collapses uniformly conserving its mass and angular momentum; hence the angular velocity $\omega \propto \rho^{2/3}$ for the inner plateau. With CAV differencing it was found that $\omega \propto \rho^{1.9/3}$ whereas with CAM differencing $\omega \propto \rho^{2.0/3}$, indicating that CAM differencing does indeed ensure local conservation of angular momentum. Furthermore, with this initial value condition the CAV code did not produce a ring while the CAM code did produce a ring of the same size as that found by Black and Bodenheimer (1976).

The analysis of two and three dimensional test cases is currently being continued. In all test cases integral conservation checks are performed for the total mass, energy, and angular momentum.

References

Black, D.C. and Bodenheimer, P. (1975). Ap. J. 199, 619-632.

Black, D.C. and Bodenheimer, P. (1976). Ap. J. 206, 138-149.

Bodenheimer, P. and Sweigart, A. (1968). Ap. J. 152, 515-523.

Bonnor, W.B. (1956). M.N.R.A.S. 116, 351-359.

Kamiya, Y. (1977). Progr. Theor. Phys. 58, 802-815.

Larson, R.B. (1969). M.N.R.A.S. 145, 271-295.

Larson, R.B. (1972). M.N.R.A.S. 156, 437-458.

Nakazawa, K., Hayashi, C. and Takahara, M. (1976). Progr. Theor. Phys. 56, 515-530.

Tscharnuter, W. (1977). Progr. Theor. Phys. 58, 802-815.

PROTOSTARS AND PLANETS, JANUARY 3-7, 1978
The University of Arizona, Tucson, Arizona 85721

FROM DARK CLOUDS TO PLANETS AND SATELLITES, H. Alfvén
University of California, San Diego, Dept. of AP&IS, La Jolla, CA 92093

An intermediate state in the evolutionary chain from dark clouds to planets-satellites is reconstructed. Two independent methods are used:

A. Reconstruction from solar system data

In order to reduce speculation to a minimum, the problem is approached in a new way which is characterized by the following principles (see ref. (1)):

1. The actualistic principle

This avoids arbitrary assumptions about the early state of the solar system, which instead is reconstructed from a detailed analysis of the present state and of the possible experimentally verified processes which may have led to it.

2. The hetegonic principle

This could also be called "comparative planeto-satellitology". As has been demonstrated in ref. (1), this is a very powerful method for discriminating between probable and improbable processes and for reducing speculation.

3. The principle of extrapolation of mechanisms

The study of plasma physics has given us the sobering experience that it is almost impossible to predict the actual behavior of a plasma through purely theoretical calculations starting from basic principles. The properties of a plasma can be understood only by very sophisticated diagnostic studies based on in situ measurements. Such measurements are now possible in the laboratory and in the magnetosphere-heliosphere.

However, neither for phenomena in distant regions of space which are inaccessible to spacecrafts, nor for cosmogonic phenomena is in situ diagnostics possible. Under such conditions the most reliable method of approach seems to be to compare phenomena in non-accessible regions with similar phenomena in the magnetosphere or in the laboratory and treat them as extrapolations of well-known phenomena. Examples are: The transfer of angular momentum from a spinning central body can be studied by comparing it to similar mechanisms in the magnetosphere. The band structure of the solar system may be clarified by laboratory studies of the critical velocity phenomenon.

An analysis of solar system data, largely supplied by space research, has resulted in the reconstruction of an intermediate state in the evolution of the solar system as shown in Fig. 1. Instead of a thin flat disc, which is hypothetically introduced in some theories, our reconstruction results in two toruses containing accreting grains and planetesimals which do not necessarily move in circular orbits but in orbits with eccentricities up to $e = 1/3$ and inclinations up to about 30°.

Fig. 1

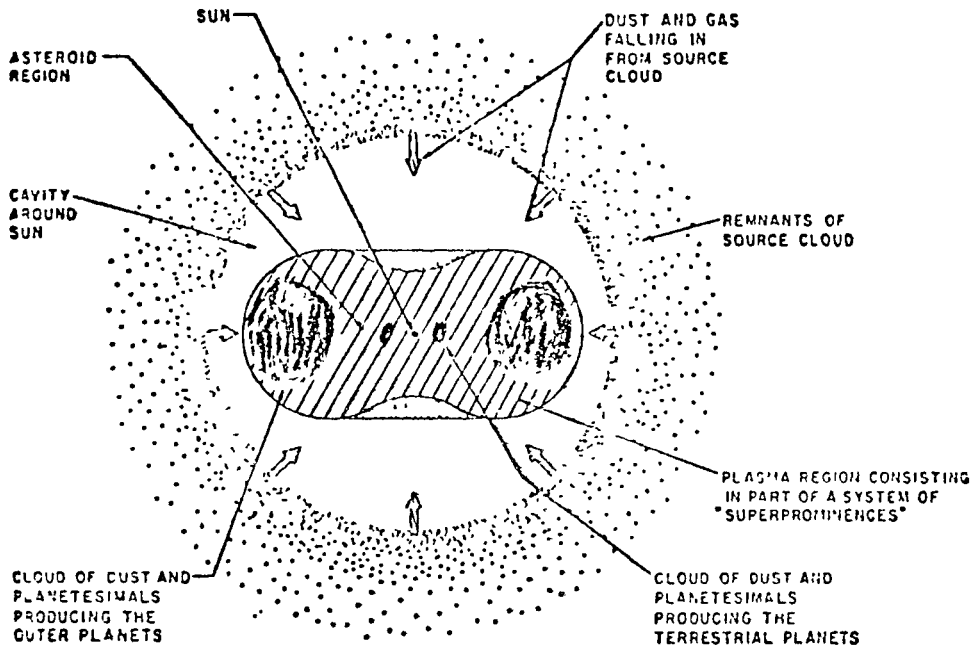

B. Reconstruction from dark cloud observations

It is very likely that solar systems of the same type as ours are formed in dark interstellar clouds. Magnetic fields are of decisive importance for their evolution but electromagnetic effects do not necessarily counteract the contraction of a cloud; they may just as well "pinch" the cloud. Magnetic compression may even be the main mechanism for forming interstellar clouds and keeping them together (see ref. (2)).

Further, star formation is likely to be due to an instability, but it is unlikely that it has anything to do with the Jeans instability. A probable mechanism is that the sedimentation of dust (including solid bodies of different sizes) is leading to a rapid gravitationally assisted accretion. A "stellesimal" accretion analogous to the planetesimal accretion can be expected to lead to the formation of a star surrounded by a low density cavity in the cloud. Matter falling in from the source cloud towards the star is stopped when the critical velocity is reached, and constitutes the raw material for the formation of planets and satellites.

The study of the evolution of a dark cloud leads to a scenario of planet formation which is reconcilable with the results obtained from studies based on solar system data. In fact Fig. 1 can just as well be presented as a result of the evolution of a dark cloud according to ref. (2).

C. Conclusion

An analysis of the processes in dark interstellar clouds studied in ref. (2) together with the processes studied in ref. (1) lead to a consistent framework for theories describing the evolutionary chain starting from the formation of a cloud and ending with planets and satellites with the present properties.

The sequence of processes is illustrated in Fig. 2.

1. Interstellar medium in galaxy

Galactic magnetic field and observed spectra of ionized atoms show that its behavior must be dominated by plasma effects. There is probably a general galactic current system analogous to the heliospheric current system (3)(4).

2. Formation of interstellar clouds

Probably dominated by hydromagnetic effects ("pinch"), but gravitation may assist. With increasing density the gas temperature in large regions may go down (analogous to the formation of prominences in the solar corona) but hydromagnetic effects till dominate. Condensation of grains increases (2).

3. Star formation ("collapse" of cloud)

May be due to pinch, possibly sometimes assisted by currents associated with shock fronts. Sedimentation of grains is probably important, which means that the formation of stars may be a non-hydromagnetic process ("run-away accretion"). However, the source cloud surrounding it is still dominated by plasma effects (2).

4. Formation of planetesimals around a star

The formation of the band structure and the transfer of angular momentum are plasma phenomena. The magnetic field of the star is not a frozen-in field from the source cloud but produced by dynamo effects in its interior (5).

5. Accretion of planetesimals to planets

This is essentially a non-hydromagnetic process. Jet streams are essential as an intermediate state. There is no indication of massive protoplanets which later explode or evaporate. The interplanetary medium is still dominated by plasma effects (6).

6. Formation of regular satellites

The same process which generates planets also generates satellites. The only difference is the mass and spin of the central body (7).

7. Capture of irregular satellites

The retrograde satellites of Jupiter and Saturn are due to the capture of planetesimals, probably during the accretional phase. Triton and the Moon were originally planets which were captured by similar processes (8).

As there are a number of theories which do not introduce plasma effects, those regions in which a neglect of hydromagnetic forces is allowed are marked in black. They are:

1. The accreting dust ball up to the point when it heats up enough to be ionized. (But its surroundings are still governed by hydromagnetic effects.)

2. The accretion of dust which has condensed from the partially co-rotating plasma, the formation of planetesimals, and jet streams leading to the formation of planets (and satellites).

References

(1) Alfvén, H. and Arrhenius, G. (1976) Evolution of the Solar System, NASA SP-345.

(2) Alfvén, H. and Carlqvist, P. (1978) Interstellar Clouds and the Formation of Stars, Astrophy. and Space Sci., in press.

(3) Alfvén, H. (1977) Electric currents in cosmic plasma, Revs. of Geophys. and Space Phys., Vol. 14, No. 3, August, 271.

(4) Alfvén, H. (1978) Double radio sources and the new approach to cosmic plasma physics, Astrophys. and Space Sci., in press.

(5) Alfvén, H. and Arrhenius, G. (1976) Evolution of the Solar System, NASA SP-345, Ch. 15, 16, 17, 21, and 25.

(6) Ibid, Ch. 6, 11, 12, and 13.

(7) Ibid, Ch. 23.

(8) Ibid, Ch. 24.

COMMENTS ON THE DISCUSSION

1. Origin of the satellites

For reasons given in details in SP-345 it is at least as important to clarify the origin of the satellites as the origin of the planets. The way the meeting was programmed made it impossible to focus the attention on this very important issue.

2. The band structure of the solar system

The solar system exhibits a band structure (see Fig. 2), a fact which is neglected in most theories. To explain this empirical fact must be a challenge to any cosmogonic theory.

3. Discovery of the Uranian ring

From the band structure follows that matter should have been emplaced very close to the surface of Uranus. See Fig. 1 which was made long before the discovery of the ring. The discovery of the Uranian ring fills the last empty box in the band structure diagram.

4. Non-hydromagnetic theories

At the meeting a number of theories--starting with Cameron's theory--were presented which did not include any hydromagnetic effects. It is utterly remarkable that it is possible 29 years after the break-through of magnetohydrodynamics. At the meeting, convincing observational arguments were given for the decisive role of plasma effects. Most of the presented theories are highly speculative and it is difficult to believe that they have any connection with reality. They are based on a gravitational collapse starting when the Jeans criterion is satisfied. There are no convincing observational arguments for such a collapse and alternatives should be seriously considered (2).

E. Summary

The topic of the meeting was very well chosen. In fact this important field is now ripe for a scientific breakthrough. The observational papers were good but much of the most important and relevant material was not included (e.g., the filamentary structure of the interstellar medium, and the inverted V events). The theoretical discussion did not fully exploit the valuable observational material. Much of the time was spent on side issues. The number of papers was much too large to permit satisfactory discussion of the central issues.

References

(1) Alfvén, H. and Arrhenius, G. (1976) Evolution of the Solar System, NASA SP-345.

(2) Alfvén, H. and Carlqvist, P. (1978) Interstellar Clouds and the Formation of Stars, Astrophy. and Space Sci., in press.

(3) Alfvén, H. (1977) Electric currents in cosmic plasma, Revs. of Geophys. and Space Phys., Vol. 14, No. 3, August, 271.

(4) Alfvén, H. (1978) Double radio sources and the new approach to cosmic plasma physics, Astrophys. and Space Sci., in press.

(5) Alfvén, H. and Arrhenius, G. (1976) Evolution of the Solar System, NASA SP-345, Ch. 15, 16, 17, 21, and 25.

(6) Ibid, Ch. 6, 11, 12, and 13.

(7) Ibid, Ch. 23.

(8) Ibid, Ch. 24.

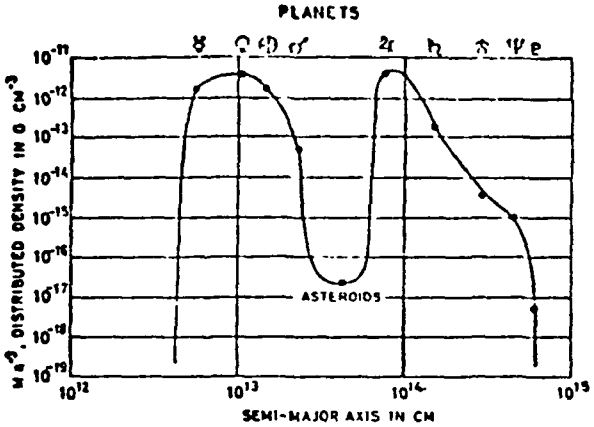

FIG. 2 a

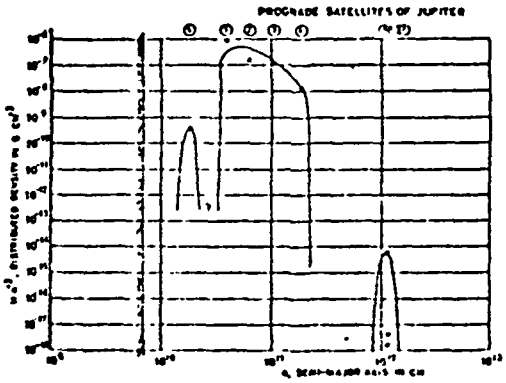

FIG. 2b

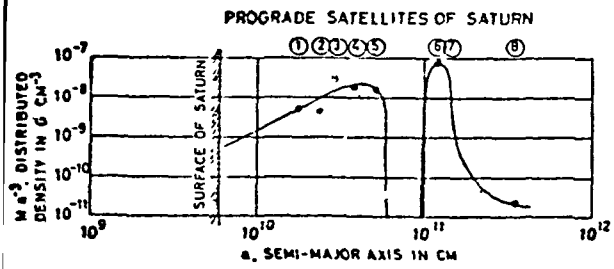

FIG. 2c

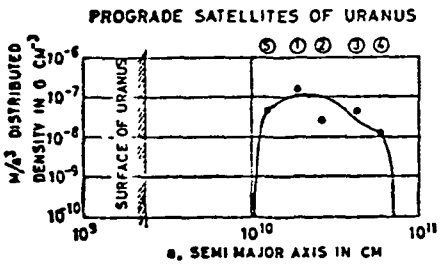

FIG. 2d

FIG. 2 a, b, c, d - Distributed density versus semimajor axis for the planets and satellites

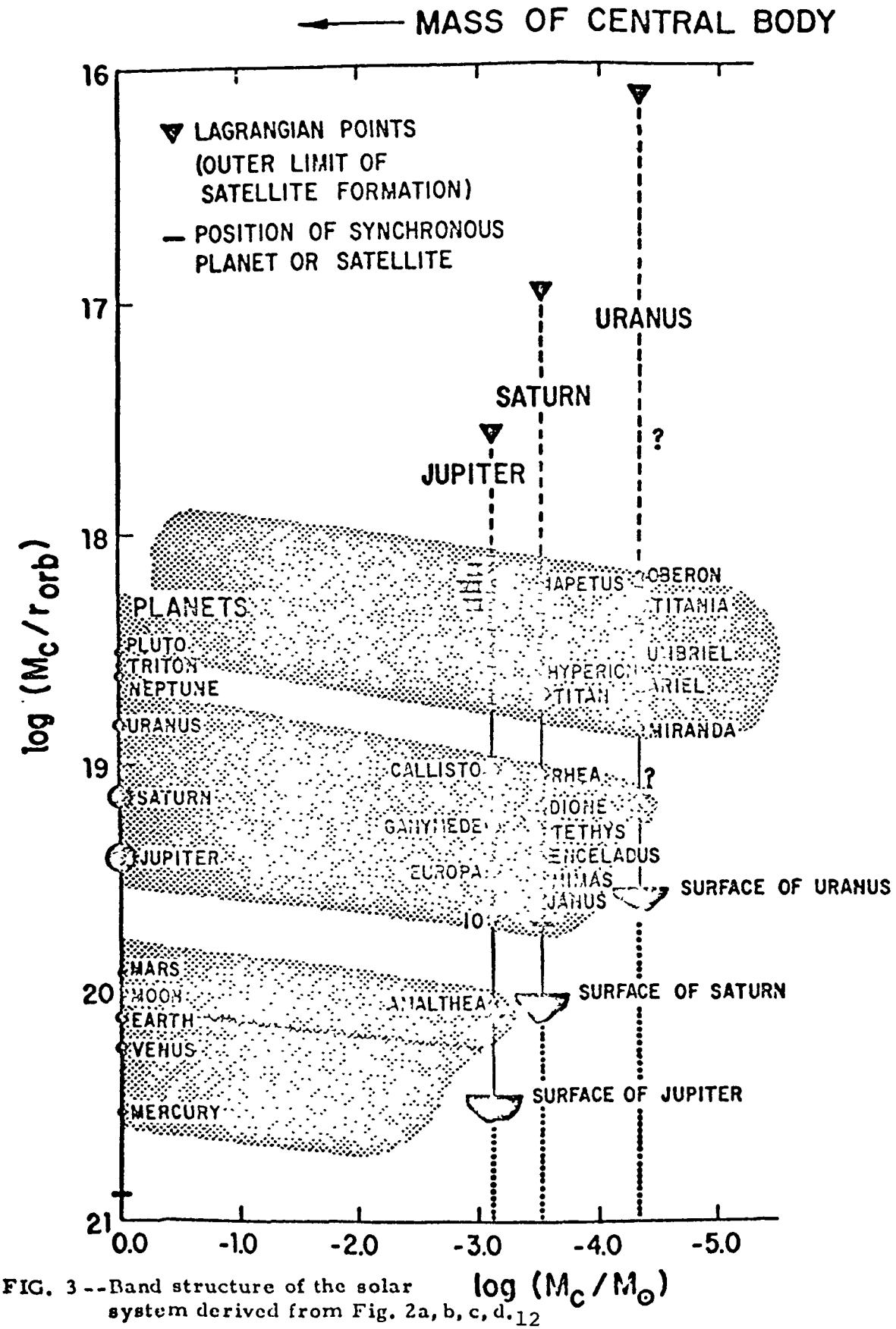

FIG. 3--Band structure of the solar system derived from Fig. 2a, b, c, d.[12]

Structure and Evolution of Giant Gaseous Protoplanets, A.G.W. Cameron, Harvard College Observatory, Cambridge, MA 02138.

In my report for a year ago (NASA TM X-3511) I described my calculations on the evolution of model sequences of the primitive solar nebula, leading to a basic conclusion that large axially-symmetric instabilities should have occurred repeatedly during the evolutionary history of the primitive solar nebula. As these rings contract upon themselves, they will become unstable along their length against a breakup into individual gaseous blobs. Many of these blobs will merge together by collision; others will be sent into eccentric orbits which may allow the blobs to avoid collision for significant periods of time. I refer to these blobs as giant gaseous protoplanets.

During the past year substantial progress has been made in understanding the structure and evolution of giant gaseous protoplanets. William DeCampli has used a stellar evolution code to study the evolution of these protoplanets. In these studies the interaction between the protoplanet and the surrounding solar nebula has been ignored, so that we refer to the objects which have been evolved as isolated protoplanets.

As a preliminary to these studies, it was necessary to improve estimates of opacity for mixtures of gas and dust at temperatures below 3000 K. The center of a giant gaseous protoplanet can hardly exceed this temperature without hydrodynamic collapse occurring; on the other hand, the surfaces of ordinary stars rarely fall below this temperature. Therefore, relatively little work has been done on the relevant opacities. The main sources of the opacity are metallic iron at temperatures below about 1500 K, and ice at temperatures below about 150 K. There are also substantial contributions to the opacity from the silicates at the lower temperatures and from molecules such as water at temperatures above 1500 K. Some preliminary work was done by Cameron and Pine in 1973 using estimated opacities for iron and ice, with the opacity at higher temperatures being primarily due to the negative hydrogen ion. Substantial increases in these opacities in some temperature ranges were found by DeCampli due to molecules and non-metallic solids, and these were used in his early calculations. Recently, J. Pollack at the NASA Ames Research Center has re-examined many of the particle opacities and has proposed higher opacities due to iron, silicates, and ice. DeCampli repeated some of his evolutionary studies using these larger opacities.

Evolutionary studies have been carried out for a number of models ranging from about the mass of Saturn to nearly 5 times the mass of Jupiter. The initial radius of the models ranged from about one astronomical unit to substantially greater. The surface temperatures of the models lay below 20 K.

When the central temperature in a giant gaseous protoplanet rises sufficiently to dissociate hydrogen molecules (above about 3000 K) a hydrodynamic collapse ensues. All of the models were followed to approximately the threshold foronset of the hydrodynamic collapse; some of them were followed through the collapse using a one-dimensional hydrodynamic code. The radii at the threshold for collapse varied from a few percent of an astronomical unit for the Saturn mass object to several tens of percent of an astronomical unit for the largest protoplanetary mass. The track in a density-temperature diagram traversed by the center of a protoplanet appeared not to depend signifi-

cantly on the opacity which was used for the model, but the surface temperature and luminosity did. However, even for the low opacity models the surface temperature hardly rose above 100 K. The uncertainty in the opacity only allows us to state that the evolution time for a Saturn mass lies in the range 10^6 - 10^7 years. This evolution time decreases rapidly as the mass of the protoplanet increases; a model having one Jupiter mass takes of the order of one or a few times 10^5 years; the heaviest masses evolve in just a few thousand years. When collapse does occur, the radius of the protoplanet decreases by almost two further orders of magnitude, if we neglect effects due to rotational flattening.

The uncertainty in the opacity and hence the evolution time leads in turn to a large uncertainty in the tidal stripping of the protoplanet. Early in the evolution of the primitive solar nebula, there is relatively little mass near the center, and the protoplanets which are formed have a large volume in which they can move around. However, as the central mass grows the protoplanets, conserving their angular momentum, will spiral closer to the center, and their inner Lagrangian point relative to the Sun and the solar nebula will move closer to the surface of the protoplanet. There is a race between the motion of this point and the evolutionary shrinkage of the protoplanetary radius to the point of gravitational collapse.

The difference in evolution times between the high and low opacity models for a two Jupiter mass protoplanet becomes crucial. Such a protoplanet can survive without envelope stripping at the position of the Earth orbit if the opacity is low, but the envelope will be stripped away at the orbit of Jupiter if the opacity is high. A model with one Jupiter mass is stripped at the Earth orbit with low opacity, and at the Jupiter orbit with high opacity. In each of these two cases, it is the onset of hydrodynamic collapse which saves a low opacity model from stripping at the position of Jupiter. In the case of a Saturn mass object, the evolutionary lifetime is sufficiently long that this effect is not important, and such a model is stripped at the position of Jupiter but not at that of Saturn.

One item of particular concern for planet formation is the ability of the giant gaseous protoplanet to form a core of condensed material. In my evolutionary sequence of solar nebula models, the giant gaseous protoplanets are formed out of gas that has never been significantly heated, so that the condensed materials in the interior will be interstellar grains or clumps of such grains, which will gradually lose volatiles as the temperature is raised.

Such grains are not in a vacuum. They should have a surface layer of gas from the primitive solar nebula and are likely to have relatively little tendency to stick together when they bump into one another. However, if the temperature rises above the melting point of common rocky materials in such grains, and if the materials are still in a condensed phase, then such liquid or partially liquid grains will coalesce upon collision. This will lead to a growth process in which the grains become progressively larger and fall out more and more rapidly towards the center of the protoplanet. It is therefore of some interest to learn under what conditions such rocky material can be condensed but molten in the interior of a protoplanet. We found that all protoplanets having about two Jupiter masses or less do pass through a region of temperature and density in which such molten condensed material can exist. The evolutionary tracks of the protoplanets subsequently pass through

a region in which the condensed materials evaporate prior to reaching the point of hydrodynamic collapse; a major portion of the evolutionary time is spent in this subsequent regime. However, if a substantial rainout of liquid materials occurs to form a core of condensed materials, the later evolutionary history of the protoplanet would be drastically altered.

This rainout process has been studied in some detail by Wayne Slattery. He has applied theory describing the rainout from water clouds in the Earth's atmosphere to a similar process which would involve materials of arbitrary density and surface tension representing metallic iron and rocky materials in protoplanetary interiors. As long as a particle is not too large, it falls through the protoplanetary gas obeying Stoke's law. However, when the size becomes comparable to a centimeter or larger, major deformations of the fluid in the drop can occur at terminal velocities, and significant departures from Stoke's law occur. Furthermore, the coalescence of colliding droplets becomes modified by the hydrodynamics of the gas flow. Thus, for two droplets of very unequal size, the larger will fall faster and will overtake the smaller. However, unless the encounter is very nearly head-on, the motion of the gas will carry a small droplet around the periphery of the larger one, thus preventing a collision and slowing the rate of growth of the larger droplet. If the two droplets are not very different in size, a collision may occur, but it is then reasonably likely that the combined droplet may fragment into several pieces. All of these effects result in a maximum droplet size being obtained during the fall. For liquid iron, this maximum size is just over 10 cm radius. For rocky materials, a maximum size of a few centimeters radius is likely. Once such large sizes are reached, the time required to fall out to the center of the protoplanet is quite short. The entire fallout period including growth from very small size may take of the order of 10^2 years.

These liquid droplets in the size range below a centimeter, where the terminal velocity is not too high, are of potential interest in connection with tidal stripping. These are candidates to become chondrules, and the protoplanetary mechanism may produce very large numbers of them. At the same time, a significant fraction of the condensed mass of the protoplanet may have rained out to form a condensed core, a process that will change the central structure and release a significant amount of gravitational energy. An obvious next step in our investigations is to carry out evolutionary studies in which the rainout of condensed materials is taken into account.

It must be pointed out that the study of these isolated giant gaseous protoplanets is only an initial exploration. The interaction of such protoplanets with the surrounding primitive solar nebula is likely to modify the behavior in significant ways. The protoplanets will have a continuous gaseous connection to the surrounding primitive solar nebula, and this is something that can lead to the gain or loss of mass,depending upon the circumstances. We call such objects embedded protoplanets, and their evolutionary study is a goal for the future.

If a protoplanet forms a core of condensed materials, that core will remain after tidal stripping. The chemical composition of the core may depend upon the degree of rainout which has occurred at tidal stripping. There are likely to be many more cores in the inner solar systems than there are planets today, so that a significant number of coalescing collisions is to be expected.

Evidence for a Primordial Magnetic Field During the Meteorite Parent Body Era,
C.P. Sonett, Department of Planetary Sciences, Univ. of Arizona, Tucson, AZ 85721.

Remanent magnetism appears to be a property of all or nearly all meteorites. Part of the magnetization is ancient and likely about the age of the solar system. Individual experiments upon selected meteorites have been carried out by a number of investigators during the past two decades and at least for some, the magnetization is reliably associated with cooling through a blocking temperature spectrum.

The total magnetic moments and susceptibilities of meteorites in Russian collections as reported by Gorshkov et al.[1] and by Gus'kova and Pochtarev[2] in various papers has been recompiled by Herndon et al.[3] We have assembled these data on a plot of moment/gm vs. susceptibility/gm (Figure 1) which shows a remarkable linear relation covering a range of nearly five orders of magnitude in each variable and includes meteorites from all classes except the irons.[4] (These are also included in Figure 1 but not in the calculation of the regression curve.)

This relation, given by

$$\log \bar{p} = (-0.75 \pm 0.07) + (0.99 \pm 0.04) \log \bar{\chi}$$

or

$$\bar{p} = (0.18 \pm 0.03)\ \bar{\chi}$$

where $\bar{p}$ is the moment/gm and $\bar{\chi}$ the susceptibility/gm, has a correlation coefficient of 0.78. The linear relation is especially surprising because a substantial component of the magnetization is expected to arise from "soaking" in the Earth's field (VRM or viscous magnetization), from entry into the Earth's atmosphere, and possibly other causes. However, internal tests on the data do not support the idea that a strong bias exists due to these artifact sources. For example, a subset of 38 pieces of Pultusk from different Russian collections shows a normal distribution of $\bar{p}/\bar{\chi}$ and the values of each variable give the small standard deviations shown in the inset box of Figure 1, indicating that the natural spread is far less than that for the larger sample; the suggestion is that the approximate 100 years of storage on Earth and diverse handling has not caused major changes. Figure 3 shows the effects of entry heating for irons. The boxed values are reentry heated according to the Hey catalog. Thus entry heating also does not appear to spread the natural distribution of $\bar{p}$ and $\bar{\chi}$.

One possible conclusion from the linear relation is that these meteorites were exposed to a common field at a very early time period. The strength of the field is a strong function of the size and shape of the grain carriers of magnetization. Qualitative calculations place the tentative value between the low of 0.04 oersted found by Brecher and Ranganayki[5] for ordinary chondrites and 0.24 oersted, near the mean of 0.29 ± 0.06 reported by Stacey and Banerjee[6] for twelve ordinary chondrites.

References

[1]Gorshkov, E.S., Gus'kova, E.G. and Pochtarev, V.I. (1975) The magnetic investigation of the Sikhote-Alin iron meteorite shower and the site of fall, Meteoritics, 10, 9.

[2]Gus'kova, E.G. and Pochtarev, V.I. (1969) Magnetic Properties of Meteorites in the Soviet Collection, in Meteorite Research, ed. P.M. Millman, D. Reidel, Dordrecht.

[3]Herndon, J.M., Rowe, M.W., Larson, E.E. and Watson, D.E. (1972) Magnetism of meteorites: A review of Russian studies, Meteoritics, 7, 263.

[4]Sonett, C.P. (1978) Evidence for a primordial magnetic field during the meteorite parent body era, Geophys. Res. Letts., in press.

[5]Brecher, A. and R.P. Ranganayaki, (1975) Paleomagnetic systematics of ordinary chondrites, Earth Planet. Sci. Letts., 25, 57.

[6]Stacey, F.D. and Banerjee, S.K. (1974) The Physical Principles of Rock Magnetism, Elsevier, New York.

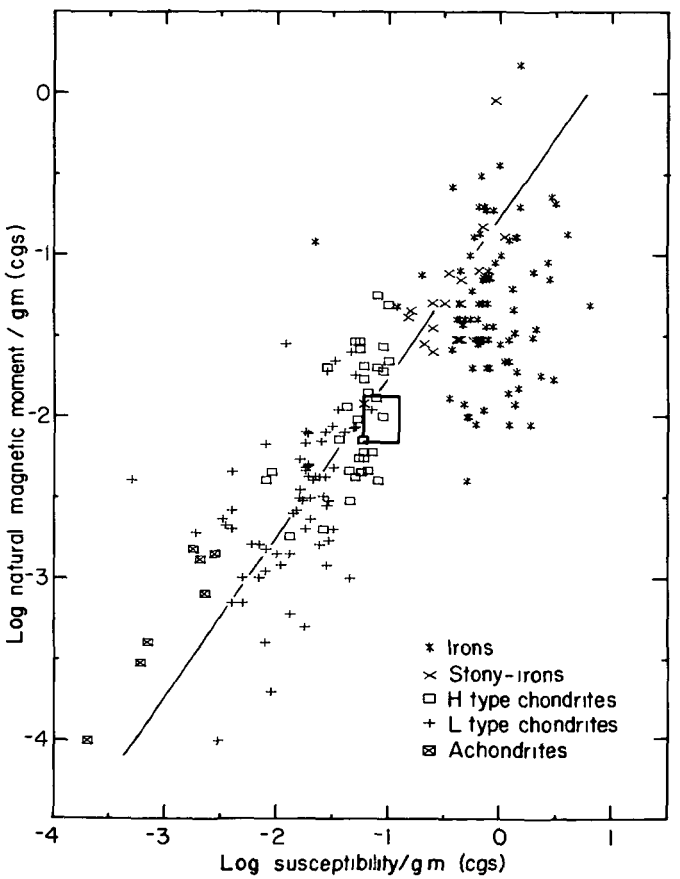

Figure 1. Log-log plot of $\overline{p}$ (magnetic moment/gm) vs. $\overline{\chi}$ (susceptibility/gm) for 200 meteorite sample measurements. The superimposed straight line is the regression line described by Eq. 1 in the text. It has a slope of 0.99 ± 0.04, thus representing a linear relation. The rectangular box indicates $\sigma_{\overline{p}}$ and $\sigma_{\overline{\chi}}$ for Pultusk.

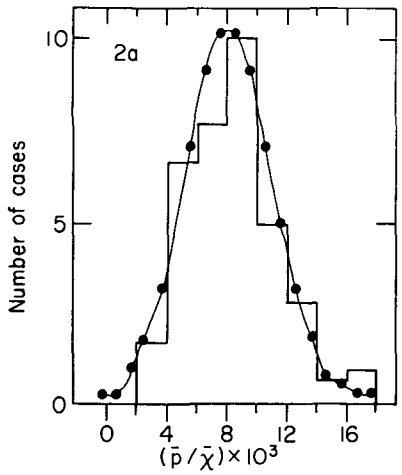

Figure 2a. Statistics of Pultusk showing the normal distribution of $\overline{p}/\overline{\chi}$. This and Fig. 2b give a qualitative basis for noting that long-term storage and handling on Earth as well as possible variability in fragments from the original fall do not create a spread comparable to the basic spread in data.

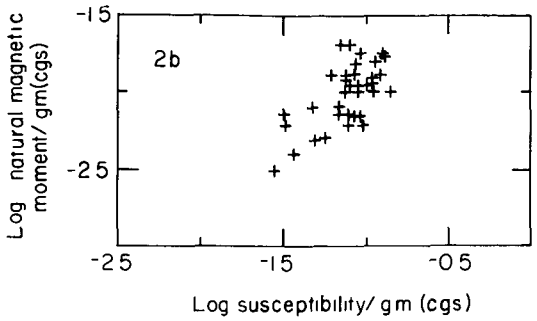

Figure 2b. Log-log plot of $\overline{p}$ vs. $\overline{\chi}$ for 38 samples of the meteorite Pultusk showing the relatively small distribution of moment and susceptibility compared to the total population represented in Fig. 1. Pultusk fell in 1868.

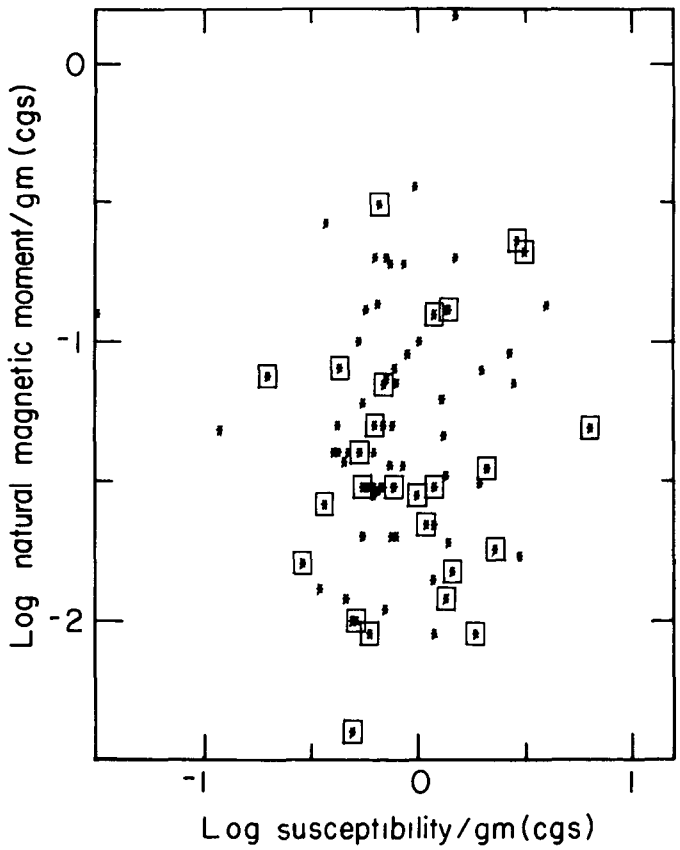

Figure 3. Log $\overline{p}$ vs. $\overline{\chi}$ for the iron sub-class of Fig. 1. The boxed values are those for which the Hey catalog suggests modification due to atmospheric entry. Although a general randomization of the data cannot be ruled out, there seems no trend to larger or smaller $\overline{p}$ or $\overline{\chi}$.

CHAPTER 2 - ASTEROIDS, COMETS, SATELLITES

Near-Earth Asteroids as Targets for Exploration, E. M. Shoemaker and E. F. Helin, Division of Geological and Planetary Sciences, California Institute of Technology, Pasadena, California 91125

The term near-earth asteroid is used here to designate small bodies of stellar appearance which pass near 1 AU at perihelion or at aphelion or are on orbits with semi-major axes near 1 AU. A few of the known near-earth asteroids are the easiest bodies to reach by spacecraft, beyond the Moon. Physical observations of these objects suggest that they have a broad range of composition; some probably are the most primitive solid objects that are readily accessible for detailed study. Thus they are of special interest for exploration.

At least two different kinds of bodies probably are represented among the known near-earth asteroids: 1) objects or fragments of objects which reside in or were derived from the main asteroid belt, and 2) non-volatile residua or cores of the nuclei of extinct periodic comets. The former category may include objects which were on Mars-crossing orbits to start with or were initially close to regions of secular resonance or of low order commensurability with Jupiter. The second category of bodies is derived ultimately from much more distant parts of the solar system. Periodic comets are captured from the Oort cloud by close encounters with Jupiter, and a small fraction of the periodic comets are trapped in very short period orbits by non-gravitational forces. An example of a very short period comet is P/Encke. Whatever non-volatile residue may remain from such an object after 10^3 to 10^4 years will be asteroidal in appearance. As a consequence of encounters with the terrestrial planets, further evolution of the orbits of both "asteroidal" and the "cometary" near-earth objects, particularly of earth-crossers, result in an extensive overlap of the orbital characteristics of the two classes of objects.

The number of Mars-crossing asteroids appears to be sufficient to sustain no more than about 10% of the earth-crossing asteroid population in steady-state (by perturbations of Mars-crossers during close encounters with Mars). Furthermore, the ratio of the number of earth-crossers to Amor asteroids ($1.02 \text{ AU} < q \leq 1.30 \text{ AU}$) appears to be an order of magnitude higher than that expected, if all near-earth objects were derived from Mars-crossers. Hence, although Amor asteroids are apparently in equilibrium with and derived mainly from shallower Mars-crossers, the earth-crossing asteroids are inferred to be primarily of different origin. The supply of extinct short period comets seems to be adequate to sustain the population of earth-crossers, but little is known about the ultimate state of degassed comet nuclei.

Precise physical observations have been made on somewhat more than a dozen near-earth asteroids; about half of these are Amors and half, earth-crossers. Observed Amors occupy a broad region in the U-B versus B-V color domain, whereas the observed earth-crossers have a more restricted range of color. The UBV fields of observed Amors and earth-crossers exhibit only a small overlap. Spectrophotometry of the best observed Amor and earth-crosser (Eros and Toro), on the other hand, suggest that these two bodies are similar in composition to common stony meteorites.

It is widely believed that extinct cometary nuclei should resemble C-type asteroids, but only one apparent C-type object, (1580) Betulia, has been discovered so far, among the near-earth objects. If earth-crossers are predominantly of cometary origin, it appears likely that either the expectations concerning the color and other properties of extinct comets is in error or that there is an unusually strong observational selection effect which decreases the chances of finding C-type objects.

Primary goals for the exploration of near-earth asteroids would be to determine their chemical and mineralogical composition and especially to determine their structure. Objects derived from the main-asteroid belt are likely to be fragments of larger bodies. As such they would provide direct evidence on the internal structure, processes, and history of the larger parent asteroids. Non-volatile cores of extinct comets, on the other hand, may yield the most direct evidence obtainable concerning the early stages of accretion of solid matter in the solar system, specifically in the outer part of the system. Return of samples would be essential to develop and decipher this evidence. Because the known near-earth asteroids are small (a few hundred meters to a few kilometers in diameter), their regoliths should be very thin. Sufficient bedrock may be exposed, in crater walls and elsewhere, to determine the structure of these objects from a combination of remote and on site observations and samples.

Study of unmanned missions shows that between 5% and 10% of the near-earth asteroids can be reached by low ΔV ballistic trajectories (ΔV from low earth orbit less than the 6.4 km/sec required for redezvous with Mars). Two of the best candidates, from the trajectory standpoint, are 1977 VA, discovered by us this past year, and (1943) Anteros. Both of these are Amor asteroids. Rendezvous is achieved near aphelion, and the minimum ΔV required for sample return to earth is very low -- of the order of 1 km/sec. Because the ΔV for landing and escape from these small asteroids is of the order of 1 m/sec, many landings could be made to visit and sample different parts of an asteroid in the course of a single mission. As shown by Niehoff (1977), a sample return mission to (1943) Anteros is well within the launch capability of a single space tug. An aggressive astronomical search for more near-earth asteroids will undoubtedly yield many more promising candidates for this type of exploration.

Our discovery of 1976 AA, ($a=0.97$, $e=0.18$, $i=19°$) indicates that there probably exist at least a few asteroids which are extremely close neighbors of the earth. The extreme near-earth objects are expected to be earth-crossers with semi-major axes near 1 AU that have acquired small e and i as a consequence of repeated close encounters with the earth. Typically, these objects would be accessible by low ΔV missions of 6 months or a year duration. Manned missions to explore such bodies might well be within the realm of both technological feasibility and the NASA budget within the next 15 years. Roughly about 1% of the earth-crossing asteroids might be sufficiently close neighbors of the earth to be considered candidates for manned missions in this time frame. The discovery rate for earth-crossers would have to be increased by a factor of about 5, however, in order to achieve a 50% expectancy of finding a suitable target within 10 years.

Reference Cited

Niehoff, J. C., 1977, Round-trip mission requirements for asteroids 1976 AA and 1973 EC: Icarus, v. 31, p. 430-438.

PLANETARY CLOSE ENCOUNTERS: CHANGES IN A PLANET-CROSSING POPULATION. A. Carusi, Lab. Astrofisica Spaziale, CNR, Frascati (Italy), F. Pozzi, Univ. Rome (Italy), G. Valsecchi, Univ. Rome (Italy).

About 3000 close encounters have been computed between Jupiter and three random populations, in order to investigate the effects due to a close approach to a giant planet on the evolution of minor object orbits in the Solar System.

The first population, ASTRID, was an asteroid-like group of objects; the second one, COMET, a comet-like group, and the third, RANDUN, an intermediate one.

These populations were generated with the primary aim to test a new method of treatment of a very close approach to a planet. Only one close encounter for each object has been computed, but the populations were so numerous to allow a statistical analysis of the orbital elements variations.

This kind of analysis has been performed, and it gave many interesting results (1,2).

In the original data sets a great number of objects has been recognized as planet-crossers, in the sense that their perihelion distances were smaller than the aphelion distances of the inner planets, or their aphelion distances were greater than the outer planets perihelion distances. However, these conditions are necessary but not sufficient to ensure a close encounter with the planet. In evaluating the possibility that the late stages of inner planets cratering were caused by asteroid-like objects, it is necessary to know if a close encounter can happen. If we define close encounter only the passage into a suitable sphere of influence around the planet, the number of objects that we can consider as planet-crossers becomes much smaller.

As a matter of fact the orientation and the lying of the orbit in the space can inhibit the actual crossing of the planetary sphere of influence.

The values of the radii of these spheres have been calculated from the

$$R = 2(m')^{2/5}a$$

where m' is the planet's mass in unit of the solar mass, and a is the semi-major axis of the orbit.

A test of appurtenance to the inner-planet-crossing population has been performed on initial and final data sets obtained collecting together the three initial populations.

Results obtained using the first mentioned planet-crossers definition (geometrical) are shown in Tab. Ia, while Tab. Ib contains the results obtained taking into account the possibility of a close encounter with the planet.

Tab. Ia	MERCURY	VENUS	EARTH	MARS
A	4	6	9	25
B	1	5	7	21
C	5	24	65	202
C/(C+A)	.55	.80	.88	.89
C/(C+B)	.83	.83	.90	.91

Tab. Ib				
A	---	4	9	14
B	---	2	5	4
C	---	1	1	1
C/(C+A)	---	.20	.10	.07
C/(C+B)	---	.33	.17	.20

A: Planet-crossers only before the encounter with Jupiter
B: Planet-crossers only after the encounter with Jupiter
C: Planet-crossers before and after the encounter with Jupiter

The total number of planet-crossers before and after the encounter with Jupiter can be obtained adding C to A, and C to B respectively for each planet. It is interesting to note that the ratios C/(C+A) and C/(C+B) are much greater in Tab. Ia than in Tab. Ib. This means that the planet-crossers definition is very important in order to evaluate the changes in a planet-crossing population. In fact, using the first geometrical definition, the planet-crossing populations are mainly formed by type C objects, showing that the efficiency of the close encounter with Jupiter is low. On the contrary, using the sphere of influence definition, the close encounter with Jupiter is very effective in diminishing and renewing the planet-crossing population.

All but one the B and C objects reported in Tab. Ib may experience a second encounter with Jupiter: therefore, if further analyses on a more conspicuous population will confirm the mentioned depletion effect, it will be possible to conclude that close encounters with the outer planets provide much less material to the inner regions of the Solar System than what they subtract.

REFERENCES

(1) Carusi A., Pozzi F., 1978a; In preparation.
(2) Carusi A., Pozzi F., 1978b; In preparation.

Asteroids as Geologic Materials: Collisions and Fragmentation. Clark R. Chapman, Donald R. Davis, and Richard Greenberg, Planetary Science Institute, 2030 East Speedway, Tucson, Arizona, 85719, and John Wacker, Department of Planetary Science, University of Arizona, Tucson, Arizona 85721.

Asteroids have been substantially altered by collisions, dominantly among themselves, but also with other interplanetary populations, subsequent to their formation early in solar system history. It is necessary to understand collisional evolution and fragmentation processes in order to address questions regarding the size distribution of the original asteroid population, or why a planet failed to form in this region, or to interpret the structure of the observed asteroid size-frequency distribution. We have developed and continue to refine a computer model to simulate asteroid collisional evolution over the 4.5 b.y. age of the solar system. In an earlier work, Chapman and Davis (1) argued on the basis of preliminary computer models that the present asteroid belt was possibly the remnant of a much larger population and, based on a genetic model for the "C" and "S" types of asteroids developed by Chapman (2, 3), the initial C population was estimated to be about 300 times its present value.

Subsequent to our preliminary study, there has been considerable new data on the size frequency distribution of separate asteroid compositional classes (4) together with an improved understanding of fragmentation processes and more sophisticated modelling of the relevant physical processes. Our present model is capable of tracing the collisional evolution of two distinct populations composed of different geologic materials over the age of the solar system. Our fragmentation algorithm considers both material strength and gravitational binding in calculating the energy requirements to disrupt and disperse an asteroid of a given size and composition. The size distribution of fragments from a catastrophic collision is calculated from available experimental results. Figure 1 depicts the collisional evolution determined by the Chapman-Davis program for one initial population of C and S type asteroids that evolves rather closely to the present distribution of these asteroids. The evolution is found to be very sensitive to physical properties, particularly material strength.

Our current collision program treats only catastrophic collisions and neglects the erosive effects of cratering events; an approximation originally suggested by the present asteroid size frequency distribution which has most of the mass contained in the largest bodies. However, this condition may not have held throughout solar system history. Also, the asteroid orbital distribution is constrained such that the mean encounter speed is constant; a condition which also may not have been satisfied at all times. We are able to assess the effect of these assumptions on the collisional evolution of a single population by comparing with a program developed by Greenberg et al (5) to model planetary accretion and evolution which incorporates both orbit evolution and cratering collisions. Preliminary runs to date indicate little change in the mean encounter speed while the importance of cratering erosion depends on the population distribution. Further comparisons currently in progress will provide an assessment of the overall validity of the collisional evolutional model together with an evaluation of the effect of the above

noted approximations.

For large asteroids, gravitational binding is the dominant cohesive mechanism. Hence, there will be many collisions imparting sufficient energy to fracture the body without dispersing the fragments before there is a catastrophic collision involving sufficient energy to overcome the gravitational barrier. A plausible model for many large asteroids is that they are thoroughly fractured, gravitationally bound, "rubble piles." When such a body experiences a catastrophic collision, the size of the largest fragment will be only a minute fraction of the size of the original body, resulting in a large population of small bodies. This contrasts with earlier models in which barely catastrophic collisions resulted in a largest fragment containing roughly 50% the mass of the original body. One consequence of such a hypothesis is that most large asteroids are not collisional fragments from catastrophic disruption of even larger objects, but rather are bodies which have been only eroded throughout solar system history.

Our studies of asteroid collisional evolution lead to the following conclusions: (1) Asteroids presently impact each other with sufficient frequency that most large asteroids must be expected to have been catastrophically fragmented within the last several billion years. Provided that 5% to 10% of the kinetic energy is available for fragment dispersal, most large asteroids have lifetimes against disruption shorter than the age of the solar system. Thus, those that we see now must be either (a) rare individuals that have chanced to escape disruption and are remnants of larger bodies that have been whittled down by gradual erosion; or (b) fragments of rare larger bodies that chanced never to have been converted into a "rubble pile" by earlier fragmenting impacts prior to catastrophic disruption. All small asteroids must be regarded as being multi-generation and/or recent fragments of larger bodies. These expectations are in accord with several observations: asteroid spins are those expected for a collisionally evolved population (7) and asteroid shapes seem to be irregular except for asteroids sufficiently large and weak that gravity induces sphericity. (2) Asteroid size-frequency distributions are not expected to be linear on a log-log plot. It had been argued previously that all asteroids (6) or at least collisionally-evolved C-type asteroids (2) should exhibit such a linear distribution. But two effects lead to non-linearities: (a) the effects of gravity holding together fragmented objects until supercatastrophic collisions disrupt them and (b) the interaction of populations of different strengths; Fig. 1 illustrates the non-linear asteroid frequency distributions. (3) The present asteroid population may be a remnant of a much larger early population (1). The arguments listed above regarding the present population of large asteroids support the augmented initial population hypothesis. Fig. 1 is typical of most runs of the collision evolution model in that input populations orders of magnitude greater than the present belt (such as "input C" in Fig. 1) always decay to distributions approximating the present belt (in both slope and intercept) after several billion years. The only initial large populations that fail to evolve to the present belt are those in which most of the mass is originally stored in bodies substantially larger than Ceres, approaching lunar size. Note that result (1), that asteroids are highly fragmented, does not depend on the early asteroid population being more populous than today; present impact rates are sufficiently high to lead to high frag-

mentation rates, even if the asteroid belt originally contained only a fraction more mass than it does today.

Several sources of uncertainty require emphasis. First, because of the relatively large ratio of target to projectile diameters sufficient for catastrophic fragmentation, the evolution of main-belt asteroids of observable sizes depends on the frequency of very-much-smaller asteroids - those too small to have measured surface compositions and often so small as not to be observable at all. Thus observations pertaining to the frequency and probably bulk compositions of asteroids in the 100 m-10 km size range would be very important. Second, more experimental and theoretical work is necessary to understand how projectile kinetic energy is partitioned into comminution energy and especially into ejecta or fragmental kinetic energy. Large quantities of energy could be partitioned into heat without necessarily melting major amounts of rock. Should much less than 1% of the energy be available for kinetic energy, asteroid lifetimes might be much longer than we have estimated. Should smaller fractions of energy be available for comminution throughout the asteroidal volume than is true at laboratory scales, asteroids might be less fragmented than we have suggested.

References: (1)C.R. Chapman and D.R. Davis, Science 190, 553 (1975); (2)C.R. Chapman, Geophys. Res. Lett. 1, 341 (1974); (3)C.R. Chapman, Geochim. Cosmochim. Acta 40, 701 (1976); (4)B. Zellner and E. Bowell, in Comets, Asteroids, Meteorites-Interrelations, Evolution and Origins (A.H. Delsemme, ed.), 185-197, Univ. of Toledo (1977); (5)R. Greenberg, J.F. Wacker, W.K. Hartmann, and C.R. Chapman, Icarus, in press (1977); (6)J.S. Dohnanyi, Icarus 17, 1-48 (1972); (7)A.W. Harris, Icarus, submitted (1977).

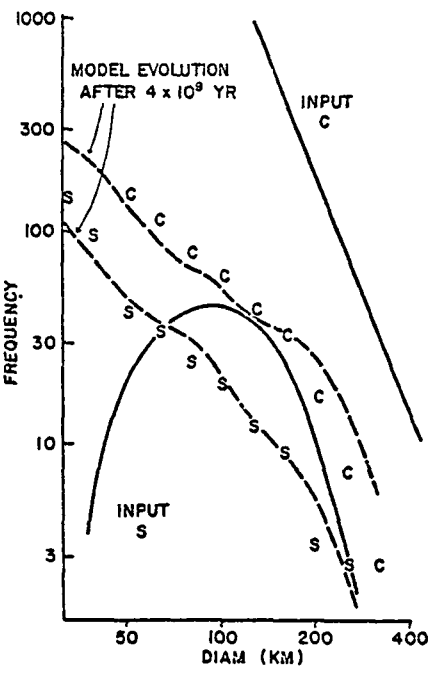

Figure 1: Comparison of Chapman/Davis evolution model with observations. For this particular run, initial size-distributions were chosen (solid lines) to model the type of scenario described by Chapman (3). C and S asteroids were taken to have crushing strengths of 5×10^7 and 2×10^{10} dynes cm^{-2}, and densities of 3 and 5 gm cm^{-3}, simulating carbonaceous and iron-rich asteroids respectively. Impact strengths were taken to be 6% of crushing strengths. The mass of the largest fragment involved in a supercatastrophic disruption was taken to be 1/8th the original mass; much smaller fractions, depending on energy density, might be more appropriate and would result in diminished production of middle-sized asteroids. The dashed curves show the evolved C and S populations after 4×10^9 years. Plotted for comparison are bias-corrected frequencies of C and S asteroids observed today by Zellner and Bowell (4). The frequencies are per interval of width 0.1 in log diameter.

Gravitational Interaction Between Fragments of a Split Comet, Z. Sekanina, Harvard-Smithsonian Center for Astrophysics, Cambridge MA 02138.

The n-body computer program by J. Schubart and P. Stumpff (1966, Veröff. Astron. Rechen-Inst. No. 18, 1-31) has been modified to study the gravitational interaction between two fragments of a split comet nucleus in the sun's gravitational field. All calculations refer to the orbit of Comet West (1975n), the velocity of separation of the fragments is assumed to be equal in magnitude to the velocity of escape, and the numerical integration of the relative motion of one fragment (called the companion) with respect to the other (called the principal fragment) is carried over the period of 200 days from separation. The motion of the companion is investigated as a function of the following circumstances at splitting:

(1) Position of the comet in heliocentric orbit at the time of splitting. Considered are three locations, whose true anomalies are -90°, 0°, and $+90^\circ$, corresponding, respectively, to heliocentric distances of 0.393 AU prior to perihelion, 0.197 AU (perihelion), and 0.393 AU subsequent to perihelion.

(2) The mass of the principal fragment. Two cases are considered: 10^{17} and 10^{15} grams.

(3) The mass ratio of the principal fragment to the companion. Calculations are done for ratios 1:1 and 100:1.

(4) The average bulk density of the fragments. Densities used are 1 and 0.1 g cm^{-3}, same for both fragments.

(5) Direction of separation of the companion from the principal. Considered are six cardinal directions: sunward; forward, i.e., perpendicular to the sunward direction in the orbit plane in the sense of the direction of the comet's orbital motion; northward, i.e., in the direction of that orbital pole from which the comet is seen to orbit the sun counterclockwise; and the respective opposite directions: anti-sunward; backward; and southward.

(6) Area of separation of the companion on the nucleus surface. Again, six basic locations are investigated: subsolar area; leading-side area, oriented in the forward direction from the center of the nucleus; north-pole area; and the areas located opposite these: anti-solar area; trailing-side area; and south-pole area.

The possible combinations of the six variables represent a total of 720 patterns. Fortunately, symmetries with respect to the orbit plane reduce the number of independent patterns by 216, and other symmetries that lead to virtually identical patterns reduce the number by additional 240 to leave a total of 264 patterns. Furthermore, the only measurable effect of the mass of the principal fragment is that on the dimensions of the companion's orbit, which scale with the cube root of the mass. This brings the number of patterns under consideration down to 132.

On computer generated plots of the results the variations with time in the separation between the fragments, in their relative velocity, and in the angle subtended by the separation and velocity vectors have been examined for similarity in appearance, separately for each of the three positions in heliocentric orbit. It has been found that the differential gravitational effect of the sun becomes noticeable about 0.5 to 1 day after separation for the breakup taking place at perihelion, and about 1 to 2 days after separation for the heliocentric distance at breakup twice the perihelion distance. It has further been found that the visual appearance of the plots is not affected fundamentally by the bulk density and by the fragment mass ratio (although the outcome of the dynamical solution may so be affected). Consequently, it has been possible to categorize the patterns in terms of only the direction of separation and the area of separation by considering the following eleven standard patterns: separation sunward from (1) subsolar area, (2) leading-side area, (3) north-pole area, (4) trailing-side area; separation forward from (5) subsolar area, (6) leading-side area, (7) north-pole area; separation northward from (8) subsolar area, (9) leading-side area, (10) north-pole area; and (11) separation backward from subsolar area.

For the splitting at true anomaly -90° the calculated patterns can be divided into 7 categories:

Category A_1 encompasses separations from the leading-side area sunward, forward, and northward, and from the trailing-side area sunward. The separation increases monotonically. The companion escapes along a very strongly hyperbolic orbit; inclination to the comet's orbit plane is zero or very low; prograde motion.

Category B_1 includes separations from the north-pole area sunward and forward. Except for a shallow minimum shortly after perihelion the separation increases monotonically. The companion escapes along a high-inclination, strongly hyperbolic orbit; prograde motion.

Category C_1 is represented by a separation forward from the subsolar area. The separation distance increases monotonically but at rather a slow rate. The velocity surges at perihelion, then follows a profound decrease and a moderate upswing. The companion appears to escape in a slightly hyperbolic orbit; zero inclination; retrograde motion.

Category D_1 is a separation northward from the subsolar area. The separation curve has a complicated shape; the velocity curve, after a sudden upswing near perihelion, displays a downward trend. The companion gets into a highly elongated quasi-stable elliptical orbit with a period $\sim$240 days; high inclination; retrograde motion.

Category E_1, a separation sunward from the subsolar area, exhibits a separation curve that gradually levels off, and a velocity curve with a very deep minimum about 30 days after splitting. The companion gets into a highly elongated quasi-stable elliptical orbit with a period of 226 days; zero inclination; retrograde motion.

Category F_1, a separation backward from the subsolar area, displays very complicated separation and velocity variations. The companion pursues a retrograde orbit, whose eccentricity is just slightly less than unity. The patterns with the bulk density 0.1 g cm^{-3} show the fragments crashing into each other 120 days after breakup for the mass ratio 1:1, 129 days for 100:1.

Category G_1, a separation northward from the north-pole area, is characterized by a crash of the fragments 15 days after breakup regardless of the mass ratio and the density.

For the splitting at perihelion there are 5 categories of patterns:

Category A_2 contains the four patterns of Category A_1. The companion's motion displays similar but still noticeably more vigorous escape characteristics (prograde motion).

Category B_2 includes the patterns of Categories C_1, D_1 and E_1. The companion's motion differs from that in Category A_2 by appreciably milder hyperbolic excess (prograde motion).

Category C_2 is represented by the pattern of Category F_1. Escape is still more hesitant, and in the case of the high mass ratio combined with the low bulk density the hyperbolic motion is replaced by an elliptical one; zero inclination; prograde motion.

Category D_2, comprising the two patterns of Category B_1, shows the companion to get into a high-inclination elliptical orbit that looks rather stable. The eccentricity and the revolution period depend strongly on the mass ratio and on the density; prograde motion.

Category E_2 contains the pattern of Category G_1 and is again characterized by a crash of the fragments, this time 16 days after breakup.

Finally, for the splitting at true anomaly $+90^\circ$ we have the following categories:

Category A_3, encompassing the patterns of Categories C_1, D_1, E_1 and F_1, shows the companion's behavior reminiscent of that in Category B_2 (prograde motion).

Category B_3 is identical in contents with Category A_1 except for a separation sunward from the trailing-side area. The companion escapes almost exactly radially and the sense of motion changes from retrograde to prograde; zero or low inclination.

Category C_3 is the separation sunward from the trailing-side area. The companion gets into a high-eccentricity elliptical orbit; zero inclination; retrograde motion.

Category D_3 contains the patterns of Category B_1. The companion's motion is elliptical, somewhat similar to that in Category D_2, but less dependent on the mass ratio and the density; high inclination; prograde motion for the separation sunward, retrograde for the forward.

Category E_3, identical in contents with Category G_1, shows again the two fragments crashing into each other, this time 90 days after breakup.

The presented results, especially the great variety of the companion's dynamical behavior depending strongly on the circumstances at breakup, have implications for the observed split comets. Some of the problems will be subject of the continuing study, including the investigation of the interrelation between the gravitational and the nongravitational perturbations, the interpretation of the time of splitting and the velocity of separation as derived from observations of the split comets (Z. Sekanina 1977, Icarus 30, 574-594; 1977, Astrophys. Lett. 18, 55-59; 1977, Proc. IAU Colloq. 39, 51-56; 1978, Icarus 33, 64-71), and the exploration of the possibility of the existence of binary and multiple comet nuclei.

This work has been supported by Grant NSG 7082 from the National Aeronautics and Space Administration.

The Rotation of Comet Nuclei

F. L. Whipple, Smithsonian-Harvard Center for Astrophysics, 60 Garden St., Cambridge, Mass. 02138.

Methods have been developed and applied for the determination of a)the axis of rotation and b) the period of rotation of a comet nucleus.

The first method(for axis)involves asymmetry of coma ejection from active areas on the nucleus. Analysis is made of the displacement direction on the sky or position angles of the coma as displaced from the observed nucleus. The method is particularly applicable to comets of large perihelion distance, q, and was applied to P/Schwassmann-Wachmann 1 with q=5.5 AU, aphelion distance, Q∿7 AU, Period=16^{y}.5 (Whipple 1977). The figure portrays the relationship between the mean directions of coma ejection and a model rotating comet nucleus (see Fig. caption). Outbursts of this comet are usually from specific limited areas but can increase its brightness by more than 100 times. The outbursts appear to take place near the meridian and in the afternoon, not too far (<∿50°)from the subsolar point. Of particular interest is the lag in migration of old active arears shown by a persistence towards the East or receding limb of the nucleus in the sense of orbital not rotational motion. Correspondingly, new active areas resist development towards the West or approaching limb.

The second method (for rotation period) depends upon measurement of coma halo diameters, produced by the wide-angle ejection of dust and/or gas by gas from active areas as they are periodically rotated toward the solar meridian of the nucleus. The velocity of ejection, v, follows very closely a law derived from Bobrovnikov's data, $v=535r^{-0.6}ms^{-1}$ where r is the solar distance in AU.

Because r and geocentric distance are known from orbital data, the halo diameters and v provide a value of the time since ejection, Δt. In turn, the observed date minus Δt provides the moment of halo initiation or zero date, ZD. If the halos arise from a single or major active area, the ZD's should be spaced at intervals which are multiples of the period. If two or more halos occur concurrently, the differences in successive Δt's should equal one period. Hence the method is self checking. Once the period is known approximately, giving a count on the revolution numbers, a further check can be made on the assumed velocity. A least-squares solution for a multiplying factor to Δt as well as for the period provides a correction to 1/v. From experience with six comets, the correction factor is ∿1.1. Thus the velocity as derived from the equation appears to be about 10% too high.

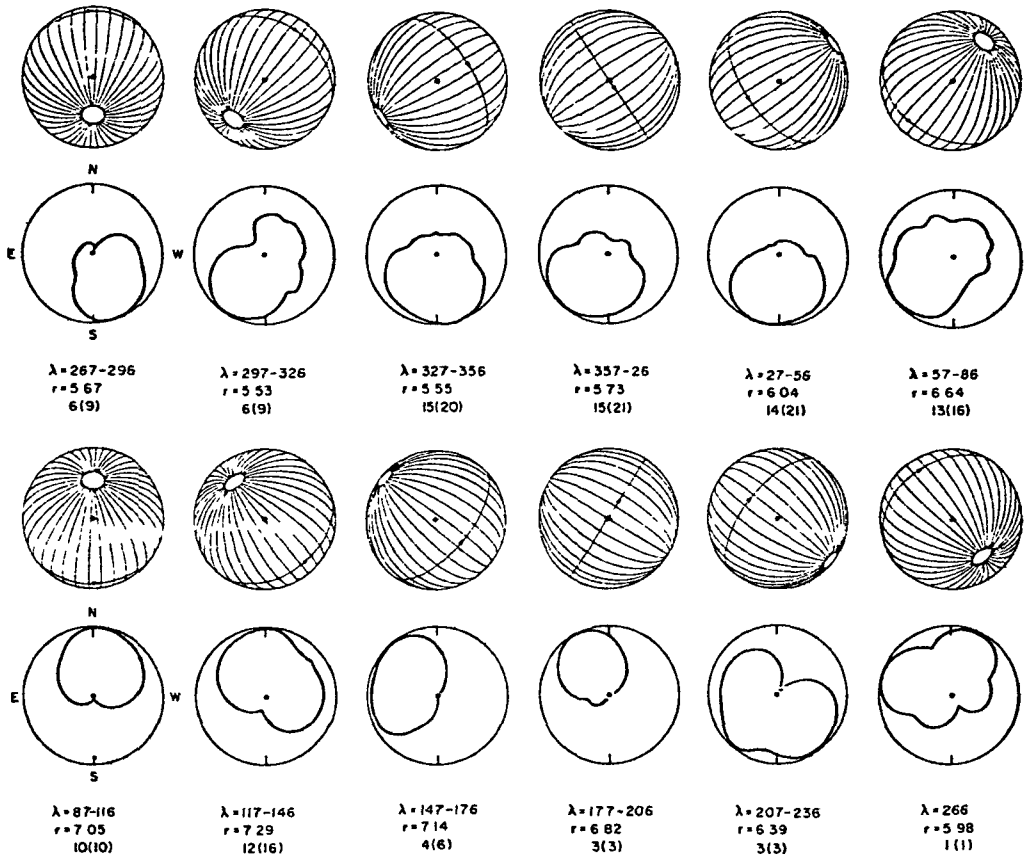

Figure: Mean directions of coma asymmetries for P/Schwassmann-Wachmann 1 at 30° intervals in orbital longitude (λ) over nearly 3 revolutions (1927-1970); r: solar distance, AU; below: number of observations combined; the spheres represent a trial of polar orientation for the comet nucleus; period of rotation, 121^h, pro-grade; obliquity of equator to orbit plane ∿65°; longitude No. Pole ∿280°.

- - - - - - - - - - - - - - - - - - - -

The Table presents the current status of rotation-period determinations for 8 comets, of which 6 are new determinations by the writer. It will be noticed that none of the comets are new (in the Oort sense) nor, indeed, very young. Apparently older comets develop theick crusts, presumably of meteoroidal debris, that inhibit activity over much of their surface. Thus only the older comets are apt to show single active areas to make solutions possible for rotation vectors. Perhaps another dozen comets can be so analysed.

A number of deductions concerning amorphous ices in comets, details of their physical and chemical structure and certain limits on the conditions of cometary aggregation follow from this research (Whipple, 1977, 1978a,b,c).

Comet Nuclei Rotations
(as of Mar. 1, 1978)

Period	Comet	Source
$4^h.62$	Donati 1858VI (P∿2000 y) Comment: Like a clock for a month! ($4^h.27$, in 1863)	F.L.W. (1978a) (J.F.J. Schmidt got
$5^h.11$	P/D'Arrest (P=6.2 y) Comment: Probably correct.	Fay & Wisniewski (1976)
$9^h.1$	Coggia 1874III (P∿14000 y) Comment: Close to final value	F.L.W.
$11^h.1$	P/Halley (P=76 y) Comment: Probably correct (small probability of 1/2 this period).	F.L.W.
$13^h.8$	Daniel 1907IV (P∿8000 y) Comment: G. Horn's 1908 value of $16^h.0$ not confirmed. Axis?	F.L.W.
33^h	Swift-Tuttle, 1862III (P=120 y) Comment: One-half value of J.F.J. Schmidt in 1863.	F.L.W.
35^h(?)	Bennett, 1970II (P∿1600 y) Comment: F.L.W. has not had success with their method.	Larson & Minton (1972)
121^h	P/Schwassmann-Wachmann 1 (P=16Y5) Comment: No. Pole, Long∿280°; obliquity equator to orbit ∿65°; Prograde. Active regions migrate slowly.	F.L.W. (1977)

References:

Fay, T.D. and Wisniewski, W. (1976) Preprint Lun. Planet. Lab., Tucson, Ariz.

Horn, G. (1908) Mem. Soc. d Spettroscopisti, Ital., 37, 65.

Larson, S.M. and Minton, R.B. (1972) "Comets Scientific Data and Missions," ed. G.P. Kuiper and E. Roemer, Tucson, Ariz., 183. (Libr. Congr. Cat. No. 72-619613).

Schmidt, J.F.J. (1863) Astr. Nach., 59, 97.

(1863) Pub. Athens Obs., Ser. 1, Vol. 1.

Whipple, F.L. (1977) Bull. Am. Astr. Soc., 9, 563 (abstract).

(1978a) CFA Preprint #894. Nature, in press.

(1978b) CFA Preprint #814. Astrophy. and Sp. Sci., in press.

(1978c) CFA Preprint #907. Protostars and Planets in press.

Phobos Globe/Mars Topography, T. C. Duxbury, Jet Propulsion Laboratory, California Institute of Technology, Pasadena, CA 91103

Arrangements have been made to obtain a globe of Phobos which was developed using Mariner 9 imaging of Phobos. The globe will be used in conjunction with the Viking imaging data of Phobos to interpret the alignment and orientations of the grooves and crater chains on Phobos. Computer programs have been modified to process Viking pictures of Mars taken during the approach to Mars to identify possible topographic variations from the outline of the lit limb. Three pictures of Mars taken with the violet, green and red filters are being processed.

Phobos: Photometry and Origin of Dark Markings on Crater Floors. J. Goguen and J. Veverka, Laboratory for Planetary Studies, Cornell University, Ithaca, New York 14853 and T. C. Duxbury, Jet Propulsion Laboratory, California Institute of Technology, Pasadena, California 91103.

High resolution images of Phobos obtained during the 1977 close flybys by Viking Orbiter 1, reveal conspicuous dark patches on the floors of many craters (eg. frame 248A05). These dark patches are especially prominent at large phase angles.

By measuring the contrast of these dark markings relative to the adjacent "average" surface on images obtained at different phase angles, we have constructed a relative phase curve and found that:

(a) While the contrast may reach more than 50% at phase angles $\alpha \gtrsim 70°$, it is $\lesssim 10\%$ at phase angles close to zero.

(b) The normal reflectance of the "dark" material does not differ by more than 10% from that of the surroundings, but the phase coefficient is at lease 25% larger than that of the surroundings. (At phase angles $\alpha \lesssim 40°$ the phase coefficient is 0.007 mag/deg larger; the difference increases for $\alpha > 40°$).

These facts suggest that the "dark" material differs from its surroundings much more in its texture than in its normal reflectance: it appears conspicuously darker at large phase angles because its rougher surface produces more shadows.

A simple model of surface roughness shows that the observed phase dependence can be reproduced by a surface covered with parabolic holes of a depth/diameter ratio $\gtrsim \frac{1}{2}$. Such a rugged texture is suggestive of a vesicular material, but we note that this interpretation is non-unique since roughness elements of positive relief (bumps rather than holes) will yield comparable phase curves. Nevertheless, we find it significant that pools of vessicular impact melt have been reported at the bottoms of the ejecta voids produced during the formation of a) terrestrial impact craters (Dence, 1968; in Shock Metamorphism of Natural Materials, p. 168), b) nuclear explosion craters (Short, 1965; Ann. N.Y. Acad. Sci., 123, 573), c) experimental craters produced in the laboratory (Stöffler et al., 1975; JGR, 80, 4062), and suggest that the patches of texturally rough, "dark" material on the floors of many Phobos craters are exposures of impact melt. The low value of g and the consequent small amount of fallback ejecta would account for the prominence of this phenomenon on Phobos.

A possible alternative explanation is that the dark patches represent evidence of near horizontal layering in the outer portions of Phobos. In this case one would expect the exposures of the coarse material to occur at concordant depths, at least locally, but this does not appear to be the case. Another possibility is that the dark patches are accumulations of coarse debris, preferentially collecting at the bottoms of craters. Since g is very small, this preference may not be significant. Nevertheless, it is possible to test this hypothesis since it predicts that, other things being equal, older crater should have more conspicuous dark markings than younger craters (since they have had more time to accumulate coarse debris). On the other hand, the

impact melt hypothesis which we favor predicts that the youngest craters should exhibit dark patches best, since micormeteroid erosion and blanketing by ejecta from neighboring impacts will eventually obliterate the contrast between the impact melt and its surroundings. The available evidence supports the impact melt hypothesis: the dark markings are most conspicuous in the fresher-looking (hence probably younger) craters.

Our hypothesis suggests that analogous dark markings may be visible at large phase angles on the surfaces of other low g bodies (Deimos, small asteroids, etc.). However, we now know that they are not prominent on the surface of Deimos — possibly because most of the craters imaged at high resolution on the surface of the outer satellite appear to have been blanketed by several meters of fine-grained material having many of the characteristics of ejecta.

A Comparative Study of Surface Features on Phobos and Deimos. P. Thomas, J. Veverka and A. Bloom, Cornell University, Ithaca, N.Y. 14853 and T. C. Duxbury, Jet Propulsion Laboratory, 4800 Oak Grove Drive, Pasadena, California 91103.

High resolution Viking Orbiter images have shown that the surfaces of the two small satellites of Mars have significantly different morphologies. For example, although both Phobos and Deimos are heavily cratered, the craters on Deimos appear to be partially filled in by what seems to be ejecta, whereas on Phobos no comparable infilling is conspicuous. Also, the surface of the inner satellite is covered by sets of very extensive linear depressions (grooves) that have no counterparts on Deimos.

The general pattern of grooves on Phobos is shown in Figure 1 with the large crater Stickney included for reference. The pattern is clearly related to Stickney. No other crater has separate associated groove patterns and no crater deforms or enlarges grooves in its vicinity. The grooves define planes cutting much of Phobos, and occur in several sets of many parallel members. The most prominently developed grooves define planes with normals that lie near the a - c plane of Phobos (the plane which includes the sub-Mars point and the poles), but there are grooves which define planes with normals at large angles to the a - c plane.

Relief inside the grooves ranges from 5 to 90 meters, widths are between 40 and 700 meters, and continuous grooves are up to 14 km long; grooves with small gaps are as much as 25 km long. Most grooves are best described as strings of coalesced depressions (pits) and have beaded outlines. Profiles across the grooves are usually smoothly concave-up; profiles along grooves have smooth concave-up depressions. Many of the pits are very subtle and groove walls may appear very straight. Only the largest grooves near Stickney have floors that are distinct from the groove walls. These floor have an irregular hummocky topography, and the adjacent walls are nearly straight. The maximum and average widths and depths of grooves decrease away from Stickney.

Some grooves grade into linear zones of hummocky topography with ill-defined margins at the same level as the surrounding surface.

The grooves are intepreted as surface expressions of fractures cutting much of Phobos. The smooth slopes of groove walls imply formation in material of low cohesion that has no significant layering. The association of the pattern and size of grooves with Stickney indicates that the fractures were formed or enlarged by the impact which formed Stickney. The beaded appearance of the grooves is best explained either by drainage of regolith into fractures or by ejection of material from the fractures by impact released volatiles. Evidence for raised rims along some groove segments is ambiguous, but it is clear that raised rims are not essential features of groove morphology.

The 60% of Deimos imaged at resolution 100 meters or better does not show any grooves. The absence of grooves on Deimos may be due to lack of a very large crater (the largest known is about 3 km across), or to a different composition and stronger mechanical strength than Phobos.

The freshest craters on Phobos have depth/diameter ratios of about 0.2, close to the value for the Moon (Pike, 1974). Crater rims are about half as high on Phobos as on the Moon. With the exception of some blocks (20-50 meters wide) near craters, a few "rays", and some hummocky "ejecta" near Stickney, ejecta deposits are not conspicuous on Phobos. However, the surface of Deimos is conspicuously blanketed by material having the characteristics of ejecta. Blocks are abundant in high resolution images; most craters have considerable sediment fill easily distinguished from the crater walls, and bright streaky albedo markings, some forming streamlined tails behind craters, suggesting movement of debris close to the surface. Obvious secondary craters are rare or absent on both satellites.

It is puzzling how so much apparent ejecta gets retained on the surface of as tiny a satellite as Deimos, and why this retention process is so much more efficient on Deimos than on Phobos. It is conceivable that the close proximity of Phobos to Mars makes it easier for impact ejecta to escape from the inner satellite, but the mechanics of such a preferential process remain to be worked out.

Pike, R. J. 1974, Depth/Diameter relations for fresh lunar craters: revision from spacecraft data. Geophys. Res. Lett., 1, p. 291-294.

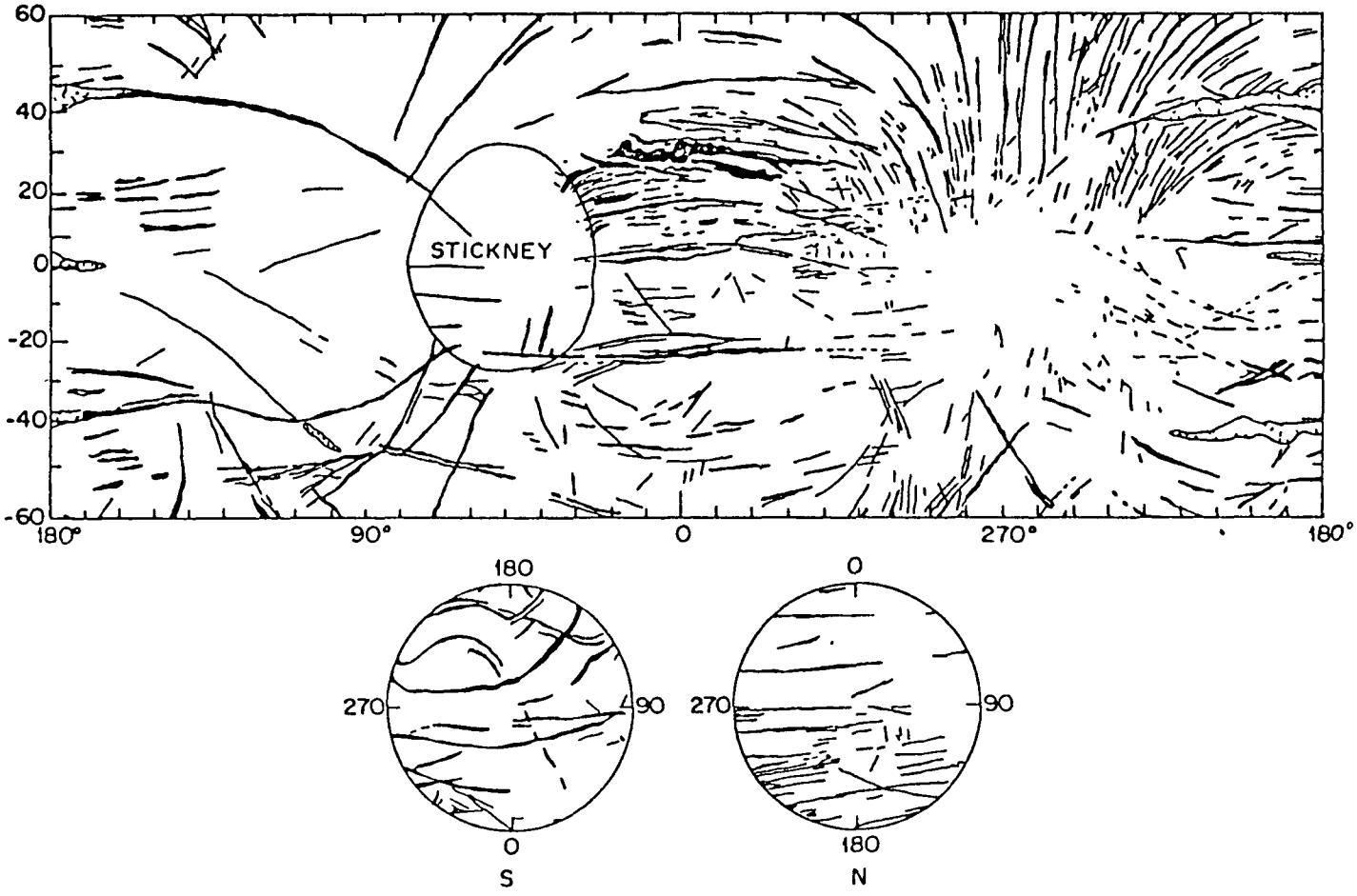

Figure 1: Sketch map of Phobos showing the location of the grooves and of the largest crater Stickney. Stippled areas are hummocky topography in grooves.

Characteristics of the Cratering Process on Small Bodies: Phobos and Deimos, M. J. Cintala, J. W. Head, Dept. of Geological Sciences, Brown University, Providence, RI 02912; and J. Veverka, Laboratory for Planetary Sciences, Cornell University, Ithaca, NY 14853.

Natural impact craters preserved on the Moon and terrestrial planets have provided an opportunity to study the cratering process under a wide variety of conditions of formation and preservation. Because of their small size, Phobos and Deimos offer a potentially significant end point in the study of the effects of gravity, target strength, and curvature in the cratering process. In addition, they may provide important information on the surface history and present characteristics of other small solar system bodies such as asteroids. In this study both moons (Table 1) were taken to be spheres as opposed to the more accurate but correspondingly more complex triaxial ellipsoid approximations, and the gravitational effects of Mars on crater ejecta were ignored.

Several major parameters will be significant in causing differences in the cratering process and resulting landforms on Phobos and Deimos. The extremely small (and variable) radii of curvature (Fig. 1) will play an important role in shock wave and cavity geometry, and in the distance that ejecta will travel (Fig. 2). In addition, the exceedingly low gravitational accelerations[1,2] imply that much ejecta from a single event should reach escape velocity and the remainder should be much more widespread over the target body (Fig. 3) than for a similar size impact on a larger planet. Gravitational modification[2,3] of the transient cavity should be minimal, and strength scaling laws[4] should govern final crater morphologies and geometries.

Cratering Process (Excavation Stage:) - A qualitative evaluation of ejecta ballistics on small bodies was obtained by extrapolating laboratory experimental results[5] (where impact velocity is 1.57 km/sec, ~25% that calculated for Phobos and Deimos). Observed ejection velocities and angles were utilized in calculating ballistic ranges over spherical surfaces (Figs. 2,3). Ejecta which was transported approximately 1 m under terrestrial laboratory conditions[5] would have traveled on the order of 1.4 km on Phobos and more than 3 km on Deimos. If larger scale events at higher impact velocities are considered[6,7], the low escape velocities (Table 1) would imply that a large majority of ejecta would be placed into escape trajectories. These paths are velocity-dependent only, as long as they do not intersect the surface of the target body on the way out. Since material nearest to the rim of the transient cavity is subjected to the lowest peak shock pressures and is transported the shortest distances[7], the largest fragments created during an impact event should come from the rim region and, at the same time, have low ejection velocities. Boulders and relatively large fragments should constitute a sizeable fraction of non-escaping ejecta on both bodies, assuming relatively coherent target material. (Modification Stage:) The sizes and masses of the two moons essentially rule out gravitationally driven modification of impact craters[2,3]. Both lithostatic pressure and ejecta fallback effects[8] (e.g., rim loading, cavity shallowing, etc.) should be virtually nonexistent in light of target strength and ejecta transport distances. For example, if an "average" lunar soil (ρ = 1.6

gm/cm^3, cohesion = 0.006 bars)[9] is taken as a model for Phobos' strength, cohesion effects alone would not be overcome until depths on the order of 50 m were attained. Obviously, a thin regolith overlying more cohesive material[1,10], a more realistic model, would increase this depth substantially. Any observed fresh crater morphologic variations, then, should be primarily considered in light of dynamic modifications which take place during the formational events themselves; formation times of various features would be governed by strength scaling laws[4]. Long-term modifications would be dominated by non-gravitational processes (e.g., impact erosion, outgassing, etc.). Martian tidal effects, although small, should be relatively more significant than gravitational effects attributable to the moons themselves.

Ejecta: As the approximately hemispherical shock wave of a major (km scale) event is driven through the target, the rapid lateral falloff of the surface due to the small effective radius of curvature keeps the free surface closer to the impact point. This effect may enhance rapid lateral cavity growth in the upper part of the cavity. Material ejected early in the event should escape. As rarefaction waves begin to dominate event dynamics[11], ejection should take place at higher angles (measured from the horizontal), but escape velocity should still be exceeded by the vast majority of ejecta. Only late-stage ejecta (that subjected to the lowest shock levels and having the least velocity) would be emplaced on the surface. Although the scaling relationships for craters formed by low-velocity impact in a regolith in a low-g environment are uncertain, the most energetic of the returning ejecta should be able to form secondary craters. The lowest velocity fraction of this ejecta should consist of the largest fragments. Their extremely low emplacement velocities would not be conducive to large crater formation; rather, the fragments may land intact, or break up (but not be totally destroyed), upon impact. This phenomenon could explain the presence of abundant boulders on the surface of Deimos. Upper bounds on the minimum cohesive strength necessary for these fragments to survive emplacement (on the basis of stagnation pressure considerations for normal incidence at escape velocity) are $\sim$0.5 bars for Deimos and $\sim$1.7 bars for Phobos, well below average rock strengths.

Mechanisms have been postulated by which a considerable fraction of escaped ejecta is swept up by Phobos and Deimos after a number of orbits[12], creating relatively find-grained regoliths[1]. This would not be possible for asteroids, implying that a large portion of the surface material on these bodies would consist of blocky ejecta as opposed to fine-grained debris. This is consistent with spectral reflectance observations of asteroids[13] which suggest immature surfaces with low glass content[14,15]. Increasing gravity would tend to decrease the average particle size in the regolith and increase its apparent maturity by preventing the escape of more highly shocked, comminuted, and vitrified material.

References: [1]J. Pollack et al. (1973) JGR, 4314; [2]J. Veverka and T. Duxbury (1977) JGR, 4213; [3]J. Veverka et al. (1977), BAAS, 517; [4]D. Gault and J. Wedekind (1978) in Impact and Explosion Cratering, in press; [5]V. Oberbeck and R. Morrison (1976) PLSC 7, 2983; [6]E. Shoemaker (1962) in Physics and Astronomy of the Moon, Z. Kopal, ed. 538 pp.; [7]V. Oberbeck (1975) RGSP, 337; [8]W. Quaide et al. (1965) A.NYAS, 563; [9]J. Mitchell et al. (1972) NASA SP-315,8-1; [10]P. Thomas

et al. (1977) BAAS, 517; [11]D. Gault et al. (1968) in Shock Metamorphism of Natural Materials, 87; [12]S. Soter (1972) Rep. CRSR 462, Cornell U.; [13]T. McCord et al. (1970) Science, 1445; [14]D. Matson et al. (1977), PLSC 8, 1001; [15]R. Schaal and F. Hörz (1977) PLSC 8, 1697; [16]T. Duxbury (1974) Icarus, 290.

MOON	MAJOR AXIS[16] (KM)	VOLUME[1] (KM^3)	DENSITY[3] (G/CM^3)	AVERAGE RADIUS (KM)	FOR AVERAGE RADIUS	
					$g(CM/SEC^2)$	ESCAPE VELOCITY (M/SEC)
PHOBOS	27 X 21 X 19	5748	2 2	11.1	0 68	12 3
DEIMOS	15 X 12 X 11	1054	2.2	6 3	0 39	7 0

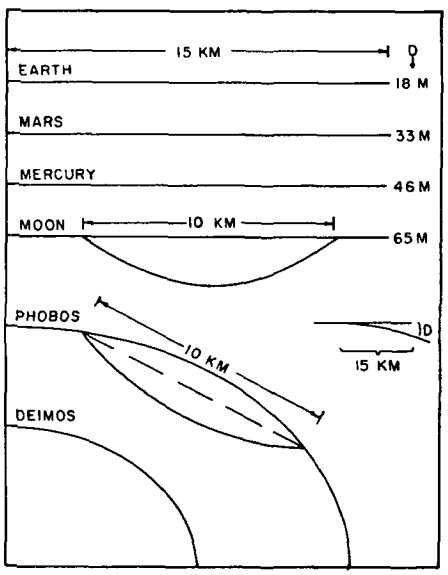

Fig 1 Comparison of curvatures of various solid bodies D represents the dropoff (in meters) of a sphere from a plane target at a point 15 (linear) km distant At this scale, the dropoffs are of the same order as the line thickness. The parabolic profile below the lunar limb segment represents an idealized 10 km crater profile (neglecting rim topography) For impacts at similar velocity on Moon and Phobos a constant effective depth of burst would cause more extensive lateral excavation on Phobos. The observed crater would occur below the dashed chord in the figure

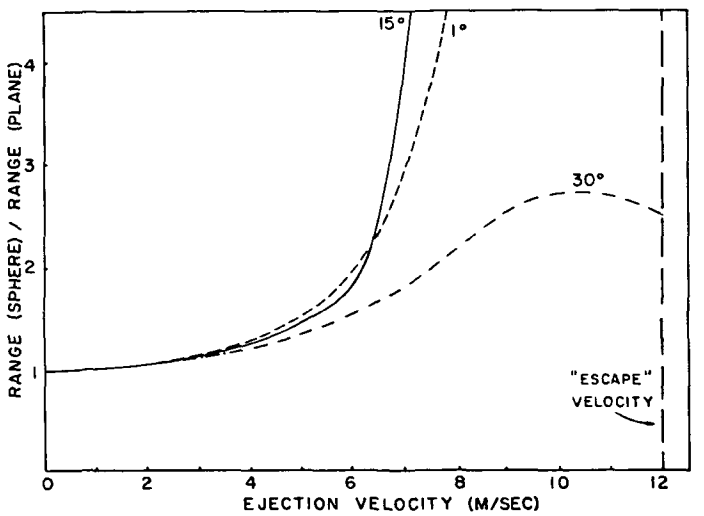

Fig 2 The effects of target curvature on ballistic ranges for a spherical Phobos model (Table 1) at various ejection angles. The calculated ranges over the sphere are normalized to the calculated range for a plane with Phobos' gravitational acceleration

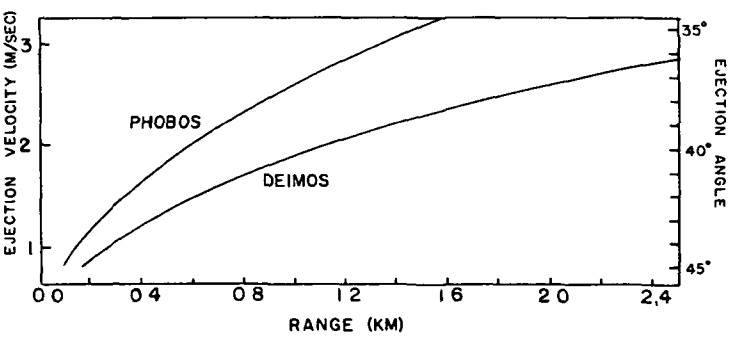

Fig. 3. Ejecta kinematic parameters for Phobos and Deimos extrapolated from an experimental crater[5] Ballistic ranges over spherical bodies are presented as functions of the observed velocity/angle relationships At this scale, the terrestrial laboratory results would plot as a nearly straight line ranging from about 0 004 to 0 03 mm from the velocity axis.

Crater Densities on Phobos and Deimos: Summary of Viking Results.

P. Thomas and J. Veverka, Laboratory for Planetary Studies, Cornell University, Ithaca, N. Y. 14853, and T. C. Duxbury, Jet Propulsion Laboratory, 4800 Oak Grove Drive, Pasadena, California 91103.

The high resolution Viking Orbiter images of the Martian satellites allow determinations of crater densities on different parts of Phobos and a comparison of average crater densities on the two satellites with those on other solar system bodies. All of Phobos and about half of Deimos have been imaged at resolutions better than 100 meters. The best resolution for Phobos is about 6 meters; for Deimos, 3 meters.

The composite incremental crater density curve for Phobos lies within a factor of two of Hartmann's (1973) extrapolation of lunar upland crater densities from large crater diameters. A straight line fit to the composite curve has a slope of -1.88 ± 0.03. The composite curve for Deimos is very similar, but slightly lower (0.8 of the Phobos density), and has a slope of -1.90 ± 0.15.

Different areas on Phobos have crater densities differing by as much as a factor of three, but most are within a factor of two. Because craters on the satellites are seen at a variety of emission angles and becasue of the limited numbers of craters, differences of a factor of two may not be significant. No extensive areas on Phobos are extremely young relative to the average age of the surface of Phobos. The area opposite the crater Stickney which is devoid of grooves and which could be interpreted as a spallation scar appears to have a crater density greater than that on the inside of Stickney, and thus may not be a scar related to the Stickney event. The grooves themselves are old — more than half as old as the average Phobos surface (Thomas et al., 1978).

Estimates of absolute ages for the surfaces of Phobos and Deimos based upon the techniques of Hartmann (1977) range upward from 8×10^8 years. These calculated ages, most at or above 3×10^9, depend upon values used for crater production rates at Mars and gravity scaling of crater diameters.

We are confident that our counts do not contain a significant fraction of secondaries because: (1) the satellites have very small escape velocities, (2) none of our curves shows a steeper slope at smaller crater diameters indicative of an added secondary component, (3) the highest resolution images do not show clusters of irregular craters, strings of impact craters or herringbone patterns. (Herringbone patterns suspected in some of the early Viking coverage have been resolved into sets of grooves by subsequent better imagery).

We conclude that the surfaces on Phobos and Deimos are well over 10^9 years old, and are at or near a maximum, or "equilibrium" crater density. Different mechanisms of crater obliteration may be capable of producing similar equilibrium crater densities. If the crater densities on the Martian satellites are not equilibrium densities, the slopes of -1.9 of the incremental crater density plots do not support a crater production curve with a slope of about -2.5 (Neukum and Wise, 1976).

It is interesting that while Phobos and Deimos have similar crater densities, the surface of Deimos appears to be smoother than that of Phobos. High resolution images indicate that the realtively smooth appearance of Deimos is related to the fact that craters on the outer satellite typically show considerable sediment fill (while their rims remain prominent); the craters on Phobos, on the other hand, do not show any distinguishable fill.

Hartmann, W. K., 1973, Martian cratering, 4: Mariner 9 initial analysis of cratering chronology. Jour. Geophys. Res., 78, p. 4096-4116.

Hartmann, W. K., 1977, Relative crater porduction rates on planets. Icarus, 31, p. 260-276.

Neukum, G. and Wise, D. U., 1976, Mars: a standard crater curve and a possible new time scale. Science, 194, p. 1381-1387.

Thomas, P., Veverka, J., and Duxbury, T. C., 1978, The origin of grooves on Phobos. Nature, in press.

Processes Effecting the Surfaces of the Galilean Satellites, J.B. Pollack, Space Science Div., NASA-Ames Res. Cntr., Moffett Field, CA 94035.

A number of processes have effected the surface characteristics of the Galilean satellites of Jupiter, especially their composition. These include the physical conditions in the circum-Jovian nebula at the time of their birth, their subsequent internal differentiation, near-surface convective motions, and the exposure of their surfaces to bombardment by meteoroids and magnetospheric particles. Below, we discuss each of these processes and indicate the constraints placed upon them by our aircraft observations of the satellites' near infrared reflection spectra (Pollack *et al.*, 1977 and 1978).

In the case of the outer three satellites, a sequence of events has tended to create surfaces rich in water ice. First, Jupiter's early high luminosity may have inhibited the condensation of water ice during the early phases of satellite formation so that free water concentrated towards their surfaces (Pollack and Reynolds, 1974). Second, subsequent differentiation would have segregated much of the rocky material towards their center (Consolmagno and Lewis, 1976). Finally, rupture of the icy crust by meteoroid bombardment or mantle convection as well as solid state convection within their icy crust (Reynolds, private communication) may have provided fresh coatings of water ice across localized areas of their surfaces.

In the case of Europa, the above processes appear to be the dominant ones since analysis of the aircraft data indicates that the fractional water ice cover is at least 85%. However, water ice constitutes only a fraction of Ganymede's surface and very little, if any, of Callisto's surface. According to the aircraft results, the fractional ice cover on the leading and trailing sides of Ganymede equal about 65% and 50%, respectively, while the fractional ice cover on Callisto is much less than 50%.

The lack of a complete water ice cover on Ganymede and Callisto can be understood in several ways. First, if the icy crust is thick enough, as may be the case for Callisto, the surface could consist of primordial material, which contains a rocky component. Second, extra-satellite dust may be continually covering over a portion of the surface. Dust grains derived from meteoroid bombardment of the irregular satellites represent a source of low velocity dust, which could be more effective in covering the surface than higher velocity interplanetary dust. The former displaces less mass upon impact.

The low fractional content of water ice on Callisto's surface appears to be in conflict with the amounts expected for a primordial surface (Pollack *et al.*, 1977 and 1978). Hence, extra- satellite dust is probably responsible for the non-icy

component of Callisto's surface. The variation of fractional ice cover among the outer three Galilean satellites with distance from Jupiter is more in accord with dust originating from the irregular satellites than from interplanetary space. This conclusion is further supported by the compositional similarity between the dark areas on Ganymede and Callisto's surfaces, as indicated by modelling of the aircraft spectra.

Particularly the inner Galilean satellites are exposed to bombardment by high energy, magnetospheric particles. Their effect of damaging the crystal structure of surface materials may be indicated by the muted character of the 1.5 and 2.0 μm water ice bands on Europa's trailing side as compared to those of its leading side. If this deduction is correct, the trailing side of Europa is preferentially bombarded, a result consistent with the larger angular velocity of Jupiter's magnetic field lines as compared with that of the satellite's orbital motion. Such a broadening needs to be factored into analyses of Io's spectra.

The innermost Galilean satellite, Io, has long been thought to have an unusual, perhaps unique, surface composition. Candidate materials for its surface composition range from low temperature materials, such as ices (Pilcher et al., 1972; McElroy and Yung, 1975); to medium temperature material, such as the salts of an evaporite deposit (Fanale et al., 1974); to high temperature substances, such as anhydrous, feldspar-rich material (Fanale et al., 1977). The first two candidates represent products of internal differentiation, while the third may be primordial material.

The aircraft observations indicate that the fractional ice cover is at most 10% and hence rule out the first model. The evaporite model is consistent with all three spectral features seen in the aircraft spectra (1.35 μm, 2.55 μm, and 4.05 μm), while the feldspar model is apparently consistent with only the shortest wavelength feature. Furthermore, the components of the evaporite deposit implied by the spectral features--ferrous bearing salts and nitrate salts--combine to give a reflection spectrum in the visible that is consistent with the observed behavior. However, it is not entirely clear that an evaporite deposit would be as anhydrous as the aircraft data indicate (fractional amount of bound water $<10^{-3}$), although sputtering by magnetospheric particles may preferentially remove an initial bound water component.

References:

G.J. Consolmagno and J.S. Lewis (1976). In "Jupiter" (T. Gehrels, ed.), pp. 1035-1051, U. of AZ, press.

F.P. Fanale, T.V. Johnson, and D.L. Matson (1974), Science, 186, 922-925.

F.P. Fanale, T.V. Johnson, and D.L. Matson (1977). Geophys. Res. Lett.

M.B. McElroy and Y.L. Yung (1975). Astrophys. J., 196, 227-250.

C.B. Pilcher, S.T. Ridgway, and T.B. McCord (1972), Science, 178, 1087-1089.

J.B. Pollack and R.T. Reynolds (1974). Icarus, 21, 248-253.

J.B. Pollack, F. Witteborn, D. Strecker, E. Erickson, B. Baldwin, and T. Bunch (1977), Bull. Am. Astron. Soc., 9, 524.

ibid (1978), Near-infrared spectra of the Galilean satellites: observations and implications, Icarus, in press.

PHYSICAL PROCESSES AFFECTING WATER ON THE GALILEAN SATELLITES. Carl B. Pilcher and Norman G. Purves, Institute for Astronomy, University of Hawaii, Honolulu.

An extensive investigation of the characteristics of and processes affecting water ice on the Galilean satellites is underway. To date, a study of the stability of water ice under conditions prevailing on the Galilean satellites has been completed and a study of the thermal migration characteristics of ice is in progress. Both of these investigations will be discussed.

In the stability study, loss of water from a Galilean satellite due to Jeans escape, photolysis, atmospheric charged particle interactions, and sputtering was considered. It was found that little water is lost in the first three processes, but that sputtering is probably an important water loss mechanism on at least Io. This conclusion was based on recent laboratory experiments (1) that indicate sputtering yields for water ice orders of magnitude higher than those anticipated from conventional sputtering theories. Sputtering of a frozen saturated salt solution, suggested by Fanale, et al. (2,3) to be the precursor of the present Io surface, would rapidly yield a thin salt layer, accounting for the satellite's unusual optical properties. It was also shown that gravitational focussing of meteoroids by Jupiter will produce a surface turnover ("gardening") rate on Io that is much larger than that on the moon. The actual rate of water loss from Io may thus be determined by the rate at which water-bearing material is exposed on the surface by gardening. The surface of Io should be heavily cratered, perhaps resembling morphologically the lunar highlands.

The study of thermal migration of water on the Galilean satellites has been approached by means of a computer model. The distribution of water resulting from evaporation from a single point on a satellite was first calculated under the assumptions of unit accommodation coefficient and ballistic motion. If no other atmospheric components are present, the latter assumption will be valid for water vapor pressures below that of an ice at 140 K. This is the temperature reached by material of albedo 0.6 in equilibrium with the insolation at the sub-solar point. This distribution function was then used with a temperature distribution calculated under the assumption of thermal equilibrium to determine the water migration characteristics at a particular rotational phase angle. The calculations were then repeated with a spatial offset introduced into the temperature distribution function to simulate satellite rotation. Repetition of this process at appropriate offset intervals yields the thermal migration characteristics averaged over a satellite rotation. The results of this study will be presented and the implications for the surface characteristics of the Galilean satellites discussed.

References

(1) Brown, W.L., Lanzerotti, L.J., Poate, J.M., and Augustyniak, W.M. (1977), B.A.A.S. 9, 527.

(2) Fanale, F.P., Johnson, T.V., and Matson, D.L. (1974), Science 186, 922-925.
(3) Fanale, F.P., Johnson, T.V., and Matson, D.L. (1977), Planetary Satellites, ed. J.A. Burns, University of Arizona Press, pp. 379-405.

X-Ray Spectroscopy of the Galilean Satellites, R.H. Parker, A.E. Metzger, J.L. Luthey, all of Jet Propulsion Laboratory, California Institute of Technology, Pasadena, California 91103, R. Pehl, Lawrence Berkeley Laboratory, Berkeley, California 74720, and H.W. Schnopper, Harvard-Smithsonian Center for Astrophysics, Cambridge, Massachusetts 02138

Determination of the surface composition of Jupiter's Galilean Satellites will provide a basic constraint for models of this mini-solar system (1). Remote observations of chemical composition can best be performed by X-ray and gamma-ray spectroscopy similar to that performed on the Apollo 15 and 16 missions (2,3). Although the intense radiation belt around Jupiter has led preliminary studies to a pessimistic conclusion for a gamma-ray experiment, the picture for X-ray spectroscopy is quite promising. X-rays produced by electron bombardment give characteristic emission lines from 0.055 keV for lithium (Z=3) to 88.23 keV for lead (Z=82). By measuring the X-ray intensity at each characteristic energy, the abundances of the various elements generating the X-ray flux can be determined.

The four Galilean satellites orbit within the Jovian magnetosphere. As a result, the large fluxes of high energy electrons and protons trapped in the Jovian magnetosphere dictate the concept and design of an X-ray spectrometer for satellite observations (4). Figure 1 shows the expected electron fluxes at Io ($\sim 6R_J$) and Ganymede ($\sim 16R_J$). On impacting the satellite surface, these charged particles create X-rays by (a) direct ionization, (b) photoionization, and (c) the bremsstrahlung process. Processes (a) and (b) contribute to the signal while process (c) contributes to the background. The charged particle flux also creates background by interacting with instrument and spacecraft materials. This environment introduces the following constraints for an X-ray spectrometer: (1) shielding to reduce the flux of charged particles, (2) a detector which is small and has good resolution (<300 eV FWHM from 1-7 keV) to minimize the count rate and optimize the selectivity of signal to background, and (3) fast electronics, capable of handling counting rates on the order of $2\text{-}3 \times 10^4$ per second.

To properly evaluate the prospects of performing compositional X-ray analysis, these interactive processes must be modeled with an accuracy limited primarily by present knowledge of the radiation field at the satellites. We have developed computer codes to calculate the X-ray spectrum emerging from the satellite surfaces and the shields of the X-ray spectrometer as a result of the electron and proton fluxes near the Galilean satellites. The bremsstrahlung generated in the satellites and shielding around the instrument is computed from the production cross-sections of thin targets for electrons with energies between 1 keV and 500 MeV (5,6). The probability of an interaction in the detector is the summation of the bremsstrahlung spectrum per electron folded into the response efficiency of the detector. The bremsstrahlung spectrum through a 1 cm tungsten shield peaks broadly at about 800 keV, an energy at which a thin detector will be relatively inefficient and therefore able to minimize this background component. The flux through the shield will also include a smaller contribution from the energetic electrons whose range exceeds the thickness of the shield.

The bremsstrahlung from the satellite surface is computed, using a thin target formulation, for sequential 1 μm thick layers to a maximum depth of 0.15 mm or until the contribution to the integral bremsstrahlung flux at depth x+ 1 μm is less than 1% of the total contribution. The characteristic emission produced by photoionization of the target atom of interest is also computed for the bremsstrahlung produced at each step in depth. To simplify, this emission is divided into just two solid angles and the incident electron flux is taken normal to the surface.

The major portion of characteristic emission from the satellite surface is produced by electron ionization. The incident electron flux is assumed to be isotropic and divided into ten equal incoming solid angles. The emission is computed as a function of depth, the electrons being retarded through a "material" of Z equal to the average surface composition, using a modified Bethe K-shell ionization cross-section (7). The characteristic emission is summed over the contribution of incoming electron energies from the ionization energy, E_k, to 30 MeV in incremental steps. The photons are attenuated through an assumed composite surface material and summed over ten outgoing solid angles.

Since active shielding would increase the dead time to ~100%, the design uses a passive tungsten (19 g/cm^2) shield. Since proportional counters are difficult to miniaturize and have relatively poor energy resolution, we have chosen to use an array of 2mm x 2mm diffused junction Si detectors operated at a temperature between 150 K and 200 K. Four 2mm x 2mm x 100μm diffused junction silicon solid state detectors have been fabricated at the Lawrence Berkeley Laboratory as part of these studies. They have near state-of-the-art energy resolution (~250 eV at 5.9 keV) and are thinner than any of this type previously developed for high resolution X-ray spectroscopy. Not only is the depletion width nearly ideal in terms of the response efficiency for the energy range of interest but a diffused junction detector has much greater radiation resistance than the conventional Li-drifted X-ray detector commonly used in laboratory work. A multiple plate X-ray imaging system with aperture shielding will be placed in front of the detector array in order to allow line-of-sight shielding of charged particles in the direction of the satellite. The imaging system will have an X-ray reflection efficiency ranging from about 5% at 7 keV to 50% at 1 keV.

Figure 2 presents the calculated signals from Aℓ and Fe, together with the bremsstrahlung emitted from surfaces assumed to have the compositions of a carbonaceous chondrite-50% water ice at Ganymede. Folding these spectra plus the calculated local background into the expected instrument characteristics (preliminary for the X-ray imager) yields 3σ minimum detectable limits for Aℓ of 0.15% at Io and 0.9% at Ganymede, and for Fe of 0.5% at Io and 0.8% at Ganymede. The calculation is based on a single flyby of each satellite as velocities and distances typical of planned JOP trajectories. Multiple passes will substantially improve the sensitivity. The results indicate that sensitivities of a percent or better for Aℓ, Si, K, Ca, Ti, Fe, and Ni can be met. The possibility exists of including Na, Mg, S and Cl in the list of elements abundant enough to be observed. Below Na (E_k = 1.08 keV) absorption in the dead layer of the detector becomes a concern although it may be pratical to observe as low as carbon (284 eV). Present theories indicate that Ganymede and Callisto are partially covered with ice while Europa is heavily ice covered. Other candidate surface materials are carbonaceous, chondritic and

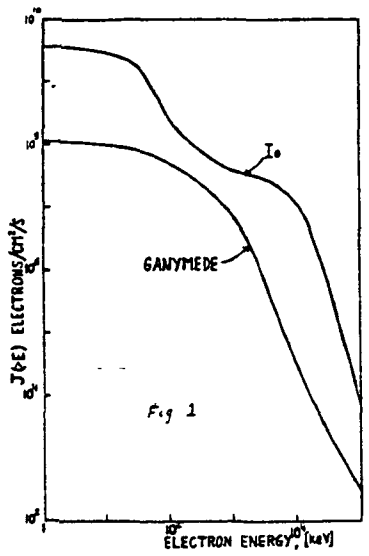

Fig 1

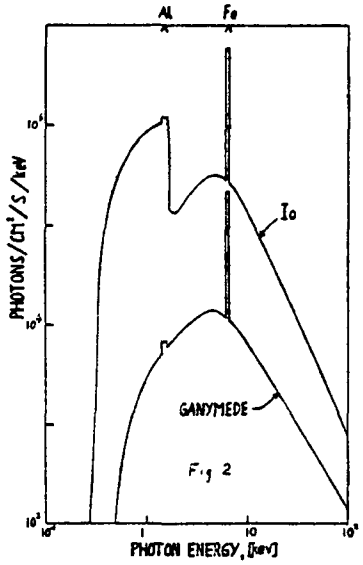

Fig 2

evaporite salts (8). The capability of observing carbon and oxygen would be an obvious advantage.

Our results show that X-ray spectroscopy can provide a determination of the surface composition of the Galilean satellites. A more complete exposition of the model will soon be submitted for publication.

References

(1) W.K. Hartman, Scientific American, 233, 3, 142 (Sept. 1975). (2) A.E. Metzger, et al, Proc. 5th Lunar Sci. Conf., Geochim. Cosmochim. Acta., Suppl. 5, 2, 1067 (1974). (3) I. Adler et al., Science, 177, 256 (1972). (4) R.H. Parker et al, Trans. American Nuclear Society, Winter meeting, Nov. 1977. (5) H.W. Koch and J.W. Motz, Rev. Mod. Phys., 31, 920 (1959). (6) C.M. Lee et al, Phys. Rev., 13, 1714 (1976). (7) M. Green, V.E. Cosslett, Proc. Roy. Soc., 78, 1206 (1961). (8) F.P. Fanale et al, Planetary Satellites (J.A. Burns, ed.) U. of Ariz. Press, Tucson, AZ (1976).

An Observational Test for the Origin of the Titan-Hyperion Orbital Resonance, S. J. Peale, Univ. of California, Santa Barbara, Calif. 93106

The theory of the origin of the commensurabilities among the orbital mean motions of the satellites of Saturn by the differential expansion of originally random orbits by tidal dissipation in Saturn has been remarkably successful in the sense that a long list of constraints on the resonances demanded by the theory are in fact satisfied (Peale, 1976). The notable exception is the excessive age of the Titan-Hyperion resonance ($\sim 6 \times 10^{10}$ years) if Saturn's tidal Q appropriate to the tidal evolution of Titan's orbit is not less than the lower bound ($Q_S \gtrsim 6 \times 10^4$) imposed by the proximity of Mimas to Saturn (Goldreich and Soter, 1966). Colombo et al. (1974) propose that Q be sufficiently frequency and amplitude dependent that a low $Q_S (<5000)$ be appropriate to Titan orbital evolution and thereby salvage the tidal hypothesis. These bounds on Q are illustrated in Fig. 1. Alternatively, it is possible that the Titan Hyperion resonance is primordial in the sense that Hyperion was left in the 4:3 orbital resonance with Titan after numerous companions were cleared from a cluttered region of space about Saturn. Such a primordial origin almost certainly applies, for example, to the Trojan and Hilda asteroids in resonance with Jupiter.

If Hyperion is near the upper bound of its possible range of radii 80 km $< R_H <$ 480 km and if it is found to be rotating in the 3:2 spin-orbit resonance, there has been little tidal evolution of Titan's orbit and a primordial origin of the Titan-Hyperion orbital resonance can be inferred. The large radius for Hyperion is necessary in order that its spin be retarded to the 3:2 spin-orbit resonance by tidal dissipation in a time short compared to the growth of its orbital eccentricity e within the orbital resonance with Titan (Fig. 2). The probability of capture into the spin-orbit resonance is large only if e is large (Fig. 3). But a rapid decay of Hyperion's spin together with its occupancy of the 3:2 spin-orbit resonance means that e was large very early in history when Hyperion approached the 3:2 spin resonance. This in turn means little increase in e due to tidal evolution of Titan's orbit while Hyperion is locked in the orbital resonance. Little tidal evolution precludes a tidal origin for the orbital resonance and the orbital mean motion commensurability must be primordial.

If Hyperion is found rotating synchronously with its orbital motion, a primordial origin for the orbital resonance is still not ruled out. This follows from Fig. 3 which shows that it is more probable to escape the 3:2 spin resonance even under the best of circumstances. If Hyperion is near the lower bound of the range of possible radii, finding it in the 3:2 spin resonance also place no constraints on the origin of the orbital

resonance. In this case most of the age of the solar system is required to slow Hyperion's spin from a reasonably high initial value (Fig. 2). This allows plenty of time for e to grow within the resonance by tidal evolution, and e would have been large, as would possibly the capture probability (Fig. 3) when Hyperion reached the 3:2 spin resonance regardless of the origin of the orbital resonance

Figure Captions

Fig. 1. Age of the Titan-Hyperion orbital resonance as a function of Saturn's effective tidal Q.

Fig. 2. Times required for the tidal retardation of Hyperion's spin angular velocity from a corresponding period of 10 hours to a period of 21 days as a function of Q_H and radius.

Fig. 3. Probability of capturing Hyperion into the 3/2 spin resonance vs. eccentricity for two tidal models.

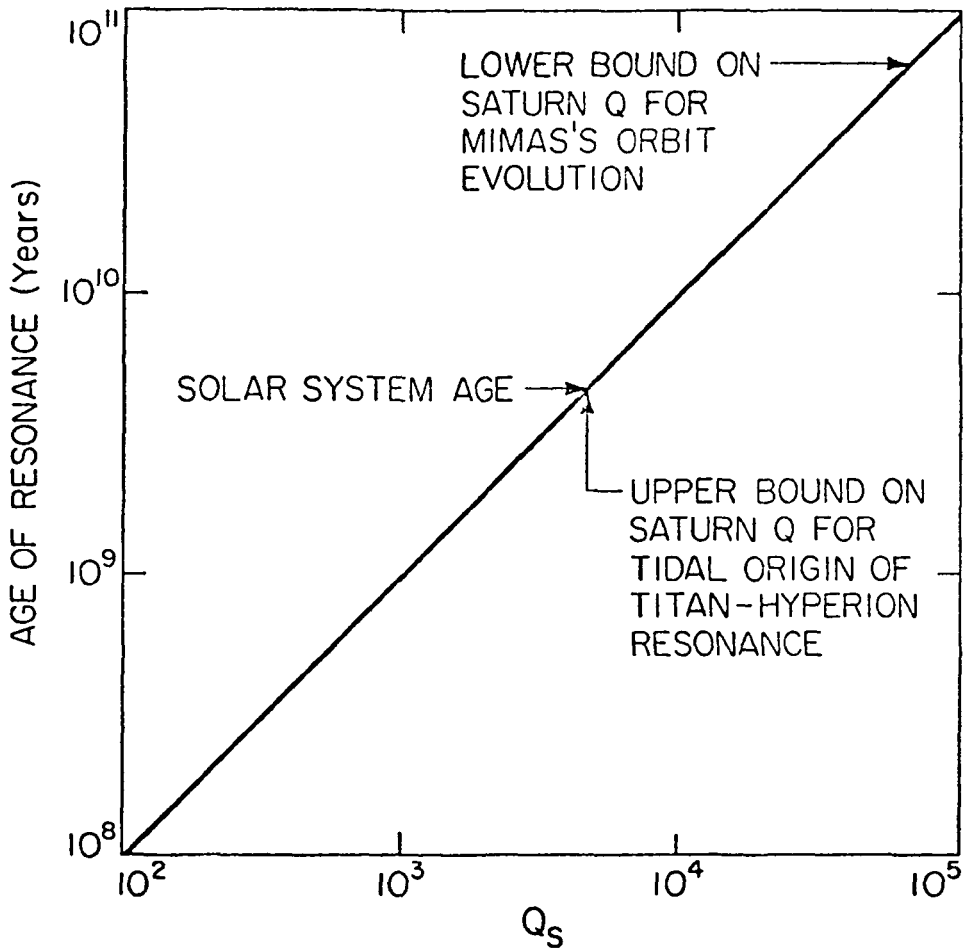

Fig. 1

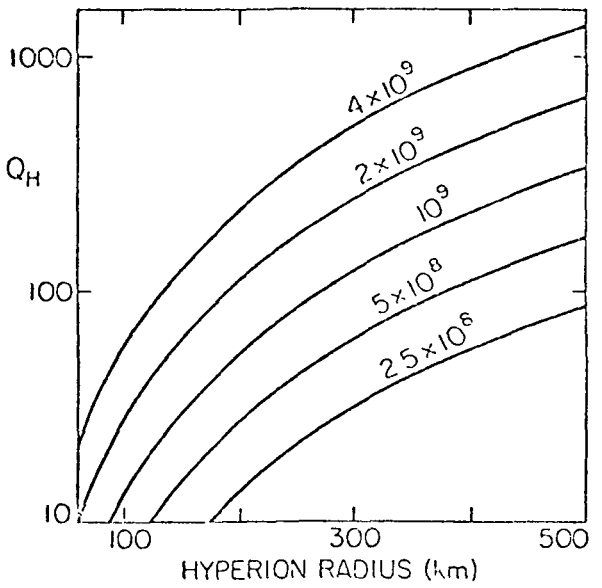

Fig. 2

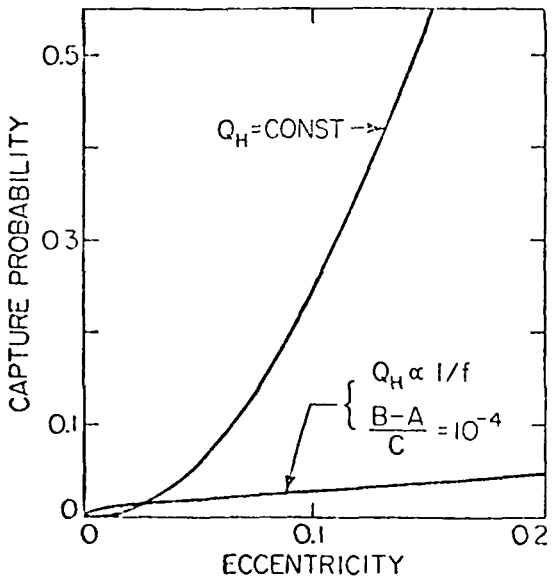

Fig. 3

References

1. Colombo, G., Franklin, F.A., and Shapiro, I.I. (1974), Astron. J. 79, 61-72.
2. Goldreich, P., and Soter, S. (1966), Icarus 5, 375-389.
3. Peale, S.J. (1976), Ann. Rev. Astron. Astrophys. 14, 215-246.

CHAPTER 3 - CONSTRAINTS ON PLANETARY INTERIORS

Comments on the Magnetic Field and Internal Heat of Saturn, Uranus and Neptune, R. Smoluchowski, Princeton University, Princeton, N.J. 08540
(after Sep. 1, 1978: Dept. of Astronomy, U. of Texas, Austin, TX. 78712)

The generation of a magnetic field by the hydromagnetic dynamo mechanism requires a sufficiently high Reynolds number in which the electrical conductivity is the major factor. On Jupiter the dynamo can operate not only in the metallic interior but also in the inner part of the H_2 layer (1) thereby increasing the volume of the high conductivity region by a factor of about two. Four recent models of Saturn have been examined from this point of view. It appears that in Saturn the volume of the high conductivity H_2 layer is 3 to 6 times greater than that of the metallic H region and that it is in the H_2 region that the Saturnian field is most likely generated (2). On Saturn the highly conductive H_2 layer is, however, more than twice as deep below the planets surface as on Jupiter and thus one does not expect the external field to show as high quadrupole and octupole components as has been observed by the Pioneers. The internal heat of Saturn is easily accounted for by the He-precipitation mechanism (3) in the metallic H(He) layer.

The sizes, masses and rotation periods of Uranus and Neptune differ much less than those of Jupiter and Saturn and thus it was not surprising that for a long time these two planets were considered to have very similar internal structures. In fact there was less difference in the radial dependence of density, pressure and temperature of Uranus and Neptune than there was between the results obtained by various authors using somewhat different models and approximations. Recently this situation has been drastically changed because of the discovery that Uranus has a magnetic field (4) while Neptune has probably none and that Neptune has a huge internal heat source (5) while Uranus has probably none (6). On top of that indications are that both planets have appreciably longer periods of rotation than those used before. In spite of this doubt several semi-quantitative conclusions can be drawn from these models. One of the most important is that the essential difference between Uranus and Neptune on the one hand and Jupiter and Saturn on the other is the absence of metallic hydrogen and the presence of huge cores in the former two especially in Neptune. It seems thus that the main theoretical difficulty in developing good models lies in our limited understanding of the composition, state and properties of these cores which in Jupiter and Saturn play a relatively small role. On the other hand the H_2(He) mantles should not present more serious theoretical difficulties than they did before.

In most of the models of Uranus and Neptune the temperature, pressure and density at all radii is lower for Uranus and the difference in temperature will be undoubtedly increased when the presence of an internal heat source on Neptune is taken into account. These differences have an important effect on the cores because, at least in some models, their temperature lies very closely to the calculated melting temperature of certain oxides at high pressures. In other models it is low enough to be comparable even to the high pressure melting temperatures of water ice. It appears that while the core is almost

certainly solid in Uranus it may be, at least partially, liquid in Neptune. At present one does not know whether the internal heat of Neptune is of primordial origin or whether it has to be generated by one of the many mechanisms which have been proposed. In any case its huge partially liquid core may be the source of heat produced by a precipitation (differentiation) reaction analogous to that active on Saturn and probably also on Jupiter. The absence of a magnetic field on this planet could be related to a too low electrical conductivity of the liquid core and a too shallow H_2 mantle.

In Uranus the absence of internal heat follows directly from the absence of a sufficiently rapid precipitation reaction in the solid core. The presence of the magnetic field may be related to the availablilty of a deep H_2(He) mantle which, at lower radii, could reach pressures high enough to produce the required metallic conductivity (1).

REFERENCES

1. R. Smoluchowski, Proc. 19th COSPAR Meeting, Philadelphia 1976.

2. F. H. Busse, Phys. Earth Plan. Int. 12, 350, 1976.

3. E. E. Salpeter, Astroph. J. 181, L83, 1973.

4. L. Kavanagh, Icarus 25, 166, 1975 and
   L. W. Brown, Astroph. J. 207, L209, 1976.

5. R. F. Loewenstein, D. A. Harper, S. H. Moseley, C. M. Telesco, H. A. Thronson, Jr., R. H. Hildebrand, S. E. Whitcomb, R. Winton and R. F. Stiening, Icarus 31, 315, 1977 and
   M. T. Stier, W. A. Traub, G. G. Fazio and F. J. Low, Bull. A.A.S. 9, 511, 1977.

6. G. G. Fazio, W. A. Traub, E. L. Wright, F. J. Low and L. Trafton, Astroph. J. 209, 633, 1976.

Cooling Histories of Terrestrial Planets, G. Schubert, Dept. of Earth and Space Sciences, Univ. of Calif., Los Angeles, Calif., 90024, P. Cassen and R. E. Young, NASA Ames Research Center, Moffett Field, Calif., 94305.

Subsolidus mantle convection and the thickening of a rigid lithosphere play significant roles in the thermal evolutions of terrestrial planets cooling from hot initial states. While convection promotes efficient cooling by bringing hot material from the deep interior near to the surface, the growth of a lithosphere inhibits cooling by making the surface inaccessible to the convection. Heat must be conducted across the lithosphere which thus acts as a blanket to insulate the interior and retard its cooling. We have developed a procedure for quantifying the effects of these competing processes in planetary cooling histories.

The model includes a temperature-dependent mantle viscosity which self-regulates the vigor of subsolidus convection. The convecting part of the mantle is nearly isothermal except for thin layers at its upper and lower boundaries. A spatially uniform time-dependent temperature is used to characterize the thermal state of the convecting region. The surface and the base of the lithosphere are held at fixed temperatures, but the temperature within the lithosphere nevertheless changes with time as well as depth because the lithosphere is allowed to thicken or thin. The constant temperature at the lithosphere base is the maximum temperature at which mantle material will remain essentially rigid over geologic time. Decaying radiogenic heat sources are uniformly distributed throughout the rigid and convecting parts of the mantle.

An energy balance of the convecting region provides an equation for the time-rate of change of its temperature. The heat flux out of the

convecting region and into the lithosphere and the heat flux (if any) into the mantle from a core are calculated from semi-empirical correlations which relate these quantities to geometrical, thermal and mechanical characteristics of the convecting region. In this regard, a most important property of the convecting part of the mantle is its viscosity. We allow this to change with time through its dependence on the exponential of the inverse absolute temperature of the convection. Even the thickness of the convecting region is time-dependent since our model assumes a mantle with a constant overall thickness and the lithosphere thickens or thins with time.

If, the heat flux into the base of the lithosphere from the underlying convection differs from the heat which the lithosphere itself carries away from its base by conduction, the lithosphere is allowed either to thin by using the excess heat brought to its base to raise the temperature of a lithospheric layer to the temperature of the convecting region or to thicken by reducing the temperature of a convecting layer to the base temperature of the lithosphere.

The equation of heat conduction in the lithosphere, together with differential equations for the thickness of the lithosphere and the temperature of the convecting part of the mantle form a highly nonlinear coupled system. We will integrate this system of equations for a number of hot initial states and follow the resulting cooling histories determining, for example, temperature and viscosity, lithosphere thickness, surface heat flux and core solidification time. The rapidity with which subsolidus convection can cool a planet and solidify its core is important for our understanding of planetary magnetic fields, especially in the cases of the smaller

terrestrial planets such as the Moon. The parameterization of the upward heat transport by subsolidus mantle convection is what makes it possible to include, in a self-consistent manner, the all-important processes of lithosphere thickening and convective cooling in a mantle with temperature-dependent viscosity. It is also what makes it practical to calculate thermal evolutions for many different initial conditions.

CONTRIBUTION OF TIDAL DISSIPATION TO LUNAR THERMAL HISTORY, S. J. Peale, Dept. of Physics, Univ. of Calif., at Santa Barbara 93106 and P. Cassen, Theoret. and Planetary Studies Branch, NASA-Ames Res. Ctr., Moffett Field, Calif. 94035.

The dissipation of mechanical strain energy associated with the tidal flexing of the moon as it librates and follows its eccentric orbit is frequently mentioned as a possibly important means of heating the lunar interior. Although it is generally recognized that such dissipation is not important at the present time, this may not have always been the case, since the Moon was much closer to the Earth in the past. Recently several investigators have proposed that tidal heating could have provided heat for producing mare lavas (Wones and Shaw, 1975; Schultz et al, 1976), complete melting of the moon (Turcotte et al., 1977) or that tidal stresses could have triggered basin flooding,(Schultz et al., 1976). Kaula and Yoder (1976) discuss several ways in which tidal heating might contribute to lunar thermal history, but conclude that such contributions are unlikely from order of magnitude calculations; they in fact anticipate some of our conclusions. The purpose of this paper is to define as precisely as possible within the bounds of the uncertainties the conditions under which tidal heating could have been an important factor in the evolution of the moon. The tidal dissipation is determined as a function of position in a homogeneous, incompressible moon and as a function of the Earth-Moon separation. The lunar obliquity as a function of Earth-Moon separation was assumed to be that corresponding to the stable equilibrium Cassini states (Ward, 1975), and results are given for two values of eccentricity e=0.0 and e=0.055, which are maintained throughout the orbital evolution.

Figures 1 and 2 illustrate the distribution of the tidal dissipation throughout an incompressible, homogeneous moon with Q=100, for the cases where the tidal variations are caused by a non zero obliquity or a non zero eccentricity respectively. Dissipation is maximal at the center. Fig. 3 shows the total dissipation and the dissipation at the center as a function of the Earth-Moon separation again with a lunar Q=100. In order to compare the tidal dissipation with heating by nuclear decay (Reynolds et al., 1972), a simplified orbital evolution is assumed, where the moon regresses from a semimajor axis $a=3a_{\oplus}$ ($a_{\oplus}$ = Earth radius) to its present location in 4.6×10^9 years with a constant dissipation factor Q for the earth. The increase in dissipation at $a/a_{\oplus} \approx 34$ results from large values of the obliquity when the moon transfers from Cassini state 1 to state 2 (Ward, 1975). Although tidal heating exceeds the radiogenic heating when the moon is sufficiently close to the earth, its total contribution to lunar thermal history is negligible in the above model. The cumulative energy deposition is shown in Fig. 4

with Q =100 for the simplified orbital evolution, and it is seen that the high dissipation rate for the small Earth-Moon separation is not effective in heating the moon since the Moon is pushed away from the Earth too rapidly. For this model of orbital evolution and lunar properties an average temperature increase not exceeding 40°K would result over a 4.6×10^9 year history. Hence, for this model tidal friction has been a negligible contributor to lunar thermal history.

Kaula and Yoder (1976) discuss the possible existence of two orbital resonances between the Sun and Moon and Jupiter and Moon as a means of keeping the Moon close to the Earth while increasing the orbital eccentricity. The increased eccentricity could easily lead to melting the moon in these resonances, but for distinct reasons, each is likely not to have occurred.

Figure 5 shows the tidal dissipation as a function of Earth-Moon separation which would have occurred in a solid lunar mantle over a molten core. The local dissipation in this two layer model exceeds that for the homogeneous Moon by a factor of 5 if the core radius r_c is 0.5 a_e (a_e=lunar radius) and a factor of 100 if $r_c = 0.95\ a_e$. If the Moon remained within about 45 $a_\otimes$ for more than 10^8 years with $r_c \gtrsim 0.5\ a_\otimes$ the above heating rates are sufficient to cause a runaway melting of the outer portion of the moon. However, the interior of the Moon would have had to have been melted by some other energy source prior to such a runaway.

As circumstances must be very special for significant heating by tidal friction, we conclude that lunar thermal history was essentially controlled by radiogenic sources and initial accretional heating. Whereas a previously molten interior or a more exotic orbital history involving large eccentricities (Turcotte et al., 1977) would drastically increase the importance of the tides, we see no compelling reasons for assuming either state of affairs ever existed. Details of the calculations and further discussion of assumptions, uncertainties and conclusions are given by Peale and Cassen (1977).

FIGURE CAPTIONS

Fig. 1. Distribution of tidal energy dissipation in the moon when inclination terms are dominant. Contours are labeled in ergs $cm^{-3}\ sec^{-1}$.

Fig. 2. Distribution of tidal energy dissipation in the moon when eccentricity terms are dominant. Contours are labeled in ergs $cm^{-3}\ sec^{-1}$.

Fig. 3. Central and total tidal dissipation as a function of lunar orbit semimajor axis. Q=100 is assumed.

Fig. 4. Cumulative energy deposition by tidal dissipation and nuclear sources as a function of time.

Fig. 5. Dissipation in the solid mantle at the core-mantle interface for $A = 0^\circ$.

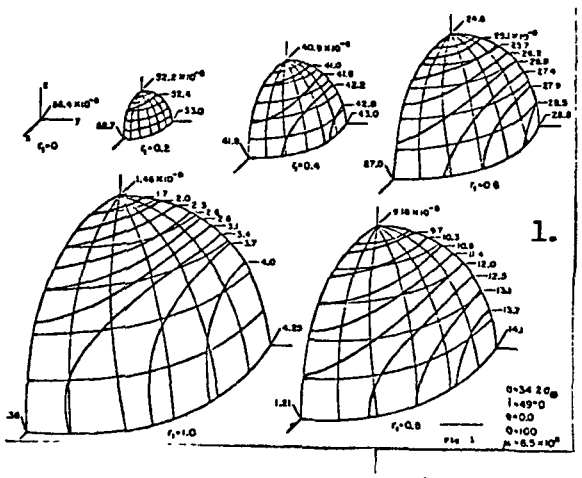

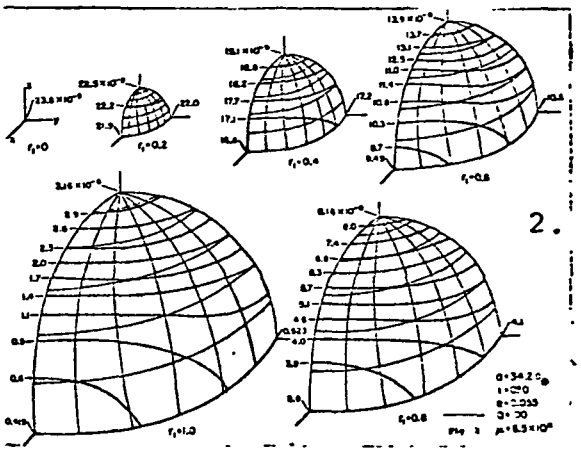

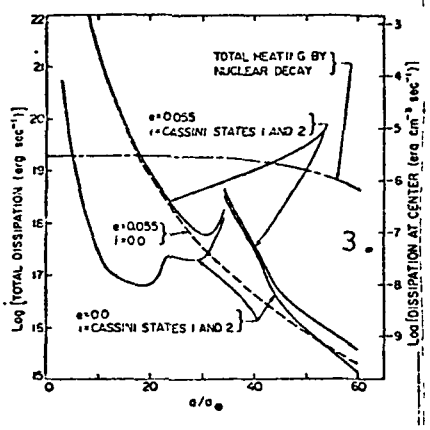

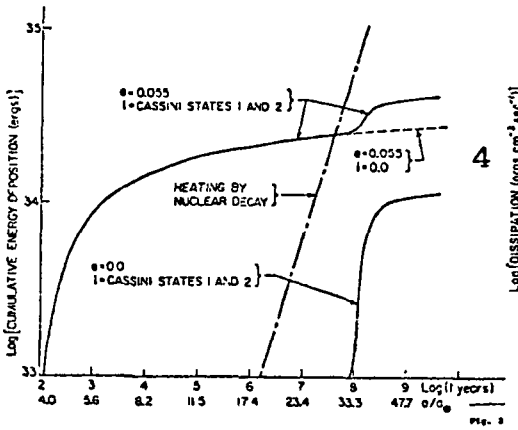

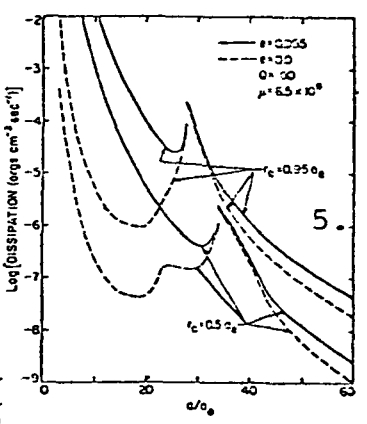

References

1. Kaula, W.M. and Yoder, C. (1976). In Lunar Science VII, pp. 440-442. Lunar Science Institute, Houston, Texas.
2. Peale, S.J. and Cassen, P. (1977), submitted to Icarus.
3. Reynolds, R.T., Fricker, P.E. and Summers, A.L. (1972). In Progress in Astronautics and Aeronautics 28: 303-337. M.I.T. Press, Cambridge, Mass.
4. Schultz, P.H., Burns, J.A. and Greeley, R. (1976). In Lunar Science VII, pp. 785-787, Lunar Science Institute, Houston, Texas.
5. Turcotte, D.L., Cisne, J.L. and Nordman, J.C. (1977), Icarus 30, 254-266.
6. Ward, W.R. (1975), Science 189, 377-379.
7. Wones, D.R. and Shaw, H.R. (1975). In Lunar Science VI, pp. 878-879, Lunar Science Institute, Houston, Texas.

The Tectonics of Filled Basins on the Terrestrial Planets, Sean C. Solomon, Dept. of Earth & Planetary Sci., Massachusetts Institute of Technology, Cambridge, MA 02139 and James W. Head, Dept. of Geological Sci., Brown University, Providence, RI 02912.

The crustal tectonics within and near major basins on the terrestrial planets are closely related to the sites of volcanic eruption and to the loading of the basin by volcanic fill. The style and timing of tectonic events also reflect the large-scale or global state of stress in the planetary lithosphere. For the terrestrial bodies Moon, Mercury, and Mars, a major and perhaps dominant global stress-producing mechanism is the thermal expansion and contraction of the deep interior associated with planetary thermal history. In this paper we show that the location and formation time of linear rilles and 'mare' ridges in the vicinity of major basins on the Moon, Mercury, and Mars can be explained as the product of a superposition of basin-related stress and the global thermal stress generated by each planet's unique thermal evolution.

On the Moon the circular mare basins show evidence for continued vertical subsidence but for a time variation in the style of tectonic activity during the history of mare emplacement (1-4). In Mare Serenitatis in particular, the oldest basalt deposits, exposed at the surface in a belt around the southern rim, were downwarped and faulted subsequent to emplacement. The faults consist of a series of basin-concentric rilles or graben which extend to the adjacent highlands. These graben were flooded by later stage lava flows, themselves subsequently downwarped toward the basin center. The central portion of Serenitatis was filled with a third stage of basalts which postdates virtually all graben formation. This youngest unit contains extensive mare ridges, which appear to be compressional features (1-3,5-7) associated with downwarping. Subsidence and ridge formation continued past the emplacement time of the youngest lavas. On the basis of this history, rille formation appears to have been limited to the period 3.5-3.7 AE, while downwarping and mare ridge formation continued to a later period.

This tectonic history can be explained by considering both the local and global stress fields. The local stress field may be modeled using the theory for stress in a spherical, liquid-filled, elastic shell (the lunar lithosphere) due to a surface load (mare basalt) with cylindrical symmetry (8). The horizontal stress component σ_r radial with respect to the basin is shown in Fig. 1 for a model of the basalt load in Serenitatis taken from gravimetric determination of the excess mass (9) and from the expected geometry of the pre-fill circular basin (10). The stress σ_r at the surface is compressional beneath the load center and extensional outside the load, with the amplitude and shape of

the radial variation strongly dependent on the elastic shell thickness T.

The global stress field we consider is that due to differential heating and cooling of the lunar interior, subject to the constraint that planetary volume and stress changes since 4 AE have not been large enough to produce global-scale tectonic features (11,12). A thermal history model that matches this constraint and gives peak lunar volume at 3.6 AE starts with initial melting to 300 km depth and an initial central temperature of 300°C. From 4 to 3.6 AE for this model, a superposition of the global extension (280 bars accumulated stress) with the local stress field (Fig. 1) will accentuate the tensional stress at the edge of the mare basin, leading to graben formation at the appropriate radial distance for T = 25 to 50 km. After 3.6 AE, the global compressive stress (540 bars accumulation between 3.6 and 2.6 AE) will reduce the extensional stress outside the mare fill margin and accentuate the horizontal compression beneath the load, accounting for later formation of mare ridges.

The tectonic history of basins on Mercury and Mars similarly reflects a combination of vertical basin movement and global stress, the latter predominately compressive for most of Mercury's history and extensional for most of Martian history (11,12). Mare-like ridges are abundant on Mars, particularly in the oldest clearly volcanic plains (13), and likely represent plains subsidence and local compression in excess of global extensional thermal stress. Mare-like ridges are also prominent in many of the smooth plains units on Mercury, especially within the Caloris basin (14). The absence of basin-concentric graben on Mercury may be attributed to global compression associated with planetary contraction. The younger extensional features in the Caloris floor, if due to uplift following smooth plains emplacement (14,15), may reflect a volcanic history for Mercury unusual in its short duration and perhaps in its eruption mechanism.

References: (1) K.A. Howard et al. (1973) NASA SP-330, 29-1; (2) W.R. Muehlberger (1974) PLSC 5, 101; (3) B.K. Lucchitta (1977) PLSC 8, 2691; (4) J.M. Boyce (1976) PLSC 7, 2717; (5) K.A. Howard and W.R. Muehlberger (1973) NASA SP-330, 31-22; (6) J.W. Head (1974) Moon 9, 355; (7) T.A. Maxwell et al. (1975) GSAB 86, 1273; (8) J.F. Brotchie (1971) Mod. Geol. 3, 15; (9) R.J. Phillips et al. (1972) JGR 35, 7106; (10) J.W. Head (1974) Moon 11, 327; (11) S.C. Solomon and J. Chaiken (1976) PLSC 7, 3229; (12) S.C. Solomon (1977) PEPI 15, 135; (13) M.H. Carr et al. (1975) JGR 78, 4031; (14) R.G. Strom et al. (1975) JGR 80, 2478; (15) M.J. Melosh and D. Dzurisin (1978) Icarus 33, 141.

Figure 1. Radial horizontal stress σ_r at the lunar surface due to the excess mare basalt load in Serenitatis. See text for discussion.

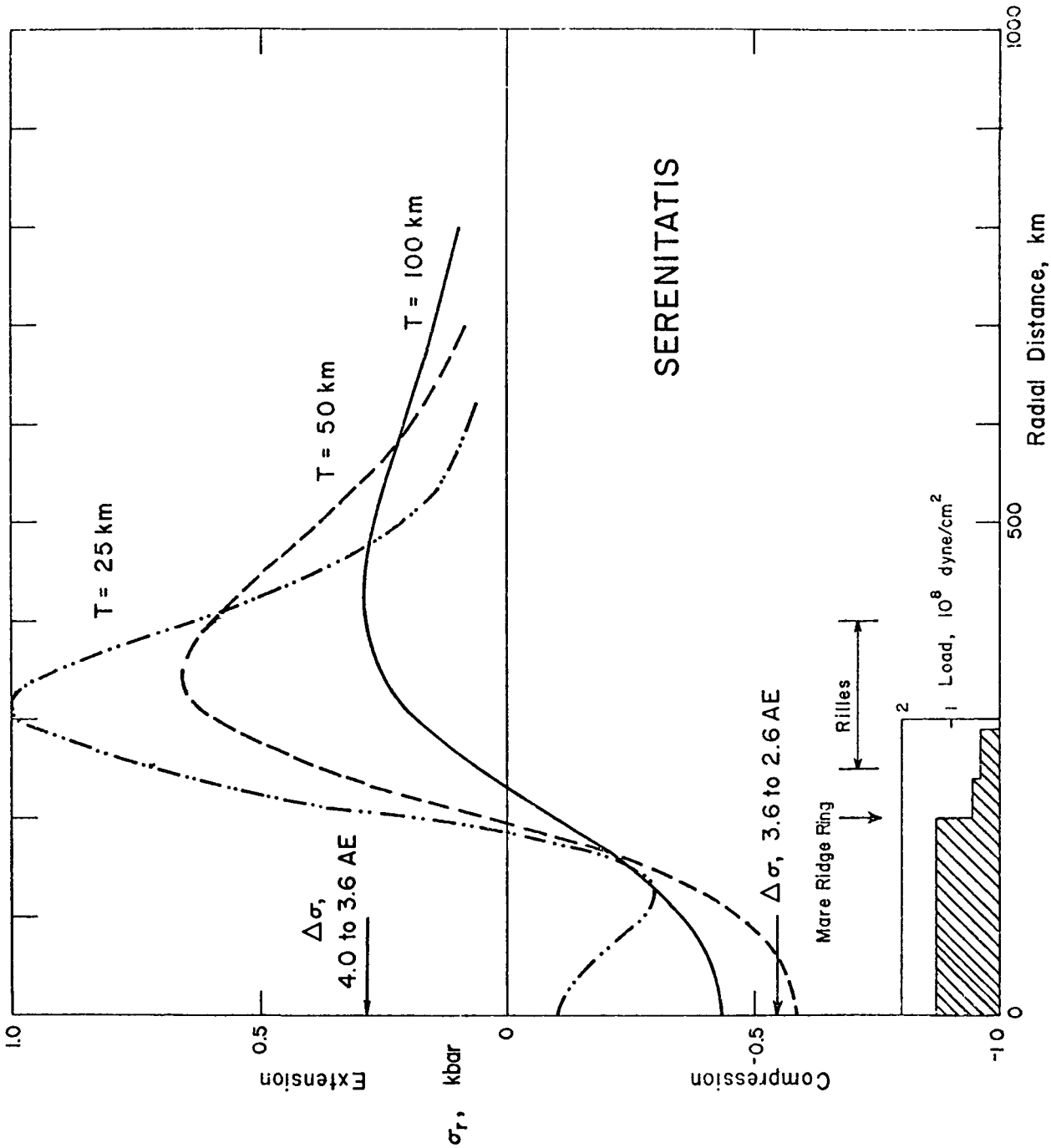

Topical Problems in Martian Geophysics, R. J. Phillips, Jet Propulsion Laboratory, California Institute of Technology, Pasadena, California 91103

Elastic Lithosphere The question of martian lithospheric thickness bears strongly on (a) constraints on the crustal thermal gradient and (b) the finite strength support of the Tharsis gravity anomaly. Previous considerations of elastic lithospheric thickness are based on several approaches. Thermal gradients from theoretical thermal models (e.g., (1)) may be used in the converse sense of (a) above as a guide to the finite strength question (2). Tensional features surrounding shield volcanoes may have resulted from lithospheric failure to the superincumbent loads. If so, the location of these fracture systems, radially outward from the volcanoes, is a function of elastic lithospheric thickness, assuming failure occurs at the point of maximum stress. For Pavonis Mons, a solution thickness of 50 to 90 is obtained (2). Other considerations of lithospheric thickness are based on maximum shear stress (3) and the height of the shield volcanoes (4,5). In the latter case, consideration of the thermal lithosphere is more appropriate, which on Earth is several times thicker than elastic lithosphere.

On Earth, the question of elastic lithosphere thickness has been most readily attacked with the use of gravity data as, for example, the flexure resulting from seamount loading (6). Low altitude orbiter gravity data from the extended Viking mission clearly show the gravity signature of the volcano Olympus Mons. A spacecraft pass at 300 km altitude just west of this feature shows a peak compressed line-of-sight free-air gravity anomaly of 158 mGals. Flexure resulting from surface loading depends mainly on lithospheric thickness and rigidity. This flexure may provide a measurable Bouguer anomaly, provided a significant density contrast exists at a depth less than approximately the horizontal extent of the load. Our previous study (7) regarding the isostatic state of martian topography, when considered with possible crustal isopach models, indicates that the crust-mantle boundary is no deeper than 200 km, and thus the depth constraint is satisfied.

We have undertaken a systematic study of the Olympus Mons gravity anomaly in order to isolate a possible component due to lithospheric flexure. In the presence of finite errors in the gravity and topography data and uncertainty in the appropriate density distributions, bounds are being placed on the flexural rigidity of the martian lithosphere and hence the lithospheric thickness.

Elysium Gravity Anomaly Support of the Tharsis doming is either by the finite strength of the lithosphere or by a dynamic mechanism in the mantle. If the latter is operative, then it may be related to geologically recent volcanism, and support of the Tharsis dome and the corresponding gravity anomaly may exist only as long as the dynamic mechanism is effective. The Elysium volcanic province provides an interesting test of this idea, because the shield volcano construction is old (8), perhaps contemporaneous

with the early plains and fracturing on Tharsis. The gravity of Elysium was not resolvable with Mariner 9 gravity data, but low altitude tracking of Viking reveals a 66 mGal free-air anomaly at 310 km altitude. This anomaly is presently being tested against isostatic models; of particular interest is a Pratt model (9) which may be more nearly isostatic for both Tharsis and Elysium than previously proposed Airy models (7).

Global Stress Patterns The relationship between the doming and gravity anomaly at Tharsis and tectonic features on the martian surface can be studied by calculating the principal deviatoric surface stresses for an assumed global elastic model. Preliminary calculations have been completed, adopting the nominal model of Phillips et al. (2), assuming a 100 km elastic lithosphere, and using only the dominant Tharsis spherical harmonic, J_{22}. The results show horizontal tensile stress of 1 kbar orthogonal to Valles Marineris, suggesting that this feature is a result of extensional tectonics associated with the Tharsis uplift (10) and that the region is still in a tensile stress state. An analogy to terrestrial lithospheric doming and fracturing, but not breakup, is warranted.

This study is being extended by including all of the important spherical harmonics and retaining longitudinal phase information among the various harmonics. Detailed relationships with a variety of linear features will be analyzed and placed in context with martian tectonic history.

References

(1) D.H. Johnston and M.N. Toksöz, Icarus, 32, 73 (1977).
(2) R.J. Phillips, R.S. Saunders, and W.B. Banerdt, J. Geophys. Res., 83, in press (1978).
(3) C.H. Thurber and M.N. Toksöz, EOS (abs.), 58, 1181 (1977).
(4) M.H. Carr, J. Geophys. Res., 78, 4049 (1973).
(5) K.R. Blasius and J.A. Cutts, Proc. 7th Lunar Sci. Conf., Geochimica et Cosmochimica Acta, Suppl. 7, 3, 3561 (1976).
(6) A.B. Watts and J.R. Cochran, Geophys. J. Roy. Astr. Soc., 38, 119 (1974).
(7) R.J. Phillips and R. S. Saunders, J. Geophys. Res., 80, 2893 (1975).
(8) M.C. Malin, Geol. Soc. Am. Bull., 88, 908 (1977).
(9) N.H. Sleep and R.J. Phillips, J. Geophys. Res., submitted (1978).
(10) K.R. Blasius, J.A. Cutts, J.E. Guest, and H. Masursky, J. Geophys. Res., 82, 4067 (1977).

CHAPTER 4 - GEOLOGICAL AND GEOCHEMICAL CONSTRAINTS ON PLANETARY EVOLUTION

REVIEW OF MERCURIAN GEOLOGY, R. G. Strom, Lunar & Planetary Lab., U. of Arizona, Tucson, AZ 85721.

The importance of Mercury as a comparison with other terrestrial planets lies in the fact that its surface is similar to that of the Moon yet its interior must be quite different. Mercury's high mean density (5.44 g/cm^3) must mean that it is composed of 65 to 70 percent by weight of metal phase (probably iron), and only some 30 percent of silicate phase. Evidence for volcanism and the detection of an intrinsic dipole magnetic field indicate the planet is chemically differentiated with a core and mantle. If most of the iron is concentrated in a core, then the core volume is about 50 percent of the total volume, and its radius is between 70 and 80 percent of the radius of the planet. A large fraction of the core may be molten or partially melted at the present time.

Mercury's surface can be broadly divided into three major terrain units: (1) heavily cratered terrain, (2) intercrater plains, and (3) smooth plains. The origin of the plains units is still a subject of debate. Smooth plains are the youngest unit and primarily occur within and surrounding the larger basins (Caloris and Northern). They are characterized by smooth rolling surfaces, often display wrinkle-like ridges, and have an albedo similar to the intercrater plains and cratered terrain. Both a volcanic (1, 2) and impact (3, 4) origin have been proposed for these plains. According to an impact origin the smooth plains are either impact melt if occuring within basins, and partially melted basin ejecta (3) or the result of ballistic erosion and sedimentation (4) if exterior to the basin. This interpretation is based largely by analogy with the lunar smooth basin ejecta facies associated with the Orientale and Imbrium basins. The volcanic hypothesis proposes that most of the smooth plains within and surrounding the large basins are lava deposits erupted in a manner similar to the lunar mare basalts. This argument is based on the similar distribution of lunar mare basalts and mercurian smooth plains, their large volume, stratigraphic relationships which indicate the plains are younger than the basins in which they lie, color differences, and the fact that some large fresh basins display only fields of secondaries without smooth exterior deposits. The intercrater plains are the most widespread surface unit on Mercury, covering about 1/3 of the surface viewed by Mariner 10. They occur in regions between craters and are characterized by a high density of small craters <15 km in diameter. Geologic mapping and the identification of very old craters and basins embayed by intercrater plains indicate they were emplaced over a range of times during the period of heavy bombardment (5, 6). They may be an older equivalent to the smooth plains. As with the smooth plains, both a volcanic and impact origin have been proposed for the origin of intercrater plains. The impact origin is basically the same as that proposed for the smooth plains. The main argument against an impact origin is the apparent lack of source basins to account for such a widespread distribution of these plains. A volcanic origin supposes a widespread (possibly global) episode(s) of volcanism occurred during the period of intense bombardment, possibly related to a period of heating and global tension during core formation.

The tectonic framework of Mercury is characterized by the widespread distribution of lobate scarps which are probably thrust or reverse faults resulting from compressive stresses (1). The scarps transect cratered terrain, intercrater plains and smooth plains, and are presumed to have a global distribution. Only relatively fresh craters are superposed on scarps and nowhere do intercrater plains embay the scarps. Therefore, scarp formation probably spans the time period from intercrater plains formation through the emplacement of the smooth plains. If the lobate scarps are global in distribution then Mercury was probably subjected to a period of global compression lasting from intercrater plains formation through the time of emplacement of the youngest surface units. This period of global compression may be the result of contraction due to cooling of the lithosphere following core formation (7). Alternatively, the period of compression may be due to a combination of compressive stresses in the equatorial regions from tidal despinning, and contraction during cooling of the lithosphere (8).

The diameter/frequency distribution of the mercurian heavily cratered regions, the lunar highlands, and the heavily cratered regions of Mars are very similar. This suggests that all three bodies were impacted by the same population of objects early in their history. Presumably this intense period of bombardment took place at about the same period of time on each body, i.e., during the first 1 or 2 billion years after their formation. The mercurian "highlands" show a paucity of craters between 15 and 50 km diameter compared to the lunar highlands which may be due to obliteration of a fraction of these craters by the emplacement of the intercrater plains. The mercurian "highlands" also show an overabundance of craters <15 km diameter compared to both the Moon and Mars (6). This may be due to the high density of smaller craters superposed on the intercrater plains and which are probably secondaries from many of the craters and basins of the heavily cratered terrain.

The peculiar hilly and lineated terrain antipodal to the Caloris basin has been interpreted to be the result of the focusing of seismic waves from the Caloris impact (9). This interpretation is based on analogous terrain at the antipodal areas of the lunar Orientale and Imbrium basins (9) and on theoretical studies (10). If this interpretation is correct then this terrain serves as a time horizon contemporaneous with the formation of the Caloris basin. In many cases crater rims have been disrupted by the process which formed the hilly and lineated terrain,but the smooth plains filling these craters has not. These smooth plains are highly localized and must be younger than the craters in which they lie, and presumably younger than the Caloris event, which suggests a volcanic origin (2).

The geologic and thermal history of Mercury is highly dependent upon the presence or absence of volcanism. Although the question of volcanism should be kept open pending more conclusive observational evidence or theoretical arguments, the following scenario presumes as a working hypothesis that at least large tracts of both smooth and intercrater plains are of volcanic origin. Shortly after accretion Mercury was subjected to a period of intense bombardment possibly contemporaneous with that which occurred on the Moon and Mars. Early in this period a large iron core formed leading to an

increase in temperature and consequently an increase in radius of about 17 km (7). During this period of extension volcanism occurred along fractures caused by the increase in volume to form large tracts of intercrater plains. This early period of volcanism occurred during the period of intense bombardment. Following core formation the lithosphere cooled and contracted (7) producing global compression leading to the formation of major thrust or reverse faults. The formation of thrust faults may have been aided by compression in the equatorial regions due to tidal despinning of the planet. Near the end of heavy bombardment the Caloris impact occurred to produce the basin and the hilly and lineated terrain antipodal to it. Shortly thereafter another period of volcanism produced much of the smooth plains in and around the major basins at a time when the heavy bombardment was ending. At this time the cooling of the lithosphere was almost complete and produced the last scarps which transect the smooth plains and other terrain. Since then only occasional impacts have scarred the surface to produce the rayed craters and other post-smooth plains craters.

References

1. Strom, R. G., et al. (1975) J. Geophys. Res. 80, 2478-2507.
2. Trask, N. J., and R. G. Strom (1976) Icarus 28, 559-563.
3. Wilhelms, D. E. (1976) Icarus 28, 551-558.
4. Oberbeck, V. R. (1977) J. Geophys. Res. 82, 1681-1697.
5. Malin, M. C. (1976) Geophys. Res. Lett. 3, 581-584.
6. Strom, R. G. (1977) Phy. Earth & Planet. Inter. 15, 156-172.
7. Solomon, S. C. (1976) Icarus 28, 509-521.
8. Melosh, H. J. (1977) Icarus 31, 221-243.
9. Schultz, P. H., and D. E. Gault (1975) The Moon 12, 159-177.
10. Hughes, H. G., and T. R. McGetchin (1976) Conf. on Comp. Merc. and Moon, 18.

The Stratigraphy of the Caloris Basin, John F. McCauley, U.S. Geological Survey, Flagstaff, AZ 86001; John E. Guest, Univ. of London Observatory, London, England; Newell J. Trask, U.S. Geological Survey, Reston, VA 22092; Gerald G. Schaber, U.S. Geological Survey, Flagstaff, AZ 86001; Ronald Greeley, Arizona State Univ., Tempe, AZ 85281; Donald E. Gault, Murphys Center of Planetology, Murphys, CA 95247; and Henry E. Holt, U.S. Geological Survey, Flagstaff, AZ 86001

The Caloris basin is surrounded by an extensive ejecta blanket that has been described by Trask and Guest (1), Strom and others (2), McCauley (3), and Guest and O'Donnell (4). As on the Moon where the ejecta sequence from the better preserved basins such as Imbrium and Orientale was used to establish a regional stratigraphy, the ejecta from the Caloris basin also can be used as a marker horizon despite the different gravitational environments. McCauley and others (in press) have proposed a formal rock-stratigraphy for the Caloris basin that has been adopted in geologic mapping of the Tolstoj (H-8) quadrangle by Schaber and McCauley and the adjacent Shakespeare (H-3) quadrangle by Guest, Greeley and Gault. This stratigraphy is patterned after that used in and around the Orientale basin on the Moon (5) and should be useful in the recognition of pre- and post-Caloris events over a broad expanse of the surface of Mercury. Crater degradation chronologies and correlations between plains units on the basis of crater frequency may aid in tying much of the remainder of the surface of Mercury to the Caloris event.

The rock stratigraphy proposed for the Caloris region includes all the morphologically distinct materials formed during the impact event that produced the basin. The terminology subsequently presented is considered informal and tentative pending publication in a format considered acceptable under the Code of Stratigraphic Nomenclature.

The rock-stratigraphic term Group is conceived of as an assemblage of formations that have something in common and it has been employed by McCauley and others (6) to include the various mappable units around the Caloris basin. The formations within the Caloris Group from the basin rim outward are: 1) the Caloris Montes Formation (Type area: The region around +18°, 184.5°, FDS-229), 2) the Nervo Formation (Type area: The region near +40°, 177.5°, FDS-193), 3) the Odin Formation (Type area: The region around +30.5, 164°, FDS-108), 4) the Van Eyck Formation, lineated facies (Type area: The southwestern edge of the crater Van Eyck near +40°, 163°, FDS-189) and the secondary crater facies (Type area: Crater cluster at -7°, 166°, FDS-0529131).

The Caloris Montes Formation was first recognized by Trask and Guest (1) and informally called the Caloris mountains terrain. It consists of a jumbled array of smooth appearing but highly segmented mountain massifs that rise several kilometers above the surrounding terrain. These massifs mark the crestline of the most prominent scarp or ring of the Caloris basin and grade outward into smaller blocks and lineated terrain. The Caloris Montes Formation is very similar in its morphology and is considered the analogous to the massif faces of the Montes Rook Formation around the Orientale basin (5). The Caloris Montes Formation is interpreted as basin

rim deposits consisting of ejecta from deep within Caloris that is mixed with but generally overlies and covers uplifted and highly fractured pre-basin bedrock (3).

The Nervo Formation consists of rolling to locally hummocky plains that lie in intermassif depressions. These plains generally lie within the annulus of rugged terrain marked by the Caloris Montes Formation and locally appear to drape and overlie some of the lower lying massifs. The Nervo Formation bears some resemblance to parts of the Montes Apenninus around the Imbrium basin (7); its closest counterpart in Orientale is the Knobby Facies of the Montes Rook Formation (5). The Nervo Formation or the intermontane plains as originally described by Trask and Guest (1) was interpreted as fallback ejecta which seems to explain its distribution pattern, relative roughness and the fact that it is generally perched above the smoother plains that encompass the Caloris basin.

The Odin Formation was originally called the Hummocky plains by Trask and Guest (1) and described as closely spaced scattered, smooth hills about 1 km across. The distribution pattern of the Odin is highly dependent on resolution and lighting but in general appears similar to that of the Alpes Formation on the Moon. The Odin like the Alpes occurs in broad lobes beyond the main basin scarp such as that seen in Odin Planitia. The Odin Formation is interpreted as part of the Caloris ejecta sequence, but its mode of origin is less clear than for some of the other formations within the Caloris Group. It may consist of blocky, coherent, late arriving ejecta from deep within the Caloris cavity later partly buried by smooth plains.

The Van Eyck Formation is the most distinctive of the circum-Caloris stratigraphic units. Like the other formations in the Caloris Group it also was first recognized by Trask and Guest (1) and called Caloris lineated terrain. The inner boundary is generally coincident with the weak outer Caloris scarp. The unit is made up of radial ridges and grooves that are extensively embayed by smooth plains. The Van Eyck Formation is similar in character but somewhat more degraded than the Fra Mauro Formation around the Imbrium basin on the Moon. Secondary cratering and the ballistic deposition of ejecta from Caloris undoubtedly played an important role in its emplacement. It is difficult to define individual secondary craters within the Van Eyck but at a distance of about one basin diameter there are numerous clusters and chains of moderately well preserved craters that are interpreted as far flung Caloris secondary craters. These have been included as a separate facies of the Van Eyck Formation because of their regional stratigraphic significance.

The plains in the floor of Caloris are a special problem and they have not been included in the Caloris Group. These plains have some features in common with the Maunder Formation in the floor of Orientale (3,5), but they do not show the radial and circumferential ridges characteristic of the Maunder which led to its interpretation as a basin floor unit. The Caloris plains have a more open and coarser fracture pattern than does the Maunder Formation on the Moon. In addition, the Caloris ridges and the fractures which cut them have a crude rhombic pattern that led Strom and others (2) to conclude that the floor of the basin subsided and then was gently uplifted to produce the open tension fractures observed. The ridges present in the floor of Caloris lack the crenulated crests that

are commonly observed on lunar ridges. Regardless of the origin and tectonic history of these plains it seems clear that they represent a deep basin fill unit that obscures the original floor of the Caloris basin.

The main Caloris Montes scarp is thought to approximate the edge of the basin of excavation of Caloris and to be the structural and stratigraphic counterpart of the Montes Rook scarp around the Orientale basin on the Moon (3). A weak outer scarp is present around most of the visible part of Caloris but it is best seen in the Shakespeare quadrangle to the north. This scarp is generally coincident with the transition between the massifs of the Caloris Montes Formation and the lineated facies of the Van Eyck Formation. The roughly rectilinear outlines of massifs within the Caloris Montes suggests structural control by a pre-basin fracture pattern. The much lower and discontinuous outer scarp is considered to be the feeble equivalent of the Montes Cordillera scarp around Orientale. Like the Cordillera it is thought to lie outside the limit of the crater of excavation. Its poor development and much closer relative spacing with respect to the edge of the basin may be due to gravitational effects as described by Gault and others (8).

References

1. Trask, N. J., and Guest, J. E., 1975, Preliminary geologic terrain map of Mercury: Jour. Geophys. Res., 80, 2461-2477.
2. Strom, R. G., Trask, N. J., and Guest, J. E., 1975, Tectonism and volcanism on Mercury: Jour. Geophys. Res., 80, 2478-2507.
3. McCauley, J. F., 1977, Orientale and Caloris: Phys. Earth Planet. Inter., 15, pp. 220-250.
4. Guest, J. E., and O'Donnell, W. P., 1977, Surface history of Mercury: A Review: Vistas in Astronomy, 20, 273-300.
5. Scott, D. H., McCauley, J. F., and West, M. N., 1977, Geologic map of the West Side of the Moon: U.S. Geol. Survey Map I-1034.
6. McCauley, J. F., Guest, J. E., Trask, N. J., Schaber, G. G., Greeley, R., Gault, D., and Holt, H. E., 1978, Stratigraphy of the Caloris Basin, Mercury: Jour. Res. Geological Survey, in press.
7. Hackman, R. J., 1966, Geologic map of the Montes Apenninus region of the Moon: U.S. Geol. Survey Map I-463.
8. Gault, D. E., Guest, J. E., Murray, J. B., Dzurisin, D. and Malin, M. C., 1975, Some comparisons of impact craters on Mercury and the Moon: Jour. Geophys. Res., 80, 17, 2444-2460.

Geologic History of the Victoria Quadrangle (H-2) Mercury. Elbert A. King, Department of Geology, University of Houston, Houston, Texas 77004, and George E. McGill, Department of Geology and Geography, University of Massachusetts, Amherst, Massachusetts 01003.

The portions of Victoria Quadrangle that are covered by Mariner 10 imagery have been photogeologically mapped at the scale of approximately 1:4,623,000 on a Lambert Conformal shaded relief base map provided by the U. S. Geological Survey. Three basic types of materials units have been mapped: terra materials, plains materials and crater materials. only one terra unit has been mapped, but two plains materials units, cratered plains materials and smooth plains materials, have been recognized. Crater materials have been subdivided into four morphologically different types that are believed, in general, to correlate with relative crater materials ages. Multiringed basins are included with the crater materials, as these are formed by the same fundamental process.

The geologic history that emerges from the mapping of these units is a rather familiar threefold pattern that seems common in the inner portion of the Solar System. The earliest history of the quadrangle is characterized by heavily cratered terra materials and very large craters, including a few multiringed basins. A declining total flux, especially of large impacting bodies, has resulted in younger materials units of moderately cratered plains with mostly intermediate size craters. The most recent identifiable materials units are identified by fewer and, in general, smaller craters and smooth plains.

We have no reason to believe that any process other than impact has been responsible for producing the mapped materials units. We do not see evidence for the volcanic origin of any of the plains units, but we cannot rule out the possibility that these units may contain some volcanic materials. No craters of volcanic origin have been identified during the course of the mapping.

Structural Lineament Pattern Analysis of the Caloris Surroundings: a pre-Caloris Pattern on Mercury, Pierre Thomas (*), Laboratoire de Géologie Dynamique Interne, Université de Paris-Sud, 91 405, Orsay Cedex, France.

Preliminary studies of the Caloris Basin exterior structure showed extensive system. This system compound of valleys and ridges radiating from the Caloris Basin is especially expressed in the N.E. and S.E. areas (1).

A preliminary study of the quadrangles near Calori (H3 and H8) demonstrated a strong Caloris related origin. These lineaments are mostly radially or tangentially oriented to Caloris (2).

This study intends to detail the distribution of the lineament system in the Caloris surrounding, and it is an attempt to interpret their distribution.

METHODOLOGY

This study was made with the Mariner 10 medium and high resolution images. Each lineament was plotted on a photo-mosaic of Caloris basin. A general lineament map of Caloris surroundings was drawn (Figure 1a). The all map, and its detailed quarters were optically filtered with a laser beam analyzer, using the Fourier transform technique.

RESULTS

The general lineament map (Figure 1a) shows several orientations. Four main trends are well separated after optical filtering: N. 15-25, N. 45-55, N. 125-135, and N. 150-160 (Figure 1b).

The lineament distribution in this area of Mercury appears to be unhomogeneous. The geographic distribution of these directions is detailed in each particular area with their lineament spectrum (Fourier transform).

+ In the NE part (between the N.53 and N.38 parallels), four directions are visible (Figure 1c):

  - The N. 45-55 system is only radially oriented in the southern part;
  - The N. 15-25 system is mainly radially oriented in the western part;
  - The N. 125-135 system is only tangentially oriented in the northern part;
  - The N. 150-160 system does not show any evident radial or tangential orientation.

    + Similar observations can be made in the two other areas: The E part (between the N.38 and the N.23 parallels); and the SE part (between the N.23 and the N.10 parallels).

It is noticeable that in the eastern area, none of the observed lineament shows a radial orientation (Figures 1d and 1e).

Structural maps of the Caloris surrounding area drawn separately for

each lineament system (Figures 2a, 2b, 2c, and 2d).

These four maps show that the N.29, N.50, and N.155 lineament systems are well visible in the entire area around Caloris; but the N.130 lineament system is locally expressed.

It is noticeable that:

-The N.50 system is mainly expressed in the area where it is near radially oriented (Figure 2b);

-The N.20 system is mainly expressed in the area where it is near tangentially oriented (Figure 2a);

-The N.155 system is homogeneously represented (Figure 2c);

-The N.130 system is only represented in the areas where it is near radially or tangentially oriented (Figure 2c).

This less represented direction is also nearly oriented to the sun direction (about N.10).

DISCUSSION

It is clear that the origin of this structural pattern could not be only related to the Caloris formation. This grid must not be considered as the result of a radial and tangential pattern, but as a consequence of the superposition of four different regular patterns.

If all of these lineaments have a structural origin, we could assume that they were preexisting to Caloris formation. Caloris was formed in a region where the fractured system was already existing. This preexisting pattern was rejuventated during Caloris basin formation. The rejuvenation was particularly important where the preexisting lineaments were in radial or tangential position; which could explain that these lineament systems are the best morphologically expressed. It could be also assumed that new fractured systems were induced during the Caloris basin formation; this new fracture system was superimposed to the old pattern.

References

1. Strom, R. G. N. J. Trask, J. E. Guest, "Tectonism and Volcanism on Mercury, J. Geophys. R. Vol. 80, 2478-2507, 1975
2. Masson, P., and P. Thomas, Report of Planetary Geology Program 1976-1977, NASA TM X-3511, 54-55.
3. O'Donnell, W. P., P. Masson, and P. Thomas, "Structural Pattern on Mercury" submitted to Icarus.
4. Thomas, P., "Recherche et étude des linéaments structuraux visibles a la surface de Mercure", D.E.A. de Géologie Structurale 1977, Université de Paris-Sud, 91 405, Orsay Cedex, France.

(*) C. N. E. S. Research grant, Contract No. 77005

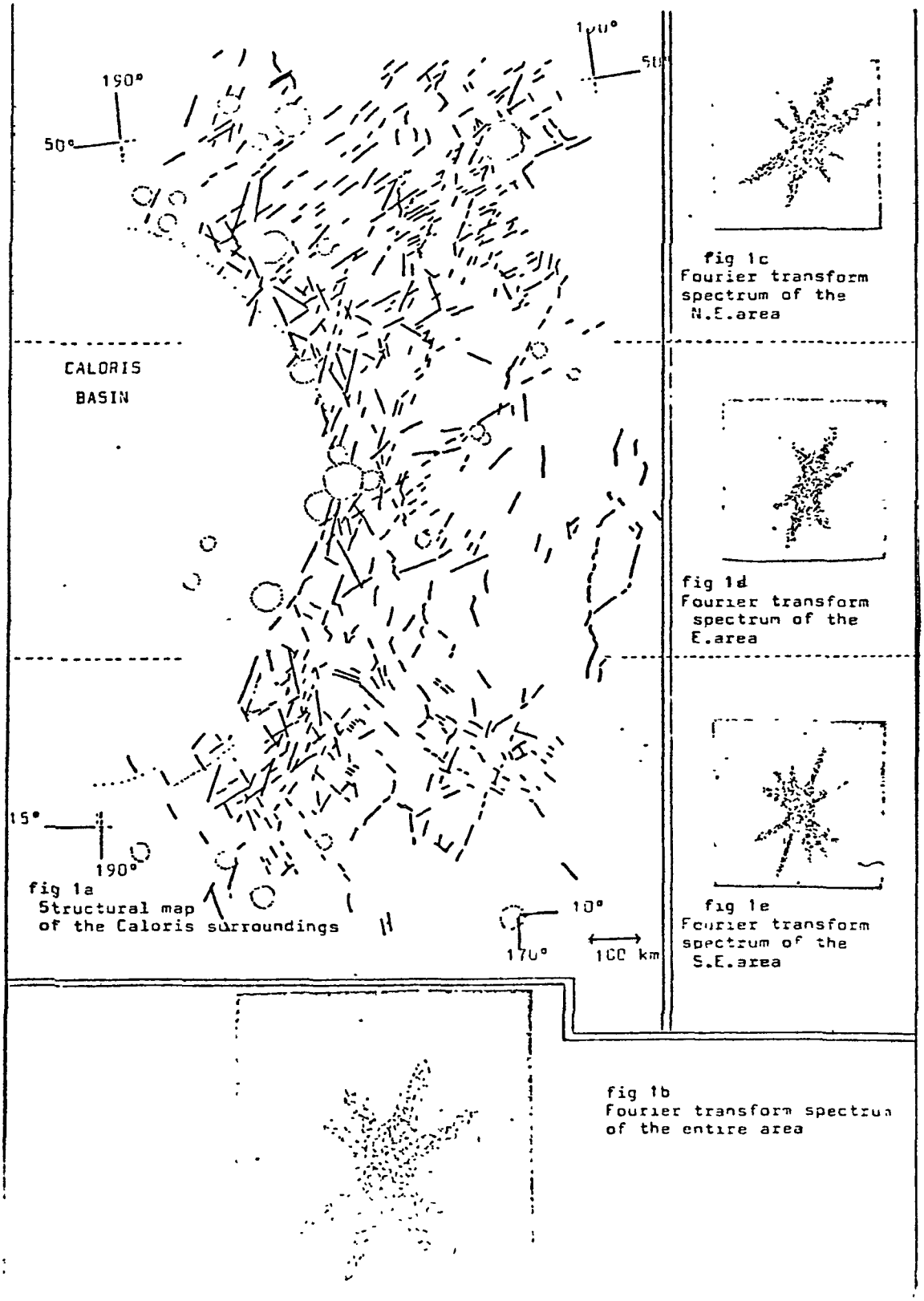

fig 1a
Structural map
of the Caloris surroundings

fig 1c
Fourier transform
spectrum of the
N.E.area

fig 1d
Fourier transform
spectrum of the
E.area

fig 1e
Fourier transform
spectrum of the
S.E.area

fig 1b
Fourier transform spectrum
of the entire area

fig 2a
Map of the N 20 lineament system

fig 2b
Map of the N 50 lineament system

fig 2c
Map of the N 130 lineament system

fig 2d
Map of the N 155 lineament system

The Nature and Origin of the Martian Planetary Dichotomy (is still a Problem), M. C. Malin, R. J. Phillips and R. S. Saunders, Jet Propulsion Laboratory, CA 91103

One of the most remarkable and least discussed observations of Mars derived from Mariner 9 data is the so-called "planetary dichotomy" - a strikingly abrupt change in physiography separating a low-lying lightly-cratered plains hemisphere from a high-standing heavily cratered hemisphere. The boundary runs along a very crude great circle inclined some 30 - 40° to the present martian equator, intercepting that equator at about 230°W, and ascending westward from there. The southern pole of this great circle is near 60°S, 330°W.

The most noteworthy characteristics of the dichotomy are the erosional landforms manifested along the boundary. Sharp (1973) first discussed these "fretted" terrains (most lying between 200° and 350°W) and surveyed their implications. Later reports (Malin, 1976; Mutch et al 1976) described in somewhat greater detail portions of the geomorphology of the erosional forms along the boundary, but in general only reiterated Sharp's findings.

Two results were, however, important in stimulating the current effort. Numerous authors (e.g. Sharp, 1973; Malin, 1976; Mutch et al 1976; Soderblom and Wenner, personal communication 1973) reported the observation of a "base-level" to which erosional landforms developed within the heavily cratered terrains. Malin (1976) further noted that the erosional landforms of the northern plains developed to this same base-level. He suggested that the intercrater plains materials seen in the heavily cratered regions of Mars were derived in part from materials redistributed from the north. The second result was Saunders' (1974) finding, reported in Mutch et al (1976), that a mantle phase change could have produced a thin and intensely fractured northern hemispheric crust.

We are attempting to evaluate several alternative models for the formation of the dichotomy, using geomorphological and geophysical observations. A zeroth order model was evaluated, based on the observation that the center of figure - center of mass offset was nearly aligned (within 30°) with the pole of the dichotomy:

CF - CM:	r = 2.501 km
(Bills and Ferrari, 1978)	θ = 62.0°S
	ϕ = 272.3°W

Thus over 80% of the CF-CM offset can be explained by the dichotomy.

A series of crustal models with varying degrees of isostatic compensation can be tested against the offset:

$$CF - CM \approx - \frac{3}{4} \frac{\Delta h \, \Delta \rho}{\rho_{mc}} \left(1 + C \frac{\rho_{cr}}{\Delta \rho} \right)$$

where Δh is the height difference between the two hemispheres, $\Delta \rho$ is the difference between the crust (ρ_{cr}) and interior (ρ_{mc}) densities, and C is a constant ranging from 0 (antisostatic) to 1 (isostatic).

In the anisostatic case (c = 0) we envision that some unknown process may have removed $\Delta h/2$ material preferentially from the north and redistributed $\Delta h/2$ debris, during the tail of heavy bombardment, among the materials of the massive equatorial blankets within the intercrater plains (*without accompanying isostatic adjustment*). To find an upper bound on the CF-CM offset resulting from this process, we take the maximum value of Δh as 7 km (actual mean value $\Delta h = 4.7 \pm 1.7$ km) and representative values of ρ_{mc} and ρ_{cr} (4 and 3 gm/cm^3, respectively). The predicted maximum CF-CM offset is ~ 1.3 km or about 1/2 the observed value (~ 9 km for mean Δh, or about 3/8 the observed offset). We thus conclude that formation of the dichotomy without an accompanying process in the planetary interior is not a valid hypothesis.

The other "end-number" model states the dichotomy is in complete isostatic equilibrium (C = 1). Here the requirement from inverting equation (1) is that $\Delta h \approx 3$ km, short of the observed mean value of 4.7 km (about 1σ off). We are thus left with two problems. First, either the observed Δh has been biased by observational technique by ~ 50%, or the global dichotomy is not fully compensated, or a simple Airy or Pratt mechanism for isostasy is not appropriate. Second, we are left with a causal paradox: is the dichotomy a product of a surface process acting in response to an internal mechanism, or did the erosion trigger internal adjustment processes which eventually over-shadowed the surface processes in terms of geophysical observables? Observations of the detailed morphology, chronology, and gravity/topography data in the transition areas between the hemispheres will hopefully provide us constraints on these relationships.

REFERENCES

Bills, B. G. and A. J. Ferrari (1978), Mars topographic harmonics and geophysical implications, Jour. Geophys. Res. (in press).

Malin, M. C. (1976), Nature and origin of intercrater plains on Mars, Ph.D. dissertation Part III, California Institute of Technology, Pasadena, CA 91103, 176 pp.

Mutch, T. A., R. E. Arvidson, J. W. Head, III, K. L. Jones and R. S. Saunders (1976), The Geology of Mars (Princeton University Press, Princeton, N.J.), 400 pp.

Saunders, R. S. (1974), Mars crustal structure (abs.), Bull. Am. Astro. Soc., 6, 372.

Sharp, R. P. (1973), Mars: Fretted and chaotic terrains, Jour. Geophys. Res., 78, 4073-3083.

Geological Implications of Regional Color Variations in the Martian Equatorial Regions, L. A. Soderblom, U.S. Geological Survey, Flagstaff, Arizona 86001

An effort was started during the last year to assemble digital maps of existing geological, geophysical and geochemical data for Mars on a global scale. The format and methodology used in this project is similar to that employed, in collaboration with the La Jolla Geochemical Consortium, to develop a collection of digital maps of lunar orbital and earth-based measurements of the Moon (Frontispiece, Proc. Lunar Sci. Conf. VIII, 1977; Eliason and Soderblom, 1977; Soderblom et al., 1977; Arnold et al., 1977; Metzger et al., 1977; Bielefeld et al., 1977; Russell et al., 1977). The overall aim of such studies is to establish genetic correlations between physical and chemical parameters related to evolution of the planetary surfaces through geologic time. In the case of Mars a variety of Mariner 9 and Viking Orbiter data are or will become available for such a global data synthesis program. The potential data sets include global topography, gravity, thermal properties, geologic maps, lava flow maps, relative ages from crater density, and a variety of atmospheric data. These data are being compiled by a variety of investigators. The purpose of this paper is to describe an important component of this global collection, i.e. a colorimetric or spectral reflectivity map (0.4μ to 0.6μ) generated from images acquired by the Viking Orbiter Images Systems. Described here are the computer generation digital maps and preliminary results of their comparison with digital global geologic and crater density maps.

Colorimetric maps were generated for surface materials exposed throughout the martian equatorial regions from images acquired by the

Viking Orbiter II vidicon cameras. Television frames acquired during the approach to the planet in martian summer in three colors (0.45 ± .03μm, 0.53 ± 0.05μm and 0.59 ± 0.05μm) were mosaicked by computer. The mosaics cover the latitudes 30° to 60° with resolution varying from 10 to 20 km per line pair. Image processing included geometric transformation to map format and removal of an average martian photometric function to produce albedo maps at three wavelengths.

The classical dark region found in the southern equatorial region and situated in the martian highlands is divided into two units on the color map. The older unit consists of topographic highs including ancient ridges, crater rims, and rugged plateaus with abundant small dendritic channels. This dark unit is among the reddest on the planet (.59μm/.45μm ≃ 3). The younger unit is intermediate in age and consists of smooth intercrater plains displaying numerous ridges similar to those found in the lunar maria. These dark plains are among the least red on Mars (0.59μm/0.45μm ∿ 2). The relatively young volcanic shields are, like the older unit, dark and very red. Two probable eolian deposits are predominant in the bright northern equatorial regions. The stratigraphically lower unit is intermediate in both color (.59μm/0.45μm ∿ 2.5) and in albedo. The upper unit, the highest albedo, is very red (0.59μm/0.45μm ∿ 3), and is probably the major constituent of the annual dust storms as based on ground-based observations; its areal extent changes from year to year. The south polar ice cap and condensate clouds dominate the southernmost part of the color map.

References

Arnold, J. R., Metzger, A. E., and Reedy, R. C., 1977, Computer-generated maps of lunar composition from gamma-ray data: Lunar Sci. Conf. Proc. Eighth, Geochim. et Cosmochim. Acta, v. 1, p. 945-948.

Bielefeld, M. J., Andre, C. G., Eliason, E. M., Clark, P. E., Adler, I., and Trombka, J. I., 1977, Imaging of lunar surface chemistry from orbital x-ray data: Lunar Sci. Conf. Proc. Eighth, Geochim. et Cosmochim. Acta, v. 1, p. 901-908.

Eliason, E. M. and Soderblom, L. A., 1977, An array processing system for lunar geochemical and geophysical data: Lunar Sci. Conf. Proc. Eighth, Geochim. et Cosmochim. Acta, v. 1, p. 1163-1170.

Frontispiece, Lunar Sci. Conf. Proc. Eighth, Geochim. et Cosmochim. Acta. v. 1, Pergamon Press.

Metzger, A. E., Lin, R. P., and Russell, C. T., 1977, On a correlation between surface remanent magnetism and chemistry for the lunar front-side and limbs: Lunar Sci. Conf. Proc. Eighth, Geochim. et Cosmochim. Acta, v. 1, p. 1187-1190.

Soderblom, L. A., Arnold, J. R., Boyce, J. M., and Lin, R. P., 1977, Regional variations in the lunar maria: Age, remanent magnetism and chemistry: Lunar Sci. Conf. Proc. Eighth, Geochim. et Cosmochim. Acta, v. 1, p. 1191-1199.

Viking Contributions: Martian Highland-Lowland Stratigraphy,
D. H. Scott, U. S. Geological Survey, Flagstaff, Arizona 86001

The northern lowland plains of Mars encircle the planet within a broad zone centered near 45° N within the Vastitas Borealis region. Highland terrain bordering the plains on the north has a highly mottled appearance on Mariner images. The mottling results from a combination of atmospheric haze and high-sun angle photographs, producing large albedo contrasts and obscuring even gross lithologic features and stratigraphic relations with adjacent units. On the south, the plains are also bordered by highland rocks that form an extensive plateau marked in many places by a high frontal scarp. Along this boundary, Mariner 9 images are generally clear but A-camera resolution is not detailed enough for the stratigraphic placement of plains and adjacent highland rock units.

This represents the first part of a continuing study using Viking photographs to determine stratigraphic and relative age relations between lowland plains and highland rocks and is concerned with the plains - plateau boundary on the south. Although in its simplest aspect the problem relates to the relative times of emplacement of the geologic units that make up these terrains, it is complicated because both the lowlands and highlands consist of several different units having a wide range in relative age (1,2,3). Thus it is conceivable that younger lava flows of the plains could embay and overlap highland rocks in some areas whereas older plains material might represent basement surfaces exposed by erosional retreat of the highland plateau in others.

Viking orbital images studied at several localities along the southern boundary of the plains have not unequivocably contributed to the solution of the problem. This is not so much the fault of picture resolution but mostly because of the covering of the plains - highland contact by detrital materials mass wasted along the base of the scarp. In the Protonilus Mensae area (44° N, 320°W) for example, photos that show the plains consist of two units: 1) old plains scarred by numerous secondary craters and, 2) young smooth plains, products of debris flows from the adjacent plateau that obscure stratigraphic relations between the older plains and highland rocks. Some pictures do show, however, that large areas of the old erosional surface left by scarp retreat and characterized by numerous projecting knobs, hummocks, and mesas have been covered by subsequent lava flows. In these areas sharp contacts between plains and remnants of highland materials are visible.

In the Acidalia Planatia region of Mars near the northeast margin of Tempe Fossae (53°N, 60°W), large re-entrants in the highlands frontal scarp are embayed by lava of the plains. Here, the older surface of the plateau is cut by grabens that terminate

sharply at the plains boundary. The plains have a relatively dark tone, lobate scarps, and small cratered cones indicative of a volcanic origin. A similar stratigraphic relation exists in places between highland material and plains material around the Isidis basin. In the Isminius Lacus, Casius, and Aeolis quadrangles the front of the plateau is highly dissected and remnants of the highlands are interspersed with plains over a width of 400 km or more and for a distance of several thousand kilometers. Ridges and flow fronts on the plains have a topographically fresh appearance and appear to be younger than adjacent highlands; also crater densities are lower on the plains. Stratigraphic relations at their boundary are not everywhere clear, but flow fronts occur in Utopia Planitia (34°N, 288°W) within a few kilometers of the dissected plateau and have overlapped some of the remanent hills. It thus seems probable that the highland plateau front may have retreated nearly 400 km before or during the emplacement of these lava flows on the old erosional surface. Comparison with terrestrial scarp retreat (4) suggests that a minimum time of about 200 million years would have elapsed between the start of lateral erosion of the highlands and the extrusion of plains basalt lying close to the present plateau.

References:

(1) Scott, D. H., and Carr, M.H., 1976, U. S. Geol. Survey, open-file report 76-573.

(2) Morris, E. C., and Dwornik, S.E., 1977, U.S. Geol. Survey, Misc. Geol. Inv. Map 1-1049.

(3) Greeley, R., and Guest, J.E., 1977, U.S. Geol. Survey Misc. Geol. Inv. Map 1-1038.

(4) Scott, D. H., 1978, ICARUS, (in press).

Stratigraphy of Amenthes quadrangle and vicinity, K. Hiller and G. Neukum, Institut für Allgemeine und Angewandte Geologie, Ludwig-Maximilians-Universität, 8000 München 2, Germany.

Viking and Mariner 9 pictures of Amenthes and vicinity have been investigated with respect to the Martian surface history. The pictures have been interpreted photogeologically (stratigraphy, morphology , albedo). Quantitative measurements of crater frequencies have been carried out for relative and absolute age determination. The crater frequency data have been reduced to a 1 km-value by application of the Martian standard crater curve (crater production size-frequency distribution) of Neukum and Wise (1976)(1).

The stratigraphy as inferred from our data reduction is displayed in figure 1. The relative ages in form of the 1 km cumulative crater frequencies can directly be converted to absolute ages in this diagram. The conversion is based on an updated version by Neukum et al. (1978)(2) of the Martian crater-ring chronology by (1). Emphasis was given to the study of the transition zone from the highland area to the Elysium Plains, (displayed in fig. 2) and to the Isidis basin area.

We draw the following conclusions from our data (fig. 1) for the different geologic domains:

a) Highlands : The oldest features visible in this area date back to $> 4.2 \cdot 10^9$ years. The crater size-frequency distributions show resurfacing activity between 3.7 and $4.0 \cdot 10^9$ years.
b) Knobby terrain : This border between highland and plains has retreated more than 400 km by erosional activity. The original highland crater population shows up in the size-frequency data of the large craters (4.1 - $4.2 \cdot 10^9$ years) that have survived the resurfacing process before $3.7 \cdot 10^9$ years ago. They show up in fig. 2a and b as intensely eroded ring structures.
c) Elysium Planitia : The crater size-frequency data show different ages at different crater sizes indicating successive resurfacing. We distinguish between two main periods: 4.0 - $3.7 \cdot 10^9$ and 3.7 - $3.0 \cdot 10^9$ years. In some cases remnants of older surfaces (4.0 - $4.1 \cdot 10^9$ years) are detectable.
d) Isidis basin rim area : The southeastern basin rim (highlands) is part of the oldest crust ($> 4.2 \cdot 10^9$ years) and shows resurfacing younger than approximately $3.9 \cdot 10^9$ years. The graben structures, associated with Isidis (Nili Fossae),show a similar age record as Elysium Planitia.

The age relationships of the investigated geologic units show some general features. In both the highlands and the plains areas resurfacing by large scale volcanic activity took

place contemporaneously at the time between $4.0 \cdot 10^9$ and $3.6 \cdot 10^9$ years ago. This was also the time when most of the aeolian and/or fluvial activity in this part of the Martian surface occurred, causing the retreat of the highland edge and resulting in the formation of the knobby terrain (Nepenthes Mensae). The presence of wrinkle ridges extending from the plains into the knobby terrain (fig. 2) and the age correspondence discussed above suggest flooding of the interknob regions by lavas from Elysium. This indicates that large scale aeolian and/or fluvial activies in this part of Mars was essentially terminated around $3.7 \cdot 10^9$ years ago.

The Elysium/Isidis plains crater frequency data show a second stage of volcanic activity at $3.7 - 3.0 \cdot 10^9$ years ago. This activity is not detectable in the highland crater frequency data except in Nili Fossae.

References:
(1) Neukum and Wise (1976) Science 194, 1381.
(2) Neukum et al. (1978) This Volume.
(3) Masursky et al. (1977) J. Geophys. Res. 82, 4016.

Acknowledgments:
This work was supported by the Deutsche Forschungsgemeinschaft and the NASA Planetary Programs Office.

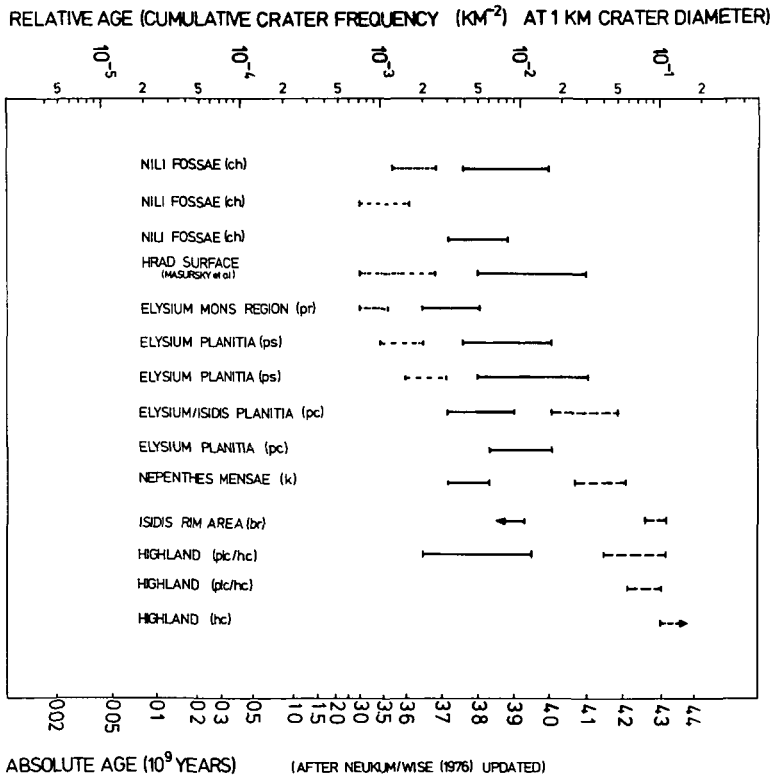

Fig.1

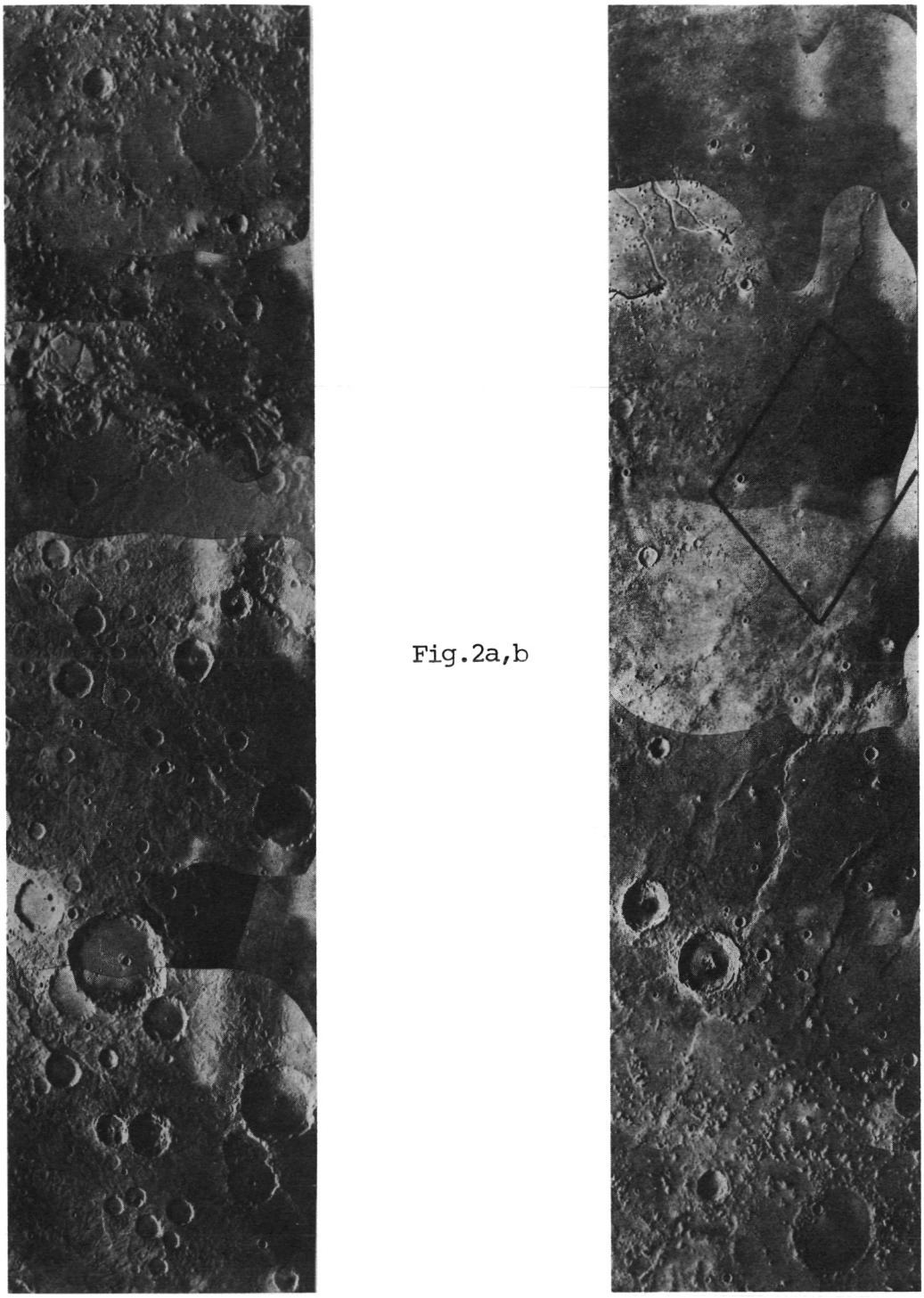

Fig.2a,b

Structural Evolution of the Claritas-Fossae Area of Mars, Philippe Masson (*), Laboratoire de Géologie Dynamique Interne, Université Paris-Sud, F-91405 Orsay (France)

The Valles Marineris - Noctis Labyrinthus - Claritas Fossae areas of Mars are apparently some of the most dramatic tectonic features of this planet. Since 1974, despite the Mariner-9 image resolution, the Valles Marineris origin was clearly interpreted as a consequence of lateral widening (i.e. extensive movements), (1, 1a, 1b). This conclusion was brightly confirmed with the interpretation of the Viking Orbiter 1 Primary Mission imagery (2). On the southern flank of the large domical structure centered in the Noctis Labyrinthus area, the Claritas Fossae system contrasts with the wide opened canyon of Valles Marineris. This system appeared on the Mariner-9 A and B frames and on the Geologic Map of the Phoenicis Lacus Quadrangle of Mars (3) to be an intensely fractured and faulted zone, roughly oriented North-Southward.

The Claritas Fossae system can be divided into three main geomorphic units (Figure 1): the Northern curvature, the Central "sigmoidal" zone, and the Southern "en échelon" faulted zone.

This area was entirely covered with Viking Orbiter 1 images. Four of these images were intensely photo-interpreted (056A49) 056A50, 056A52) in order to understand the mecanisms which generated or at least modified this major structure.

In the Northern curvature, a system of parallel grabens extends regularly from the Labyrinthus Noctis area (North) to the sigmoidal zone (South). This system seems to continue through the central sigmoidal zone where it is intersected by another system of grabens extending transversely (E/W). These two zones (curvature and sigmoid) are separated by a large dextral strike-slip fault oriented N.NW/S.SE. The first described system (curvature) outlines the circular Syria Planum area. Its grabens could be due to extensional movements related to an old stage of updoming of the Syria Planum area.

In the Central (sigmoidal structure) and southern ("en échelon" fault) zones, three main groups of trends are distinguished: N/S trends essentially expressed in the southern part of Claritas Fossae where dextral strike-slip faults are seen; N.NW/S.SE structures appearing to be the southern extension of the system observed around Syria Planum. These structures show some horizontal displacements (sinistral); E/W graben system intersecting the two other groups of structures described above.

These groups of structures seem to be the result of several tectonic episodes. The N/S trends may be the consequence of an old extensional period which influenced the entire area of Syria Planum - Noctis Labyrinthus - Claritas Fossae before the updoming episode or during the first steps of this episode.

Then a major updoming step occurred giving the curvature trends and their southern continuation (N.NW/S.SE structures). A new episode of uplifting with axial deformations took place: final updoming with opening of tensional factures in the Noctis Labyrinthus area; extension of the Valles Marineris system; and compressive movements (oriented W.SW/E.NE) giving the dextral and sinistral strike-slip faults in the southern part of Claritas Fossae, and N/S perpendicular extensive movements which generated the E/W grabens of the sigmoidal zone.

Finally the Claritas Fossae structures could proceed of extensive forces due to a regional updoming, as described by Carr (4), and compressive forces due to crustal expension in other parts of the dome flanks (Valles Marineris, for ex.). These assumptions have to be confirmed with further detailed studies of the stress fields in the Solis Planum - Sinai Planum areas (work in process).

References

1. Masson, P., in Internat. Coll. Planetary Geology exp. abstr., Rome 1975.

1a. Masson, P., in Internat. Coll. Planetary Geology Proceed., Geologica Romana, 1976.

1b. Masson, P., Icarus 30, 49-62, 1977.

2. Blasius, K. R., J. A. Cutts, J. E. Guest, H. Masursky, J. Geophys. R. Vol. 82, 4067-4091, 1977.

3. Masursky, H., A. L. Dial, M. H. Strobell, Geologic Map of the Phoenicis Lacus Quadrangle of Mars (in press).

4. Carr, M. H., J. Geophys. R. Vol. 79, 3943-3949, 1974.

* INAG Research Contract No. B 650.323.

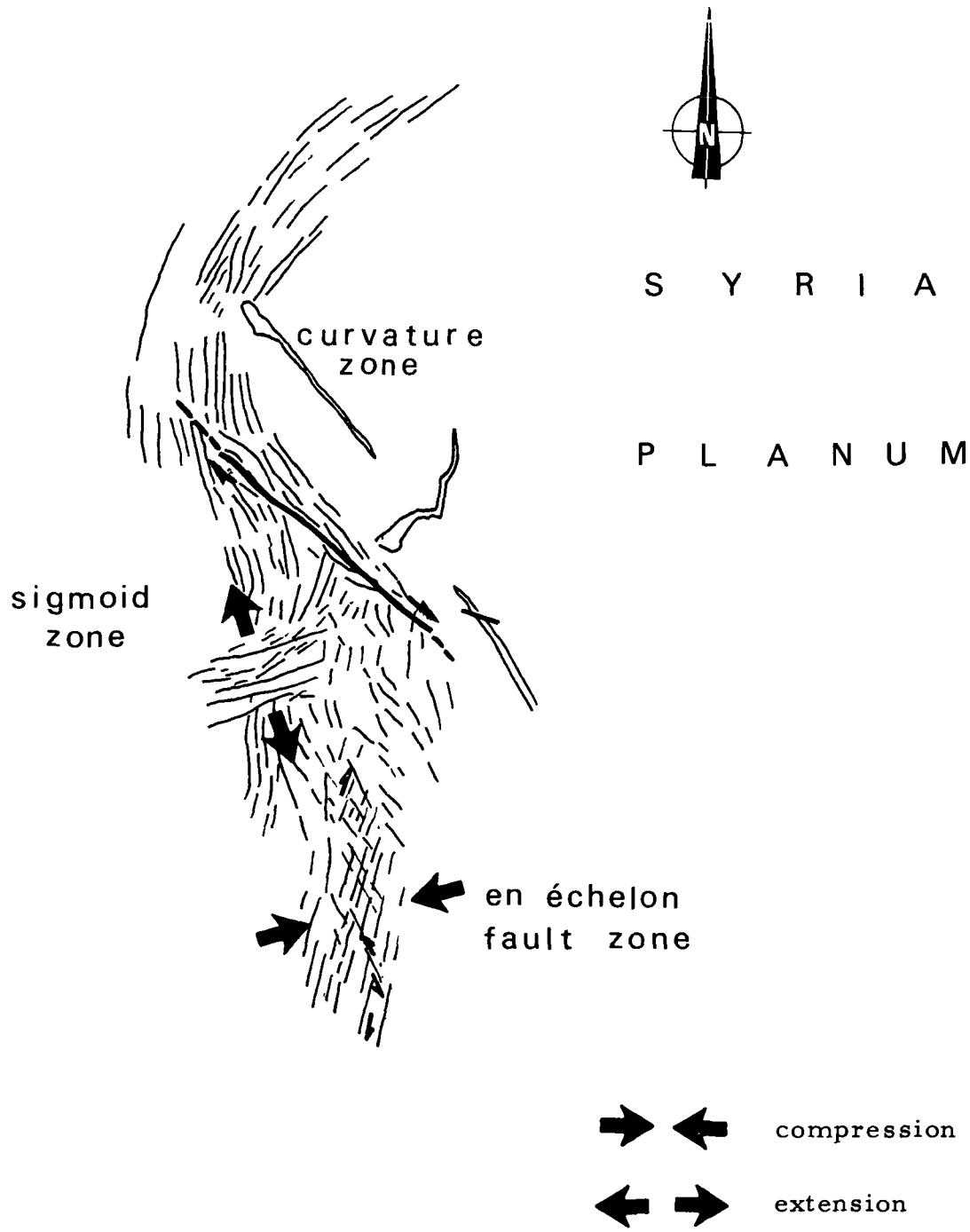

Fig. 1: Claritas Fossae Structural Sketch Map (scale 1:5, 000, 000).

Polygonal fractures of the martian plains, E. C. Morris, U. S. Geological Survey, Flagstaff, Arizona 86001, and J. R. Underwood, Kansas State University, Manhattan, Kansas 66506.

Polygonal patterns consisting of fractures which form individual polygons up to 20 km across are commonly found throughout martian plains in the 40°-50° N latitude belt. These fracture patterns are well displayed in the high resolution (<100m/line pair) Viking Orbiter pictures. Their origin has been difficult to explain mainly due to their scale. Polygonal-patterned ground is common in terrestrial periglacial regions but individual polygons rarely achieve dimensions of more than 100 m. Various origins for the martian polygonal fractures which have been suggested include ice wedging (1), contraction cracks in cooling lava (2), desiccation cracks (3), or tectonic fractures (1). On the basis of observations made in this study the following characterize the martian polygonal fractured plains:

(1) The polygonally fractured plains occur mainly in the 40°-50° N latitude band.

(2) The polygonal fractures are formed in older or exhumed surfaces from which a younger layer of plains material has been stripped.

(3) Younger material overlying polygonal fractured surfaces do not show the fracture pattern. This is true of remnants of overlying material that has been stripped off or younger material that has subsequently blanketed fractured surface.

(4) The edges of the fractures are rounded and do not have rims or ramparts, such as those associated with terrestrial ice

wedges polygons.

(5) A few blocks or polygons appear to have been displaced vertically or tilted in relation to adjacent blocks.

(6) Many of the polygons are incomplete or not closed, i.e., one or more sides are not developed. Circular fractures are common and often closed.

(7) Most of the fracturing is randomly orthogonal, i.e., primary fractures with random secondary orthogonal systems.

(8) Individual polygons vary in size from several kilometers to about 20 kilometers. Fractures widths vary up to 2 km and are typically a few hundred meters deep.

An origin of the polygonal fractures which is favored here and satisfies most of the above observations is contraction cracking of cooling lava. Initial fracturing occurred after emplacement of relatively thick volcanic flows which, in turn, were buried by other plains-forming material. The fracture pattern may have been attenuated by compaction or desiccation of less competent underlying material. The fractures were subsequently etched out in strong relief, probably by eolian processes that stripped off the overlying plains material. The problem of scale arises with cooling fractures of this magnitude, as is also the case for all other explanations for the fractures. Contraction cracks of this magnitude would require lava flows of several km thick.

The largest polygonal fractures on earth are associated with desiccation of thick playa sediments

(possibly 300m thick) where polygon diameters are up to 1 km (4). On the basis of scale alone an alternate explanation of the Mars polygonal fractures would be desiccation of a thick layer of ice or water saturated sediments.

Tectonic fractures responding to a regional stress field would probably exhibit a more regular geometry than that displayed by the polygonal fractures of the martina plains.

References:

(1) Carr, M.H., and Schaber, G.G., 1977, Martian permafrost features. Jour. Geophys. Res., v.82, no. 28, p. 4039-4053.

(2) Carr, M.H., Masursky, H., Baum, W.A., Blasius, K.R., Briggs, G.A., Cutts, J.A., Duxbury, Thomas; Greeley, Ronald; Guest, J. E., Smith, B.A., Soderblom, L.A., Veverko, Joseph, Wellman, J.B., (1976) Preliminary results from the Viking Orbiter Imaging Experiment. Science, v.193, no. 4255, p. 766-776.

(3) Mutch, T.A., Arvidson, R.E., Binder, A.B., Guinness, E. A., Morris, E.C., 1977, The geology of the Viking Lander II site, Jour. of Geophy. Res., v.82, no. 28, p. 4452-4467.

(4) Pratt, W. E., 1958, Large-scale polygonal jointing. AAPG Bulletin, v.42, #9, p. 2249-2251.

Graben Geometry and Crustal Structure, George E. McGill, Dept. Geology/Geography, Univ. of Mass., Amherst, MA 01003.

Both the mechanical properties of rocks and the stresses that have acted on them are reflected in the attitudes of fractures, and the attitudes and movement histories of faults. The major problems encountered in attempts to infer mechanical properties and stress histories from faults and fractures derive from the multiplicity of possible causes for even a simple fracture or fault pattern. Sorting faults and fractures in the field according to various objective criteria, such as size, roughness, and chronology, is motivated by the hope that the additional constraints will eliminate many hypothetical causes for the observed pattern of orientations and movements.

Grabens and, in particular, graben systems are potentially more useful than sets of individual faults and fractures for inferring rock properties and stress history because they contain more geometrical information. Thus kinematic and mechanical interpretations are constrained by the three-dimensional geometry of an individual graben and by the plan-view geometry of a graben system as well as by the attitudes of the individual faults bounding the grabens. We have developed this concept for a specific example, the grabens of the Needles District, Canyonlands National Park, Utah, in a series of papers and reports (e.g., McGill and Stromquist, 1974, 1975, in review; Stromquist, 1976).

In detail, the geometries of grabens must be highly variable. However, if we consider only relatively simple grabens without significant transverse rotation or extensive secondary faulting of the down-faulted block, it is possible to envisage three basic styles of cross-sectional geometry (Figs. 1-3). Very little information concerning crustal structure can be gleaned from even simple grabens if they have cross sections such as shown in figure 1. On the other hand, the grabens illustrated in figures 2 and 3 require that the faults bounding them meet at some depth beneath the surface, and that the mode of deformation or failure in the rocks beneath the line of intersection is different from that in the rocks nearer the surface. The basic assumption underlying the use of graben geometry to infer crustal structure is that the intersection line of the faults bounding a graben marks the contact between crustal materials with contrasting mechanical properties. Commonly, grabens on the Moon and Mars occur in systems in which the individual grabens tend to have similar widths and in which the distances between grabens are nearly constant. Such regularity strengthens the inference that the depth to fault intersection coincides with some sort of material boundary within the crust. Also, the constancy of graben widths and spacings reduces the probability that the geometry

of individual grabens is as illustrated in figure 1 (although we cannot prove this contention, it seems unlikely to us that faulting on vertical fractures that do not intersect or otherwise interact at depth will result in facing pairs of faults producing grabens of systematic width and spacing).

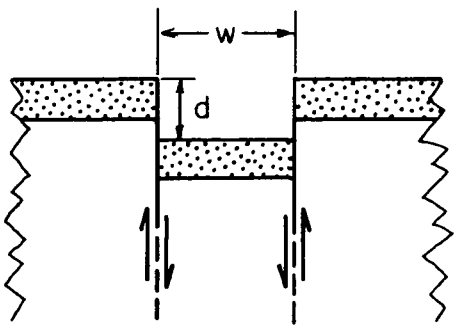

FIGURE 1

Vertical bounding faults. Little or no information about crustal structure.

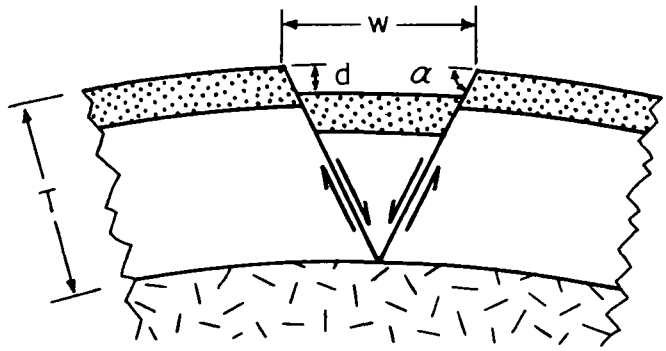

FIGURE 2

Inward-dipping bounding faults. Graben-forming stresses due to bending (either elastic or "viscous"). Minor secondary faulting or marginal brecciation needed to avoid open gaps along the faults.

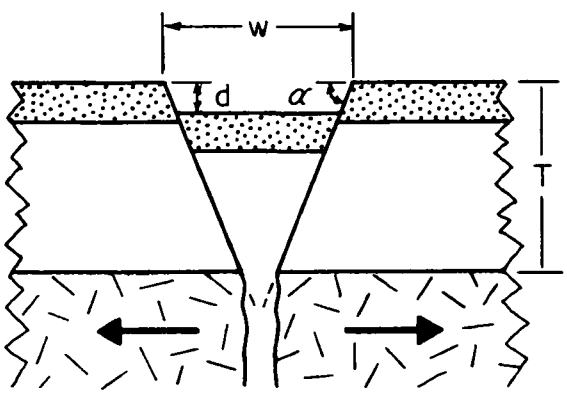

FIGURE 3a

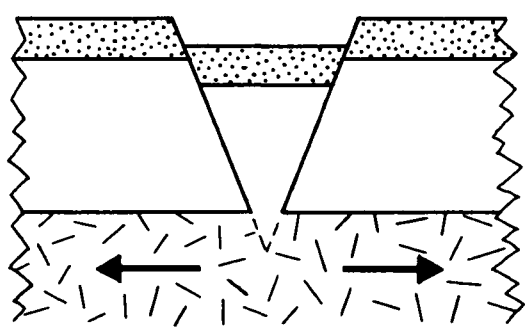

FIGURE 3b

Inward-dipping bounding faults. Graben-forming stresses due to simple extension of crust. Rocks below depth, T, more brittle than shallower rocks in 3a, more ductile than shallower rocks in 3b.

If w, d, and α (Figs. 2 and 3) can be determined independently, it is possible to calculate the thickness, T, of the faulted layer unambiguously. It is commonly very difficult to measure all three of these in the field, and generally verges on the impossible to measure all of them on photographic images of planetary surfaces. However, reasonable approximate solutions are possible in some instances if α can be constrained within close limits (Golombek, this volume). Alternatively, if w and d can be measured and if the increase in w due to crustal extension and graben formation can be estimated, the thickness of the faulted layer can be determined approximately (Stromquist, 1976; McGill and Stromquist, in review). Although other data generally will be required to determine the specific nature of the boundary implied, the areal variability of graben geometry permits correlation of the depth to the boundary with other crustal characteristics, such as gross topography and areal geology.

McGill, G.E., and Stromquist, A.W., A model for graben formation by subsurface flow; Canyonlands National Park, Utah, Univ. Mass., Dept. Geology/Geography, Contr. No. 15, 79pp., 1974.

McGill, G.E., and Stromquist, A.W., Origin of graben in the Needles District, Canyonlands National Park, Utah, Four Corners Geol. Soc. Guidebook, 8th. Field Conf., Canyonlands, 235-243, 1975.

McGill, G.E., and Stromquist, A.W., The grabens of Canyonlands National Park, Utah; geometry, mechanics, kinematics, ms. submitted to Jour. Geophys. Res.

Stromquist, A.W., Geometry and growth of grabens, Lower Red Lake Canyon area, Canyonlands National Park, Utah, Univ. Mass., Dept. Geology/Geography, Contr. No. 28, 118pp., 1976.

Geometry of Lunar Grabens: Implications for Shallow Crustal Structure, Matthew P. Golombek, Dept. Geology/Geography, Univ. of Massachusetts, Amherst, Mass. 01003.

The geometry of grabens can be a useful indicator of crustal structure (Stromquist, 1976; Golombek and McGill, 1977; McGill, this volume). This abstract will describe the geometry of lunar grabens, possible models for graben formation, and some inferences concerning the shallow crustal structure of the Moon derived from graben geometry.

Extensive work on the attitude of shear fractures bounding lunar grabens indicates that they dip ~60° and are inclined towards one another. Knowing this, two models of graben formation are possible; faulting may be the result of arching (Fig. 2) or simple extension (Fig. 3). In either case, faults are assumed to originate at a depth, T, which marks a major mechanical discontinuity, and to propagate upwards at some angle, α_0 (Fig. 1).

Bending or arching of layer T can produce a graben if stresses exceed the fracture strength of the rock (Fig. 2). The volume of the graben wedge is assumed to remain constant between initiation of faulting (Fig. 1) and graben formation (Fig. 3) (i.e., bulk dilatancy negligible). The final width, w, and the depth to intersection of faults directly beneath the graben, D, are obtained from graphical models of graben geometry resulting from successive finite rotations. Values for the final dip of the faults, α_1, and the amount the graben floor has dropped, d, can be calculated for initial graben width, w_0, and α_0 by utilizing the following equations: $T = .5w_0\tan\alpha_0$; $\alpha_1 = \tan^{-1}(2D/w)$; $A = .5w_0T$ (where A = cross-sectional area of the graben wedge); $(w-2d/\tan\alpha_1) = 2\sqrt{A/\tan\alpha_1}$; $(D-d) = 2A/(W-2d/\tan\alpha_1)$; $d = D-(D-d)$. These data can be summarized in a plot of α_1 versus d. For measured values of d and w, α_1 must have decreased such that $\alpha_0-\alpha_1 \simeq 10°$. But the slopes of the surfaces away from the graben also equal $\alpha_0-\alpha_1$ (Fig. 2). Slopes such as these are not associated with lunar grabens; hence this model is not applicable.

The simple extension model begins as did the rotation model (Fig. 1) and opens a distance, Δw, at the bottom of layer T (Fig. 3). Stromquist (1976) derived the following relation by equating the space above the graben floor plus the initial area of the wedge with the final total space: $0 = 2T^2\Delta w-2dT(w_0+\Delta w)-d^2 w_0$ (bulk dialatancy negligible). This equation can be solved for d in terms of Δw and $\tan\alpha_0$ for specific values of w_0 because $T = .5w_0\tan\alpha_0$. A family of curves can be generated (each curve for a different w_0) which relates d with Δw and $\tan\alpha_0$. Specific solutions for lunar grabens ($\alpha_0 \simeq 60°$) indicate that for observable d and $w_0+\Delta w$, Δw is commonly 50 to 100m. So this model results in reasonable Δw values for observed d, $w_0+\Delta w$, and α_0.

The walls of lunar grabens do not retain the ~60° dips

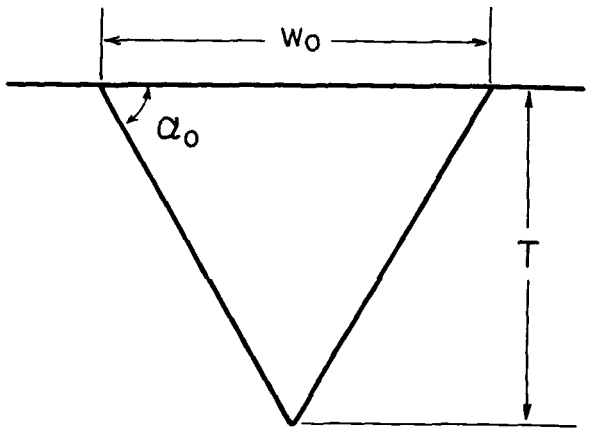

FIGURE 1

Graben faults initiate at depth T and propagate upward at angle α_0 resulting in initial width w_0.

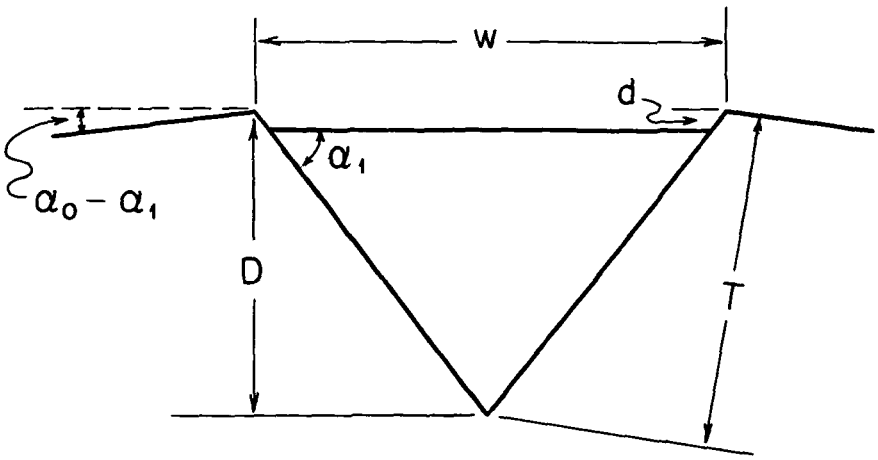

FIGURE 2

Rotation (arching or bending) model. $\alpha_1 < \alpha_0$, D<T.

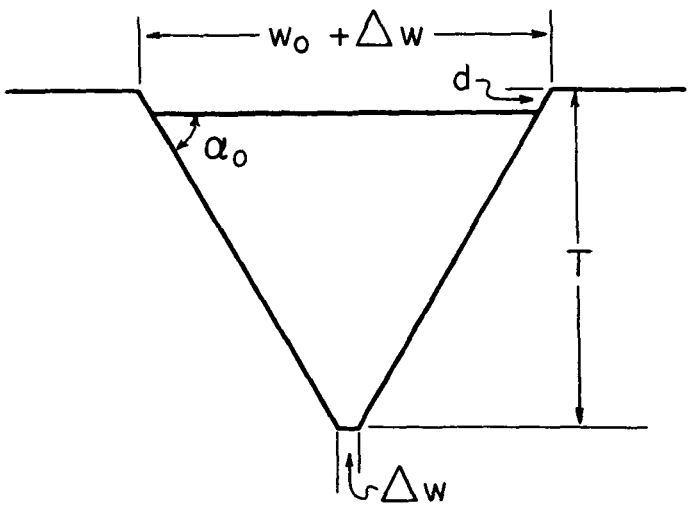

FIGURE 3

Simple extension model. $w_0+\Delta w$ = final width. α_0 and T are the same as in Fig. 1.

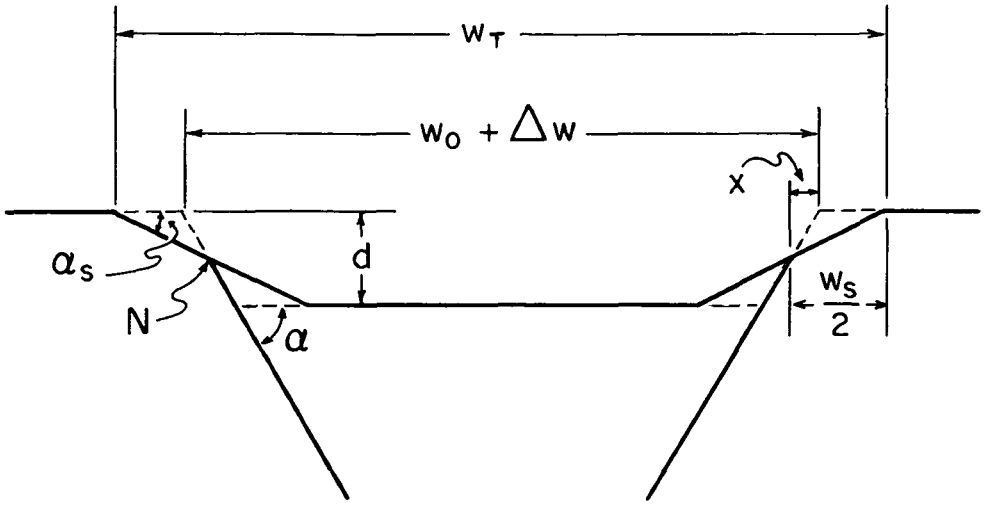

FIGURE 4

Mass wasted graben walls, $\alpha_s \simeq 18°$. Model assumes point N is located at 1/2 w_s and 1/2 d on the graben wall. $2X = d/\tan\alpha_0$ $w_0+\Delta w = w_T - w_s + d/\tan\alpha_0$.

of the bounding fractures (Fig. 4). Best available topographic data indicate average wall slopes of ~18°. The true width, $w_0+\Delta w$, may be estimated using the model in Fig. 4. Therefore, an unbiased determination of T is possible if α_0 can be determined within reasonable limits.

The depths to intersection of the bounding fractures of lunar grabens correlate with 1) areal geology, 2) theoretically predicted thicknesses of total ejecta, and 3) the major seismic discontinuity at the Apollo 17 site. These data support the contention that faults bounding lunar grabens originate at the base of a layer of fractured or brecciated rock. Thus this major mechanical discontinuity probably corresponds to the base of the megaregolith.

Golombek, M.P., and McGill, G.E., Straight and arcuate lunar rilles as indicators of shallow crustal structure (abst.), EOS, 58, 1180, 1977.

Stromquist, A.W., Geometry and growth of grabens, Lower Red Lake Canyon area, Canyonlands National Park, Utah, Univ. Mass., Dept. Geology/Geography, Contr. No. 28, 118p., 1976.

Application of Anisotropy of Magnetic Susceptibility Measurements to Transport Mechanisms on Planetary Surfaces, J. Hatten Howard III and Brooks B. Ellwood, Dept. of Geology, Univ. of Georgia, Athens, GA 30602

Numerous transport mechanisms have been proposed to explain emplacement of distinctive materials observed on the surfaces of the Moon, Mars, and Mercury. Some transport processes (lava flow, wind) are readily identified by the morphology of the features produced. The real nature and mechanics of emplacement mode of many planetary materials--such as crater ejecta, smooth plains, landslide deposits, patterned ground--are not known, however. Suggested transport mechanisms are varied and include impact with base-surge and/or ballistic transport, flow or "rain" of impact melt, several types of lava flow, ash flow, fluvial braided and channel flow, gelifluction, surface flow of impact ejecta, and landslide (debris or mudflow, rockfall avalanche).

Such transport mechanisms vary as a result of the proportion of solid to intermixed gas or liquid; mechanical properties and velocity of the flow; the type of flow (laminar or turbulent); and the manner of flow cessation (cooling or settling of material). Final orientation of elongate or flat components, which result in the rock fabric, are due to transport effects and may be characteristic of a specific transport mode, so that analyses of sample fabric may serve both to identify the transport mechanism and to understand the dynamics of particle movement.

Anisotropy of magnetic susceptibility (AMS) in rocks, which is related to magnetic mineral shape and orientation, is a useful measure of the magnetic fabric and results from inhomogeneity of magnetic properties in the rock. The magnetic susceptibility, K (volume susceptibility), or χ (the more easily determined mass susceptibility), measured for any rock sample is a second-rank tensor which relates an inducing magnetic field $\overline{H_j}$ to an induced intensity of magnetization $\overline{J_i}$, so that

$$\overline{J_i} = \overline{\overline{K_{ij}}}\,\overline{H_j} \quad \text{or} \quad \overline{J_i} = \overline{\overline{\chi_{ij}}}\,\overline{H_j} \; . \tag{1}$$

For low magnetic fields the AMS can be represented by an ellipsoid, with orthogonal axes of maximum, intermediate, and minimum susceptibility magnitude K_a, K_b, and K_c, respectively, and corresponding azimuthal directions. The data are commonly derived from measurements using a low-field torque magnetometer (9) and susceptibility bridge (1).

AMS parameters, derived from ellipsoid magnitudes, permit analysis and interpretation of the magnitude and orientation of the magnetic properties within one or more oriented samples from a specific rock body. K (or χ) is also an indication of bulk ferrimagnetic content of the sample; representative values are 10^{-3} volume cgs units for basalts and 10^{-5} mass cgs units for some loosely consolidated sediments.

Percentage anisotropy (% AN), given by the function

$$\% \text{ AN} = (K_a - K_c)K_b^{-1} \times 100 \ , \qquad (2)$$

describes the magnitude of total anisotropy, that is, of the AMS ellipsoid, and shows departures from randomness in orientation of ferrimagnetic mineral grains. A more useful parameter, E (8), describes the shape of the AMS ellipsoid, where

$$E = K_b^2(K_aK_c)^{-1} \ . \qquad (3)$$

For E > 1.0, the ellipsoid is oblate (flattened); for E < 1.0, the ellipsoid is prolate (elongated). Since in an individual sample the AMS reflects the integrated effect of magnetic-grain shape, values of E increasing from 1.0 indicate increasingly planar orientation of magnetic grains, and values of E decreasing from 1.0 indicate increased grain elongation or alignment.

An AMS parameter which is very sensitive to differences in long-axis magnetic-grain alignment is F, where

$$F = K_a'(K_b'K_c')^{-\frac{1}{2}} \qquad (4)$$

(2); K_a', K_b', and K_c' are, respectively, the maximum, intermediate, and minimum AMS magnitudes recalculated for a standardized K (representative of the material being examined) so that variation of F between samples is not affected by simple variations in K. This F value, therefore, emphasizes the linear magnetic fabric in the rock.

Grain orientation--resulting from crystal growth or grain settling--is controlled by major forces: gravity; the planet's magnetic field (for small particles); currents; and stresses resulting from cooling and compaction. For example, planar grain fabrics may result from particle settling and/or from compaction, whereas linear fabrics are due to the action on elongated grains of forces tangential to the bed, such as drag of depositing currents. AMS techniques have been applied to several geologic proglems, including:

(1) the effect of cooling stresses on mineral orientation during formation of basalt columns (3);
(2) distinction of mode of occurrence of basalt layers (2, 6) and of relative abundance of intrusive and extrusive basaltic units (5);
(3) the effect of currents on particle alignment (7, 4);
(4) particle alignment in turbidites (unpublished data); and
(5) AMS variations in an ash-flow unit (unpublished data).

AMS measurements are now being made on terrestrial deposits formed by different transport mechanisms, including those deposits which are possible analogues of processes operating on other planetary surfaces, in order to

determine the variability of AMS parameters throughout units of known origin and to understand the mechanisms by which the AMS parameters develop. Types of deposits being studied include fluvial deposits, coastal dunes and beaches, lava flows, ash flows, and impact/explosion ejecta. Analyses will be extended to dune forms and ash falls.

The AMS measurements represent both magnitude and direction of the induced magnetic properties and as such have several applications to planetary studies. AMS analyses of lunar samples could be used to distinguish intrusive and extrusive basaltic rocks and to determine stress orientations in breccias and glasses. Many useful interpretations could be made from the rock stratigraphic relationships observed in core samples, especially should core orientation become known; in addition to identifying emplacement modes of the layers, the direction of movement may allow source identification (crater or vent of origin) and thus aid in interpreting local geologic history.

The instrumentation for measuring AMS could be miniaturized for use on planetary lander, or perhaps penetrator, missions. Such data for cores obtained from a planetary surface could serve to identify the mode of occurrence and emplacement mechanics of features such as those observed on Mars and Mercury by Mariner and Viking missions, as well as aiding in the interpretation of stratigraphic variations found in core samples. Such a magnetometer could measure the remanent magnetic properties as well as the AMS.

References

(1) Collinson, D. W., B. D. Stone, and L. Molyneux, J. Sci. Instrum. 40, 310-312 (1963).
(2) Ellwood, B. B., J. Geophys. Res. 80, 4805-4808 (1975).
(3) _____, and M. R. Fisk, Earth Planet. Sci. Letters 35, 116-122 (1977).
(4) _____, and M. T. Ledbetter, Earth Planet. Sci. Letters 35, 189-198 (1977).
(5) _____, and N. D. Watkins, J. Geophys. Res. 81, 4152-4156 (1976).
(6) _____, and N. D. Watkins, in F. Aumento, W. G. Melson et al., Initial Reports of The Deep Sea Drilling Project, Wash., D. C., 37, 511-514 (1977).
(7) Hamilton, N., and A. I. Rees, in S. K. Runcorn (ed.), Paleogeophysics, Acad. Press, N. Y., 445-464 (1970).
(8) Hrouda, F., and F. Janak, Sediment. Geol. 6, 187-199 (1971).
(9) King, R. F., and A. I. Rees, J. Geophys. Res. 67, 1565-1572 (1962).

Mars: Near Infrared Spectral Reflectance and Compositional Implication, T.B. McCord and R.N. Clark, Univ. of Hawaii, Honolulu, HI 96822, R.L. Huguenin, Univ. of Mass., Amherst, MA 01003.

Several distinct absorption features, some recognized for the first time, are evident in a newly obtained reflectance spectrum ($\lambda\lambda$ = 0.62 - 2.6 μm, $\frac{\lambda}{\Delta\lambda}$ = 83) of the integral disc of Mars. The new observations were made on April 21 - 23, 1976 at the 2.24 meter telescope on Mauna Kea, Hawaii, using a newly developed infrared circular variable filter spectrometer.

The reflectance spectrum of Mars (Figure 1, bottom) contains features due to both martian atmospheric and surface constituents. Since we are concerned primarily with surface mineralogy, we attempted to remove the strong contribution by atmospheric CO_2. We divided the Mars spectrum by the laboratory spectrum of 100 m-atm CO_2 gas at 0.01 atm and 250°K as measured by Kieffer (1968). The resultant Mars spectrum, with CO_2 artificially removed, is shown as the upper curve in Figure 1. The CO_2 removal is, of course, approximate and neglects variations in surface topography, path length, non-linear line growth, temperature, and suspended dust.

There are several apparent absorption features that remain in the Mars spectrum after the gaseous CO_2 contribution is removed (Figure 1, top). There is a strong drop in reflectance at the shortest wavelengths and an asymmetric (composite) absorption between 0.75 and 1.15 μm. These features were interpreted previously (Adams and McCord, 1969; Huguenin et al., 1977). The drop in reflectance shortward of 0.75 μm was attributed primarily to absorption by an Fe^{3+} electronic transition band near 0.62 μm. Also contributing in part are absorptions from limbs of Fe^{3+} bands near 0.5 μm.

The feature between 0.75 and 1.1 μm in the full disc spectrum is dominated by absorption by bright area dust attributable to the $^6A_{1g}(^6S) \rightarrow {}^4T_{1g}(^4G)Fe^{3+}$ transition in Fe_2O_3-FeOOH at 0.87 μm. Other contributions to this feature could be due to absoprtion by $Fe^{2+}[^2T_{2g}(^2D) \rightarrow {}^2Fg(^2D)]$ in dark areas. Small differences between 1973 reflectance spectra (Huguenin et al., 1977) and the present spectrum could be due to different contributing silicate Fe^2 bands between 0.9 and 1.1 μm or, alternatively, to a higher average hydration state of the surface dust on the visible disc in 1976 than in the bright areas observed in 1973.

The 1.22 μm band was not reported previously, although it can be seen in earlier Mars spectra (Kuiper, 1964; McCord and Westphal, 1971). This 1.22 μm band is seen weakly in spectra of Kolinites 9 and 218B by Hunt and Salisbury (1970) and in a warm ice spectrum by Kieffer (1968). Thus, the 1.22 μm band is probably due to H_2O ice or mineral hydrate and the strength of the feature may be due to "intensity-borrowing" from mineral hydrate and water bands [1.15 μm (mineral + 1.16 μm (mineral) + 1.20 μm (water) + 1.23 μm (water)]. The 1.58 μm feature is asymmetric, with a long-wavelength limb extending beyond 1.75 μm. The feature is very similar to the 1.5 μm feature in the spectrum of laboratory ice but is shifted to longer wavelengths. The shift is possibly due to incomplete removal of the CO_2 or different phases of

water and a mineral hydrate.

The 1.95 μm feature is difficult to interpret due to large error bars due to thermal fluctuations of the circular variable filter, and possible incomplete removal of the CO_2 bands. This band position does indicate, however, that it may be due to mixtures of H_2O and mineral hydrate.

Assignment of the Mars features to ice + dessicated mineral hydrate is consistent with current models of martian surface composition. H_2O ice has been identified as a principal constituent of the polar caps, and it occurs at numerous other locations on the planet as ground ice, frost, haze, and clouds (Farmer et al., 1976, 1977; Kieffer et al., 1976, 1977). The occurrence of hydrated minerals on the surface was deduced by Houck et al. (1973) and Pimentel et al. (1974) from 2-4 μm spectra. Using Mariner 9 IRIS spectra, Hunt et al. (1973) deduced that the hydrated clay mineral montmorillonite was the principal constituent of the 1971 dust clouds, while Aronson and Emslie (1975) and Toon et al. (1977) included hydrated clays as possible constituents of the dust. Evidence for highly dessicated mineral hydrate in the soil was provided by the Viking molecular analysis experiments (Biemann et al., 1976, 1977), which showed that no detectable H_2O evolved from samples heated to 200°C, while ∿0.2% H_2O was driven off when the samples were heated to 350°C and 500°C. These observations support the proposal by Huguenin (1974, 1976) that a large fraction of the martian surface is composed of mineral hydrate dust produced by photochemical weathering of basalt, and that these weathering products undergo subsequent photodessication by exposure to UV sunlight (Huguenin et al., 1977; Andersen and Huguenin, 1977).

REFERENCES

1) Adams, J.B., and McCord, T.B., 1969, J. Geophys. Res. 74, 4851-4856.
2) Aronson, J.R., and Emslie, A.G., 1975, J. Geophys. Res. 80, 4925-4931.
3) Biemann, K., Oro, J., Toulmin, P. III, Orgel, L.E., Nier, A.O., Anderson, D.M., Simmonds, P.G., Flory, D., Diay, A.V., Rushneck, D.R., and Billev, J.A., 1976, Science 194, 72-76.
4) Biemann, K., Oro, J., Toulmin, P. III, Orgel, L.E., Nier, A.O., Anderson, D.M., Simmonds, P.G., Flory, D., Diay, A.V., Rus-neck, D.R., Billve, J.E., and Lafleur, A.L., 1977, J. Geophys. Res. 82, 4641-4658.
5) Farmer, C.B., Davies, D.W., and LaPorte, D.D., 1976, Science 194, 1339-1341.
6) Farmer, C.B., Davies, D.W., Holland, A.L., LaPorte, D.D., and Doms, P.E., 1977, J. Geophys. Res. 82, 4225-4248.
7) Houck, J., Pollack, J.B., Sagan, C., Shaack, D., and Decker, J., 1973, Icarus 18, 470-480.
8) Huguenin, R.L., 1974, J. Geophys. Res. 79, 3895-3905.
9) Huguenin, R.L., 1976, Icarus 28, 203-212.
10) Huguenin, R.L., Adams, J.B., and McCord, T.B., 1977, Lunar Science VIII, 478-480.

11) Huguenin, R.L., Prinn, R.G., and Maderazzo, M., 1977, Icarus 32, 270-298.
12) Hunt, G.R., Logan, L.M., and Salisbury, J.W., 1973, Icarus 18, 459-469.
13) Kieffer, H.H., 1968, Doctoral Dissertation, Cal. Institute of Technology.
14) Kieffer, H.H., Chase, S.C., Jr., Martin, T.Z., Miner, E.D., and Palluconi, F.D., 1976, Science 194, 1341-1343.
15) Kieffer, H.H., Martin, T.Z., Peterfruend, A.R., Jokosky, B.M., Miner, E.D., and Palluconi, F.D., 1977, J. Geophys. Res. 82, 4249-4291.
16) Kuiper, G.P., 1964, Comm. Lunar and Planetary Lab. 31, 79-112.
17) McCord, T.B., and Westphal, J.A., 1971, Astrophys. J. 168, 141-153.
18) Pimentel, G.C., Forney, P.B., and Herr, K.C., 1974, J. Geophys. Res. 79, 1623-1629.
19) Toon, O.B., Pollack, J.B., and Sagan, C., 1977, Icarus 30, 663-696.

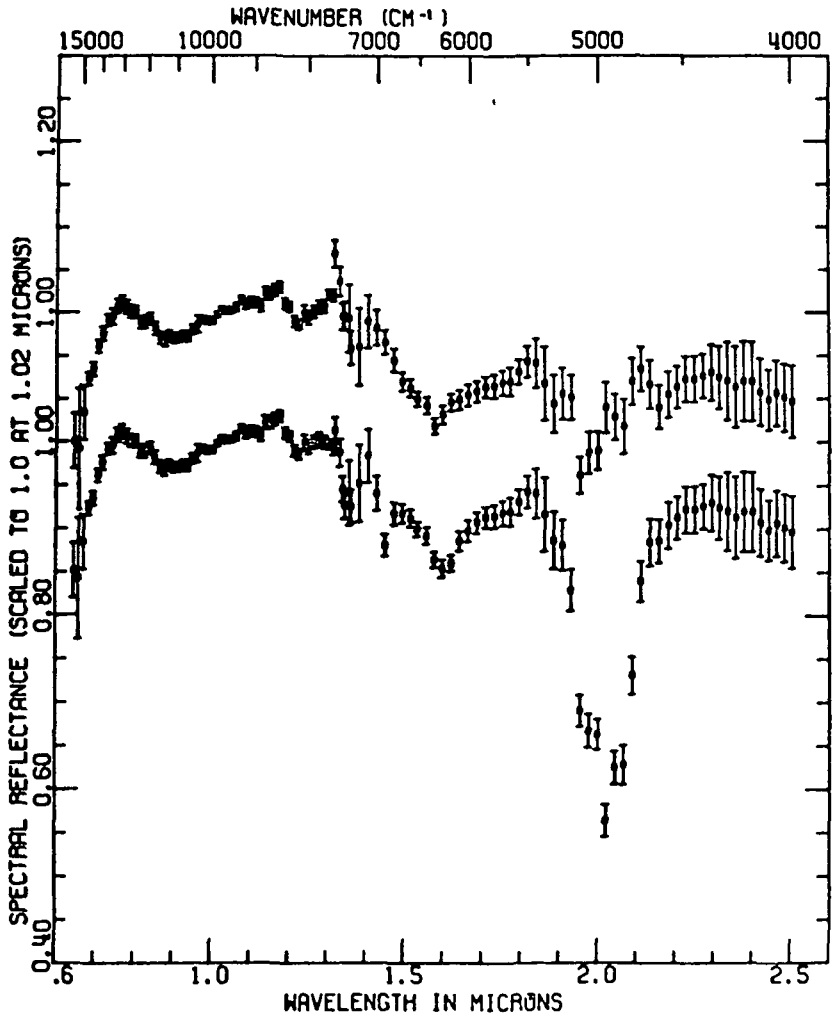

Figure 1

Characterization of Mars Surface Units, T.B. McCord and R.B. Singer, University of Hawaii, Honolulu, HI 96822 and MIT, Cambridge, MA 02139.

Recently, Soderblom et al. (1) prepared the first Mars global multispectral map using Viking II orbiter imaging data. Surface unit boundaries and extents can now be defined. We attempt to characterize these units using information on martian surface mineralogy obtained with groundbased telescopes and reflectance spectroscopy (2). We combined these two data sets also to check for agreement and to suggest the future direction of observing programs.

Viking images were taken in three bands covering a limited spectral range in the visible: 0.45±.03 μm, 0.53±.05 μm, 0.59±.05 μm. In the false color multispectral map, blue has been assigned to the ratio .45/.53 μm, red has been assigned to the ratio .59/.53 μm, and green represents the albedo at .59 μm. Figure 1 is a black and white reproduction of our combination of the Soderblom et al. multispectral map and a 1975 USGS Shaded Relief Map, showing as well the location of the groundbased observations.

Normalized telescopic reflectance spectra are shown in Figure 2. Table 1 gives .45/.53 μm and .59/.53 μm ratio values from the reflectance spectra for comparison to the multispectral map. Spectra are listed in order of decreasing slope (red color) given by the ratio .59/.45 μm.

The bright area spectra show great similarity to each other while the dark area spectra show greater regional variation, especially in the 1 μm Fe^{2+} absorption region, indicating a variety of compositions (3). Bright areas are redder in color.

The multispectral map and the reflectance spectra generally agree. The bright areas, with greater spectrum slope, appear on the map as yellow-green with varying small amounts of blue. The dark areas, with lower spectrum slope, show generally as dark blue, with varying small amounts of orange. Orange regions on the map imply a relatively low albedo and steep positively-sloped spectrum. These regions, the largest of which are centered near (0°, 32°S) and (250°, 30°S), are a high priority for future observations.

The multispectral maps cover only a narrow region of the spectrum (Figure 2) where complex charge-transfer absorption features appear in the reflectance spectra. These intense blue-uv absorptions cause slope changes in the spectrum and are due to electronic transitions characteristic of ferric oxides (3).

The existence of a variety of mineralogically distinct basaltic bedrock units has also been pointed out, based primarily on the variety of Fe^{2+} absorptions near 1 μm in the dark area spectra (3). Even for the dark areas the charge-transfer absorption features dominate in the spectral region covered by the multispectral map and the color characteristics shown in the map are probably strongly influenced by the weathering products of the basement rock. Our ability to characterize the units defined in the dark area is hindered by the limited telescopic data available for homogeneous units and the limited spectral coverage of the multispectral map.

Future studies may derive more information from these data but it

is clear that more information is needed. Telescopic reflectance spectra of more homogeneous areas can be obtained now that the multispectral map exists. Laboratory and theoretical studies can be directed at this problem. Future Mars spacecraft missions should carry multispectral mapping experiments covering a broader spectral region, particularly including the mineralogically important 1 μm region. The first opportunity may be the JOP spacecraft swingby of Mars in 1982.

ACKNOWLEDGEMENTS

We thank Dr. Larry Soderblom for providing the multispectral map prior to publication and for his help in understanding and interpreting the map.

REFERENCES

1) Science News, 1977, 112, 326-328
Soderblom, L.A., 1978, in preparation
2) McCord, T.B., and Westphal, J.A. 1971, Astrophys. J. 168, 141-153
McCord, T.B., et al., 1977, Icarus 31, 25-39
3) Adams, J.B., and McCord, T.B., 1969, J. Geophys. Res., 74, 20, 4851-4856
Huguenin, R.L., et al., 1977, Lunar Science VIII, 478-480
McCord, T.B., et al., 1977 Icarus 31, 25-39

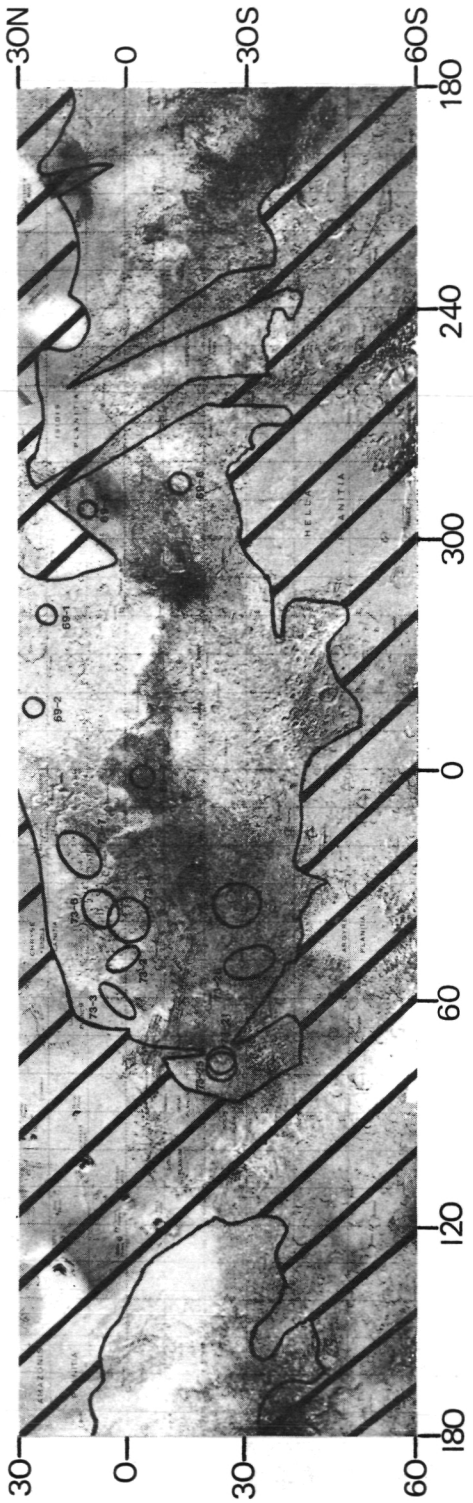

Fig. 1 - Viking II multispectral map modified from Soderblom et al. (1). Regions of questionable validity have been masked by diagonal stripes. Numbered ellipses show spots where reflectance spectra have been obtained in the reliable portions of the map. Because the original map is a false color presentation, light and dark areas in this black and white reproduction represent color units in the Martian surface, but not necessarily albedo units.

MARS SURFACE UNITS

McCord, T.B. et al.

TABLE 1

Spot	Bright or Dark	0.59/0.45μm	0.45/0.53μm	0.59/0.53μm	Color on Map
73-2	B	3.34	0.52	1.74	patches
73-3	B	3.28	0.53	1.72	of
73-4	B	3.22	0.53	1.70	yellow-green
73-7	B	3.11	0.54	1.67	and
73-6	B	3.10	0.55	1.69	blue
69-1	B	2.97	0.56	1.67	well mixed
69-2	B	2.91	0.57	1.63	blue-yellow-green
73-20	D	2.58	0.62	1.60	blue w/orange patches
73-21	D	2.53	0.60	1.51	mainly blue
73-25	D	2.41	0.61	1.47	mainly blue
73-26	D	2.38	0.63	1.50	blue w/orange patches
69-6	D	2.37	0.61	1.44	yellow-orange w/slight blue
69-7	D	2.31	0.64	1.47	blue
69-5	D	1.95	0.69	1.35	blue

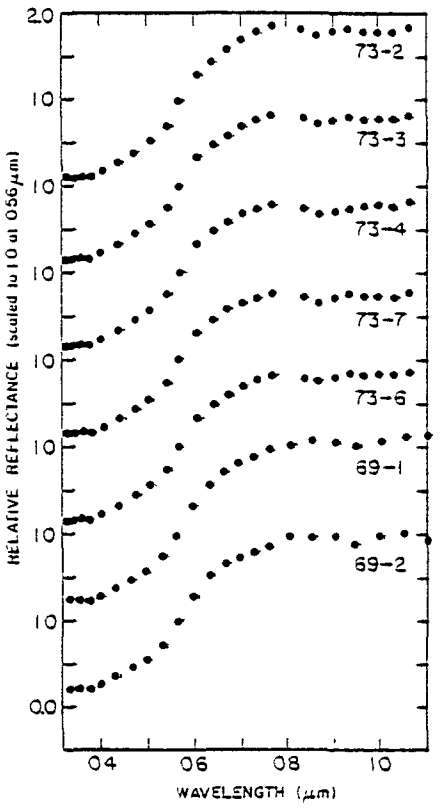

Fig. 2a Mars bright area spectra

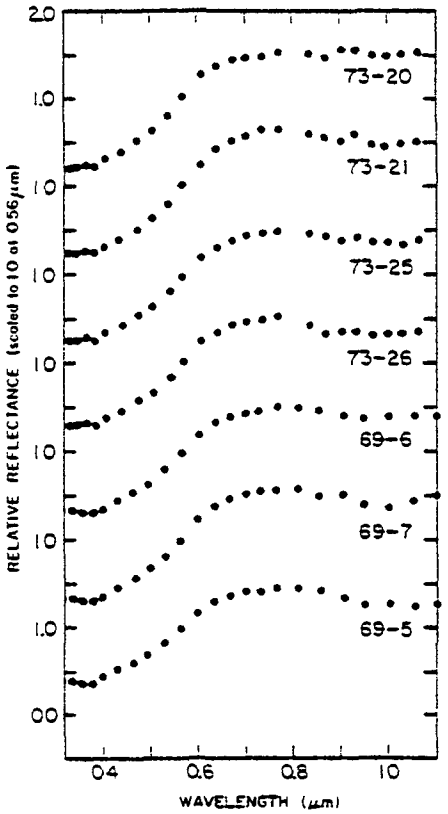

Fig. 2b Mars dark area spectra

Martian Surface Composition: Comparison of Remote Spectral Studies and In Situ X-Ray Fluorescence Analysis, O.B. Toon*+, B.N. Khare*, J.B. Pollack+ and Carl Sagan*

X-ray fluorescence spectrometry (XRFS) by Viking has determined many of the major elements composing the surface materials on Mars, but does not directly specify the mineralogy of the Martian surface, although it may allow mineralogy to be inferred. Many minerals have characteristic spectral features in the ir (0.7 to 50 μm). Analyses of Mariner 9 ir transmission spectra of dust in the great 1971 Martian dust storm, and analysis of Viking near-ir broadband spectrophotometry of atmospheric dust are informative about mineralogy. Here we compare mineralogy inferred from the Viking XRFS with mineralogy indicated by spectral data. The comparison is done both by taking laboratory spectra of Viking analog minerals and by calculating spectra of Viking analog mineral mixtures. We find XRFS and ir data are consistent with clays as the dominant SiO_2-containing minerals on Mars. The X-ray fluorescence data might also be consistent with the dominance of certain mafic SiO_2 igneous minerals, but the spectral data are probably inconsistent with such materials. Sulfates, inferred by XRFS, are consistent with the spectral data; indeed inferences following Mariner 9 that high-SiO_2 minerals were important on Mars may have been biased by the presence of sulfates. Calcium carbonate, in the quantities indirectly suggested by XRFS (≈ 7%), are inconsistent with the spectral data, but smaller quantities of $CaCO_3$ are consistent, as are large quantities of other carbonates. Spectral data do not exclude maghemite, but they do require opaque minerals with a near ir band structure closely resembling that of magnetite. The quantities of magnetite thus required equal those observed as soil components by the Viking magnetic experiments. Hence the spectral and magnetic data suggest magnetite as the dominant magnetic iron compound, rather than maghemite as inferred by X-ray fluorescence studies.

*Laboratory for Planetary Studies, Cornell University

+Theoretical Division, Ames Research Center

The Composition of Mars, Kenneth A. Goettel, Dept. of Earth and Planetary Sciences, and McDonnell Center for the Space Sciences, Washington University, St. Louis, MO 63130

The observed mean density of Mars places a fundamental constraint on models for the bulk composition of Mars. The mean density, $\sim$ 3.94 g/cm^3, is determined accurately from mass and radii data (Anderson, 1974). Correction of this mean (i.e., compressed) density to zero pressure (i.e., STP conditions) is slightly model-dependent; however, the zero pressure density of Mars, $\sim$ 3.7 g/cm^3, is distinctly lower than the zero pressure density of the Earth, $\sim$ 4.0 g/cm^3. Thus, Mars is composed of material of intrinsically lower density than the Earth. The most plausible causes for this lower Martian density are: (a) lower total iron content, (b) greater oxidation of iron to iron oxides in silicates, or (c) a combination of these causes.

The moment of inertia factor, C/MR^2, constrains the density distribution within Mars, and thus places additional constraints on the internal composition. Reasenberg (1977) revised previous estimates of the moment of inertia factor by considering the non-hydrostatic contribution of the Tharsis gravity anomaly to J_2. His estimate of the moment of inertia factor, 0.3654 $\pm$ 0.001 is significantly lower than previous estimates which were near 0.376. Thus, an increase of density with depth which is substantially greater than previous estimates is now indicated. The core of Mars must be larger and/or denser than previous estimates. The density contrast between the mantle and core must be increased. To be compatible with the moment of inertia value, without violating the constaint of Mars' mean density, the density of the mantle must be lowered.

Unfortunately, even for simple models in which core and mantle compositions are not a function of radius, knowledge of Mars' mean density and moment of inertia factor is sufficient to specify only two of the three basic model parameters: mantle density, core density, and core radius. Additional constraints on the composition of Mars must be obtained from models for the formation of planets or from data on the magnetic field, photogeologic evidence for planetary evolution, mass and composition of the atmosphere, composition of surface soils, etc. However, interpretation of such data in terms of the bulk composition of Mars is strongly model-dependent.

Over the past several decades, many previous authors have produced models for the bulk composition of Mars. Pre-Mariner models were severely limited by major uncertainties in the optically determined radius of Mars and the resulting major uncertainties in the mean density. In the early 1970's, several quantitative models were based on accurate mean density data and on values near 0.376 for the moment of inertia factor. Ringwood and Clark (1971) and Anderson (1972) considered Mars models based on meteorites. Binder and Davis (1973) and Johnston et al. (1974) considered models based on analogies to terrestrial core and mantle materials. In all of these models, Mars had a smaller core and a much higher density mantle than the Earth.

Recently, two models consistent with the downward revision of the moment of inertia factor have been proposed. Johnston and Toksöz (1977) found that

models fitting the mean density and moment of inertia data had mantle densities ranging from 3.47 to 3.58 g/cm^3, with corresponding core radii ranging from 1500 km ($Fe_{85}S_{15}$) to 2050 km (FeS). McGetchin and Smyth (1978) considered the petrologic implications of model Martian mantles with a density of 3.55 g/cm^3.

Goettel (1977) calculated a bulk composition for Mars, based on the chemical equilibrium model for condensation in the solar nebula. The requisite assumptions, and resulting limitations of this approach have been discussed in detail by Goettel and Barshay (1978). Goettel's previous Mars model, based on the solar proportions of major rock forming elements, had no metallic Fe, an Fe-Ni-S core constituting about 12% of Mars' mass, and a very FeO-rich mantle (31 wt. %). The downward revision of the moment of inertia factor necessitates revision of this model.

A model Mars composition (Table 1) which is consistent with the mean density and moment of inertia data, and has the identical (i.e., solar) relative proportions of Fe, Mg, Si, S, and other major non-volatile constituents as the previous model is possible if significant amounts of metallic Fe are allowed in Mars. In this model, the mantle constitutes 77% of the mass of Mars, and the core 23%. Without changing the bulk composition, these model mantle and core compositions could be modified by incorporating modest amounts of FeS in the mantle, or modest amounts of FeO in the core.

Table 1
Composition of Mars (wt. %)

mantle[1]:	SiO_2	30.96	Al_2O_3	3.14
	MgO	43.49	CaO	2.93
	FeO	18.15	Na_2O	1.34
core:	Fe	73.98	S	19.23
	Ni	6.78		

[1] includes crust

In Goettel's 1977 model, all Fe was assumed to be oxidized to FeS and FeO. In the present work, models with various ratios of FeO to metallic Fe were considered; the model (Table 1) in which 50% of the FeO was reduced to Fe was found to be in good agreement with the mean density and moment of inertia data.

Decreasing the FeO content and increasing the metallic Fe content of Mars is possible in several ways: (a) increasing the postulated formation temperature of Mars, such that metallic Fe is only partially oxidized to FeO, (b) mixing a large fraction of higher temperature condensates (i.e., low FeO) with oxidized material condensed at Mars' formation temperature, or (c) allowing a limited amount of disequilibrium during condensation in the solar nebula. The compositional effects of these three mechanisms are essentially indistinguishable; all three many have occurred to some extent.

Increasing the postulated formation temperature of Mars would produce the required increase in metallic Fe, although this mechanism is somewhat ad hoc. However, as noted by Goettel and Barshay (1978) the hypothesis that planets accreted material formed at only one temperature is clearly an oversimplification. Mars may well have accreted material with a range of degree

of oxidation of Fe. Hartmann's (1976) calculations suggest that a significant fraction of the late-accreted mass of Mars probably came from the regions of Earth and even Venus. This mixing may account for some of the metallic Fe in Mars, but probably not for all of it; the fact that the terrestrial planets retain distinct differences in composition suggests that mixing was not too extensive. The third mechansism, limited disequilibrium during condensation in the nebula, may be the most viable. Kinetic limitations will probably preclude complete attainment of equilibrium, especially at lower temperatures. Thus, kinetic limitation of the oxidation of Fe to FeO may account for much of the postulated metallic Fe in Mars.

The present model suggests that a viable Mars model can be generated without requiring differences in Fe:Mg:Si ratios between Earth, Venus and Mars. Other models for the composition of Mars, with core and mantle densities varying within the limits outlined by Johnston and Toksöz (1977), are also compatible with the present mean density and moment of inertia data. However, compositions significantly different from the present model require either substantial revisions in solar system abundances of major rock forming elements, or substantial metal/silicate fractionations during the planet-forming process. The present approach of attempting to understand the composition of Mars in the context of a model for condensation in the solar nebula is perhaps somewhat more fundamental and less ad hoc than models based on arbitrary proportions of various types of meteorites or on addition of arbitrary amounts of FeO to Earth mantle materials.

References

Anderson, D.L., 1972, Internal Constitution of Mars, J. Geophys. Res. 77 789-795.

Anderson, J.D., 1974, Geodetic and Dynamical Properties of Planets, Eos, Trans. Am. Geophys. Un. 55 515-523.

Binder, A.B. and Davis, D.R., 1973, Internal Structure of Mars, Phys. Earth Planet. Inter. 7 477-485.

Goettel, K.A., 1977, Composition of the Terrestrial Planets, in Reports of Planetary Geology Program, 1976-1977, NASA TM X-3511 7-10.

Goettel, K.A. and Barshay, S.S., 1978, The Chemical Equilibrium Model for Condensation in the Solar Nebula: Assumptions, Implications and Limitations, in S.F. Dermott (ed.) The Origin of the Solar System, in press.

Hartmann, W.K., 1976, Planet Formation: Compositional Mixing and Lunar Compositional Anomalies, Icarus 27, 553-559.

Johnston, D.H. McGetchin, T.R. and Toksöz, M.N., 1974, The Thermal State and Internal Structure of Mars, J. Geophys. Res. 79 3959-3971.

Johnston, D.H. and Toksöz, M.N., 1977, Internal Structure and Properties of Mars, Icarus 32 73-84.

McGetchin, T. and Smyth, J.R., 1978, The Mantle of Mars: Some Possible Geological Implications of its High Density, Icarus, in press.

Reasenberg, R.D., 1977, The Moment of Inertia and Isostasy of Mars, J. Geophys. Res. 82 369-375.

Ringwood, A.E. and Clark, S.P., 1971, Internal Constitution of Mars, Nature 234 89-92.

Mars: Petrologic Units in the Margaritifer Sinus and Coprates Quadrangle,
R. L. Huguenin, Planetary Chemistry Lab, U. Mass Dept. of Physics and Astronomy, Amherst, MA 01003 and Brown U. Dept. of Geological Sciences, Providence, RI 02912, J. W. Head, Brown U. Dept. of Geological Sciences, Providence, RI 02912, and T. R. McGetchin, Lunar and Planetary Institute, Houston, TX 77058.

Earth-based reflectance spectra (0.3-1.1 μm) of 200-400 km diameter areas (1) and spectral vidicon images (200 km resolution (2) reveal that a large fraction of the martian surface is covered with a mantle of high albedo dust. This dust is remarkably uniform in composition everywhere, and it is apparently composed of weathering products of basaltic to ultrabasic material (3). The dust does not mantle the entire surface of Mars, however. Reflectance spectra show that the martian dark areas are windows through the dust mantle to crustal rocks, and that surface mineralogy in these areas varies from region to region (1,2).

Most of the dark areas for which both spectra and vidicon coverage have been obtained are located in the Margaritifer Sinus (0 to -30° latitude, 0 to 45° longitude) and Coprates (0 to -30° latitude, 45 to 90° longitude) Quadrangles of Mars. Spectra for some areas were measured with a photometer (1) while spectra for other areas were derived from vidicon ratio images (2). The vidicon ratio images were formed by dividing each of the images measured at 20 wavelengths (0.35-1.03 μm) by the 0.566 μm image, thus providing 20-point spectra for each spatial resolution element. In addition to providing spectra, the ratio images also revealed the spatial extents of numerous geochemical units on the surface, particularly in the dark areas of the Margaritifer Sinus and Coprates quadrangles (2).

Ten distinct units are visible in the two quadrangles and they are presented in Fig. 1. Interpretations of unit mineralogy are primarily those of Huguenin et al. (3), and are still being refined by laboratory modeling.

Units 1 and 2. Unit 1 corresponds closely in spatial extent with the dark area Margaritifer S. Unit 2 corresponds to a higher albedo region, Pyrrhae R, that lies between Margaritifer S to the north and a dark region, Erythraeum M, to the southwest. The spectrum of Unit 2 shows absorption bands at 0.87-0.90 μm, 0.93-0.97 μm, and beyond 1 μm. The band at 0.87-0.90 μm is stronger than the other two and it is probably due to a mixture of enstatite and ferric oxide (contaminant dust) (3). The band at 0.93-0.97 is of roughly equal strength to the band longward of 1 μm, and it can be attributed to a pigeonite or augite (3). The band beyond 1 μm is probably due to olivine or basaltic glass (3). It could also be due to an Fe^{3+}-bearing diopside, but the absence of the diopside $Fe^{2+} \rightarrow Fe^{3+}$ charge transfer band at 0.75-0.8 μm argues for olivine (or glass) as the dominant phase (4). Opaques cannot exceed ∿10 wt%, since the bands are relatively unmasked (3). Since olivine and glass produce weaker bands than pyroxenes, we conclude that olivine (or glass) is the dominant phase in Unit 2, followed by the orthopyroxene (enstatite), and then clinopyroxene (pigeonite-augite). Unit 2 has weaker absorption features between 0.93 and 1.03 μm and slightly stronger features between 0.45 and 0.65 μm than Unit 1. The stronger absorption at 0.45-0.65 μm indicates contamination by ferric oxide in Unit 2, but probably not enough to account for the weakness

(by band masking) of the absorptions beyond 0.93 μm (2). With the similarity of band strengths at 0.87-0.90 μm and the differences beyond 0.93 μm, it appears that Unit 1 contains more olivine (or glass), slightly more clinopyroxene, and less orthopyroxene than Unit 2. In summary, for Unit 1 ol (or glass) > cpx >opx while for Unit 2 ol (or glass) >opx >cpx (pigeonite-augite).

Unit 3 corresponds to a region in the eastern part of Erythraeum M. Unit 3 has weaker absorptions longward of 0.93 μm, while shortward of 0.93 μm there are no differences from the Unit 1 spectrum. This suggests that Unit 3 contains less olivine (or glass), less clinopyroxene, and more orthopyroxene than Unit 1. Comparison with spectra of Units 1 and 2 suggests that ol (or glass) >cpx $\gtrsim$ opx.

Unit 4 occurs in the central part of Erythraeum M. The spectrum shows absorption characteristics of titaniferous augite or diopside with bands at 0.96-1.00 μm and a strong 0.6-0.77 μm $Fe^{2+} \rightarrow Ti^{4+}$ charge transfer band. Considering the strength of the 0.6-0.77 μm absorption, the TiO_2 content of the pyroxene is probably at least 1% (4). There is also strong absorption beyond 1 μm, indicating that olivine and/or glass is again the dominant phase. Absorption at 0.87-0.93 μm is conspicuously absent, suggesting a low orthopyroxene-pigeonite content. In summary ol (or glass) > cpx (Ti-augite or Ti-diopside; TiO_2 > 1 wt%) >> opx.

Unit 5. Unit 5 is in the western third of Erythraeum M, and its spectrum shows strong absorption between 0.87 and 1.1 μm that is apparently due to bands at 0.87-0.93 μm (orthopyroxene or pigeonite); 0.93-0.97 μm (augite); and beyond 1 μm (olivine or glass) (3). All bands have approximately equal strengths, while the pyroxenes characteristically absorb more strongly than olivine and glass; thus olivine and/or glass are again most abundant, and the two pyroxenes are probably present in roughly equal amounts. In summary, ol (or glass) >cpx (augite) $\approx$ opx.

Unit 6. Spectra in the dark areas Solis Lacus and Meridiani Sinus are quite similar; thus both regions have been assigned to Unit 6. Both spectra show strong absorptions at 1 μm due probably to diopside-salite. Olivine or basaltic glass may be present, but relatively less than in Unit 5 (1,3). There are no apparent bands corresponding to orthopyroxene, pigeonite, or augite; thus cpx (diopside-salite) > ol (or glass) >> opx and/or pigeonite.

Units 7, 8, and 9. Each of these units is a distinct albedo and spectral unit, but masking of silicate absorption bands by contaminant dust precludes identification of any of the phases present.

Unit 10. This is part of the global dust mantle, which Maderazzo and Huguenin (6) proposed is composed of 72-78% silicate clay, 13% $MgSO_4$, 6-10% FeOOH, 3-5% lag magnetite, and minor amounts of carbonates, salts, and oxides.

It has been proposed independently by McGetchin and Smyth (5) and Maderazzo and Huguenin (5) that Martian primary magmas should be picritic olivine basalts (normative: 37-38% ol, 20-32% plag, 20-29% cpx, 4.4-7% mt, 2.5-5% neph, 0.6-2.4% or, trace il, and no opx). The unit mineralogies derived here are consistent with differentiation of the proposed primary melts by any of several possible mechanisms, including ol or ol + mt separation and/or partial melting. The ol + 2px mixes suggest a possible differentiation sequence of ol → opx → cpx, with progressive Si-enhancement, and such differen-

tiation of ultramafics can lead to late stage melts enriched in cpx and TiO_2 (S. Haggarty, personal comm.), which is consistent with the observations here.

The petrologic units correlate closely with albedo units in these two quadrangles. Units 7, 8, and 10 are covered with dust and have medium high to high albedos, while Units 1-6 have exposed Fe^{2+}-silicates and are medium dark to dark. Unit 9 (Aurorae S) is normally dark, but it was obscured by a dust cloud during our observations (2). Within Units 1-6 there is a further correlation with albedo: the darkest units (Units 1, 4, and 6) have the lowest opx/cpx + ol (or glass) ratios, while the lightest of the dark units (Unit 2) has the highest opx/cpx + ol (or glass) ratio. The medium dark units (Units 3 and 5) have ratios that are intermediate to these extremes. This suggests that differentiation may possibly involve ol separation and not ol + mt separation. If true, this suggests that the magmas may have formed in low fo_2 environments. A low fo_2 combined with the possibility of a high magmatic sulfur content (high observed soil sulphate content) further suggests the possibility that the opaque phase could be a sulfide rather than magnetite.

Correlations with geologic units are not straightforward. The boundaries of Unit 5 correlate with those of a densely cratered plains unit (pc), while Unit 6 comprises both densely cratered plains (Solis Lacus) and cratered uplands (Meridiani S.). Units 1-4 are within cratered uplands; with Units 1 and 4 containing major channels and chaotic terrain and Units 2 and 3 not. It may or may not be significant that Units 1 and 4 (with channels) have low opx/cpx + ol (or glass) ratios (late stage differentiates), while Units 2 and 3 (no channels) have high opx/cpx + ol (or glass) ratios.

Acknowledgment. Contribution No. 6 of the Planetary Chemistry Laboratory.

References. (1)McCord, T. et al. (1977) Icarus 31, 25. (2)McCord, T. et al. (1977) Icarus 31, 293. (3)Huguenin, R. et al. (1977) Lunar Science VIII, 478. (4)Adams, J. B. (1975) Infrared and Raman Spectroscopy of Lunar and Terrestrial Minerals (C. Karr, Jr., Ed.), Academic Press, p. 91. (5)Smyth, J. et al. (1978) Lunar and Planetary Science IX, 1077. (6)Mutch, T. et al. (1976) Geology of Mars, Princeton Press, 354 p.

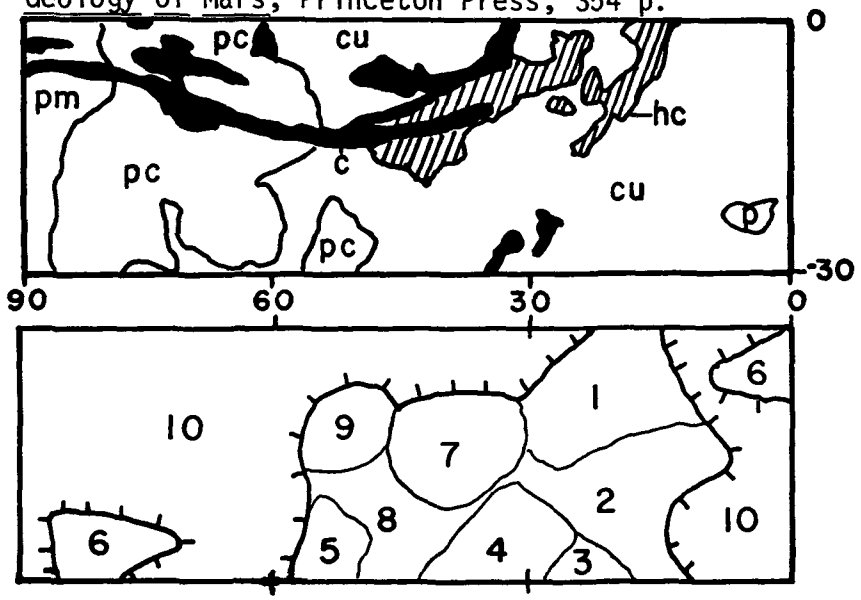

Fig. 1. Geologic map (6) and units derived from spectra and vidicon images. p=plains (m=moderately cratered, d=densely); cu=cratered terrain; c=channels; hc=hummocky/chaotic. Hatchures point toward regions obscured by dust.

CHAPTER 5 - RADAR STUDIES OF PLANETARY SURFACES

Comparative Imaging Radar Planetology, Charles Elachi and R. S. Saunders, Jet Propulsion Laboratory, Pasadena, CA 91103

Airborne imaging radar data are commonly used by geologists as part of a large set of remote sensing data for geologic mapping and exploration in many areas around the world, especially in the equatorial regions. The radar sensor provides high resolution images independent of cloud cover or sun illumination. Because of its geometric configuration, the radar is particularly useful for planimetric and topographic mapping provided such aspects as viewing and illumination angles are judiciously chosen.

Most of the radar image data presently available were taken with X-band or K-band sensors at very large incidence angles (i.e., small depression angles), used mostly for planimetric mapping and owned by private exploration companies or foreign governments. On the other hand, planned spaceborne imaging radar missions (Seasat-A, SIR-A, VOIR) will use L-band frequency and will have small to medium look-angles (i.e., 20^0 to 60^0). These choices are imposed by the tight restrictions on spaceborne systems or by the global planetary environment (Venus atmosphere has high microwave absorption at frequencies equal to or higher than X-band).

A four-year program for comparative imaging radar planetology work was started in FY-78 as a joint JPL/USGS effort. The objective of this program is two-fold: 1) To develop the data base necessary for planning and later for analysis of data obtained with planetary orbiting imaging radars, in particular VOIR. 2) To develop a better understanding of the imaging radar signature of a variety of geologic surfaces which would allow a good interpretation of future spaceborne radar data. This effort will capitalize on ongoing work for the use of Earth orbiting spaceborne radars in conjunction with Landsat for Earth resources (including geologic) evaluation and monitoring.

The data base is being acquired using the JPL airborne dual polarisation L-band imaging radar. This system has been operated since 1970, and is one of the two systems available (the other is at ERIM) in that frequency band. Radar imaging of interesting regions will also be obtained with the Seasat-A (1978) and SIR-A (1979) spaceborne radars. This set of data will be compiled with Landsat data, ground imagery and geologic information of the same regions. A data center for this purpose has been established for this purpose under this program and the SIR-A program.

In conjunction with this effort, work is ongoing at JPL and USGS for the understanding of the radar signature of different geologic surfaces. Schaber, et al. (1976) and Daily, et al. (1978) have conducted extensive work in Death Valley, and they have shown that the radar data can differentiate all the geologic units in that region. This year, our emphasis is on the study of the signature of volcanic lava fields. We mapped and studied the data from the Snake River Plain, Mt. Lassen region, Kelso lava field, Amboy lava field, the SP flow and Askija caldera flow. Our conclusion is that the radar imagery gives planimetric information and discerns surface configurations equally as well as photography. We also found that, at L-band frequency,

lava flows of different ages can be discriminated unambiguously, in most cases, using direct polarization and even better if we use cross-polarization. If dual polarization data is used, the type of lava flow can be determined with some degree of confidence. At X-band the discrimination is marginal in most cases. The addition of K-band data allows the determination of the blockiness of the lava field. These effects can be explained using wave scattering theories, and have been checked in detail by field investigations.

Another area under study this year is the capability of radar to see major stratigraphic layers in the Grand Canyon. Our preliminary results show that a spaceborne radar has a better capability than photography to show stratigraphy in major canyons if it is reflected in abrupt, large changes of the slope as is the case in the Grand Canyon. This can also be explained by the geometric configuration of the radar sensor.

References

Daily, M.; C. Elachi; T. Farr; W. Stromberg; S. Willaims and G. Schaber (1978), "Application of Multispectral Radar and Landsat Imagery to Geologic Mapping in Death Valley," JPL Technical Report, in print.

Schaber, G.; G.L. Berlin and W. E. Brown (1976), "Variations in Surface Roughness Within Death Valley, California: Geologic Evaluation of 25 cm Wavelength Radar Images," Geol. Soc. of Am. Bulletin, 87, 29-41.

Spectral or Time Series Analysis of Surface Roughness: Correlation with Radar Backscatter Cross-Section Measurements, Gerald G. Schaber, U. S. Geological Survey, 2255 N. Gemini Drive, Flagstaff, AZ 86001

Synthetic aperture radar (SAR) image data of the type expected from the proposed Venus Orbital Imaging Radar (VOIR) mission (1983 period) will contain basically two categories of geologic information: (1) simple morphologic and structural data enhanced by surface slope and radar shadowing and (2) surface roughness information.

The first category of data is obtained primarily by standard radar-photogeologic, visual inspection and is very analogous to conventional photogeologic techniques. The second, surface roughness, is much more difficult to interpret as it can be disguised by higher than average surface dielectric constant and slopes. Surface roughness values on relatively flat natural terrain surfaces can be ascertained from radar backscatter measurements (qualitative or quantitative) only if backscatter models are empirically derived for a variety of terrain types.

Early in the studies related to instrumenting an imaging radar system to orbit the planet Venus and map the surface through the dense cloud cover, the question arose as to how the radiometric radar image returns could be interpreted with a minimum of equivocation; that is, if an area is relatively radar-bright (lighter grey tone on the image), is it because the surface has a greater roughness (height variance), a more favorable slope, and/or a higher dielectric constant? As part of this NASA funded study, radar images of Death Valley, CA at X- and L-bands (3 cm and 25 cm wavelength) were obtained as a basis for detailed study and roughness calibration. It is anticipated that a L-band radar will be used for the VOIR mission. We have reported on earlier results (1, 2, 3, 4) that show there is a correlation between the size of the surface scatterers and the relative image brightness on L-band images. Therein, the Rayleigh scattering model that predicts a break in the scattering cross-section at scatter radii between $\lambda/5$ and $\lambda/6$ was observed at L-band (λ = 25 cm wavelength).

During the funding period 1977-1978 we have concentrated on verifying earlier radar image observations using high resolution surface relief statistics (including mean relief, variance in relief and variance in the spectral frequency of relief) and quantitative measurements of actual radar cross-section values obtained from aircraft platforms.

Spectral or time series analysis enables examination of the frequency content of topographic or surface roughness profiles. In natural terrain surfaces, profiles are generally statistically random functions that can only be represented by the continuous variance spectrum. Elevation amplitudes that contribute to variability of a random isotropic surface above its mean height value are thus associated with a continuum of wavelengths. Separating a random profile into wavelength bands yields the spectral density of the relief variance which is given as the square of the amplitude per unit bandwidth of the contributing wavelength bands (5). This value has been called the power spectral density (PSD) or more correctly the "variance spectral density."

Figure 1 shows example surface profiles obtained for rough, intermediate and smooth geologic units within Death Valley and figure 2 illustrates the least squares best fit values of the variance spectral

density functions. The "variance" of power spectral density graphs are sloping lines representing continuous functions of topographic (spatial) wavelength. Since the greatest relief within a surface profile (natural terrain) is generally associated with the longer wavelengths, the spectral density decreases rapidly with decreasing terrain wavelengths. The slopes of the PSD curve describe a relation between the relief content of the long and short wave features. An overall slope of -3 is thought to indicate a "uniformity" of topographic slope for all relief features in the sample area, regardless of their size. A slope less steep than -3 indicates that small topographic features (high frequency) are rougher than large (low frequency) features. This is a common aspect of the surface profiles of the Death Valley salt pan surfaces. Likewise, a spectrum slope steeper than -3 suggests more rough coarse grain features and less smooth, fine-grained relief forms. The PSD curve slopes for the Death Valley salt pan geologic surfaces range from -1.6 to -3.00 and average -2.34, indicating a surplus of high frequency small scale relief (see figure 1).

Figure 3 shows preliminary radar cross section values (σ°) as measured with the Johnson Space Center airborne 1.6 Ghz radar scatterometer. Note the reduced backscatter power at all incidence angles for surfaces of descending topographic relief (Figure 1) and decreasing PSD value (Figure 2). Backscatter models are currently being derived from these calibration data with the ultimate goal of using them to calculate the surface roughness (including PSD value) of relatively flat Venus surfaces following acquisition of data from the proposed Venus Orbiting Imaging Radar mission. A discussion of backscatter models derived from the surface variance spectra and scatterometer measurements is in preparation for publication during 1978.

References

1. Schaber, G. G. and Brown, W. E., 1972, Long-wavelength Radar Images of Northern Arizona - A Geologic Evaluation: Geological Survey Research - U.S. Geol. Survey Prof. Paper 800-B, p. B175-B181.
2. Schaber, G. G., Berlin, G. L. and Brown, W. E., 1976, Variations in Surface Roughness within Death Valley, California: Geologic Evaluation of 25-cm Wavelength Radar Images: Bull. of Geol. Soc. America, 87, p. 29-41.
3. Schaber, G. G., 1976, Measurement of Small-Scale Terrain Roughness: A Bonus from Airborne or Spacecraft-Borne Side-Looking Imaging Radar Systems, in Reports of Accomplishments of Planetology Programs 1975-1976: NASA TMX-3364, p. 80-89.
4. Schaber, G. G., 1977, Side-Looking Airborne Radar/Photogrammetric Analysis of Small Scale Surface Roughness, in Reports of Planetary Geology Program 1976-1977: NASA TMX-3511, p. 267-269.
5. Pike, R. J. and Rozema, W. J., 1975, Spectral Analysis of Landforms: Annals of the Assoc. of American Geographers, vol. 65, no. 4, p. 499-516.

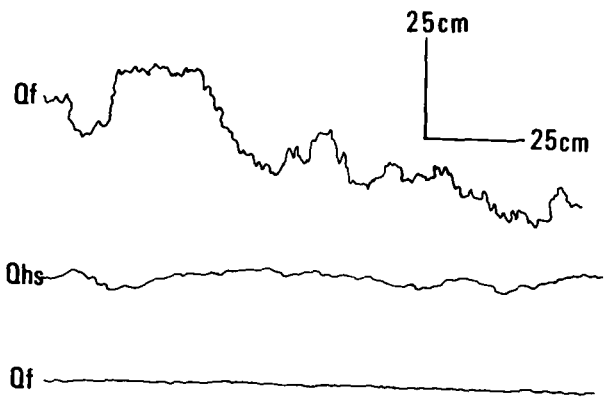

Figure 1

Surface profiles of Death Valley Salt Pan geologic units Qh(Quaternary massive halite); Qhs(halite, smooth); and Qf(flood plain)

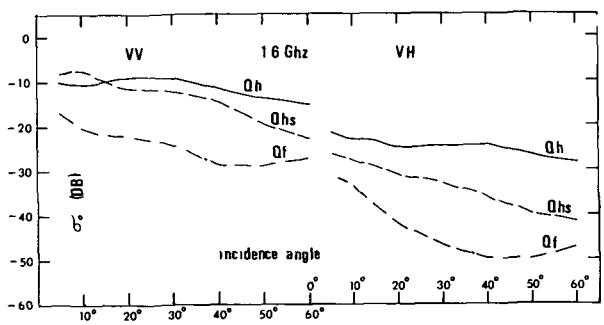

Figure 3
Radar backscatter cross section(σ_o) versus incidence angle for Death Valley geologic units Qh, Qhs and Qf. Both HH and VH polarization data given. Data obtained by personnel of the Experiments Systems Div.(Microwave Section), Johnson Space Center-Houston, Texas

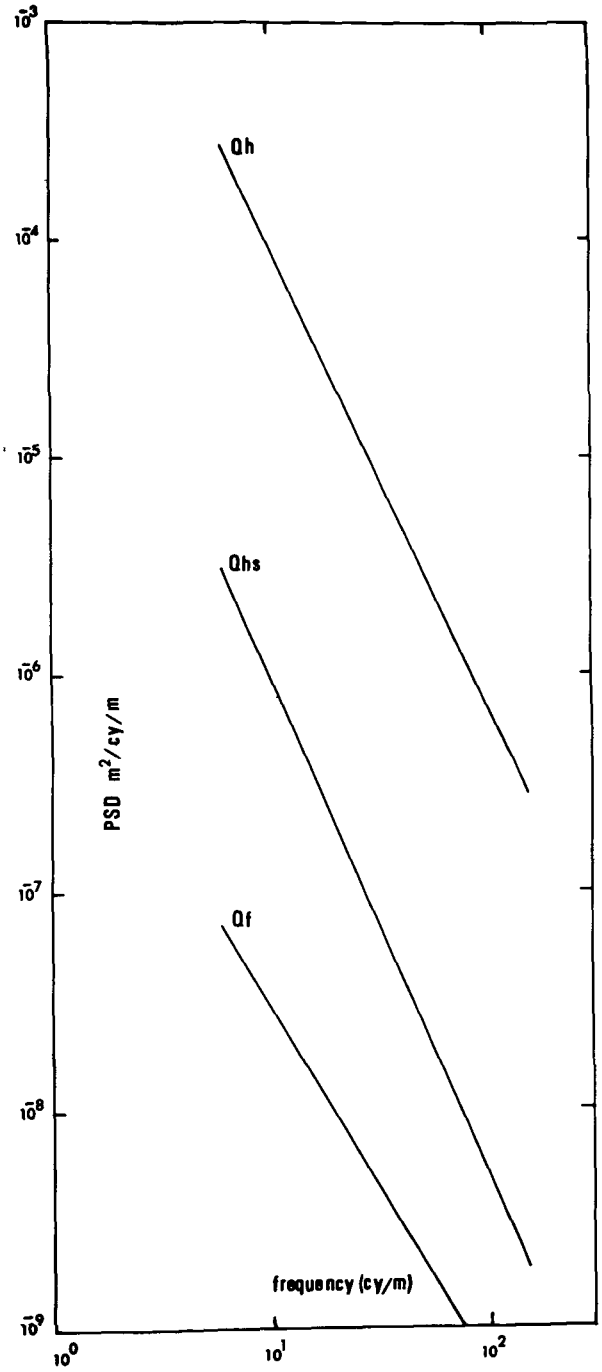

Figure 2
Power spectral density(PSD) function plot for geologic units described in figure 1.

Radar Backscatter from Martian-type Geologic Surfaces, M. Kobrick, Jet Propulsion Laboratory, Pasadena, Ca. 91103

The attempted use of Earth-based radar to aid in defining the small scale properties of the Martian surface for Viking landing site selection (Tyler, et al, 1976, Simpson, et al, 1978) has underscored the difficulty that exists in the interpretation of radar backscatter from real geologic surfaces. In particular, the scattering law that was applied to the Mars data is derived in terms of the RMS slope of a smoothly undulating surface, and may not be the optimal one to describe the response of a more complicated surface with unknown subsurface characteristics. It is especially interesting to determine whether radar can be useful in differentiating between a relatively smooth, flat surface, and a similar one strewn with scatterers such as the Viking landing sites.

To this end the Radar Science Group at JPL has undertaken a series of experiments to measure the radar signature of sites on the Earth similar to the Viking landing sites and to compare the data with that from other geologically different areas. The experiments will consist of overflying each region with the JPL L- and X-band radars on board the NASA Convair 990. These are imaging radars and the entire radar return is recorded on photographic film for interpretation later. In addition to measuring the falloff of the quasi-specular component with angle (as was done with the Earth-based data), the effects of polarization and multiple frequencies will be studied to evaluate just which parameters are most useful in determining the properties of an unknown surface.

Actual data flights are due to begin in April, 1978, concurrent with a program of ground truth collection. It is anticipated that some preliminary results will be available by June of that year.

Tyler, G.L., Campbell, D.B., Downs, G.S., Green, R.R., and Moore, H.J., Radar Characteristics of Viking I Landing Sites, Science, 193, 812, 1976.

Simpson, R.A., Tyler, G.L. and Campbell, D.B., Aricebo Radar Observations of Martian Surface Characteristics Near the Equator, Icarus, 33, 102, 1978.

Radar Topography of The Arsia Mons - Claritas Fossae Region of Mars,
R. S. Saunders, L. E. Roth, C. Elachi, Jet Propulsion Laboratory, Pasadena, Calif. 91103, G. Schubert, Dept. of Earth and Space Sciences, University of California, Los Angeles, Calif. 90024.

Radar observations of Mars are taken at each opposition at the Jet Propulsion Laboratory's Goldstone Deep Space Network Tracking Station (see for example, Downs et al., 1975). The data include determination of the time delay between the transmitted and the return signal at about .16 degree intervals. These data provide elevation profiles with uncertainties of less than 100 meters.

These topographic profiles were used to determine the slopes in a region south of Arsia Mons and including a part of the Claritas Fossae. The local topography of this region is important for studies of slope control of lava flow morphology (Hulme, 1974). The findings strongly suggest that published maps of martian topography should not be used for studies that require a quantitative measure of heights or slopes.

The general outline of the behavior of lava flows on the south flank of Arsia Mons can be understood. We observe that flow directions on the Arsia flanks, (see Carr et al., 1977) are everywhere consistent with the radar topography, that is the apparent flow direction is in the direction of maximum slope. This observation supports the validity of the radar topography. In general, the Claritas Fossae form a sharp ridge of broken terrane with a distinct radar signature (Simpson et al., 1977). This ridge provides a natural barrier for the flows.

In addition to the excellent correspondence of flow direction and radar topography, the flow morphology may also be related to topography. Carr et al. (1977) mapped zones within the flows on the flanks of Arsia Mons. The inner zone extends out for about 400 km from the summit and consists of 3 km and narrower flows often with central channels. The second zone, about the same extent outward, has 4-7 km wide flows. Beyond this the flows are broad and irregular. Carr et al. (1977) correctly surmised that slopes in the inner zone are steeper than indicated on the topographic map (USGS Map I-984). In fact, we find these slopes to have gradients of 0.01 to 0.03 compared to 0.008 measured on the published map.

As a further confirmation of the photogeologic techniques applied by Carr et al. (1977) we see a distinct break in slope between Carr's inner zone and the second zone. Radar topography gradients in the second zone range from 0.002 to 0.006 while no break at all is seen on the published topographic maps.

The steeper slopes well out on the flanks of Arsia Mons suggest to us that the shield itself extends much further south than previously thought. The radar topography indicates that the change in slope probably bounds the Arsia shield, extending both the total relief and the diameter of Arsia to dimensions that are more similar to those of Olympus Mons. This has important implications for the volcanic volumes involved and the interpretation of the gravity anomalies being obtained by Viking Orbiter.

Crater density data published by Carr et al. (1977) show that average crater density increases outward from the summit of Arsia. We would interpret this to indicate that the average age of the surface in the central regions is younger, just as on many large shields of the Earth (M. C. Malin, personal communication). If most of the eruptions came from the summit region, those frequent flows of low volume and low eruption rate would form the upper region and the apparent age of the region would be young. The less frequent flows of high volume and high extrusion rate extend far out onto the flanks. Although perhaps this mode is more significant in terms of total volume, the average surface age would be greater.

References:

1) Carr, M. H., Greeley, R., Blasius, K. R., Guest, J. E., and Murray, J. B., Some Martian Volcanic Features as Viewed from the Viking Orbiters: J. Geophys. Res., 82, 3985-4015.

2) Downs, G. S., Reichley, P. E., Green, R. R., 1975, Radar Measurements of Martian Topography and Surface Properties: The 1971 and 1973 Oppositions: Icarus, 26, 273-312.

3) Hulme, G., 1974, The Interpretation of Lava Flow Morphology: Geophys. J. R. Astr. Soc., 39, 361-383.

4) Simpson, R. A., Howard, H. T., and Tyler, G. L., 1977, Radar Geology: Reports of Planetary Geology Program 1976-1977, NASA TMX-3511, 272-274.

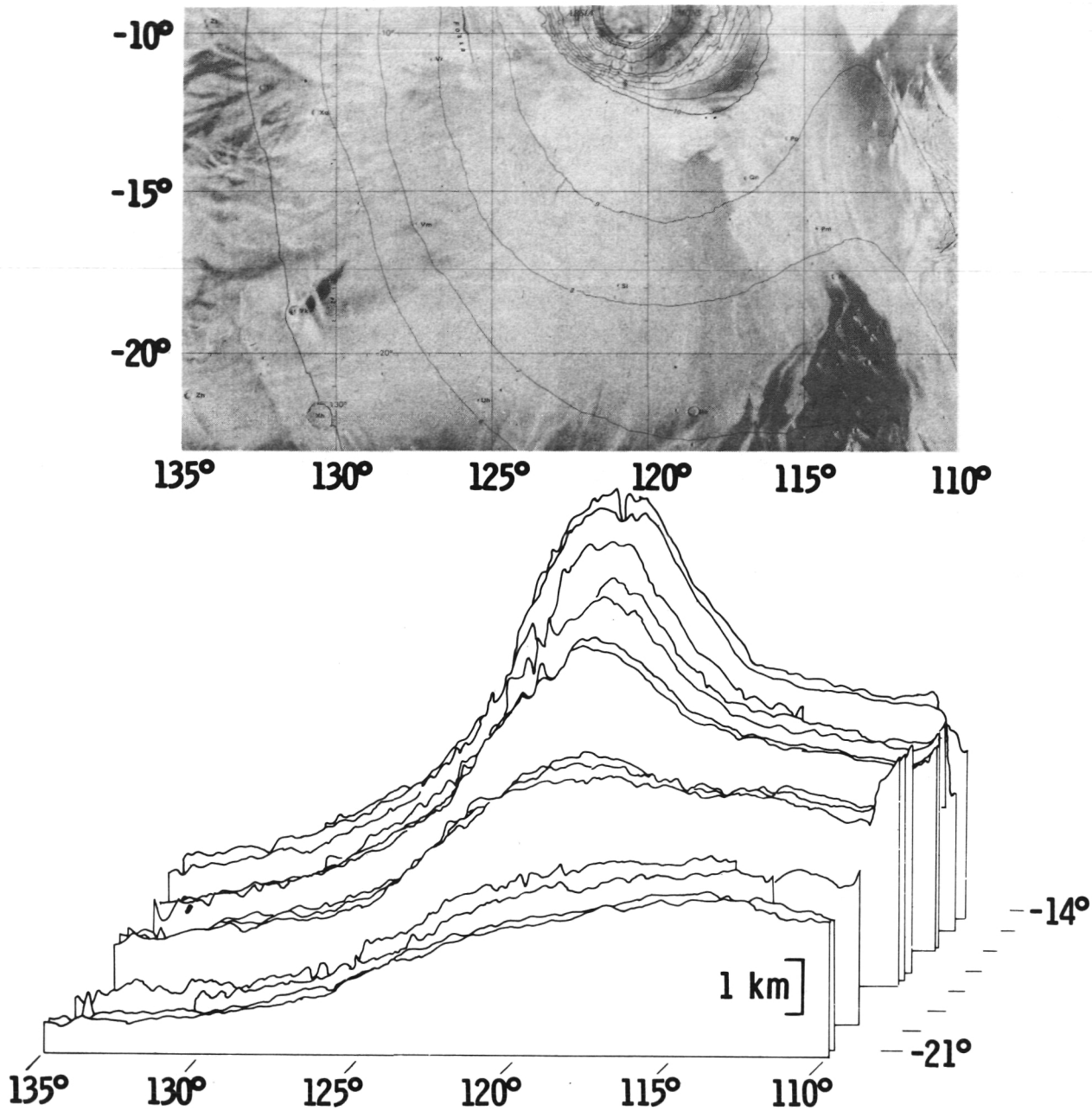

Figure 1: Radar Topography of region south of Arsia Mons.

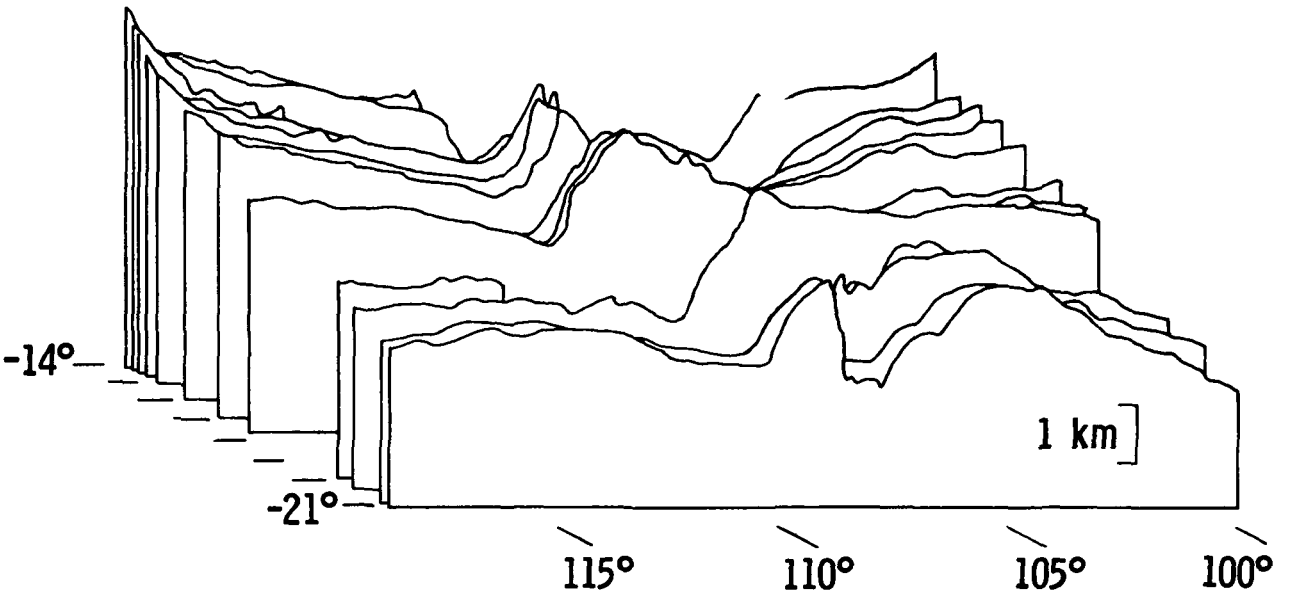

Figure 2: Radar Topography of region adjacent and to the east of that in Figure 1. Includes Claritas Fossae ridge near the center.

Radar Profiles and the Depth/Diameter Ratios of Large Martian Craters, L.E. Roth, C. Elachi, R.S. Saunders, Jet Propulsion Laboratory, Pasadena, CA 91103; G. Schubert, Department of Earth and Space Sciences, University of California, Los Angeles, CA 90024

The data obtained during the 1971 and 1973 radar ranging of Mars by the Jet Propulsion Laboratory's Goldstone radar System[1,2] have been used to produce altitude profiles of the planet's surface within a strip extending from from -14° to - 22° to -22o in latitude, and from 0° to 360° in longitude. Each individual profile runs along an arc of constant latitude and spans up to 100° in longitude.

Detailed morphometric evaluation of the radar altitude profiles, currently under way, has yielded information on the general shape of the largest Martian craters located along the path of the subradar point, and on the depth/diameter ratio of over 100 craters encompassing diameters from 18 to 475 km. The depth/diameter data set compiled in this study revises and augments the data reported previously[3,4] and complements the data obtained through the use of other techniques.[3,5,6,7]

The following observations have been made:

(I) The Martian craters are systematically shallower than fresh lunar and Mercurian craters, in agreement with previous investigations.

(II) Radar profiles of large craters (Figure 1, Wislicenus (-18.0°; 348.0°)) show subdued crater rims (rarely higher than 300-400 meters), shallow interior walls; and, along the exterior walls, very little structure of the magnitude detectable by the Earth-based radar. These observations confirm the visual impressions gained from the Mariner 9 and Viking Orbiter photography.

(III) Floors of the large flat-bottomed craters display a topographic relief larger than the uncertainties caused by a possible error in the range measurement. In addition, the floors often appear to be tilted with respect to the horizontal plane. The maximum observed tilt was 0.6° (un-named, (-13.7°, 317.0)).

(IV) Basin boundaries were determined in those cases where the photographic evidence was inconclusive or insufficient, e.g., (Ladon (-17.0°, 28.0°)).

(V) The accuracy of the radar crater-depth determination is restricted by a number of factors, most notably by the size of the radar footprint on the Martian surface. Higher-accuracy, higher confidence depth measurements were grouped together. The smoothed plot of the depths vs. diameters for this group of craters shows only a weak dependence of depth

on diameter, in contrast to the conclusion reached from analysis of the Mariner 9 UVS data.[6] The smoothed Mariner 4 photoclinometric data set[7] also shows little dependence of depth on diameter for large craters.

(VI) The averaged depths of the largest craters are essentially independent of diameter and may even show a decrease with increasing diameter. This latter dependence may be real since the depths of the largest basins were determined with the highest accuracy.

1. Downs, G.S., Goldstein, R.M. Green, R.R., Morris, G.A., Reichley, P.E. (1973). Icarus 18, 8-21.

2. Downs, G.S., Reichley, P.E., Green, R.R. (1975). Icarus 26, 273-312.

3. Malin, M.C., Dzurisin, D.D. (1977). J. Geophys. Res. 82, 376-388.

4. Schubert, G., Lingenfelter, R.E., Terrile, R.J. (1977). Icarus 32, 131-146.

5. Burt, J., Veverka, J., Cook, K. (1976). Icarus 29, 83-90.

6. Cintala, M.J., Head, J.W., Mutch, T.A. (1976). Proc. Lunar Sci. Conf. 7th,

7. Pike, R.J. (1971). Icarus 15, 384-395.

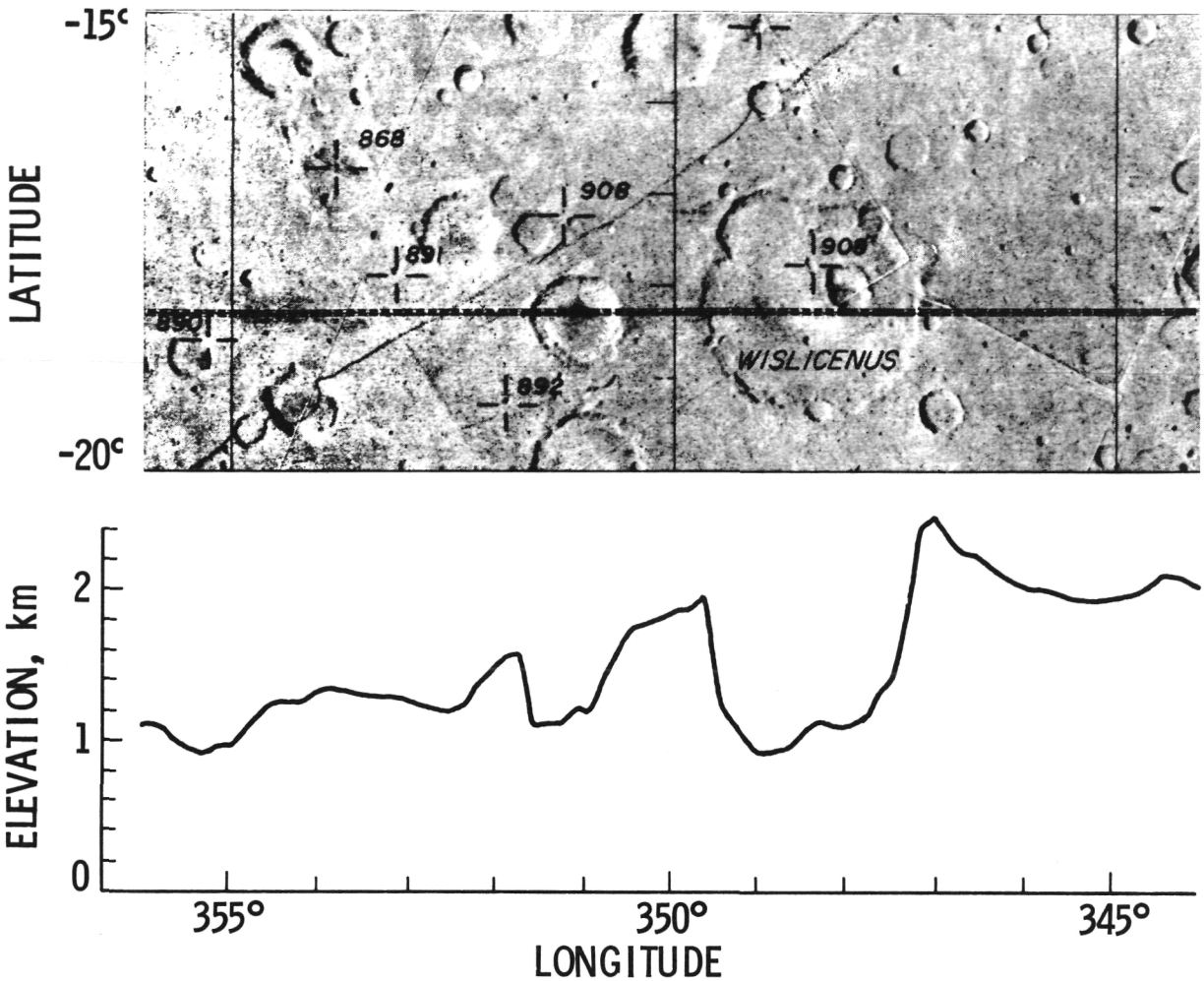

Figure 1: Radar altitude profile of the crater Wislicenus (-18.0°, 348.0°). The dashed line represents the path of the subradar point. (USGS Map Mc-20, Semicontrolled photomosaic).

Mars Bistatic Radar, R. A. Simpson, G. L. Tyler, and H. T. Howard, Center for Radar Astronomy, Stanford University, Stanford, CA 94305.

The Viking Bistatic Radar Experiment is being conducted to determine the radio wave scattering properties of the Martian surface. Considerable work on this problem has already been carried out using earth-based radar systems. The bistatic geometry, however, permits us to study parts of Mars (e.g., the polar regions) which are inaccessible to earth-based systems. It also allows us to vary the scattering geometry in ways which are impossible when transmitter and receiver are co-located.

As of this writing, 25 of the 29 bistatic observations planned have been executed. Except for two upon which we are awaiting word, all but two have produced good quantities of usable data. These include tracks near several proposed Viking landing sites (as well as Chryse), Tharsis, and Hellas. There is an abundance of data from tracks above 60°N, including one which goes within kilometers of the North Pole. We hope to obtain funding for reduction of these runs now that the data have been acquired. In the meantime we have examined a half hour segment from one of the two Hellas runs to see what can be done with the data using a relatively unsophisticated analysis.

The segment chosen runs approximately linearly from 47°S, 296°W to 40°S, 300°W. It was selected because the incidence angle of the wave on the surface decreased from 60° to 57°. In previous studies of Mars and the moon, reflectivities corresponding to dielectric constants of about 3 have been inferred. If this were the case for Hellas, we would expect equal received power in our right and left circularly polarized channels at the Brewster angle, 60°. In fact, the data show considerable variation (aside from being noisy) and there are three separate locations where received power is equal in the two channels. A subjective straight line fit to the data points leads to an effective dielectric constant of $\varepsilon = 3.4$. Though there were several sources of possible error which we could not account for in this preliminary analysis, it would appear, at least, that the dielectric constant of the surface material in this part of Hellas (and therefore probably its density) is somewhat higher than has been inferred for the planet as a whole.

Estimates of surface roughness are less susceptible to measurement errors. The results show surprisingly little variation over this 500 km long track (in spite of the noise), suggesting that Hellas may be more uniform in its scattering than many of the near-equatorial regions studied with earth-based radar. Our analysis shows an rms surface roughness on the order of 3° near the northern end of the track; this would be about "average" for equatorial regions studied from earth. Our roughness estimates decrease to about 2° at the northern end of this half-hour sample. The slow drift, combined with our knowledge of the changing experimental geometry over this period, implies that the restricted areal illumination of the spacecraft antenna may be artificially limiting the roughness estimate. This source of error, and that of a noisy signal will cause our estimates to be low, so we conclude that (on horizontal scales of 10-100 meters) Hellas has at least a 3° rms surface roughness. This makes it "average" or above in comparison with equatorial regions.

In spot checks of North Polar data we have obtained prelminary dielectric constant estimates of 3 ± 1 and roughness estimates from less than 1° to 3° (or more). These were obtained at latitudes above 60°N and are believed to be in regions covered by at least seasonal frost, if not permanent ice.

Further analysis will be performed as time and resources allow. We hope to begin a fairly large scale data reduction program in October 1978.

Radar Backscatter From Sand Dunes, W. E. Brown, Jr. and R. S. Saunders, Jet Propulsion Laboratory, Pasadena, Calif. 91103.

Radar images of the Algodones dunes in Southern Califronia illustrate an interesting phenomenon in the backscatter characteristics of the dune surface. The backscatter intensity in the images goes from a maximum at vertical incidence (aircraft nadir) through a somewhat lower value and then at about 33^{o} incidence it reaches another maximum and then drops off sharply at higher incidence angles to very low values. We feel that the maximum at 33^{o} is backscatter from slip faces of dunes at the angle of repose. The reflectivity above 33^{o} incidence drops sharply because there are no natural surfaces in the dunes with facets having this orientation, that is, greater than the angle of repose for dry sand. Two perpendicular flight paths that illustrate the phenomenon are shown in the figures. The dunes rise 100 to 200 feet with slip face irregularly oriented. There is little small scale roughness.

This observation has implications for interpretation of radar images of planetary surfaces where eolian phenomenon may be encountered. A natural experiment for VOIR, for example, would be to search for backscatter dependence on angle of repose.

The work is done in conjunction with field observations that include plane table mapping of slip face orientations, stereo photography and measurement of ripple size and orientation, and laboratory determination of electrical properties of the sand.

JET PROPULSION LABORATORY

JET PROPULSION LABORATORY

Venus Tristatic Radar Status, Raymond Jurgens, Jet Propulsion Laboratory, California Institute of Technology, Pasadena, California 91103

In March and April of 1977, radar observations were made on 9 days of which 7 appear to be adequate to give high quality radar images. The effort in processing these data has been divided into three areas so far, there are: (1) preliminary processing; (2) algorithm research and simulation; and (3) mapping software. Each of these areas are described below.

Preliminary processing is composed of several areas in that different types of operations were done. Initially, a sampling of the raw radar types was processed by a modified 2-station program to ascertain the proper operation of all three radar sites. These tests primarily checked the phase stability of the three stations relative to each other. A computer program was written to check the radar sensitivity and measure the radar cross section variation during the day. This program was also used to develop the power calibration and data editing software used in the mapping programs that follow.

A second program was designed to do the three station data preprocessing and incorporates algorithms to automatically start up the processing with no external data except for the ephemerides of the day and the edit files. This program aligns the frequency and phase between the stations and provides either phased-corrected voltage spectra or power and complex cross spectra summed for a time-of-flight. The latter mode gives a data reduction of about 10 to 1. Program 2 has been used to process one data tape from each day of operation to be sure that the program operates properly with differing data configurations and to provide radar ranging data for another program.

The algorithm research can be divided into three general areas as follows: (1) procedures that attempt to solve the voltage equations directly; (2) sub-optimum procedures using the cross spectra; (3) optimum procedures based on maximum likelihood estimators. Attempts to solve the voltage equations directly have not been very successful unless the signal-to-noise ratio is very large, however, reflectivity maps can be made without loss if the spherical heights are used. The sub-optimum procedures of Type 2 generally yield good reflectivity maps but inadequate height measurements. Considerable effort was spent on these procedures primarily because they deal only with one spectrum at a time or a short span of data, for example, one time-of-flight. The optimum procedures require a global data approach, i.e., all data for any point being mapped must be available in memory. This creates several difficult problems, i.e., only a small number of points may be mapped at a time and many passes must be made through the data, the point being mapped moves through the delay-doppler grid and must be focused, the point being mapped does not have a fixed conjugate point so the northern and southern hemispheres cannot be solved simultaneously. In spite of these complications, simulations indicate that improved height

measurements can be made. The extent of the degradation caused by the motion of the conjugate point has not been considered in the simulation and is presently unknown. The effect of the varying fringe frequency during the day has not been simulated, however, this would seem to help not hinder.

The mapping programs which are under development convert the 3 station delay-doppler data into north-south separated delay-doppler grids that can be mapped by existing programs into planetary coordinates. The third processing program is designed for non-global procedures and gives adequate reflectivity maps. This program is essentially finished and could be used to do a production mapping run within a few weeks. The primary use of this program has been to develop and test routines for the fourth program which is being designed to do the global mapping procedure. This program is about 50% complete.

Presently, a few projects remain to be completed. These are:

1. Program 4 as described above.
2. Testing of the global height determination algorithm using simulated data.
3. A small interface program to convert the maps formed by programs 3 and 4 into data acceptable by the planetary coordinate conversion program.
4. Production mapping runs.
5. Programs to deal with data recorded on the high density recorder. These are most likely modifications of existing programs.

ON PREDICTING DENSITIES OF DOUBLET CRATERS, A. Woronow, Lunar & Planetary Lab, University of Arizona, Tucson, Az. 85721.

Doublet craters could be created by three classes of processes:

Class I: random doubling. Two impact events occur in close proximity to one another, but the events are unrelated.

Class II: constructional doubling. Two craters are created in close proximity to one another through a nonrandom process. Examples of such processes are secondary cratering, disruption of a single parent meteoroid, and the formation of volcanic craters.

Class III: destructional doubling. Local obliteration of craters can cause large variations in the crater density with the result that more doublets are observed than would have been expected if the crater density distribution were uniform. Examples of such processes are crater and ejecta blanket overlap, aeolian and fluvial erosion and deposition, and isostatic rebound.

In order to determine the contribution a particular class of processes makes to an observed population of doublets, the other two classes of processes must be accurately modeled. The nature of Class I processes allows them to be modeled analytically. To varying degrees, however, analytical treatment of Class II and Class III processes are difficult to construct. For these classes a Monte Carlo approach is easiest.

We have produced a low-order Monte Carlo model which includes Class I processes and crater overlap from Class III--no Class II processes were modeled. In attempting to apply this model to the data of Oberbeck and Aoyagi (1972), we found that the number of doublets produced was sensitive to the details of the assumed production function (crater size-frequency distribution). We could produce either significantly more, or significantly less, doublets than were observed depending only on the assumed production function. Unmodeled processes aggravate the problem. Until all pertinent processes can be reliably modeled, we can not expect to resolve the contributions made by one particular process. Therefore, we find no justification for the assertion made by Oberbeck and Aoyagi (1972) that a Class II process has significantly contributed to the martian doublet population, particularly so because their model included no Class III processes, a production function which assigned the same diameter to all craters, and contained an erroneous definition of their parameter Δ.

REFERENCE:

Oberbeck, V. R. and M. Aoyagi (1972) J. Geophys. Res. 77, 2419-2432.

Crater Production and Erosion on Mercury. W. P. O'Donnell, University of London Observatory, Mill Hill Park, London, NW7 2QS.

A crater-counting exercise was undertaken of the Intercrater Plains (and largely superposed Heavily Cratered Terrain (11), (2).) of Mercury. The incoming side of the planet was used since it provides a particularly homogenous outcrop of this unit. The count was carried out using the RT-5 resolution set and involving different degradation groups after the method of Guest and Gault (2), except that the number of groups was expanded experimentally from 3 to 12. The 12 classes are based approximately on the lunar crater degradation groups of Pohn and Offield (9). A small region of Hilly and Lineated Terrain covered by the RT-5 set was also crater-counted.

The total crater-count curves for both terrains are shown in Fig. 1. The surface is saturated for craters up to about 200km diam. and deficient in craters below about 70km where the curves leave the 10% saturation line (1), (5), (2). Oberbeck (7) has suggested that the deficiency is due to the larger impacting bodies having a different population to the smaller ones. Fig. 2. shows that the deficiency increases with age. The state of the craters composing the oldest curve is such that it is difficult to see how all (or many) of the small craters in this group have survived in recognisable form. Thus, it is clear that the extreme 'kink' in this curve is at least partly due to erosion. Lessening impact flux with time correspondingly decreases the erosional effect on the other curves. Primary population deficiences are therefore unnecessary to explain the shape of the total curve (Fig. 1.) and are inadequate alone to explain the changing shape of the group curves with time. The Hilly and Lineated Terrain total curve (Fig. 1.), has a more pronounced curve than that for the Intercrater Plains. This is consistent with the theory that it suffered heavier erosion during the Caloris impact due to its position at the antipode to this basin (10), (2), (3), (8). Thus, the 'oldest' curve for the Hilly and Lineated Terrain (Fig. 3.) contains a much larger proportion of the total number of craters thereon, than does the appropriate Intercrater Plains curve.

The 'oldest' Intercrater Plains curve in Fig. 2. has a more accentuated 'kink' than the preceeding curves and indeed cuts across two of them. This could indicate an erosional unconformity and is seen more clearly in between groups 3 and 2.5 in Fig. 4. Large time differences between these groups, as compared to other group transitions, corresponding only to degradational criteria are discounted since no other transitions display a similar 'jump'. The diagram which contains approximate Mercury-mapping crater age groupings (C1 - C5, J. E. Guest, personal communication) for future reference, is interpreted as follows. Overall: regularly increasing number of impacts going back in time until the unconformity (3 - 2.5) from which time small numbers of mainly larger craters are preserved. This is consistent with a tail-off in terminal accretional bombardment rather than a catastrophic episode (6).

Group 5: Slight decrease in small craters recorded due to the seismic (and other) disturbances accompanying the formation of the lobate scarps.
Group 4.5: Marked decrease in small craters corresponding roughly to time of Caloris and the Guest/Gault (2) deficiency.
Group 3.5: Deficiency in larger craters. Possibly due to a fluctuation in primary crater production or a chance dearth in the sample area.
Group 3 - 2.5: Marked unconformity in number of craters of all sizes recorded, due to; a) isostatic adjustments in an early, thin, plastic crust, affecting large craters especially; b) ejecta from Tolstoj sized basins (500 km); c) end of formation of most Intercrater Plains. Formation of this unit corresponds roughly to groups 2.5, 2 and 2>. The existence of craters containing Intercrater Plains is consistent with this (4), (3); d) some form of atmospheric weathering may be considered. The proposed widespread volcanism at this time is in accord with this suggestion.
Finally if c) and a) do not apply to the Moon then the erosional theory predicts the absence of a comparable unconformity in any similar study of the Moon.

1. Gault, D. E. Radio Sci. 5, (2), 273-291 (1970).
2. Guest, J. E. and Gault, D. E. Geophys. Res. Let. 3, (3), 121-123 (1976).
3. Guest, J. E. and O'Donnell, W. P. Vistas in Astron. 20, 273-300 (1977).
4. Malin, M. C. Geophys. Res. Let. 3, 581-584 (1976).
5. Murray, B. C. Science 185, (4146), 169-179 (1974).
6. Murray, B. C. et al 80, (17), 2508 (1975).
7. Oberbeck, V. R. NASA Tech. Memo. 3511, 39-41 (1976).
8. O'Donnell, W. P. in press. (1978).
9. Pohn, H. A. and Offield, T. W. Geol. Surv. Res., 153-162 (1970).
10. Schultz, P. M. and Gault, D. E. Moon 12, 159-177 (1975).
11. Trask, N. J. and Guest, J. E. J. Geophys. Res. 80, (17), 2461-2477 (1975).

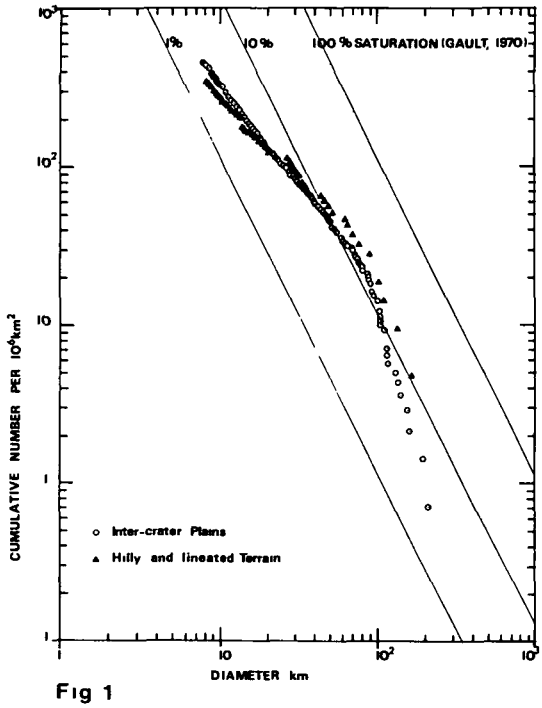

Fig 1

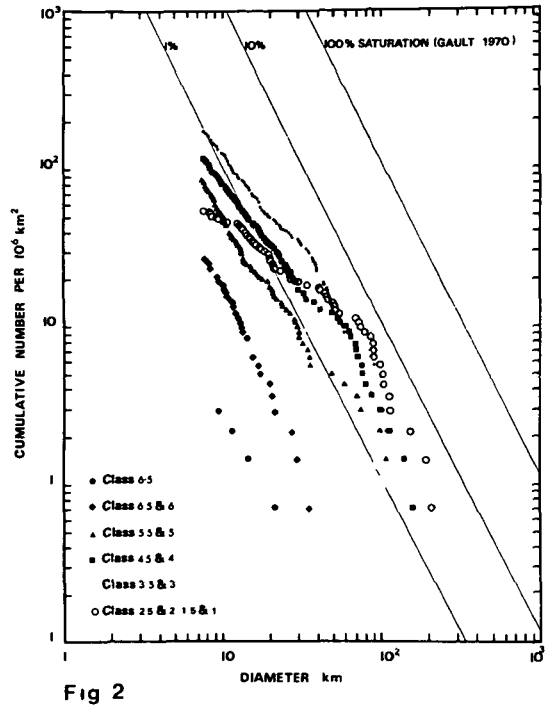

Fig 2

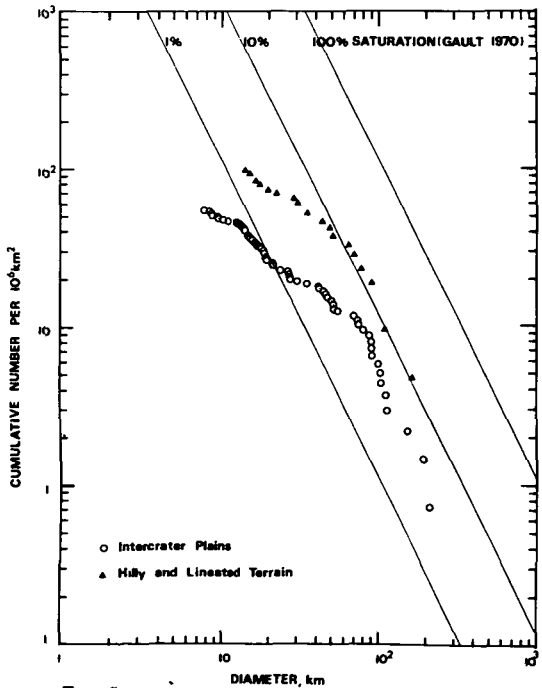

Fig.3.

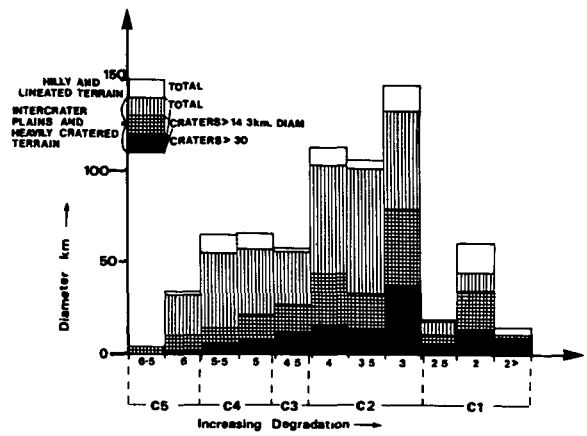

Fig 4.

Crater Shape-Size Profiles for Fresh Craters on the Moon and Mercury. Eugene I. Smith and Jill Ann Hartnell, Division of Science, Univ. Wisconsin-Parkside, Kenosha, WI 53141

Past interplanetary comparisons of fresh crater morphology have lead to conflicting results (1,2,3,4,5,6). This situation is mainly due to the lack of reliable size-shape profiles for the freshest craters on each planet. Previous size-shape studies were either incomplete, used a large number of craters below 10 km in diameter (D) or did not follow rigorous criteria for choosing fresh craters. We present here refined size-shape profiles for fresh lunar and mercurian craters that may be used for interplanetary comparisons. Even though our sample size is small when compared to other size-shape studies, our data are based on the examination of all craters on each planet, and include all craters that meet strict criteria for freshness (most bowl-shaped craters with D<10 km were not selected). Also we show that there are significant differences in the crater size-shape characteristics for different lunar terrains, and that differences in crater shape between the Moon and Mercury may reflect differences in g between these planets.

Refined Lunar Crater Shape-Size Data- For the Moon, we refined the crater data of Smith and Sanchez (7). Each crater selected by them was re-examined for freshness and shape index, and each Lunar Orbiter frame was searched for additional fresh craters. The revised data include fresh craters on the Moon's farside. Criteria for crater selection are the presence of a sharp unbroken rim and the lack of obvious volcanic or impact modification. A size-shape profile for fresh lunar craters constructed using these data (fig. 1D) shows that terraces and central peaks develop initially in the diameter range 10-20 km. All studied craters above D=65 km are terraced and have central peaks. Swirl-floor texturing is most common in craters in the diameter range 20-30 km, but it occurs less frequently as terraces become a dominant feature of crater interiors.

Terrain Effects on Crater Shape- To study the effects of terrain type and substrate properties on the shape of lunar craters, the Moon was divided into 4 major terrain types, 1) highlands, 2) mare in the central part of the circular basins ("thick mare"), 3) mare on the margins of the circular basins ("thin mare"), and 4) farside basins. Terraces and central peaks are more abundant in craters with D<60 km on the mare than on the

highlands (fig. 1A & 1B). Also craters with swirl-like floor texturing are more common on mare material than on the highlands. Differences in target materials (thick regolith and breccia in the highlands versus thin regolith and unbrecciated volcanic flows in the maria) probably account for these differences. Also craters with D<35 km on the "thick mare" are more complex in shape for a given crater diameter than are craters on the "thin mare" (fig. 1C). Substrate and/or target properties may cause these differences.

Interplanetary Comparisons-Mercury and the Moon- A higher percentage of craters on Mercury have central peaks than do lunar craters in the diameter range 5-75 km. Above D=75 km, all fresh craters on the Moon and Mercury have central peaks (fig. 1E). A higher percentage of craters on Mercury are terraced than are lunar craters up to a diameter of 45 km (fig. 1F). These differences are significant (up to 60% difference for some diameter intervals) and support the suggestion of Gault et al. (1), Smith (2), and Smith and Hartnell (8) that g plays an important role in affecting crater shape.

References: (1) Gault et al., Jour. Geophys. Res., 80, 2444-2460 (1975); (2) Smith, E.I., Icarus, 28, 543-550 (1976); (3) Wood et al., Comparisons of the Moon and Mercury, 38 (1976); (4) Cintala et al., Lunar Science VIII, 181-183 (1977); (5) Malin M.C. and Dzurisin, D., Comparisons of the Moon and Mercury, 21, (1976); (6) Carr et al., Jour. Geophys. Res., 82, 4055-4065 (1977); (7) Smith, E.I., and Sanchez, A.G., Modern Geology, 4, 51-59 (1973); (8) Smith, E.I., and Hartnell, J.A., Paper presented to the 8th annual PGPI meeting, St. Louis (1977).

Table 1- Revised Crater Data for the Moon and Mercury

D (km)	MOON (221 craters) (%) Terraces	MOON (221 craters) C. Peaks	MOON (221 craters) Swirl-like floor	MERCURY (152 craters) (%) Terraces	MERCURY (152 craters) C. Peaks
0-9	0	0	0	0	0
10-19	12	30	16	29	62
20-29	26	50	23	59	79
30-39	67	72	9	79	97
40-49	83	87	5	81	100
50-59	95	95	0	91	100
60-69	100	92	0	100	93
70-79	100	88	0	100	100
> 80	100	100	0	100	100

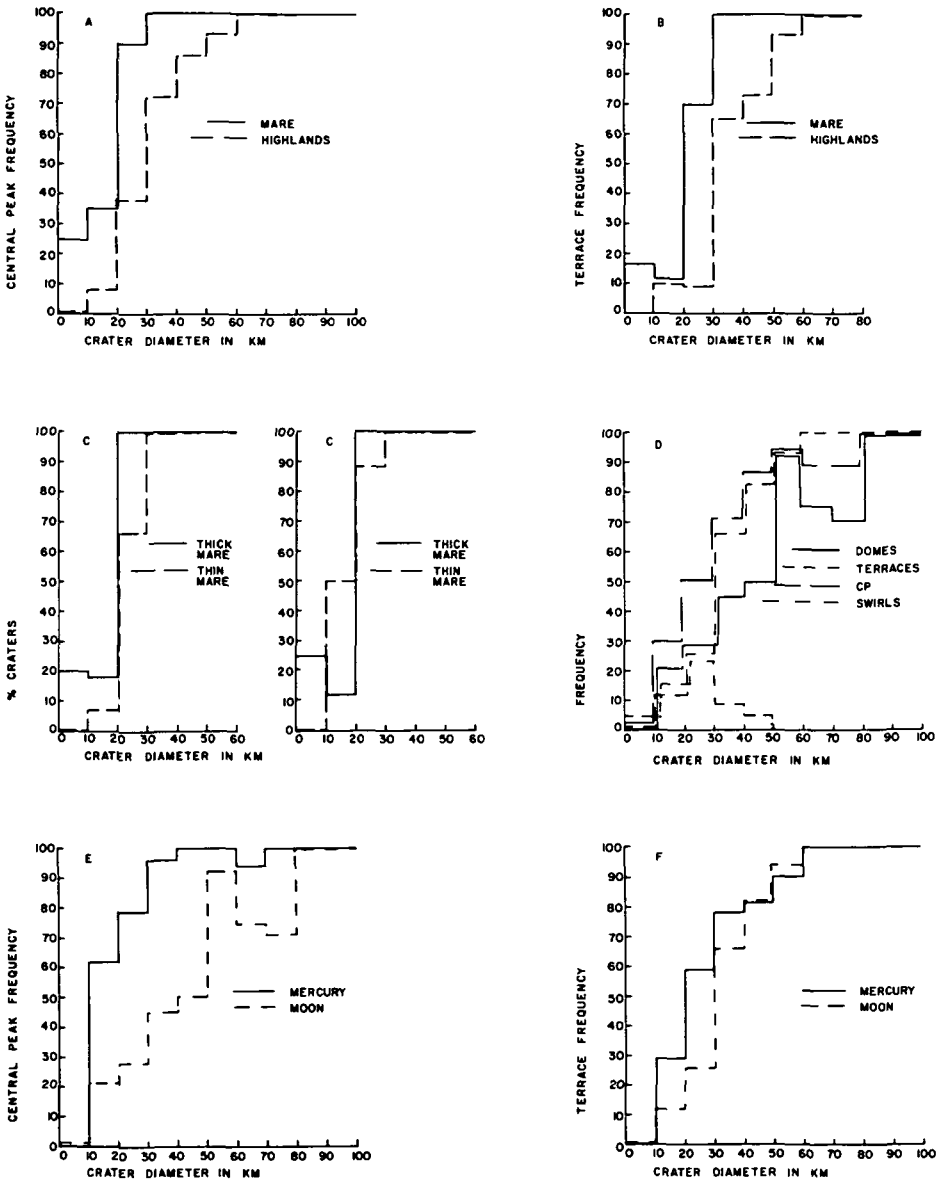

Figure 1. A) Central peak frequency-size data for craters on the mare and highlands, Moon. B) Terrace frequency-size data for craters on the mare and highlands, Moon. C) Left: Central peak-size data for craters on "thin mare" and "thick mare", Right: Terrace-size data for craters on "thin mare" and "thick mare". D) Size-shape profile of fresh lunar craters, CP=central peaks, domes refer to dome-like floor texturing. E) Comparison of central peak-size data between Mercury and the Moon. F) Comparison of terrace-size data between Mercury and the Moon.

IN SEARCH OF ANCIENT ASTROBLEMES: MERCURY, R. A. De Hon, Department of Geosciences, Northeast Louisiana University, Monroe, LA 71209.

Double ringed basins and filled basins with raised outer rings 150 km to 300 km diameter are relatively commonplace on Mercury (1,2). The largest basin, Caloris, is 1340 km in diameter, but between diameters of 300 km and 1000 km basins are apparently rare in initial surveys of the surface. Either the impact flux on Mercury was such that there was a paucity of impacting bodies of the size required to produce large basins (3) or these basins have not survived in easily recognizable form to the present day. A search has been initiated to delineate possible and probable large basins that may exist on the surface in a highly degraded form.

Recognition of the oldest basins presents itself as a search for the last stages of highly degraded basins. The term "basin" is used here in the general sense because many structures are too degraded to exhibit inner ring structures. In the final stages of degradation the outer rim ejecta is no longer preserved; the rim crest is reduced to incomplete low, rounded, raised topography or none at all; and the inner wall is, in like manner, low, incomplete or missing entirely. The basin interior is roughly circular and shallow, having been battered by repeated impacts and filled by volcanic material and/or ejecta debris from impact craters and basins beyond the depression. The task of identifying large impact basins is primarily one of recognizing large shallow depressions which may have a slightly reduced crater count or contain circular or irregular patches of interior fill (volcanic or ejecta plains). The presence of plains-forming material within basins enhances recognition by accentuating the basin outline. The oldest basins may be somewhat similar in appearance to the Australe basin on the moon if filled by volcanic materials or to the oldest lunar far side basins if unfilled. Identification of basins in extremely advanced stages of degradation becomes largely problematical.

A preliminary search of the mercurian surface reveals 42 basins greater than 250 km in diameter with varying degrees of degradation and varying degrees of certainty (Table I and Fig. 1). As work presently in progress continues it is expected that this number will increase. Caloris remains the largest basin and the general distribution of basins appears to be uniform within the constraints imposed by surface illumination and resolution by the Mariner cameras. The newly identified basins fill the apparent gap in basin population between 300 km and 1000 km diameter. Most of the largest basins are highly degraded, and consist as crudely circular patches of plains materials within topographic depressions

In most filled basins, partially buried craters indicate that the total thickness of the plains-forming material is not great and that the basins are shallow. The preliminary search used a subjective rating system to rank basins as (1) possible, (2) probable, or (3) certain. There are currently 18 basins, greater than 250 km in diameter, rated as certain; 11 rated as probable; and 13 rated as possible. Generally, the older a basin, the less certain its identification. Most, but not all, of the "certain" basins are named features and fall in to Trask's categories 1 to 4 (4). Few of the rank 1 and rank 2 basins are named features and most are unclassifiable (category 6) features. Current studies are designing a more rigorous system of basin identification as well as a relative age assignment based on the degradation of specific features. Comparison of basin production rates on the planets are premature as such comparisons require identification of all basins on all planets or identification of a time equivalent datum on each of the planets.

References

1. Wood, C. A. and Head, J. W. (1976), Abs. Lunar Science VII, LSI, p. 950-952.
2. Malin, M. C. (1976), Abs. Lunar Science VII, LSI, p. 533.
3. Schaber, G. G. and Boyce, J. M. (1976) Conf. on Comparisons of Mercury/Moon, LSI, p. 28.
4. Trask, N. J. (1976), Conf. on Comparisons of Mercury/Moon, LSI, p. 36.

TABLE I

	BASIN	LOCATION	DIAM. (km)	CONFIDENCE
1.	Caloris	30N; 194W	1340	3
2.	---	2N; 130W	840	2
3.	Sobkou	36N; 133W	650	2
4.	Beethoven	20S; 124W	640	3
5.	Budh	20N, 150W	620	3
6.	Odin	23N; 170W	580	2
7.	---	19N; 103W	570	1
8.	---	0 ; 54W	550	2
9.	---	32N; 24W	520	1
10.	---	2S; 151W	500	2
11.	---	34S; 154W	470	1
12.	---	18S; 133W	470	2
13.	Shakespeare	49N, 151W	420	3
14.	---	14N; 172W	420	1
15.	Suise	63N; 151W	400	1
16.	---	55S; 102W	400	1
17.	---	27N; 159W	390	2
18.	---	62S; 138W	390	1
19.	---	27N; 146W	380	2
20.	Dostoevskij	45S, 176W	380	3
21.	---	14S; 173W	370	1
22.	---	16S, 23W	360	2
23.	---	6N; 156W	360	2
24.	Tolstoj	16S, 164W	360	3
25.	---	79S, 90W	340	1
26.	---	28S, 57W	340	2
27.	---	38S; 136W	330	1
28.	---	65N; 195W	330	3
29.	---	2S; 44W	330	3
30.	Raphael	20S; 77W	320	3
31.	Goethe	80N, 44W	315	3
32.	Homer	1S; 36W	300	3
33.	---	47S; 163W	290	1
34.	Vyasa	48N; 80W	270	3
35.	Mozart	8N; 191W	270	3
36.	---	56N; 105W	260	3
37.	---	16S; 31W	250	1
38.	---	15S; 15W	250	3
39.	---	10N; 17W	250	1
40.	Rodin	22N, 18W	250	3
41.	Monet	45N; 9W	250	3
42.	Van Eyck	43N; 159W	250	3

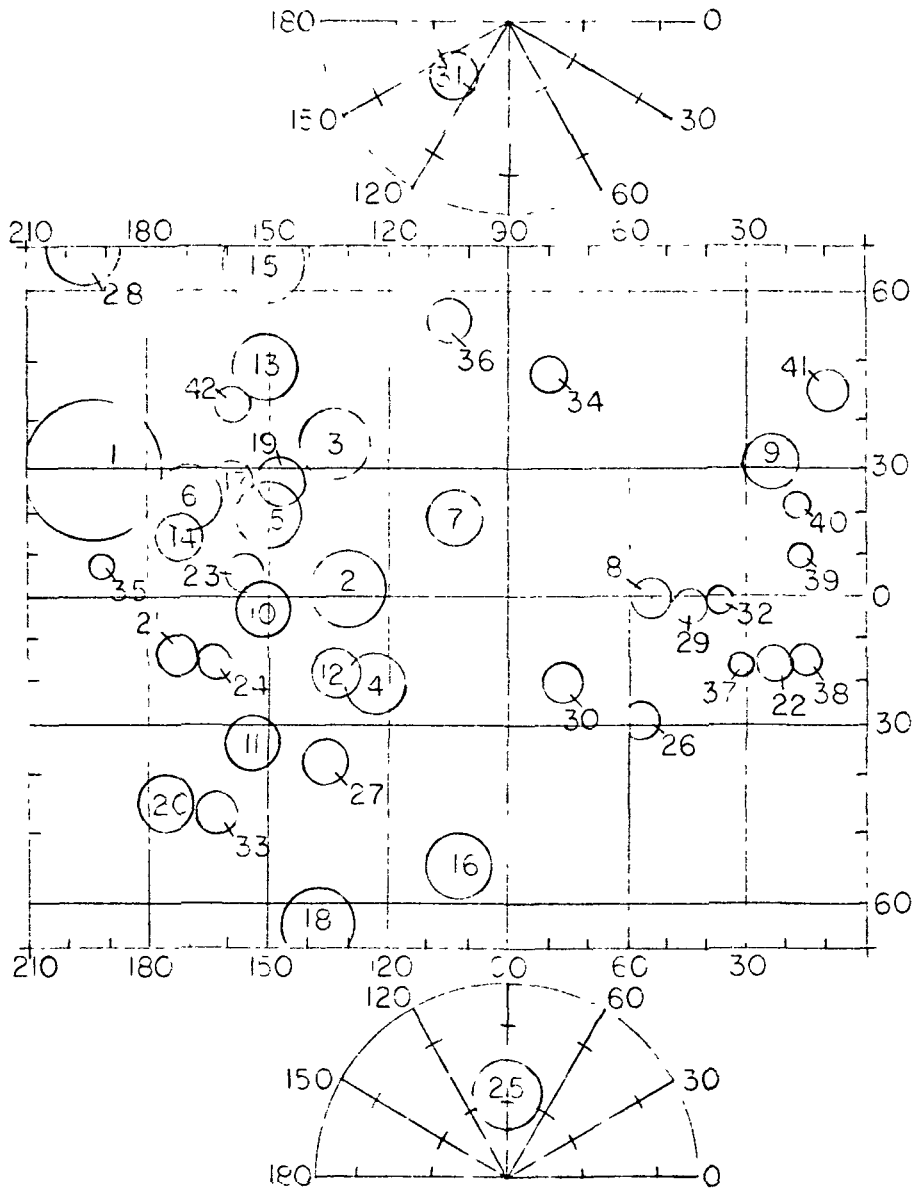

Fig. 1 Location of basins 250 km or more in diameter.

The Significance of Buried Craters Associated with Basins on the Moon and Mars. John S. King, S.U.N.Y. Buffalo, Amherst, N.Y. 14226, and David H. Scott, U.S.G.S. Flagstaff, Arizona 86001.

As planetary geology is broadened by studies of photographs and remote sensing data from satellites, it is possible to extend analog studies between the earth and planets to direct comparisons between features of the planets themselves. During the geologic mapping of the Arabia quadrangle (15° N, 340° W) on Mars (1), numerous circular features were observed around the north margin of the Schiaparelli Basin that were interpreted to be the outlines of buried crater rims. Many of these buried craters lie well within the inferred outer ring of the basin and thus constrain the size of the original cavity, provided they predate the impact that formed Schiaparelli. Geologic studies of the Orientale Basin on the Moon (2) also revealed circular outlines within the outer major ring of this basin which, although less distinct than those of Schiaparelli, are believed to be pre-Orientale craters buried by ejecta originating from the impact that formed the basin.

The Orientale Basin (Fig. 1) is located on the west limb of the Moon and is the youngest and freshest appearing lunar basin. Orientale is unique in that it is defined by a series of four concentric mountain ranges or rings. The diameter of the outermost ring, known as the Cordillera Mountains, is about 900 km. Many craters buried and partly buried by ejecta are visible beyond the Cordillera ring. Between the Cordillera Mountains and the next inner ring (Rook Mountains), however, are several indistinct circular outlines from 20 to 60 km in diameter which have been interpreted to be prebasin craters deeply buried by ejecta from the impact that formed this basin about 3.5 - 4.0 billion years ago (2). The presence or absence of these buried craters is important to the current controversy regarding the size of the original crater of excavation of Orientale.

Some investigators believe that the original or transient cavity of Orientale lies well within the third ring formed by the Rook Mountains and recent data including gravity (3) seem to support this. However, other investigators favor the interpretation that the original crater was larger and is delimited by the scarp bounding the Cordillera Mountains. If indeed the first hypothesis is correct, then buried craters would be expected within the annulus between the Rook and Cordillera Mountains, inasmuch as this surface, though covered by ejecta, would otherwise remain a relatively undisturbed part of the prebasin crust. Alternatively according to the second hypothesis, no pre-Orientale craters could exist inside the Cordillera Mountain ring as that surface was excavated by impact.

The reported presence of buried craters adjacent to the Schiaparelli Basin on Mars can possibly be used as an analog to aid in resolving the Orientale controversy. The Schiaparelli Basin is located astride the equator about 15° east of the prime meridian. Although most of the Schiaparelli Basin is within the Sabaeus Sinus quadrangle (15° S, 340° W) located south of the equator, the buried ring structures lie wholly within the Arabia quadrangle which is north of the equator.

Schiaparelli displays two identifiable rings. The outermost ring has a diameter of 650-700 km and the inner ring, about 400-450 km. Both rings, although readily visible, are much less prominent and less continuous than those of the Orientale Basin. The circular structures, which are interpreted

as buried craters, lie between the two rings around the northern part of the basin (Fig. 2). They appear to be buried by a map unit identified as "ridged and grooved material," originally described as "a 'scaly' surface made up of many overlapping, intersecting, and extremely subdued crater rims ranging from 20-50 km in diameter (1)." This map unit was interpreted to be the most ancient surface in the map area. If this material is analogous to the smooth and hummocky ejecta visible between the Rook and Cordillera Mountains of the Orientale Basin, then it too was formed as a result of impact, and the visible buried craters predate the Schiaparelli Basin lending credence to the existence of pre-Orientale craters within the Cordillera ring. An alternative interpretation is, of course, that the material may be volcanic in origin as other ridged material has been interpreted elsewhere on Mars (4, 5). If this were the case, the surface would probably be younger and not necessarily genetically related to the Schiaparelli Basin and the buried craters could either postdate or predate the basin. The lack of any visible volcanic source for lava flows in the region lends some support to the first hypothesis, but vents are often difficult to recognize, and this evidence is qualified.

Interpretation of the Schiaparelli Basin structures was made entirely from images having a resolution less than half that of photographs of the Orientale Basin. However, the two impact basins are sufficiently similar to be compared, and the indistinct -ut discernible buried craters that occur in both examples seem to predate basin formation, in each case supported by different criteria. Comparison of details of the two features works mutually to help define the size of the original impact structures and could be generalized to large impact craters on other planets provided the same criteria are present.

References

1. King, J. S., 1976, Geologic map of the Arabia quadrangle of Mars: U.S. Geol. Survey, Misc. Geol. Inv. Map I-996.

2. Scott, D. H., McCauley, J. F., and West, M. N., 1977, Geologic map of the west region of the Moon: U.S. Geol. Survey, Misc Geol. Inv. Map I-1034.

3. Scott, D. H., 1975, The geologic significance of some lunar gravity anomalies: Proceedings of the Fifth Lunar Conference, Supplement 5, Geochemica et Cosmochimica Acta, v. 3, pp. 3025-3036.

4. Milton, D. J., 1975, Geologic map of the Lunae Palus quadrangle of Mars: U.S. Geol. Survey, Misc. Geol. Inv. Map I-894.

5. Meyer, J. D. and Grolier, M.J., 1976, Geologic Map of the Syrtis Major quadrangle of Mars: U.S. Geol. Survey, Misc. Geol. Inv. Map I-995.

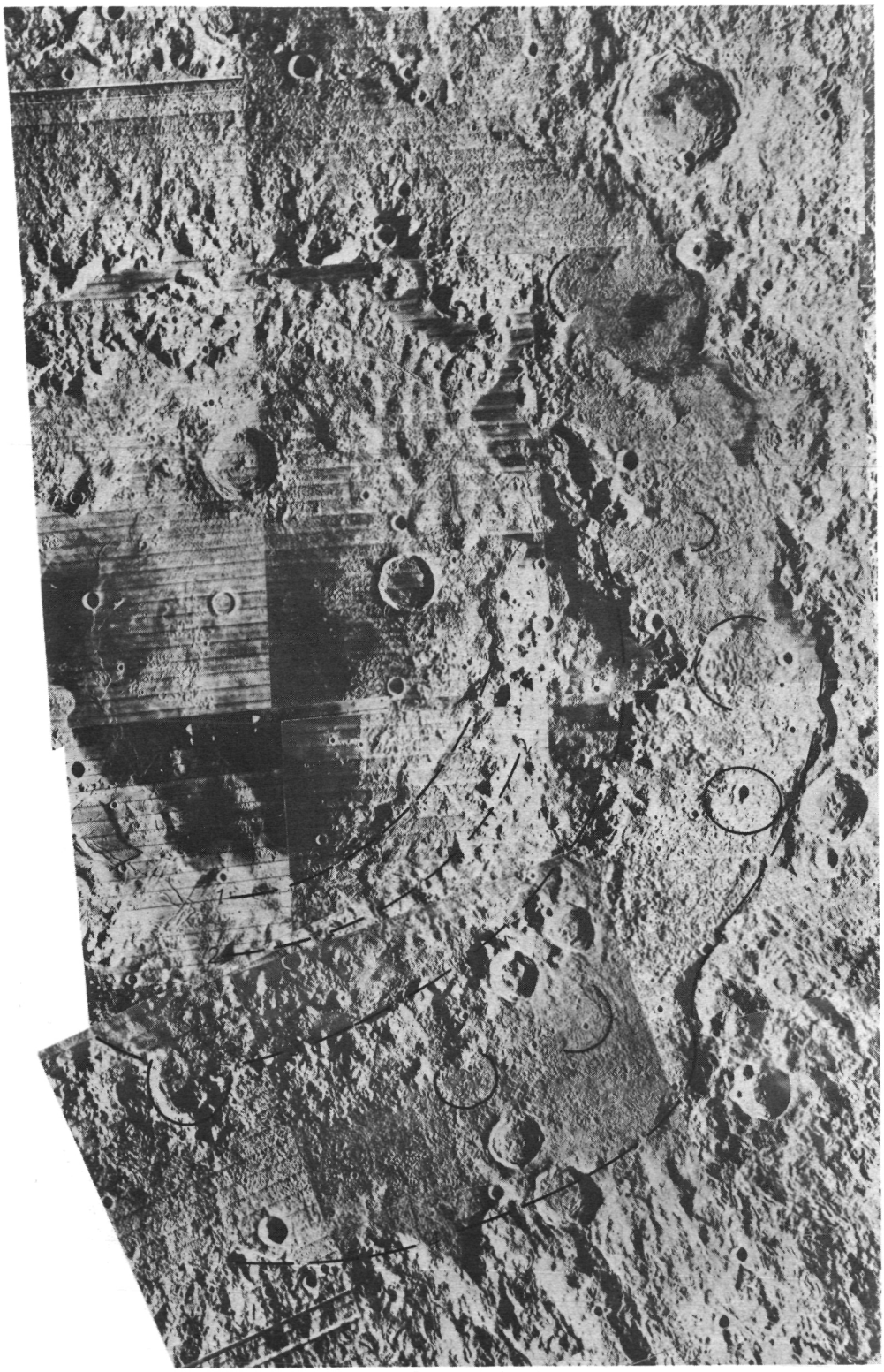

Figure 1. Eastern half of Orientale Basin on the Moon. Dashed lines show location of four rings of basin. Outer ring (4) has diameter of about 900 km. Relict pre-basin craters shown as circles or parts of circles.

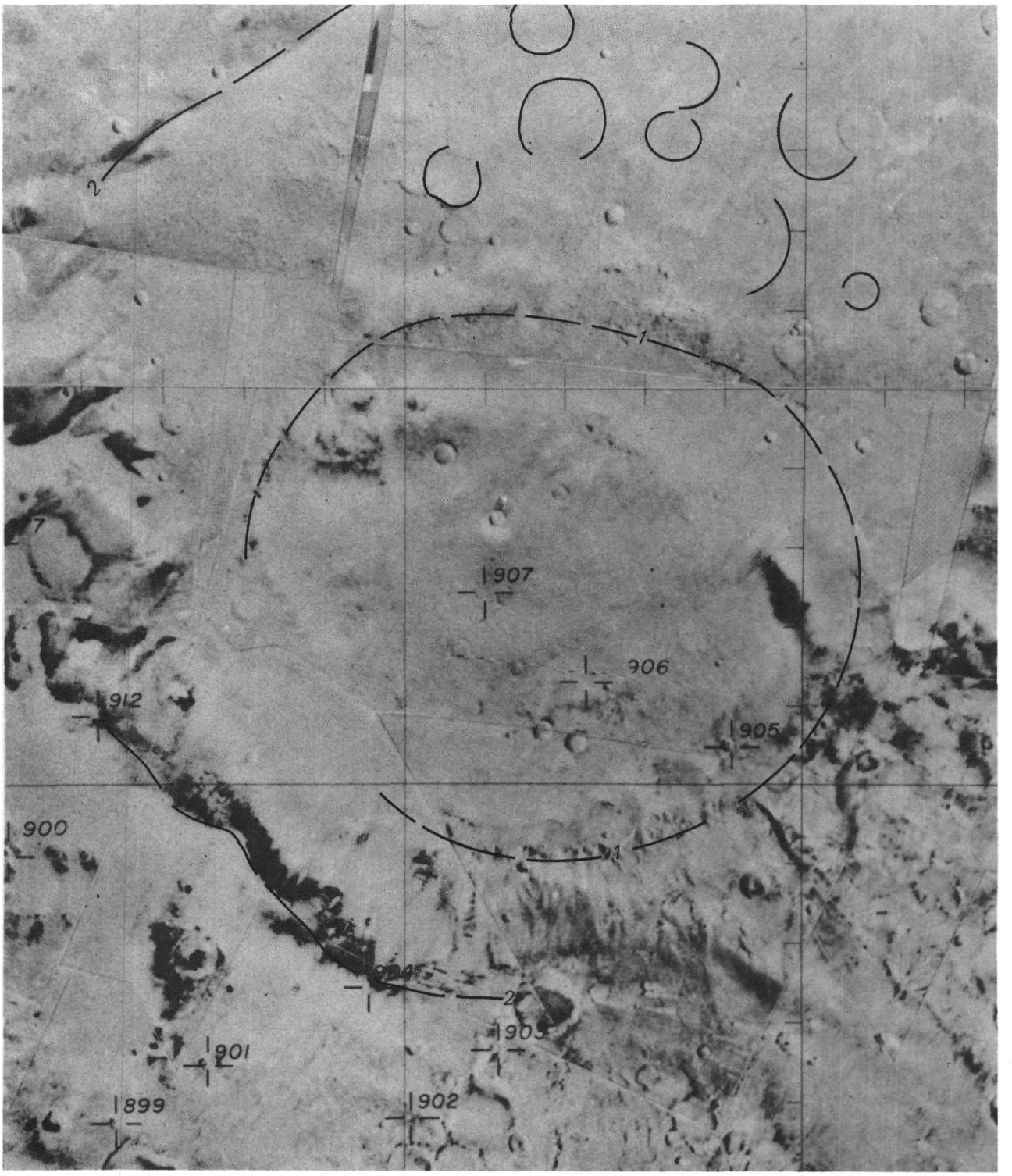

Figure 2. Schiaparelli Basin on Mars. Two rings shown by dashed line. Outer ring diameter about 650-700 km. Pre-basin crater outlines shown by circles or parts of circles.

Topographic Confirmation of 500 km Degraded Crater North of Ladon Valles, Mars, R.S. Saunders, L.E. Roth, C. Elachi, Jet Propulsion Laboratory, Pasadena, CA 91103; G. Schubert, Department of Earth and Space Science, Univ. of Calif., Los Angeles, CA 90024

The occurrence in Margaritifer Sinus Quadrangle of a system of radiating channels and an approximately circular ring of mountainous topography (Fig. 1) led earlier to the conclusion that a large crater had been obliterated by erosion of some kind early in Martian history (R.S. Saunders, Preliminary Geologic Map of MC-19). By analogy with the crater degradation sequence observed on the Moon, the isolated mounds were interpreted to be the erosional remnants of a crater rim. The radial channels were thought to result from flow into a local depression.

This interpretation is confirmed by traces of radar topography across the feature (see references in Roth, et al., this volume). The maximum observed relief is about 2 km and the depression is approximately 500 km across. The northern rim is at about 14^{o} south latitude where little relief is seen. The basin center is at 30^{o} west longitude and 18^{o} south latitude.

Although the isolated mounds may be interpreted as remnants of the crater rim by the lunar analogy, the mechanism of erosion is quite different on Mars. In the lunar case the mechanism is impact cratering. On Mars, with this particular example, the crater density on the present surface is far too low to have contributed significantly to the destruction of this crater. We would infer that the erosional process responsible for modifying this terrain was gravity driven and related to the formation of the small radiating channels. As in other areas, runoff of liquid water remains a strong condidate for the agent.

It should be noted that this particular basin lies on the axis of the so-called Chryse Trough and contributes to the valley-like form of that feature. That the trough may have, in part, an impact origin has been suggested previously by M.C. Malin (Pers. Commun.). We would only note that Nirgal Vallis and Samara Vallis also conform to a broad trough in this region and are themselves far outside the influence of this crater.

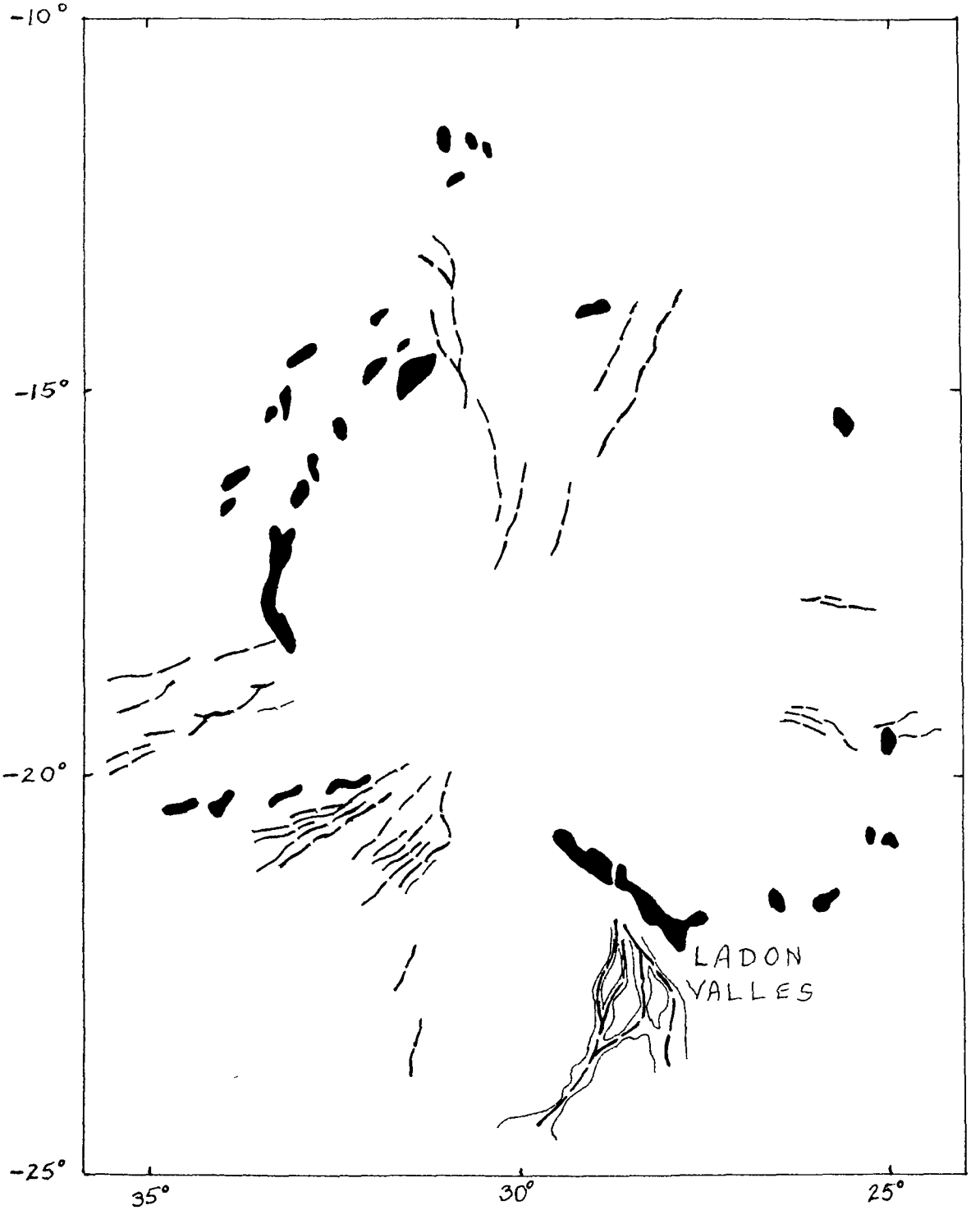

Figure 1: Abstracted from the preliminary geologic map of Margaritifer Sinus quadrangle by R.S. Saunders. The solid areas are isolated mounds interpreted to be remnants of an originally continuous ring of mountainous crater rim deposits. The dashed lines indicate small channels. Based on Mars Mariner 9 data.

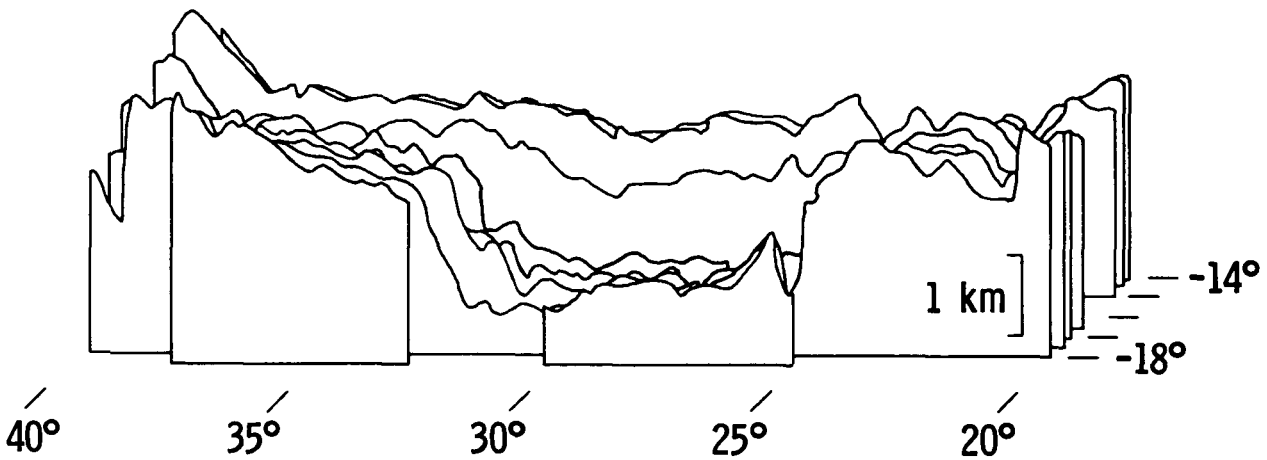

Figure 2: Radar topography across the crater (see Roth, et al., this volume, for references).

Areal Distribution of Rampart Craters on Mars, Carlton C. Allen, Department of Planetary Sciences, University of Arizona, Tucson, AZ 85721

Mariner IX and Viking orbital imagery have revealed a host of geologic features on Mars which appear to be unique to that planet. Among these are "rampart craters", ie craters displaying ejecta blankets characterized by lobes of material, often in layers, showing raised distal edges and often extending from 1-2 crater diameters from the parent crater rim. The mode of emplacement of the ejecta appears to involve entrained volatiles, and the source of these volatiles is a subject of continuing debate.

Rampart craters were recognized on Mariner IX imagery, but the morphology of their ejecta blankets was generally thought to be the result of wind erosion (1). However, some aspects of the size, shape and interactions of the ejecta blankets were suggestive of impact-related emplacement (2). The improved resolution of the Viking imagery has disclosed many rampart-type ejecta blankets not previously recognized, and has permitted detailed study of their morphologies. Such examination has led to the conclusion that many rampart crater ejecta blankets are indeed primary features, with morphologies resulting from ground flow facilitated by volatiles (3).

Two sources have been suggested for these volatiles: entrapped atmospheric gases, possibly from a denser early atmosphere, or water and/or ice in the target material. A study of the areal distribution of rampart craters, searching specifically for correlations between the presence or absence of such craters and distinct geologic units, might serve to differentiate between these possible sources. If rampart craters were found to be restricted to only certain geologic units, a strong case could be made for the dependence of the ejecta blanket morphologies on volatiles within those units. Rampart craters might thus be used as indicators of the presence of subsurface water and/or ice.

A search of the Viking orbital imagery was carried out to map the areal distribution of rampart craters. All frames taken from a range of less than 20,000 kilometers prior to October 21, 1977 were examined, and rampart craters were located within $5^{o}x5^{o}$ latitude and longitude blocks. Limitations on Viking coverage and atmospheric clarity restricted the areas on which rampart craters could be identified to approximately one-fourth of the 2592 $5^{o}x5^{o}$ blocks on the planet, and in many of these only a portion of the area was clearly pictured. Thus, a definitive statement of the absence of these features within a particular block was generally

difficult to make. The presence of at least one rampart crater within any 5°x5° block was obviously a much easier determination.

As a result of this study, the following statements can be made:

A. Rampart craters are common on nearly every geologic unit recognizable on Mars.

B. The units where no rampart craters were identified include the polar caps, the slopes and fresh-appearing flows of some of the large shield volcanoes,* and the floors of some of the large channels and canyons. In many of these areas very few impact craters of any size are visible, so the absence of rampart craters does not necessarily imply the lack of conditions suitable for their formation.

C. Small rampart craters are visible on the floors of several larger craters and basins.

D. Rampart craters occur in all longitudes and from approximately 75°N - 85°S latitude.

E. Rampart craters have formed at altitudes ranging from approximately 2 kilometers below the 6.1 millibar reference level, within the Hellas Planitia, to around 9 kilometers above the reference level, on Tharsis.

F. The two most widespread geologic units on Mars, namely the southern heavily-cratered terrain and the northern plains, display rampart craters in all areas where suitable Viking imagery exists.

G. Rampart craters invariably appear fresh, based on rim morphology. Most, but not all such craters, possess central peaks. Few, if any, very fresh craters do not exhibit at least some suggestion of rampart structure in their ejecta blankets.

Based on this study, no correlation between the presence or absence of rampart craters and major geologic units exists which can be used to distinguish the source of the volatiles entrapped in their ejecta blankets. If rampart craters are indicators of subsurface water and/or ice, such material exists presently, or at least existed in the recent geologic past, beneath almost the entire surface of Mars.

References:
(1) Arvidson, et.al., Icarus 27, 503, (1976).
(2) Head and Roth, in Symposium on Planetary Cratering Mechanics (abstract), Lunar Science Institute Contribution 259, 50, (1976).
(3) Carr, et.al., Journal of Geophysical Research 82, 4055, (1977).

* Rampart craters have been identified on Elysium lavas and on the slopes of Tharsis Tholus.

Martian Rampart Craters: Crater Processes that May Affect Diameter-Frequency Distributions, J. M. Boyce* and D. J. Roddy, U. S. Geological Survey, Flagstaff, Arizona 86001.

The high quality images returned by the Viking Orbiters show several types of impact crater and ejecta morphologies that appear unique to Mars. One type, called a rampart crater by McCauley (1973) from the earlier Mariner photography can be seen in the high-resolution Viking imagery to commonly exhibit massive central peaks and a surrounding ejecta blanket with a pronounced flow-like character (Carr et al., 1977). This type of crater appears widely distributed on Mars, ranging in size from a few kilometers across with little or no central peak evident, to multi-kilometer diameter craters with rim terracing and multiple central peaks, each surrounded by an ejecta blanket exhibiting one or more flow characteristics, such as lobate extensions,and an abrupt rampart-like terminal end. Allen (1978) indicates that these types of craters have not been identified in certain areas on Mars such as the Polar region, but appear common over most other areas photographed to date.

Another type of crater morphology, common to the Earth, Moon and Mercury (Shoemaker, 1962; Gault et al., 1975) has a normal ejecta blanket without pronounced flow-like patterns. This type of crater also occurs over most of Mars, and locally is in association with the rampart craters in some areas.

An accurate description of the distributions, ages, and parameters of martian craters, however, is not yet defined. Consequently, the crater morphologies have not been generally used to interpret regional material properties and stratigraphy. It has been suggested, however, by Carr et al. (1977) and others that the flow-like pattern of the ejecta of the rampart craters indicates that the impacts may have occurred in permafrost material or that entrained atmospheric gasses were instrumental in inducing the ejecta flow process. Cratering data from experimental explosions, however, suggest that only a limited amount of water in the target media

* Present address: NASA Headquarters, Washington, D. C.

is necessary to produce significant flowage in the ejection process (Roddy, 1976). The crater diameters in such experiments are commonly increased by a factor of 2 or more in saturated targets and volumes can increase as much as a factor of 4. A second consequence of a net target media is that the continuous ejecta blanket will normally not be distributed as for in an identical dry target media (Roddy, 1978). The percentage of water saturation (and consequent strength reduction) was far more critical, in these explosion experiments, than entrained atmospheric gasses in terms of inducing ejecta flow mechanisms. On Mars, we would also not envision any net contributions from the atmosphere, especially due to its very rarefied state. We would suggest that martian impacts accompanied by instant shock melting of a thick permafrost zone with partial vaporization could produce ejecta blankets with flow characteristics.

Of a number of conclusions that can be drawn from the explosion and impact analog data, two are of interest here. One centers on the potential problems created in crater diameter-frequency distributions by impacts in low strength target media and then attendent increase in diameters versus dry media. The explosion cratering data indicates that diameters of flow-related craters may be increased by as much as a factor of 2 versus the lunar or mercurian craters. Assuming comparable (though not identical parametric) increases on Mars, and a crater diameter-frequency of the form,

$$N = kD^{\gamma}$$

where N is the number of craters/unit area with diameters greater than D, k is a constant, and γ is an exponent with a value of approximately -1.5 to -3.5, one would expect small changes in D to yield large changes in N. That is, the diameter-frequency distributions for different areas, even the same areas for mixed crater types, may not be directly comparable and may yield abnormally high flux values for a given D range. Our point is that diameters enlarged by a low material strength property are not directly comparable with diameters in adjacent media of higher strengths and smaller diameters. An obvious consequence of not incorporating this effect is to derive an erroneous crater production function.

Another interesting consequence is suggested by the reduction of ranges for the terminal edge of the continuous ejecta blanket formed by an impact in a permafrost or fluidizable target media. A preliminary study by ourselves suggests that the ratio of the range from ground zero to the outer edge of continuous ejecta vs the rim crest diameter (corrected for terracing) is about 1.0 to 1.5 for wet-type events. This ratio appears to increase to about 2.0 to nearly 3.0 for lunar, mercurian, and dry explosion cratering experiments. Basically, this argues that impacts in dry target media have a wider distribution (although thinner) of continuous ejecta than does a wet-type event. From this, one might conclude that the Viking 2 landing site, some 200 km from the rim of the 100 km diameter crater Mie, may not be on the continuous flow ejecta as suggested by Mutch et al. (1977) and Arvidson (1978). It is certainly permissable, however, that the region may represent part of the discontinuous ejecta blanket or a discrete continuous flow lobe. A detailed topical photogeologic map and scaling study would be useful for the Mie crater area.

References:

Allen, C., 1978, Areal Distribution of Rampart Craters on Mars (abs.), this volume.

Arvidson, R., 1978, Viking Implications for Martian Aeolian Dynamics, this volume.

Carr, M. H., Crumpler, L. S., Cutts, J. A., Greeley, R., Guest, J. E., and Masursky, H., 1977, Martian Impact Craters and Emplacement of Ejecta by Surface Flow, J. Geophys. Res., 82, p. 4055-4065.

Gault, D. E., Guest, J. E., Murray, J. B., Dzurisin, D., and Malin, M. C., 1975, Some Comparisons of Impact Craters on Mercury and the Moon, J. Geophysics.Res., 80, p. 2444-2460.

McCauley, J. F., 1973, Mariner 9 Evidence for Wind Erosion in the Equatorial and Mid-Latitude Regions of Mars, J. Geophys. Res., 78, p. 4123-4137.

Mutch, T. A., ARvidson, R. E., Binder, A. B., Guinness, E. A., Morris, E. C., 1977, The Geology of the Viking Lander 2 Site, J. Geophys. Res., 82, p. 4452-4467.

Roddy, D. J., 1976, High-Explosion Cratering Analogs for Central Uplift and Multiring Impact Craters, Proc. Lunar Sci. Conf. 7th, Vol. 3, p. 3027-3056.

Roddy, D. J., 1978, Morphologic and Structural Analogs in Central Uplift and Multiring Impact Craters, (D. J. Roddy, R. O. Pepin, and R. B. Merrill, eds.), Pergamon Press, New York, in press.

Interior Morphometry of Fresh Martian Craters: Preliminary Viking Results, C. A. Wood, M. J. Cintala, and J. W. Head, Dept. of Geological Sciences, Brown University, Providence, RI 02912.

Viking imagery provides high resolution views of martian craters permitting improved statistics of the occurrence of central peaks and wall failure. Similar statistics for Mercury and the Moon have demonstrated a dependence of interior morphology on terrain type[1]. To test for possible terrain effects in martian craters, data for wall failure, central peaks, and central peak pits were collected for 107 craters on 3 surfaces mapped as plains units (PU) and interpreted as volcanic flows by the USGS[2] (Viking 1 landing area, Lunae Planum, and a region SSE of Arsia Mons) and for 68 craters in 3 areas mapped as cratered terrain (CT) (SW of Apollonius Patera, eastern Iapygia quad., and W of Hesparia Planum). The CT sample does not include areas with lunar mare-like ridges, and no data were collected from middle or high latitude zones suspected of being mantled[3]. All fresh, shadow-free craters in a sample area were measured. Freshness was based solely on rim sharpness and continuity, but the presence of ramparts and/or other ejecta around 80% of the craters provides independent confirmation of the pristine nature of most of the craters. Although the data set presently consists of only 175 craters, the preponderance have diameters of 1 to 15 km, the critical transition zone from simple to complex interior morphology. The new results differ significantly from all previous Mars crater statistics[4,5], including our own[6]. Central peaks and wall failure are much more prevalent (at least in the sample areas) than previously thought. The high resolution of Viking imagery is probably responsible for the increased detection of peaks and wall failure compared to surveys based on Mariner 9 records[4,6]. An additional reason for disagreement with Mariner statistics stems from a unique feature of martian central peaks. Pits that occur on many peaks often obliterate all but small remnants of the peak, and poor resolution or slight undetected degradation of crater morphology would readily mask the peaks. The poor agreement between our data and that of Carr et al.[5] may be due to their sample selection, inclusion of degraded craters, or small data set (n=59).

Wall Failure. Wall failure in martian craters is characterized by slump blocks on the floors of smaller craters and by more massive terrace development in intermediate and large craters. The smallest crater with detected slumps in the PU sample is 4.9 km in diameter (D) vs. ~7 km for the CT sample, and wall failure is consistently more abundant in PU craters, reaching 100% in the 10-15 km D interval (Fig. 1). All sampled CT craters with D >20 km exhibit wall failure. More than 99% of the craters examined have flat floors with a clear break in slope at the contact with the crater wall; bowl-shaped craters probably result from slight degradation[7].

Central Peaks. Central peaks are very common in the martian craters examined (Fig 2): 25% of the CT craters <5 km D have peaks (vs. 6% in PU). Peaks occur in 100% of CT craters >15 km and in all PU craters inspected >10 km.

Central Peak Pits. Smith[4] recognized that many martian craters have central pits in place of peaks as well as occasional summit pits on central peaks. Our data confirm that pits are a fundamental characteristic of martian cra-

ters and suggest that there is a morphological sequence in pit development. About 50% of craters with peaks have no pits; 28% have tiny summit pits in relatively massive peaks, 16% have a low incomplete ring of peaks surrounding pits, and 6% have rimless pits lacking any evidence of peaks. There is no obvious diameter or terrain dependence in this sequence, except that rimless pits appear to be ∿3 times more common in CT than PU craters. If pits are considered as peak equivalents Fig. 2 would show that all CT craters >10 km have central structures. Pits are somewhat more abundant in CT craters (59%) than in PU craters (50%), but PU pits are systematically larger than CT pits (Fig. 3).

Floor Diameter. Diameters of crater floors (F) steadily increase with D, with no obvious difference for CT or PU craters (Fig. 4). There is an inflection in the F-D relation at D ∿4 km, confirmed by least squares analysis. The lunar F-D relation inflects at ∿22 km[7].

Simple-Complex Transition. The diameter of transition from simple craters lacking wall failure and abundant central peaks to complex craters with these features has been used for interplanetary comparisons. Wood and Andersson[7] have shown that, for lunar craters, wall failure is the most important morphological change relating to the simple-complex transition, which occurs at D ∿17 km[8,7]. For martian craters the transition is completed between 5 and 15 km, with 50% wall failure near D ∿7-9 km, compared to the F-D inflection at D ∿4 km. Based on the 50% wall failure criterion the transition on Mercury occurs at D ∿20 km[1], although depth-D data place the break at D ∿10 km[9].

Discussion. The data presented here demonstrate that the occurrence of wall failure, central peaks, and central pits are all modulated by the type of terrain in which a crater formed. Similar results have been documented for the Moon and Mercury[1], and martian terraces using Mariner 9 data[10]. Our results for Mars shown that central peaks are more abundant on CT than on PU, whereas wall failure is more common on PU. This is intermediate between the case for Mercury (both peaks and wall failure are more prevalent in CT) and for the Moon (both peaks and wall failure are more common in maria). Comparison of the diameter dependence of peaks and wall failure (Fig. 5) reveals that both crater interior features attain maximum development (100%) at lower D for Mars than for the Moon or Mercury. This argues that the development of crater interior morphology is not a simple function of either gravitational acceleration ($Mars_g$ = $Mercury_g$ = 2.3 $Moon_g$) or impact velocity ($Moon_v$ ∿$Mars_v$ = ½ $Mercury_v$). However, the observed terrain effects on each planet suggest that the major differences between planets could also reflect differences in their upper crusts. Indeed, abundant evidence from crater exterior morphology[11,5] and other features (channels, chaotic terrain, etc.) imply that Mars is unique among terrestrial planets in having significant amounts of volatiles imprisoned in permafrost or ice layers beneath the surface. Smith and Hartnell[10] have speculated that martian central pits are due to interaction with such a layer. We propose that explosive decompression of subsurface volatiles after near-adiabatic compression[12] and addition of irreversible heat during the impact event could account for the formation of at least some of the central pits. If this were the case, the relative sizes of the pits between the PU and CT would imply that the explosions are more violent in the PU for a given D cra-

ter, possibly indicating (a) a greater volatile concentration trapped under impermeable lava flows, (b) that volatile layers are closer to the surface in the PU, and/or (c) that target strength differences cause smaller craters in the PU for a given energy event. The rapid expansion of volatiles and entrained dust could result in localized snowstorms; however, these would probably occur too late in the event and be too small a volume to significantly affect the final crater ejecta morphology.

References [1]Cintala, M J , Wood, C A , and Head, J W (1977) *Proc Lunar Sci Conf , 8th*, 3409 [2]Carr, M H , Masurky, H , and Saunders, R S (1973) JGR 78, 4031 [3]Soderblom, L A et al (1974) Icarus 22, 239 [4]Smith, E I (1976) Icarus 28, 543 [5]Carr, M H et al (1977) JGR 82, 4055 [6]Cintala, M J , Head, J W , and Mutch, T A (1976) GRL 3, 117 [7]Wood, C A and Andersson, L , this volume [8]Pike, R J (1974) GRL 1, 291 [9]Malin, M C and Dzurisin, D (1977) JGR 82, 376 [10]Smith, E I and Hartnell, J A (1977) Repts Planet Geol Prog NASA TMX 3511, 91 [11]Head, J W and Roth, R (1976) Sym Planet Cratering Mechanics (Flagstaff), 50 [12]Kieffer, S W (1977) LS VIII,543

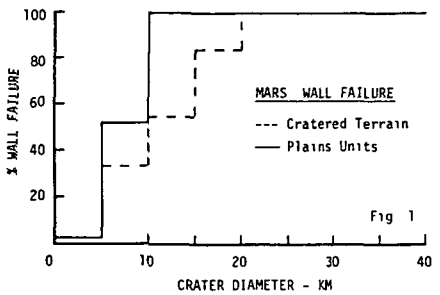

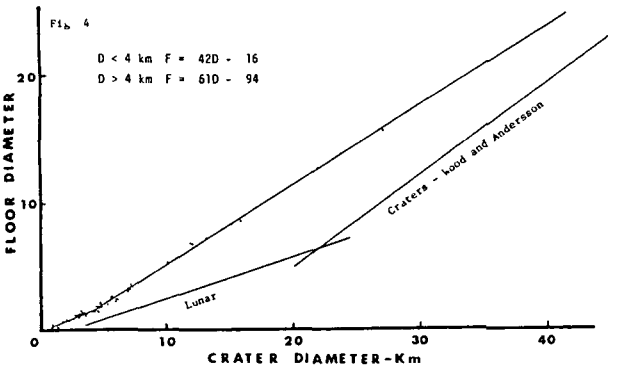

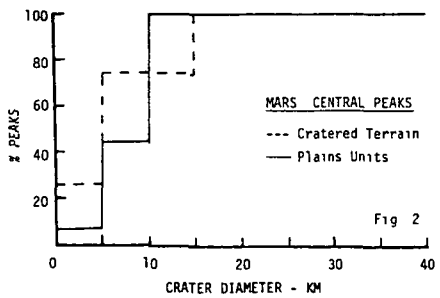

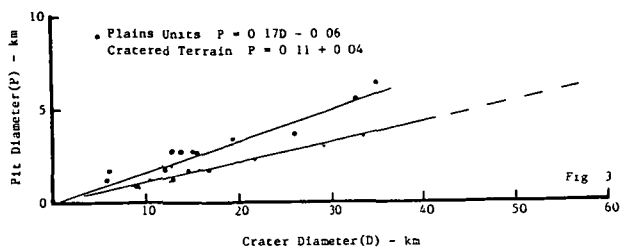

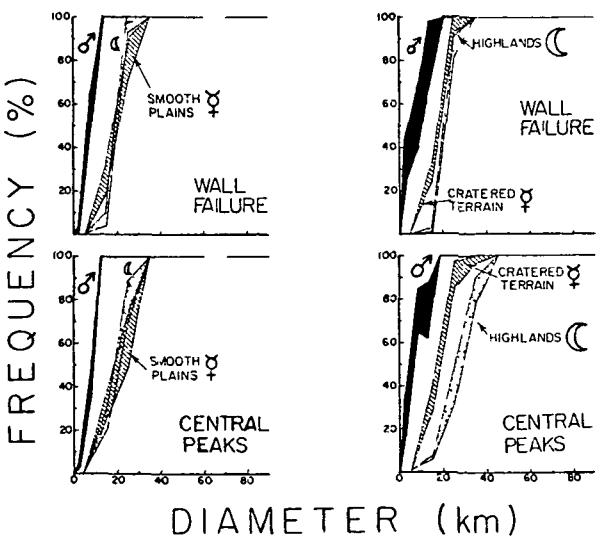

Central Pit Craters, Peak Rings, and the Argyre Basin. Carroll Ann Hodges, U.S. Geological Survey, Menlo Park, CA 94025.

Impact craters having a crater-in-crater configuration with distinct central pits -- either instead of peaks or at the summits of peaks -- are relatively common on Mars. Rims of most of these inner pits are blocky but continuous rings, uplifted above the surrounding crater floor, although some are simply benches in the floor. Craters with central pits so far observed range in size from about 15 km to as much as 90 km across and vary from extremely fresh to degraded; the inner pit corresponds to the surrounding crater in degree of degradation. Except for the greater continuity and smaller size of the upraised central-pit rims, they strongly resemble the blocky peak rings in such basins as Schrödinger and Compton on the Moon and Lowell on Mars. More specifically they appear to duplicate the morphology of Australia's Gosses Bluff, a 5-km circular ring of sandstone blocks uplifted at the center of a 20-km impact crater. As interpreted by Milton et al. (1), the core of the doughnut-shaped bluff was evacuated during rebound, so that the central peak assumed a ring morphology.

Analogy has been drawn previously between Gosses Bluff and the peak rings of lunar two-ring basins (2,3,4), but the enormous scale differences (Schrödinger is 320 km across) and the obscuration of internal morphology (Schrödinger is nearly filled with plains material) precluded conclusive interpretation. Further, the Milton et al. (1) interpretation of Gosses Bluff has been disputed (5,6). The size of central pit craters on Mars, however, is in the same order of magnitude as that of Gosses Bluff, and the nearly pristine morphologies of some martian examples compel the interpretation that the central-peak core was excavated during cratering, independent of analogy with Gosses Bluff. In many fresh craters, the inner depressions surrounded by uplifted rims are "clean" and bowl-shaped, not irregular with blocky floors as would be expected if they had formed by collapse. These craters appear to provide the transitional link (largely lacking on the Moon) between central peaks and peak rings, supporting the hypothesis that peaks expanded and "grew" into rings as material was ejected from their cores (2,3,4,7,8); indeed, the martian craters offer persuasive support for the hypothesis formulated at Gosses Bluff. Lithologic properties facilitated the process of core excavation at Gosses Bluff; the deepest rocks uplifted at the center were less resistant to excavation (as well as to subsequent erosion) than the overlying sandstone that formed the surrounding bluff (1). On Mars also, lithologic properties of the substrate may have influenced the configuration of craters; not all craters of the same size display this nested-crater morphology, suggesting that kinetic energy of impact is not the sole controlling factor. The tendency for central pit craters of different sizes to be somewhat clustered in specific areas may be indicative of subsurface discontinuities in the target materials that promote excavation of the central peak core. Craters of this type are prominent, for example, in the regions of lat 0° to 30°, long 60° to 80°, and of lat -20° to -35°, long 110° to 130°. The depth to a less resistant stratum may be indicated by the diameter of the smallest crater with a central pit configuration.

Central pit craters (as here interpreted) appear to support the origin of central peaks by dynamic rebound (1,9) rather than by uplift due to peripheral gravitationally-induced collapse (10,11,12), which would seem unlikely to cause ejection of central-peak cores.

A few martian craters have an arcuate ridge outside the central pit rim, suggesting the beginnings of an intermediate ring, and several craters have poorly-defined rings surrounding peaks, much like the lunar basin Antoniadi; but well-defined three-ring basins, similar to Orientale, are lacking on Mars. Multiple rings on the Moon possibly result from interaction of the shock wave with crustal stratigraphic discontinuities (2,3,4,13,14); the scarcity of such rings on Mars may also be attributable to subsurface characteristics. Argyre, probably the youngest of the large martian basins (15), is notably ambiguous with respect to rings (16). An outer concentric scarp (1600 km across) is distinct in places, nonexistent in others. The rugged materials bounding the central plain form an inner ring, although its exact delineation is uncertain. Where Viking pictures reveal detail on the central plain, it is relatively featureless, with only a few small craters and a couple of long narrow ridges. The initial cavity, after rebound and isostatic adjustment, was likely inundated by non-impact debris; remnants of small, stream-like channels are visible among the massifs surrounding the plain. The configuration of Argyre may possibly be due to stripping during excavation of a poorly cohesive surface layer, composed partly of ground ice, across a diameter of about 1600 km, and uplift of the more resistant bedrock beneath to form the rugged massif materials -- the peak ring -- surrounding the plain. A few remnants of concentric graben are evident in the rugged rim materials, but rings between the inner massifs and the outer scarp are not readily defined.

Although the interpretation of multiple basin rings appears to be as elusive for Mars as for the Moon, the double-ring basins seem clearly explained as expansions of central pit craters. These well-developed martian features, the apparent small end-members in a gradational series, provide strong support for the rebound hypothesis of central peak origin and for the transitions of peaks to peak rings by excavation of their cores.

References

(1) Milton, D. J., Barlow, B. C., Brett, R., Brown, A. R., Glikson, A. Y., Manwaring. E. A., Moss, F. J., Moss, E. C. E., Van Son, J., and Young, G. A., 1972, Gosses Bluff impact structure: Science, v. 175, p. 1199-1208.

(2) Hodges, C. A. and Wilhelms, D. E., 1976, Formation of lunar basin rings [abs.], in Abstracts, 25th International Geological Congress, Sydney, Australia, v. 2: p. 612-613.

(3) Hodges, C. A. and Wilhelms, D. E., 1978, Formation of lunar basin rings: Icarus (in press).

(4) Wilhelms, D. E., Hodges, C. A., and Pike, R. J., 1977, Nested-crater model of lunar ringed basins; in Roddy, D. J., Pepin, R., and Merrill, R. B., eds., Impact and explosion cratering: Planetary and terrestrial implications: Elmsford, New York, Pergamon Press, p. 539-562.

(5) Dence, M. R., 1973, Dimensional analysis of impact structures: Meteoritics, v. 8, p. 343-344.

(6) Gault, D. E., 1977, Personal communication.

(7) Head, J. W., 1976, Significance of substrate characteristics in crater morphology and morphometry [abs.], in Lunar Science VII: Lunar Sci. Inst., Houston, p. 355-356.

(8) Head, J. W., 1977, Origin of central peaks and peak rings: Evidence from peak-ring basins on Moon, Mars, and Mercury: EOS, Trans. Am. Geophys. Union, v. 58, p. 424.

(9) Milton, D. J. and Roddy, D. J., 1972, Displacements within impact craters: Intl. Geol. Congr. Rep. Ses. 24th, p. 119-124.

(10) Dence, M. R., 1968, Shock zoning of Canadian craters, petrography and structural implications, in French, B. M. and Short, N. M., eds., Shock metamorphism of natural materials: Baltimore, Md., Mono, p. 169-184.

(11) Dence, M. R., 1971, Impact melts: Jour. Geophys. Res., v. 76, p. 5552-5565.

(12) Gault, D. E., 1974, Impact cratering, in Greeley, R. and Schultz, P. H., eds., A primer in lunar geology: Mountain View, Calif., Ames Res. Center, p. 137-175.

(13) Oberbeck, V. R., 1975, The role of ballistic erosion and sedimentation in lunar stratigraphy: Reviews Geophysics and Space Physics, v. 13, p. 337-362.

(14) DeHon, R. A., 1977, Multi-ringed basins: A model for formation in multi-layered media, in Arvidson, R. and Wahmann, R., eds., Reports of Planetary Geology Program, 1976-1977: NASA TM X-3511, p. 111-112.

(15) Wilhelms, D. E., 1973, Comparison of martian and lunar multiringed circular basins: Jour. Geophys. Research, v. 78, p. 4084-4095.

(16) Hodges, C. A., 1978, Geologic map of the Argyre quadrangle of Mars: in prep.

Mars Chronology, G. Neukum, K. Hiller, J. Henkel, J. Bodechtel, Institut für Allgemeine und Angewandte Geologie, Ludwig-Maximilians-Universität, 8000 München 2, Germany.

The cratering chronology relationship given by Neukum and Wise (1976)(1) has been updated in reconsidering the gravitational cross-section effect of Mars on bodies at encounter. In addition, the relationship between the lunar production size-frequency distribution and the Martian one has slightly been modified. The resulting cratering chronology is shown in figure 1 in comparison with models by Soderblom et al. (1974)(2) and Hartmann (1973)(3). Contrary to the display given by (1), the data by (2) have here been reduced to Martian conditions by application of the standard Martian crater curve of (1). As in (1), some ages of Martian provinces have been inserted into the diagram (data partly taken from Carr (1976)(4)). This modification results in shifting the Martian chronology of (1) to slightly younger values at old ages ($> 3.10^9$ years) and having a somewhat greater effect at ages $\leq 3.10^9$ years (e.g. Olympus Mons now $1.8 \cdot 10^9$ years instead of $2.5 \cdot 10^9$ years before).

The application of different Martian model crater chronologies given in fig. 1 results in substantially different histories of the Martian crust. Masursky et al. (1977)(5) have pointed out that Mars has been active until very recently (less than 200 mio years on the basis of the crater chronology of (2). We do not agree with this view because of the following:

a) the chronology by (2) has to be reexamined and should not be used without great caution as pointed out by (1). Arguments for its validity quoting agreement with asteroid impact rate calculations by Shoemaker (1977)(6) seem to be inconclusive to us because of the immanent high uncertainties.
b) Aside from plausible arguments given for the validity of our chronology (1),the investigations of the history of the Martian atmosphere (7) and the measured seismic non-activity (8) exclude in our opinion, that erosional and volcanic processes took place as recent as 200 mio years ago (or even less).

We have reexamined published Mars crater size-frequency data (5) and have also carried out a number of measurements in various Martian provinces (9). Contrary to (5), we applied the standard Mars crater curve of (1) to all data. This curve (the Mars impact crater production size-frequency distribution) is shown in fig. 2 in comparison with the one (average lunar mare) used by (5). It is obvious that the application of the two different curves to the same data may yield very different values at a reference crater diameter (here 1 km), especially for data obtained for craters with diameters $\gtrsim 10$ km. Orders of magnitude error may result in such cases. Thus, the precise determination

of the Martian production size-frequency distribution and its relationship to the lunar one, is an important matter for relative and absolute age determinations of Mars.

The Martian stratigraphy as inferred from our data reduction is displayed in fig. 3. The relative ages in form of cumulative crater frequencies taken at 1 km crater diameter can directly be converted to absolute ages in this diagram. We draw the following conclusions:

1. The oldest crust investigated shows ages in excess of $4.15 \cdot 10^9$ years, the bulk lying between 4.2 and $4.3 \cdot 10^9$ years. These ages are given by the frequencies of large craters (diameters > 10 km) which survived successive resurfacing processes. Such processes are commonly visible in irregularities of the highland crater size-frequency distributions at smaller crater sizes from which resurfacing ages can be deduced in many cases and which are also given in fig. 3.
2. The resurfacing activity began at about $4 \cdot 10^9$ years ago with most of the processes taking place between 3.9 and $3 \cdot 10^9$ years ago, but seeming to have occurred as recently as $(0.5 - 1) \cdot 10^9$ years ago in a few places.
3. In the period of $(3 - 3.9) \cdot 10^9$ years ago, two major episodes of resurfacing can tentatively be determined. These resurfacing effects also show up in irregularities of the respective crater size-frequency distributions at the small crater sizes. A more detailed study of those effects for the Elysium/Isidis region is given by (9) (part of the data of (9) are incorporated in fig.3).
4. The resurfacing is clearly due to large scale volcanic activity in most areas (e.g. Elysium/Isidis Planitia, Nepenthes Mensae, Nili Fossae, N. E. Alba Patera). In part, however this volcanic activity was intermixed with aeolian and/or fluvial processes (e.g. Nepenthes Mensae). A detailed discussion is given in (9).
5. Piling up the large shield volcanoes was the final stage of volcanic activity, starting probably before $3 \cdot 10^9$ years and ending approximately $1 \cdot 10^9$ years ago (data partly in fig.1).
6. The main aeolian and/or fluvial activity seems to have taken place between 4 and $3.7 \cdot 10^9$ years ago. Most of the resurfacing activities in the time $< 3 \cdot 10^9$ years ago seems to have been volcanic with possibly few exceptions like Hrad Valles.

References:

(1) Neukum and Wise (1976) Science 194, 1381.
(2) Soderblom et al. (1974) Icarus 22, 239.
(3) Hartmann (1973) J. Geophys. Res. 78, 4096.
(4) Carr (1976) NASA Tech. Memo. TM X 3364, 152.
(5) Masursky et al. (1977) J. Geophys. Res. 82, 4016.
(6) Shoemaker (1977) NASA Tech. Memo. TM X 3511.
(7) Mc Elroy et al. (1977) J. Geophys. Res. 82, 4379.

(8) Anderson et al. (1977) J. Geophys. Res. 82, 4524.
(9) Hiller and Neukum (1978) This Volume.
Acknowledgments:
This work was supported by the Deutsche Forschungsgemeinschaft and the NASA Planetary Programs Office.

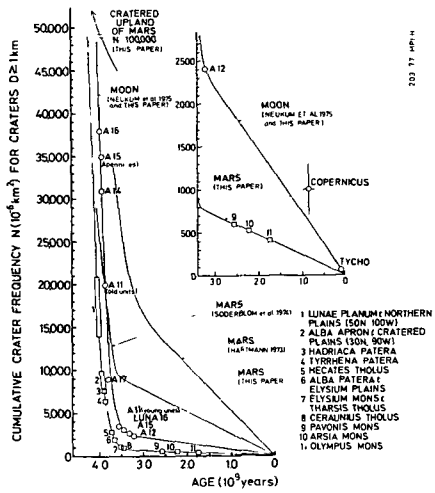

Fig.1

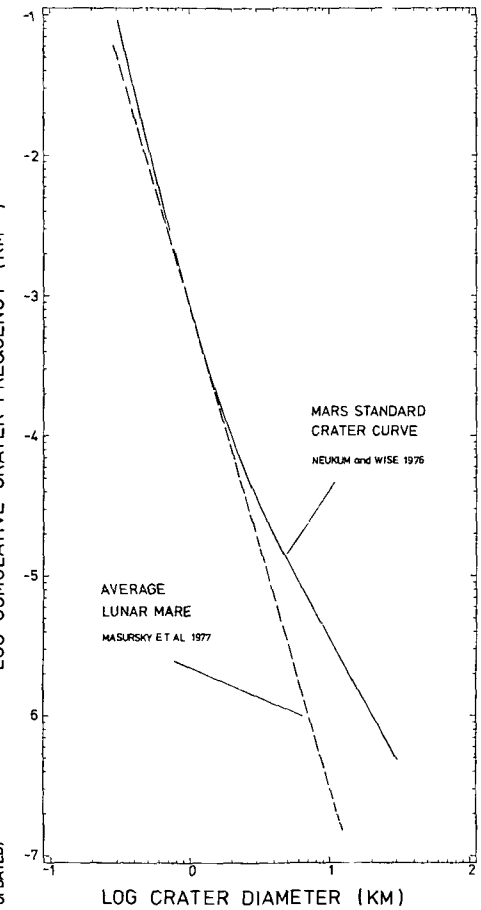

Fig.2

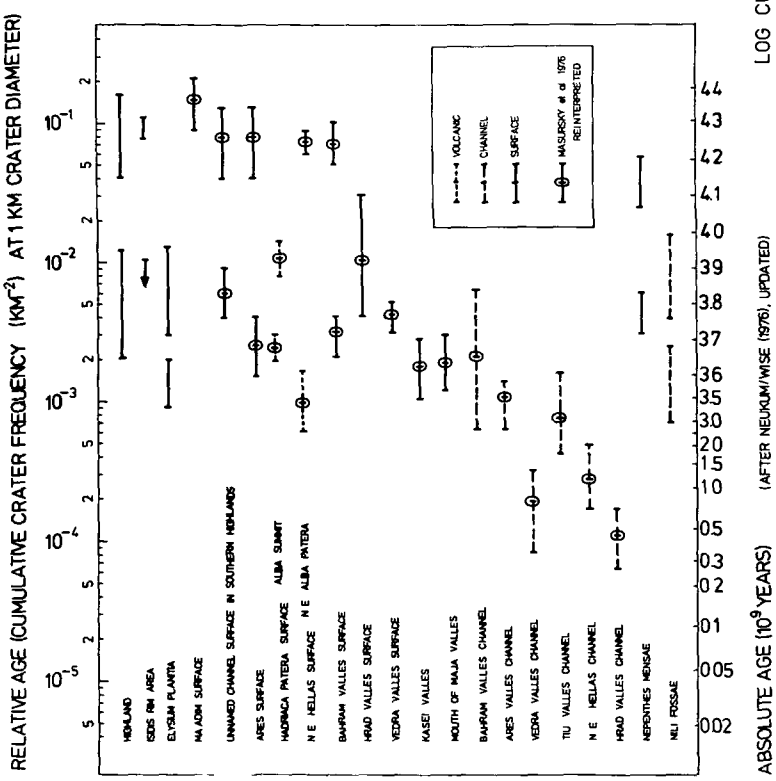

Fig.3

Intermediate Diameter (2-10 km) Crater Density Maps of Mars

C. D. Condit and D. A. Johnson

Crater density data have usually been assembled and presented in the form of crater frequency curves. Such plots are used to estimate the relative ages of small areas on the surfaces of the solid planets. In contrast, several workers (1, 2, 3) have attempted to use crater density data as a mapping tool for defining global geologic units on Mars. In this method the frequency of occurrence of craters in a limited diameter range is mapped continuously. Because of the poor resolution of the Mariner 9 images of Mars on which such studies were based, these early efforts were limited. New photomosaics of Mars generated from much higher quality Viking images, provide the opportunity for a much more detailed application of this technique for mapping units of varying relative age.

One of the disagreements in mapping areal crater density has been the choice of the diameter size range which best reflects the relative age of the surface. The craters must be large enough so that they represent a complete accumulation since the surface was formed; they cannot be in or approaching steady state due to erosion or saturation. To insure this we use the criterion that the craters be fresh, steep, and bowl-shaped. On the other hand the craters must be small enough so that they clearly postdate the surface whose age is being estimated. Craters older than martian plains which show highly degraded morphologies (flooded flat floors, absence of ejecta blankets) are generally larger than 15 to 20 km. Therefore, we use an upper limit of 10 km. Craters smaller than this are almost universally fresh and bowl-shaped. The lower limit must be as small as possible to maximize statistics and thereby provide best resolution of unit boundaries.

The new maps were generated from the Viking 1:1.25 million sub-quad mosaics, hence the lower limit was based on the resolution of those mosaics (about 1 km). To insure completeness we selected a lower limit of 2 km. Additionally, Soderblom et al., (1) suggest the break between primary craters and secondary craters on Mars appears to be a 1 km. Examination of craters on the Viking images revealed that secondary clusters are uncommon above this 2 km diameter limit.

The 250 new Viking 1:1.25 million sub-quad mosaics were used as the data base in this study to map crater density in the diameter of 2-10 km. Only the Mercator zone ±30° were included as crater populations at higher latitudes are apparently altered by erosional and depositional processes (4). Within the ±30° latitude zone, new coverage is available for roughly 25 percent of the area so far. The majority of mosaicking has been done in 54 subquadrangles of Mars Quadranges MC 8, 9, 10, 16, 17, and 18 where coverage is roughly 50 percent. In general the crater density data collected for these areas agree well with those of Condit (3). The increased statistical strength, however, allows much better definition of geologic unit boundaries. A comparison of the new crater density maps with detailed volcanic flow maps, generated by Schaber et al., (5) for the Tharsis volcanic region, reveals good agreement between the two data sets. Several major contacts, for instance in the central part of MC 17 between cratered plains and ridged plains material, have been redefined. This redefinition of unit boundaries, along with the increased statistical strength of the data, will permit a much clearer and concise classification of relative age for geologic units on the whole-wide planet of Mars.

References

(1) Soderblom, L. A., Condit, C. D., West, R. A., Herman, B. M., and Kreidler, T. J., 1974, Martian planetwide crater distribution: Implications for geologic history and surface processes: Icarus, 22, 239.

(2) Scott, D. H., and Condit, C. D., 1977, Correlations: Martian stratigraphy and crater density: NASA TM X-3511, p. 56.

(3) Condit, C. D., 1978, Distribution and relations of 4-10 km diameter craters to global geologic units on Mars, Icarus (in press).

(4) Soderblom, L. A., Kreidler, T. J., and Masursky, H., 1973, Latitudinal distribution of a debris mantle on the martian surface: J. Geophys. Res. 78, 4117-4122.

(5) Schaber, G. G., Horstman, K. C., and Dial, A. L., 1978, The distribution and eruptive history of lava flow materials in the Tharsis region of Mars: Abs. 9th Lunar Sci. Conf. Houston, TX.

CRATER DENSITY DETERMINATION IN THE THARSIS REGION OF MARS. R.S. Saunders and Therese Gregory, Jet Propulsion Laboratory, Pasadena, CA 91103

As part of the continuing program to study the nature and origin of the Tharsis region of Mars (see R.J. Phillips, this volume) we are documenting the relative ages of the various surface types. The primary data source is Viking Orbiter images. All crater diameters are measured and recorded. Most pictures can be divided into geologically homogeneous areas. These areas are combined in various ways to display the data in either cumulative or incremental plots. The data are obtained using a Hewlett Package digitizer and are displayed with a plotter that is peripheral to the H-P programmable desk calculator. To date 800 pictures have been analyzed representing a large number of surface units.

Table 1 contains a selection of the data for some areas of the Tharsis region to give an idea of the data available. Many more regions have been reduced and are being tabulated for easy reference. The range of values of number of craters per 10^6 km^2 equal to or larger than one km diameter represents a weighting by the inverse of the square root of the number of craters. This is only one way to compare relative ages, but the method has the advantage that it can potentially be reduced to a single number.

Table 1

Surface	No. Craters	No. Craters $\geq$ 1 km/$10^6$$km^2$
Lava flows south of Arsia Mons	180	630-830
Arsia Mons flows (near summit)	26	275-480
Arsia Mons flows (Southern most)	157	790-1000
Plains south of Arsia flows	1383	2512-3160
Western Sinai Planum	436	1585-2140
Eastern Labyrinthus Noctis (Plateaus)	133	1200-2000
Eastern Labyrinthus Noctis (Canyon Floors)	26	250-500
Olympus Mons Scarp	26	16-80
Plains adjacent to Olympus Mons	128	20-63
Olympus Mons, Shield	33	40-110
Plains NE of Olympus	694	3470-4570
Fractured terrain N. of Olympus	699	1150-1660
E. of Ceraunius Fossae	214	690-1000

The Viking I landing site crater diameter-frequency distribution,
A. L. Dial, Jr., U. S. Geological Survey, Flagstaff, Arizona 86001.

The recent acquisition of very high resolution images (15m/line pair) of Mars by the Viking Orbiter Imaging Systems has made it possible to extend crater diameter frequency distributions to diameters 27 meters. New images of the Viking I landing site acquired during the extended mission by the Viking II Orbiter cameras from an altitude of 500 km (resolution 25m/line pair) allow crater frequency distributions to be measured for craters down to about 25 m diameter. High resolution images included in the crater counts cover an area of about 221 km^2 centered on the landing site. All of the craters counted appeared fresh and bowl-shaped, having raised rims. The lack of degraded forms suggests that this distribution represents the production function or complete accumulation since the surface was formed. A crater frequency distribution roll off between 25 m and 100 m (Fig 1) is observed which is typical of resolution "cut off;" although it is possible that some of the effect is real.

Craters in the size range between a few hundred meters and a few kilometers were counted on images acquired by Viking Orbiter I during Rev 20 (1). Three craters in the Viking I site area (Yorktown, Lexington, Bristol) are larger than 3 km in diameter exhibit fresh well-defined ejecta deposits. These craters are bowl-shaped, displaying sharp distinct rims, smooth bowls and rough floors (2). All the other craters counted were fresh and bowl-shaped, having raised rims and smooth appearing walls and floors. Flooded or filled craters, such as Clough crater were not counted (3).

In order to determine the crater size frequency distribution for craters in the size range from 1 to 20 km diameter, a larger region was studied with images of similar resolution (75 m-150m/line pair). A controlled mosaic of western part Chryse Planitia was used to obtain this data. Only craters larger than 1 km in diameter were counted in an area of 211900 km^2 surrounding the Viking landing site. Again, all craters appear fresh and pristine. Distinction was clear between the pristine craters and the few flooded or buried craters which were counted. No gradation in morphology was apparent.

Because all craters counted exhibit fresh morphologies with raised rims it is concluded that the population of craters counted from 25 m to 20 km diameter represents the complete average production function. Because the diameter frequency distribution of different size ranges join each other well within the statistics (1 Sigma error bars) of overlap regions, it is inferred that all the

three areas counted, although different in total area, represent a single surface age.

An important characteristic of the production function seen in Figure 1 is a sharp break in slope near a diameter of 1 km. Craters larger than 1 km show a cumulative slope of -1.0 to -1.5; small craters <1 km diameter display a steeper slope of -2.5 to -3.0. Shoemaker (4) noted a similar break in slope for lunar crater populations at 3 km diameter based on Ranger VII photography. He explained this break as the point where the production function for secondary craters exceeded primary production for craters smaller than this diameter. Similarly, Soderblom (5) predicted that the background secondary populations produced by primary impacts in the range of 1-50 km on Mars should exceed the production function of primaries near 1 km. Furthermore, those authors showed that the slopes of the production function should change from roughly -1.5 (estimated for bowl-shaped craters a few kilometers in diameter) from Mariner-9 data to a slope near -3.0. Results of this work support that interpretation. On the contrary, Neukum and Wise (6) suggested that the steep parts (-2.5 to -3.0 slope) of the standard curves at D<km are not due to an admixture of secondary craters, but represent the original primary production size-frequency distribution based on morphological criteria. In any case, the average production function seen in Figure 1 represents both primary and secondary crater populations.

References:

(1) Masursky, H., Boyce, J.M., Dial, A.L., Schaber, G.G., and Strobell, M.E., 1977, Classification and time of formation of martian channels based on Viking data. Jour. Geophys. Res. v.82, 4016-4038.

(2) U.S. Geological Survey, 1977, Atlas of Mars, Controlled mosaic of the Yorktown region of Mars, M250k 22/48 CMC I-1059.

(3) U.S. Geological Survey, 1977, Atlas of Mars, Controlled mosaic of the western part of the Chryse Planitia region of Mars, MlM 23/50 CMC I-1069.

(4) Shoemaker, E.M., 1965, Ranger VII, II, Experimenter's analysis and interpretations. Tech. Rep. 32-700, Jet Propulsion Lab. Pasadena, Calif.

(5) Soderblom, L.A., and Lebofsky, L.S., 1972, Technique for rapid determination of relative ages of the lunar areas from orbital photography. Jour. Geophys. Res. 77(2), 279-296.

(6) Neukum, G., and Wise, D.U., 1976, Mars: A standard crater curve and possible new time scale. Science, v.194, p. 1381-1387.

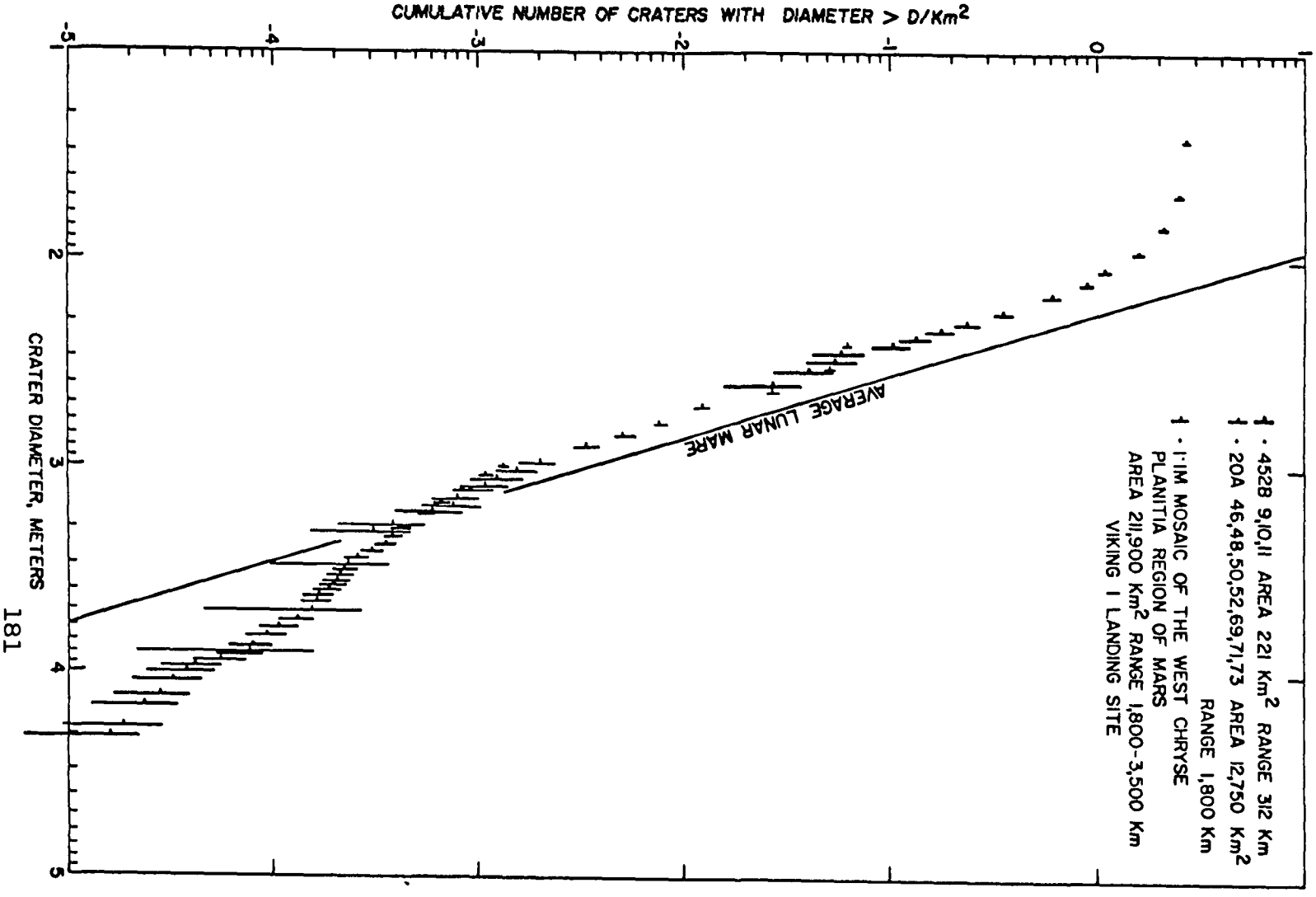

Figure 1. Composite of three crater-size frequency distribution curves for the Viking I landing site. Each curve pertains to a different area centered on the landing site corresponding to coverage available for a particular high, medium or low resolution and area range. Note the "roll over" of the curve at the 100 m diameter position probably due to resolution cut off.

Preliminary Study of North Tesihim Butte, Navajo County, Arizona, T. L. Burmeier, Department of Geology, State University of New York at Buffalo, Amherst, New York, and H. E. Holt, U. S. Geological Survey, Flagstaff, Arizona 86001.

Area of Study. North Tesihim Butte is a diatreme of Early Pliocene age located in the Hopi Buttes volcanic field in Northeastern Arizona at 35° 34' N and 110° 5' W. It is somewhat triangular in plan view, about one mile in length and stands 200 feet above the surrounding plain. Exposed at the base of the structure is a 60 foot sequence of lacustrine clay and siltstones. Overlying this unit is a 50 foot thick sequence of flat lying bedded tuffs, agglomerates and crudely bedded tuffs. Capping the structure are flows of alkali basalt with a gently domical topography.

Ultramafic Xenoliths. Numerous rounded black and green ultramafic xenoliths, up to eight inches in length, are contained in the basalt and tuff. These rocks consist mainly of mica-clinopyroxenite and to a lesser extent clinopyroxenites, hornblende pyroxenites, websterites and hornblendites. Petrographic examination of these inclusions reveal igneous textures, with a large percentage of these being cumulus textures. Amphibole, biotite and magnetite are intercumulus phases. Augtite is the cumulus phase, commonly subhedral in shape and often shows resorption along the grain boundaries. Poikilitic textures are common and extensively developed in some samples. Although the rocks exhibit cumulus textures it is not possible to say if they are cumulate rocks, that is, those derived from a layered igneous body.

Formation of North Tesihim Butte. Four separate basalt flows have been mapped at North Tesihim and several small dikes and a thin, three foot thick sill are intruded into these units. An intrusive tuff dike, 3400 feet long borders North Tesihim Butte. A very small intrusive tuff dike intrudes basalts in North Tesihim. It appears that a mixture of gas and basalt fragments was injected into pre-existing fractures in the bedrock forming these unusual features. Fluidization or the mobilization of particulate material by upward moving, high velocity gas is the mechanism suggested by a number of field investigators for the formation of diatremes (Shoemaker and others, 1962; McGetchin, 1968). The large deposits of pyroclastic ejecta, intrusive tuffs, rounded sedimentary blocks and rounded ultramafic xenoliths suggest fluidization played a major role in the formation of North Tesihim Butte.

References:

(1) Shoemaker, E.M., Roach, C.H., and Byers, F.M., Jr., 1962, Diatremes and Uranium Deposits in the Hopi Buttes, Arizona, Geol. Soc. Amer. Buddington Vol., p. 327-355.

(2) McGetchin, T. R., 1968, The Moses Rock Dike: geology, petrology and mode of emplacement of a kimberlite bearing breccia dike, San Juan County, Utah. Unpub. PhD thesis, California Institute of Technology.

Mosby Butte, A Volcanic Shield of the South-Central Snake River Plain, Idaho.

Paul W. Foster and John S. King, State University of New York at Buffalo, Amherst, New York 14226

Mosby Butte is a volcanic shield of Pleistocene-Holocene age located within the southwestern portion of the eastern Snake River Plain. The Butte encompasses an area of approximately 36.3 square kilometers and lies 50 kilometers northwest of American Falls and 7.9 kilometers east of the Great Rift System.

The Mosby Butte shield displays a typical low broad profile on its distal surfaces with a slope of 2°. Its vent area, with a slope of 12° rises about 36.6 meters above the local surface and is the most prominent topographic feature within a radius of 4.8 kilometers. This high relief vent is characteristic of a divergent group of shields located in the eastern Snake River Plain.

The Butte is composed of a locally unique Snake River Plain basalt characterized by abundant lath-shaped plagioclase phenocrysts which distinguishes this rock type in outcrop. Initial petrographic analysis indicates that the basalt contains 25% to 30% plagioclase phenocrysts as compared to the typical Snake River basalt which contains less than 10% plagioclase phenocrysts (Karlo and King, 1977).

Field relations indicate that Mosby Butte is flanked by eight vents from which lava flows erupted. All of these flows are younger than the Mosby flow as indicated by their overlap relations. Preliminary chemical data, based on the silica trend exhibited by a differentiating magma, applied to the observed overlap relationships suggests that the Wild Horse Corral flow whose vent is located to the southwest of Mosby Butte, is one of the youngest flows within the area.

Over 200 basalt samples were collected from Mosby Butte and the adjacent flows. Since Mosby Butte was the primary object of this study, it was imperative that representative samples of the entire flow be obtained. To accomplish this, three different traverse patterns were established with an average sampling interval of 460 meters. These patterns were as follows: (1) a circular pattern within the vent area, (2) a series of four radiating traverse lines from the vent area to the contact zone, and (3) a final traverse pattern conforming to the border of the entire contact zone. Sampling of the surrounding flows entailed a single traverse line which extended from the vent area to the respective contact zone with the Mosby Butte flow.

The present objectives of this study, in the process of being conducted, are to petrographically and chemically analyze these samples to determine if any variations exist within the Mosby Butte flow and, if so, whether they are related to obvious changes in slope of the shield. Further it will be determined whether any differences exist between this flow and the adjacent ones.

Reference:

Karlo, John F. and John S. King, 1977, Controls of Physical Properties of Snake River Plain Lavas on Surface Morphologies (Abs.), NASA Technical Memo #TM X-3511, p. 132-133.

Characteristics of Terrestrial Cinder Cone Fields, Mark Settle, Dept. of Geological Sciences, Brown University, Providence, RI 02912.

On the earth, cinder cones occur in two distinctive types of geological provinces. Cinder cones are found along the flanks and near the summits of large volcanoes such as Mauna Kea, Hawaii (i.e., volcano cone fields). In this geological setting cinder cones are commonly concentrated within radial or arcuate zones that are interpreted to be the surface expressions of major fractures within a volcano's edifice(1). Cinder cones also occur in relatively flat-lying volcanic terranes in association with extensive lava flow deposits as observed in the San Francisco volcanic field in Arizona (i.e., volcanic field cone fields). In this geological setting small subgroupings of cones may be locally aligned along a linear or arcuate lineament but the overall distribution of cones within volcanic fields appears to be random. Few comparative studies of the shape and distribution of cinder cones occurring in different cone fields have been conducted. As a result, the structure of terrestrial cinder cones has been largely inferred on the basis of observations of a few individual cones considered to be representative examples, such as Northeast Crater at Mt. Etna(2), and Sunset Crater within the San Francisco Mts. volcanic field(3,4). Similarly, although past investigators have commented upon the relationship between regional structural trends and the areal distribution of cinder cones within specific volcanic provinces, the physical factors governing the emplacement of cinder cone fields are not well understood.

The distribution and relative sizes (volumes) of the youngest cinder cones within a field reflect the configuration of the subsurface system of conduits and dikes connecting the regional surface to a magma reservoir at depth. Future studies of extraterrestrial volcanic provinces may employ observations of the morphology, structure and spatial distribution of cinder cones on other planetary surfaces in order to (a) identify areas of current or recent volcanic activity, (b) determine crustal structural trends within specific volcanic provinces, (c) classify different types of volcanic terranes, (d) classify different stages in the evolution of a specific type of volcanic province on another planet, or (e) investigate the nature of explosive volcanic processes operating on other planets. In order to conduct interplanetary comparisons of cinder cones, however, it is first necessary to better understand the morphological and morphometric characteristics of terrestrial cinder cones. This abstract partially summarizes the results of a larger study(5) that seeks to: (a) characterize the dimensions of terrestrial cinder cones found within volcano cone fields and volcanic field cone fields in a statistical manner, (b) determine if the shape or spatial distribution of cinder cones is uniquely correlated with the type of volcanic province in which cinder cone fields occur, and (c) explore the mechanics of the volcanic processes responsible for the construction of cinder cone fields.

Three volcano cone fields, Mauna Kea (Hawaii), Mt. Etna (Italy) and Kilimanjaro (Tanzania), and three volcanic field cone fields, the San Francisco Mtn. field (Arizona), the Paricutin region (Mexico), and the Nunivak Island field (Alaska) were investigated. The location, basal diameter, and, if pos-

sible, the height of each cinder cone within these fields were measured. The majority of cinder cones within the six cone fields examined in this study were constructed over a roughly contemporaneous period of time extending over the past 0.3-0.5 million years. The average areal density of cinder cones within these fields ranges from 3-11 cones/100 km^2. However, maximum values of local cone density are consistently greater within the volcano cone fields (4-5 cones/10 km^2) in which cinder cones are preferentially aligned or clustered. Cinder cones constructed on the flanks of volcanoes have been emplaced over an elevation range of 2500-4000 m, whereas cones formed within relatively flat-lying volcanic fields were emplaced over a 300-1100 m elevation range. The advent of coneforming eruptions does not appear to signal a unique stage in the evolution of these volcanic provinces. In some cases the eruptive phase in which cinder cones are constructed represents one stage in the continuous evolution of a province (e.g., Mt. Etna and Nunivak Island cone fields), whereas in other provinces coneforming eruptions represent a recommencement of basaltic volcanic activity after a period in which more silicic magmas were erupted (e.g., San Francisco Mtn. and Paricutin cone fields).

Median values of cone basal diameter determined within individual cone fields range from 369 m for the Mt. Etna cone field to 1158 m for the San Francisco cone field. Although the range of values of cone diameter measured within the two types of volcanic provinces are similar, the median basal diameter of cinder cones occurring within each of the three volcanic fields is consistently greater than the median diameter of cinder cones found within each of the three cone fields situated on the flanks of volcanoes.

Median values of cone height determined within individual cone fields range from 53 m for the Nunivak Island cone field to 111 m for the San Francisco cone field. These two cinder cone fields have both been emplaced within a volcanic field, indicating that there are no systematic differences between the average height of cinder cones occurring within volcanic fields and those cones constructed on the flanks of volcanoes. Differences in the average height of cinder cones found in two or more cone fields cannot be attributed to the relative ages of the cone fields due to limited understanding of: (a) the variability of coneforming eruptions, (b) the morphometric response of cinder cones to various erosive processes, and (c) the nature of the weathering environment within a cinder cone field throughout its geologic history.

Median values of cone separation distance range from 780 m for the Mt. Etna cone field to 1547 m for the Nunivak Island cone field. In general, the average spacing between cones occurring within volcanic fields is greater than the average spacing between cones formed upon the flanks of volcanoes, although median cone separation distances determined for the Paricutin and Kilimanjaro cone fields are not significantly different.

On the basis of the data compiled for the six cone fields examined in this study there appears to be a general association between the type of volcanic province in which a cinder cone field forms and the average separation distance and basal diameter of cones within the field. Cinder cone fields emplaced within relatively flat-lying volcanic fields are characterized by larger basal diameters and greater separation distances, on average, than cone fields formed on the flanks of volcanoes.

Fracture zones exposed upon the flanks of volcanoes commonly extend over a wide range of elevation, encompassing several km of vertical topographic relief. There are numerous examples of eruptive activity moving to higher or lower elevations along such fracture zones in response to variations in magmatic pressure during a particular eruption (e.g., 1971 Mt. Etna eruption{6}). The comparatively smaller average size and spacing of cinder cones formed upon the flanks of volcanoes may reflect the relative ease with which eruptive activity can shift to higher or lower elevations along a continuous fracture zone in response to variations in magmatic pressure during periods of active eruption. Such a mechanism would tend to limit the growth of individual cones and result in smaller separation distances between cones, as is observed within volcano cone fields.

In contrast, volcanic fields are typically crosscut by multiple sets of fractures and consequently the mechanical force required to initiate an eruption at an adjacent site would generally be greater than the effort required in the case of a continuous fracture zone. In addition regional topographic variations across volcanic fields are typically much less than elevation differences encountered along the flanks of a volcano. Consequently, variations in subsurface overburden pressure, which might serve to redirect the flow of magma to the surface, are small. Under these circumstances, variations in magmatic pressure during a period of eruptive activity would more likely be accommodated by variations in the rate at which magma is discharged at the surface rather than by a change in the site of eruptive activity. Such a mechanism is consistent with observations of larger cone diameter and greater cone spacing, on average, within volcanic field cone fields.

References

1. Nakamura, K. (1977) Jour. Volc. Geotherm. Res. 2, p. 1-16.
2. McGetchin, T. R., Settle, M. and Chouet, B. (1974) Jour. Geophys. Res. 79, p. 3257-3272.
3. Colton, H. S. (1967) The basaltic cinder cones and lava flows of the San Francisco Mountain volcanic field, Revised ed., Museum of Northern Arizona, Flagstaff, AZ.
4. Hodges, C. A. (1962) Plateau 35, p. 15-35.
5. Settle, M. (1978) The structure and emplacement of cinder cone fields, manuscript in preparation.
6. Walker, G. P. L. (1973) Phil. Trans. Roy. Soc. London A, 274, p. 177-179.

Evolution of Composite Volcanoes, C.A. Wood, Dept. of Geol. Sci., Brown Univ., Providence, RI 02912.

Composite volcanoes (stratovolcanoes), composed of layer deposits of pyroclastics and lavas, are the characteristic volcanic landform of subducting plate margins, and are the most common type of large volcano on Earth. A few composite cones have been studied in sufficient detail to provide general models of their structure and eruptive behavior. In this note, observations of eruption characteristics and chemical/petrologic trends for a number of composite cones are synthesized with newly determined measurements of cone morphometry to document statistically the evolution of composite volcanoes. Attention is also devoted to comparisons with cinder cones.

Morphometry. Ideally, to determine a volcano's original or constructional geometry, only uneroded isolated cones should be considered, yet the eruptive process itself erodes flanks and modifies vents. Practically, the availability of topographic and bathymetric maps determines which volcanoes can be measured, and only those with obvious calderas or other major modifications are excluded. Preliminary data for 26 composite cones (most historically active) from the circum-Pacific belt document systematic relations in cone morphometry (Figs. 1-3) and, since the cones are at different stages of growth, evolutionary development. The cones have the following ranges of dimensions (km): basal width (Wco) = 0.6-22; summit crater width (Wcr) = 0.03 -0.7; crater depth (Dcr) = 0.03-0.45; cone height (Hco) = 0.2-3. Within these limits there are consistent linear variations that suggest geometrically uniform cone growth:

$$Hco = 0.122Wco + 0.45 \quad (n=17;\ r=.95) \qquad (1)$$

$$Wcr = 0.027Wco + 0.048 \quad (n=14;\ r=.91) \qquad (2)$$

$$Wcr = 0.222Hco - 0.054 \quad (n=18;\ r=.92) \qquad (3)$$

There is no significant (r=.62) relation between Dcr and Wcr. Volcano volume can be calculated from the equation for for a cone ($V = (\pi/3)(Wco/2)^2(Hco)$) or, if either Hco or Wco is unknown, incorporating (1):

$$V = (Wco)^2(0.032Wco + 0.117) \qquad (4)$$

or

$$V = Hco(17.6(Hco)^2 - 15.88Hco + 3.58) \qquad (5)$$

The sampled cones range in volume from 0.17 - 395 km^3. Equation (1) may be used to estimate original heights of composite cones that have collapsed to form calderas. For example, Wco for Mt. Somma, the ancestrial cone of Vesuvius, is ~15 km, implying a pre-collapse height of ~2.3 km, in good accord with the estimate of 2.5 km based on extrapolation of slopes (Imbo, 1965).

Eruption Characteristics. Eruptions of composite volcanoes are variable in style, duration and frequency. Many composite cones exhibit nearly continuous mild strombolian activity, occasionally interrupted by paroxysmal eruptions of greater violence and volume (e.g. Izalco, Fuego, Stromboli). Average mild strombolian explosions at Stromboli produce about .065-.005 m^3 of ejecta once every ~11 minutes (Chouet et al., 1974). At this rate ~10^{11} explosions (1.7 x 10^6 yrs) would be necessary to construct Izalco, a cone that was born in

1770. Thus, mild strombolian activity is insignificant in cone construction. Intense explosive activity ejecting both juvenile and non-juvenile material (vulcanian eruptions) often results in small pyroclastic flows (Fuego, Cerro Negro, Ngauruhoe) with volumes of 10^6-10^7 m^3 (Rose et al., 1973). More important changes in cone morphology occur during cataclysmic peléean eruptions (Pelée, Santa Maria) that produce rapidly moving nuée ardentes often associated with formation of viscous domes (Roobol and Smith, 1975). The least frequent, but most extreme, style of activity is plinian eruption with caldera collapse and voluminous (km^3) pumice deposition (Krakatoa, Coseguinia). Although caldera formation often appears to be the final stage of volcano evolution, in numerous cases activity resumes with a new cone rebuilting the destroyed summit (Vesuvius, Fuji).

Growth Rates. Only a few composite volcanoes have formed within recent centuries and generally few details are known for these eruptions. Since Izalco was born in 1770 a cone of ~0.76 km^3 has been constructed, for an average eruption rate of 0.41 km^3/100 yrs, although during periods of intense activity (e.g. 1951-56) the rate is 10X greater. In the first 121 yrs of its lifetime Cerro Negro has averaged 0.15 km^3/100 yrs. For comparison, Kilauea, a basaltic shield volcano, has averaged 1.2 km^3/100 yrs for the 51 years ending in 1969. Repose Periods for 20 Central American composite cones listed by Mooser et al. (1958) are most frequently 1 year or less; this statistic is biased, however, by separate entries for frequent mild eruptions at Fuego and Izalco which really represent persistent activity. Excluding repose periods < 1 yr yields a median value of 7 yrs. Longer repose periods are common (the longest being 302 yrs for Santa Ana); a number of volcanoes regularly active in the 17th century (Chichigalpa, Santa Clara, El Viego) have been in repose nearly 400 yrs, while other cones with no historic activity have erupted unexpectedly (Santa Maria, Ceboruca, Acatenango). Suggestions that repose periods increase with volcano age (e.g. Rose et al., 1977) are reasonable, but no systematic relation has been found between repose period and Wco/(~age).

Petrological/Chemical Trends. Although some composite volcanoes are formed of basaltic materials (Fuji, Fuego, Izalco) the majority are predominately andesitic (Kuno, 1969). Only a few volcanoes have been sampled at close enough intervals to document systematic changes in composition, although gross changes (e.g. andesitic cone with dacitic summit plug) are well known. Generally, tephra and lavas become more silicic as a volcano grows - this is well documented for Santa Maria and the Myoko volcanoes. At Santa Maria SiO_2 increases up a 240 m section from 52% to 57% at the summit and there are associated systematic increases in K_2O, Rb, and Zr, and decreases in MgO and CaO (Rose et al., 1977). These variations were interpreted in terms of increasing crystal fractionation due to cone growth and increasingly long repose periods. Similar chemical changes are observed in the Myoko cones, with petrology changing with eruption stage (cone growth=pyr-ol-bst, pyr and; caldera formation=hbd-pyr-and; inner cone/dome growth=hbd-and, dacite) (Hayatsu, 1977). The rate of SiO_2 enrichment at Izalco and Cerro Negro is ~2.2% ΔSiO_2/100 yrs, but at Santa Maria is only 0.03%/100 yrs. The differences between these two rates may reflect the periods represented (200 yrs vs. ~ 13000 yrs, respectively), but faster crystal settling in the more mafic magma

of Cerro Negro and Izalco (49-54% SiO_2 vs. 52-57% for Santa Maria) may also be important. Major evolutionary changes within composite cone magma chambers are indicated by (1) the common occurrence of hornblende in late stage eruptions (Shastina, Santa Maria, Myoko) (2) late stage satellitic eruptions of basaltic magmas while acidic eruptions continue at the summit (Shasta, Rainier; Condie and Swenson, 1973), and (3) the common construction of composite cones on basaltic shield volcanoes (Thielson, Makalia).

Comparison of Composite and Cinder Cones. Crowe (1977) proposed that cinder cones (CC), strengthened by dike and sill emplacement, evolve into large composite volcanoes (CV); Mt. McLoughlin, a strongly dissected CV in the Cascades built around a large CC (Harris, 1976) is a possible example. Although the two types of cones may be related there are a number of significant differences. Cinder cones are considerably smaller (ave. Wco = 0.9 km) than CVs (8 km), and have different Wco-Wcr-Hco relations (Porter, 1972). The principal morphological difference is in Wcr: for Wco = 2km, Wcr = 0.8 km for CCs vs. 0.1 km for CVs. The wide craters of CCs are principally formed by ballistic deposition of of ash (McGetchin et al., 1974) and are enlarged by slumping and reaming (Wood, 1977). Composite volcano craters are eruption vents built by lava flows and pyroclastic deposits with enlargement due to collapse and reaming during violent eruptions (Vesuvius, 1906). Commonly, CCs are basaltic whereas CVs are typically andesitic. Complete eruptive histories for CCs range from a few days (Monte Nuovo) to ~10 yrs (Paricutin), whereas CVs have lifetimes of 10^4-10^5 yrs. CCs typically result from a single eruptive episode with later volcanism producing new cones with separation distances of a few km (Settle, this vol.). CVs are built by thousands of eruptions from the same vent with prolonged repose periods being common. Strombolian eruptions dominate CC growth, whereas all styles of eruptions occur in CV activity, and frequently a succession of CVs form with only slight vent offsets (Vesuvius). These differences indicate that if CCs and CVs are related, fundamental changes in morphometry and eruption style occur at Wco ~ 2 km.

B. Chouet et al (1974) JGR 79, 4961. K.Condie and D. Swenson (1973) BV 37, 205. B. Crowe (1978) Abst. Composite Volc. Symp , GSA, Tempe. K. Hayatsu (1977) Mem. Fac. Sci. Kyoto Univ. Ser. Geol. Min. 43, 1. G. Imbo (1965) Cat. Active Volc., Pt. 18-Italy. H Kuno (1969) Ore. Dept. Geol. Min. Ind. Bull 65, 185. F Mooser et al (1958) Cat. Active Volc , Pt. 6-Central Am. S. Porter (1972) BGSA 83, 3607 M Roobol and A Smith (1975) BV 39, 214. W. Rose et al (1973) BV 37, 365. W. Rose et al (1977) J. Geol 85, 63. C. Wood (1977) Abst. IASPEI-IAVCEI Assembly, Durham, 241.

Morphometry of Composite Volcanoes

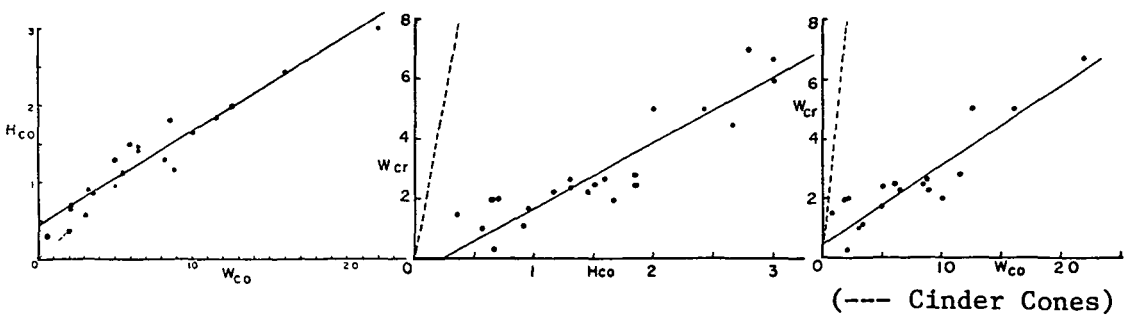

(--- Cinder Cones)

Planetary Studies of Kilauea Volcano, Hawaii: The Role of Satellitic Shields in Kilauea's Recent Evolution, Daniel Dzurisin, Hawaiian Volcano Observatory, Hawaii Volcanoes National Park, HI 96718

The Tharsis volcanoes on Mars are generally considered on the basis of gross morphology to be basaltic shields similar in most respects except size to the younger shields of the Hawaiian Islands. Nevertheless, the unambiguous identification on Mars of many structures and landforms characteristic of Hawaiian shield volcanoes (e.g., rift zones, pit craters, vent structures) has proved difficult. A primary goal of the ongoing planetary research program at the Hawaiian Volcano Observatory is therefore the identification and study of terrestrial forms and processes of potential relevance to martian volcanism.

Carr and others (1977) have recently argued for the existence of rift zones on Arsia and Pavonis Mons on Mars. They cite as evidence the non-random distribution of pits on both volcanoes, and note that the implied rift direction is consistent with a line of low domes, inferred to be satellitic shields, on the floor of Arsia Mons caldera. Satellitic shields are a common feature at Kilauea Volcano on Hawaii, and their importance in the growth of Kilauea may not previously have been fully appreciated.

Perhaps the most direct Hawaiian analog of the Arsia Mons domes is a low shield built around Halemaumau, the central collapse crater within Kilauea Caldera which has served as the principal summit vent during historic time. Halemaumau shield is roughly 2 km in diameter and attains a maximum height of 20 meters. It is composed primarily of thin, prehistoric basalt flows emplaced during overflows of recurrent Halemaumau lava lakes.

More prominent satellitic shields exist along both Kilauea Rift zones. Two have formed during the twentieth century: Mauna Ulu on the East Rift (1969-1974) and Mauna Iki on the Southwest Rift (1919-1920). The Mauna Ulu and Mauna Iki eruptions contributed roughly 40% and 60% of the total volume of material erupted from the East and Southwest rifts, respectively, since 1800 A.D. Other prominent satellitic shields include Thurston, Kane Nui O Hamo, and Heiheiahulu shields along Kilauea's East Rift zone (Table 1). Field work in progress is intended to assess the roles played by these shields in the late prehistoric growth of Kilauea. Preliminary results suggest that shield-building eruptions have been an important, and perhaps primary, mode of growth at Kilauea during the past few centuries. If martian and Hawaiian eruption rates have been comparable, more detailed studies of Hawaiian satellitic shields may shed light on the eruptive mechanisms responsible for construction of

similar features on Mars.

TABLE 1

Kilauea Shield-Forming Eruptions

Site	Date	Approximate Shield Diameter (km)	Shield Height (m)
Mauna Ulu	1969-1974	2.0	120
Mauna Iki	1919-1920	1.6	30
Heiheiahulu	~1750	1.3	70
Halemaumau	Mostly prehistoric	2.0	20
Kane Nui O Hamo	Prehistoric	1.2	75
Thurston/ Kilauea Iki	Prehistoric	3.4	65

Reference: Carr, M. H., R. Greeley, K. R. Blasius, J. E. Guest, J. B. Murray, 1977, Some Martian Volcanic Features as Viewed From the Viking Orbiters, J. Geophys. Res., 82, 3985-4015.

Subglacial Volcanism - Terrestrial Landforms and Implications for Planetary Geology, Carlton C. Allen, Department of Planetary Sciences, University of Arizona, Tucson, AZ 85721

Volcanic eruptions beneath glacial ice have produced large-scale landforms highly diagnostic of their source. The recognition of such features on a planetary surface should provide important information about the history of volatiles on that body.

Recent eruptions of the Icelandic volcanoes Katla and Grimsvötn, located beneath the Mýrdals and Vatna glaciers, respectively, have resulted in devastating meltwater floods, or jokulhlaups. These are thought to be the largest floods presently occurring on earth, with recorded peak flow rates in excess of 10^5 m^3/sec (1). The sandur plains of Iceland's southern coast are scarred by jokulhlaup channels which clearly exhibit morphologies associated with chatastrophic flooding.

Central-vent eruptions beneath Pleistocene ice sheets resulted in flat-topped, steep-sided forms called table mountains (2). These have been recognized in Iceland and British Columbia. The form of the table mountains is controlled by the glacial ice, which provides both lateral confinement and rapid cooling of the lava. The subaerial equivalents to the Icelandic table mountains are shield volcanoes.

Pleistocene subglacial fissure eruptions within Iceland's central graben produced narrow, serrated ridges directly above or adjacent to the fissures. The ridges, and the table mountains as well, are composed of palagonite and pillow lavas in a combination known locally as the móberg formation (3). The material is the subglacially-erupted equivalent of basalt. Subaerial fissure eruptions in Iceland produce widespread lava flows, such as the Laki flows of 1783.

This suite of features is highly diagnostic of the interaction of volcanism with ice layers hundreds of meters thick, and the features will remain long after the ice has melted. They are large enough to be identifiable at Landsat resolution, approximately 80 meters. If such features exist on other bodies in the solar system they may be similarly recognizable on spacecraft imagery. Their recognition would provide strong evidence of the past existence of massive layers of surface or subsurface ice, even if that ice had subsequently been lost.

A search for these indications of the interactions of ice and volcanism on the planet Mars is presently underway, using Mariner IX and Viking orbital imagery. All Viking

frames taken from a range of less than 20,000 kilometers have been examined, and the locations of flood channels, flat-topped mountains and ridges noted. Innumerable flood channels have been noted by other investigators (4). This study has also located several dozen features, scattered across the planet, which resemble the Icelandic ridges and table mountains. Detailed examination of regional geologic relationships will be undertaken in an attempt to establish which, if any, of these features are the result of Martian volcano-ice interactions. Positive results should be very useful in understanding the history of water and other volatiles on Mars.

Water ice is a major planet-forming compound at temperatures such as those thought to have existed during planetary formation beyond the orbit of Mars. The Galilean satellites of Jupiter are of particular interest in this regard. These lunar-sized bodies are thought to have been formed with varying compliments of water ice, in accord with their distances from a radiant proto-Jupiter (5). Each is thought to be differentiated, with a rocky core and an ice mantle. The ice layers on Callisto and Ganymede are thought to be hundreds of kilometers thick, while that of Europa is probably less than a few tens of kilometers and on Io the ice, if ever present, may have been completely lost (6). Icelandic-type features indicative of volcano-ice interactions may have been formed on these satellites, and may be visible at the surface on Io and Europa. If so, they will provide important constraints on models of the thermal histories of these bodies. Predicted resolution of the Voyager imaging systems indicate that features of the scale occurring in Iceland should be clearly recognizable on Io and marginally so on Europa.

References:
(1) Thorarinsson, Bulletin Volcanologique 23, 45, (1960).
(2) Van Bemmelen & Rutten, Tablemountains of Northern Iceland, E.J. Brill, Leiden, (1955).
(3) Kjartansson, in On the Geology and Geophysics of Iceland, Excursion guide No. A2, 21st International Geological Congress, Reykjavík, (1960).
(4) Masursky, et.al., Journal of Geophysical Research 82, 4016, (1977).
(5) Pollack & Reynolds, Icarus 21, 248, (1974).
(6) Consolmagno & Lewis, in Jupiter (T.A. Gehrels, ed.), University of Arizona Press, Tucson, 1035, (1976).

Multi-Stage Evolution of the Tharsis Shield Volcanoes of Mars from Viking Orbiter Imagery, L. S. Crumpler,[1] Jayne C. Aubele,[1] and Wolfgang E. Elston, Dept. of Geology, Univ. of N. Mex., Albuquerque, N.M. 87131

Arsia Mons, Pavonis Mons and Ascreus Mons seem to have had similar histories. Arsia Mons developed by (1) construction of a main shield volcano, (2) eruptions from parasitic centers on the northeast and southwest flanks, (3) volcano-tectonic subsidence of the summit and formation of concentric fractures and grabens, possibly by evacuation of an underlying magma chamber during parasitic eruptions, and (4) continued volcanism along a fissure or rift that bisects the main shield, resulting in flooding of the floor of the volcano-tectonic depression and inundation of the northeast and southwest flanks of the main shield by voluminous lavas from parasitic shields. Pavonis Mons developed to stage (3) and Ascreus Mons to stage (2). This interpretation is supported by frequency-diameter distributions for superimposed impact craters between 0.1 and 3.0 km. Impact craters can be distinguished from volcanic pit craters by raised rims, ejecta blankets, and random distribution. Volcanic pit craters lack raised rims and ejecta blankets and tend to be aligned on ring fractures and associated with the heads of late flows and with rille-like channels.

Counts of impact craters on the three volcanoes (Figs. 1a,b,c) indicate that the main shields are of about the same age but that differences in impact-crater densities for different areas on the flanks of Pavonis and Ascreus Mons may be real (Figs. 1b,c). The crater frequency for the floor of the summit depression of Arsia Mons is much lower than for the flanks of its shield. Impact crater frequencies on lava flows from a zone of volcanic pits on the south flank of Arsia Mons vary (Fig. 2). Some

flows were impacted as densely as the main shield, others as little as the floors of the summit depressions of Arsia Mons and Pavonis Mons (Fig. 3). The summit depressions may have formed as a result of collapse during late-stage outbreaks from flank pits.

[1]Current address: Lunar and Planetary Lab., Univ. of Ariz., Tucson, Az. 85721

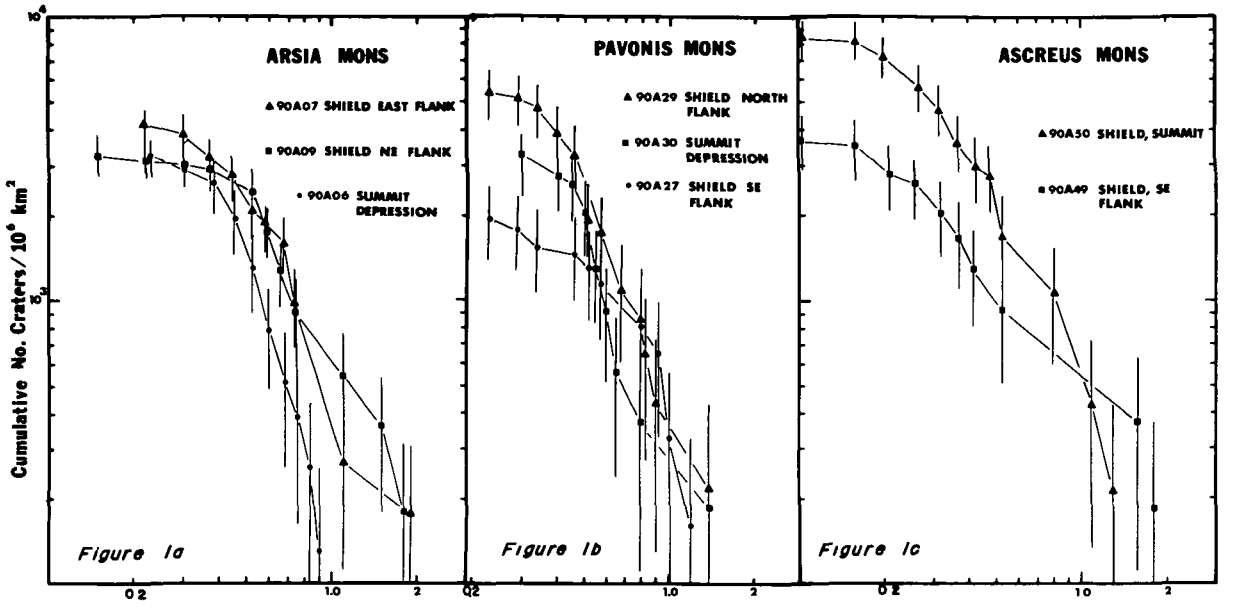

Note: Numbers refer to Viking Orbiter Images

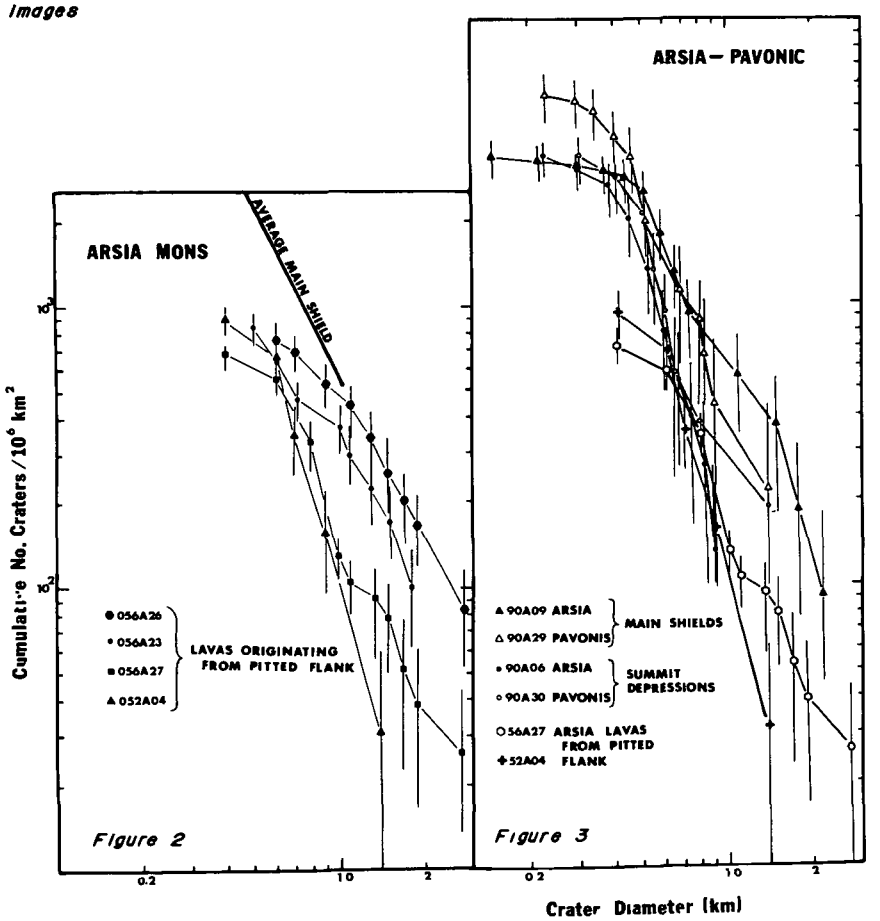

RHEOLOGIC PROPERTIES OF ARSIA MONS LAVAS. Plescia, Jeffrey B. and R. S. Saunders, Jet Propulsion Laboratory, Pasadena, CA 91103

Investigation of the lava flows on the southern flank of Arsia Mons was undertaken to determine both the lava rheologic properties and to generate a model to predict slopes from lava flow morphology.

Radar data from Goldstone were used to construct a topographic map of the section between 14°S and 21°S across the southern flank of the volcano (see Saunders et al., this volume). Using this map slopes were calculated for regions in which clearly defined lava flows were present. Using the Model of Hulme (1974), yield stresses and several other parameters were calculated for these flows. The equations that relate surface morphology to rheologic properties are:

$$S_y = 2g\rho\alpha^2 w_b \quad (1)$$

$$\log \eta = 0.266p - 8.06 \quad (2)$$

$$W = w/2w_b \quad (3)$$

$$\mathcal{F} = 2W^{5/2}/15 + W^2/2 + W/6 - 1/20 \quad (4)$$

where $$\mathcal{F} = F\eta(g\rho)^3 d^4/S_y^4 \quad (5)$$

where S_y = yield stress, g = gravitational acceleration, ρ = density of lava, α = slope, w_b = width of bank, w = lava flow width, η = viscosity, p = percent silica, W and F are dimensionless parameters.

The above equations were applied to the flows where radar deduced slopes were available. The results are listed in Table 1. It can be seen that the silica contents are in the low 50% range, which corresponds to basalt-andesite. These results are compatible with those of Hulme (1976) for a flow on Olympus Mons. These results are, however, not compatible with those of Carr et al, (1977). Carr et al, (1977) cite $\mathcal{F}$ values for smaller flows which are an order of magnitude lower than those calculated here. This suggests that the same assumptions regarding bank formation do not apply over a large range of flow widths.

The viscosity and yield stress of a magma is not only related to the silica content but also depends on extrusion temperature, water and other volatile content and amount of Fe. Considering the multitude of variables and the state of theoretical modeling the method of Hulme (1974) at least provides a way to intercompare Martian lavas.

Using the data generated in this study an average yield stress was computed and assumed to be constant over the surface of Arsia Mons.

Measurements of flow width and bank width were made and a slope calculated from those measurements for areas outside of radar control. Slopes calculated from the model range from ≤ 0.02 at 600km to > 0.06 at less than 100 km from the center of the caldera. Carr et al, (1977) recognized 3 zones influenced by lava. Zone 1 corresponds to a slope of 0.04, Zone 2 to a slope of 0.03 and Zone 3 to a slope of 0.02. Slopes calculated in this model are an order of magnitude larger than those reported by Carr et al, (1977).

Flow widths were measured and plotted against distance from the caldera, figure 1. It can be seen that for the region surveyed there is a roughly linear relation between the two. The equation best representing the distribution is $y = 7.31(x) + 114.26$ with an r^2 of 0.68. A wide scatter can be expected as many measurements will reflect local topographic control. The plot does somewhat support the dependence of flow width on slope, and hence adds confidence to the extrapolation of slopes from morphologic properties. However, the relation between effusion rate and length also needs to be factored in. For example, Walker (1973) reports a log-log relation between flow length and average rate of effusion. Our next stage of work will incorporate this additional information.

Reference:

Carr, M.H., Greeley, R., Blasius, K.R., Guest, J.E., and Murray, J.B., 1977, Some Martian Volcanic Features as Viewed from the Viking Orbiters: J. Geophys. Res., Vol. 82, p. 3985-4015.

Hulme, G., 1974, The Interpretation of Lava Flow Morphology: Geophys. J.R. Astr. Soc., Vol. 39, pp. 361-383.

Hulme, G., 1976, The Determination of the Rheological Properties and Effusion Rate of an Olympus Mons Lava: Icarnus, Vol. 27, pp. 207-213.

Walker, G.P.L., 1973, Lengths of Lava Flows: Phil. Trans. R. Soc. Lond. A., Vol. 274, p. 107-118.

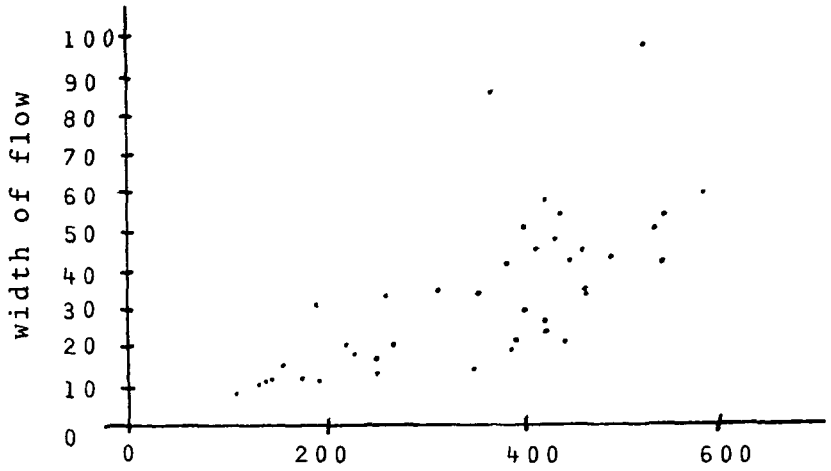

Figure 1. Flow width in km. plotted plotted versus distance from center of caldera.

Table 1

w	w_b	α	log Sy	SiO_2%	W	F	η
12.5 ± 1.3	4.3 ± 1.2	0.05	4.38	52.23	1.45	1.05	6.8×10^5
13.1 ± 2.1	4.9 ± 1.7	0.04	4.24	51.15	1.34	0.90	3.5×10^5
19.4 ± 1.6	7.3 ± 0.9	0.04	4.41	52.46	1.33	0.88	7.8×10^5
25.3 ± 2.8	8.5 ± 1.8	0.03	4.23	51.08	1.49	1.11	3.4×10^5
41.7 ±11.4	16.4 ± 4.1	0.03	4.52	53.31	1.27	0.08	1.3×10^6
20.1 ±10.3	7.2 ± 2.1	0.03	4.16	50.54	1.40	0.98	2.4×10^5

Parameters for several flows calculated from the equations of Hulme (1974). w = flow width in dm., wb = bank width in km., α = slope, Sy = yield stress, W and F are dimensionless parameters, and η = viscosity.

Small Volcanic Constructs in the Chryse Planitia Region of Mars, Ronald Greeley and Eilene Theilig, Dept. of Geology and Center for Meteorite Studies, Arizona State Univ., Tempe AZ 85281.

Viking Orbiter pictures taken of the southeastern part of Chryse Planitia during the search for the landing site for Viking Lander I reveal a field of about 60 small, low-profile structures tentatively identified as volcanic constructs, termed low shields. The field is in a major channel of probable fluvial origin. The low shields appear to post-date both the channel and the plains on which they occur, making them among the youngest features on the planet, as well as the smallest vent-type feature observed thus far. The low shields average 2.5 km across; many have summit knobs - giving a two-part profile - and summit craters. Three possible terrestrial analogs are suggested: 1) eroded vent structures, similar to the Hopi Buttes of Arizona (B. Lucchitta, pers. comm.), 2) low-profile basaltic shields of the type in the Snake River Plain, Idaho, and 3) 'pseudocraters,' which are structures in Iceland that formed when lavas poured over water-saturated ground and formed hundreds of small phreatic constructs. In size and morphology, the martian features most closely resemble the low shields of Idaho; however, in morphology and relation to local geology (the martian low shields are in an area where ground water and/or permafrost may have occurred), the Icelandic features may be the best analog.

Tharsis Province of Mars: Deformational History and Fault Sequence, D.U. Wise, M.P. Golombek, G.E. McGill, Dept. Geology, U. Mass., Amherst, MA 01003.

The Tharsis Province of Mars is characterized by a variety of topographic, volcanic, and structural features. However, the unifying element of the Province and the one that also defines its outer limits is a system of semiradial faults, crater chains, grabens, and structurally controlled canyons. These faults and fractures reach some of their most complex development at the north and south ends of the Province where detailed geologic mapping and crater counts on small geologic units provide partial control on the sequence of faulting and deformation.

Crater counts were performed on areas which by visual inspection seem to have a homogeneous crater fabric. (Homogeneous in this context does not necessarily imply a single age but rather a seemingly uniform density of craters within comparable size ranges. Where several ages of superimposed units were present, the bumps in the crater curves caused by survivor craters were used to read different ages for the different units.) Cumulative plots of the crater data were prepared and the data were projected to a 1 km value by the standard curve of Neukum and Wise (1976). A crater density number was read for the cumulative frequency of craters >1 km diameter per 10^6 km^2. This number is used here as an indicator of relative age for the various events.

The Thaumasia Quadrangle, at the south end of the Province, has a large arcuate scarp more or less concentric to Solis Planum and marking the southward disappearance of the topographic rise of Tharsis. This scarp, here informally called the Thaumasia lobe of Tharsis, seems to be formed by one or more monoclinal crustal flexures with the north or Tharsis side uplifted. The frontal edge of this upwarp apparently tilts and distorts at least one crater in the manner of a southward moving lobe. Four distinct fault events can be recognized in the lobe; all seem to die out southward. (A) An E-W system of subdued lineaments and diffuse scarps appears in terrains yielding crater numbers of 70,000 or older. An ENE (B) and a NE (C) fault system both appear much fresher than (A). Members of these fracture systems have distinct graben-like cross-sections and well defined fault scarps. At their intersections the ENE (B) set appears older than the NE (C) set. A fourth fault system is approximately radial to Solis Planum and the lobe (McGill, in press). This fanning system (D) cuts all the older fractures of the lobe and extends into the foreland to the south of the lobe. It is generally covered by a number of plains units with crater numbers between 3000 and 5000, but these units locally are slightly disturbed by minor late reactivation of the fanning system. The lobe front is locally covered by units as young as crater number 7500, thus placing a minimum limit on its age. The fanning fracture system (D) is for the most part older than the 7500 unit but a few fractures of that system cut the unit. This fault system also appears to curve through an angle of 10-15 degrees of strike as it passes through the edge of the lobe suggesting a warping of the stress trajectories by local stress fields or anisotropy near the lobe front. Gross bending of the faults seems to be precluded by the lack of similar curvature in some of the older faults in the same area. Other fault systems show an abrupt change in strike at the

front of the lobe. The precise dating of these intermediate age Thaumasia faults is still under investigation with the Viking imagery systems but (B) and (C) seem to be associated with units of crater number approximately 20,000. Some of the later fanning faults may be associated with gross southward motion of the Syria-Sinai-Solis Planae block in the time span 7,500-10,000. These dates are derived from intensely faulted areas on the Claritis Fossae anticline and by some of the older areas of ridges on Melas Dorsa.

At the northern end of Tharsis, the Tempe Fossae fault system postdates the Lunae Planum of crater number 15,000-20,000 with most of the fault activity at 10,000-15,000 (Wise, in press). As in the southern areas, hints of older fault systems appear to be associated with the pre-20,000 units which define what is now the Mareotis Fossae. Later northern events included the development of early lava flows yielding crater numbers of 5,000-10,000 in the region west of Alba. (These Viking numbers for the western Alba apron are considerably older than those derived from the Mariner imagery). The central cone of Alba yields a crater number of 2000 and predates some of the intense fault development which splays around the cone. Locally some of the faulted surfaces surrounding the central cone yield numbers as low as 1000.

Throughout the Tharsis Province, particularly in the vicinity of the great volcanoes, local intense faulting disrupted small areas in the time span of crater numbers 2,000-4,000. Examples include the Ceraunius Fossae and the faulted region 500 km SE of Olympus Mons. Other lesser fault movements as young as crater number 800 occurred on the westward extensions of Noctis Labrinthus, most likely as minor extensions of the Valles Marineris zone.

The history of the Tharsis movements suggests an early development of Province-wide semiradial fault systems in the time span represented by crater numbers 10,000-30,000. This was probably a time of doming of the region and of extensive resurfacing of many areas. Some of the resurfacing materials, as for instance those of Lunae Planum, probably included extensive volcanic flows. During the span of crater numbers 5,000-10,000 many of the more local stress systems began to break the region into smaller blocks and sub-provinces, such as the Tempe Plateau and the Syria-Sinai-Solis region. Most of the faults of these regions are now covered with plains materials of crater numbers 2,000-4,000, showing only local, minor signs of fault reactivation. In the vicinity of the great volcanoes, small, local areas were intensely faulted in the time span 4,000-1,000. These areas are now largely covered with the young volcanic edifices, their debris aprons, or young eolian plains. The great young volcanoes may be the most impressive topographic features of the Province but it is the older semiradial fracture systems which provide the tectonic glue to hold the Tharsis Province into a single entity.

McGill, G.E., (in press), Geologic map and text for the Thaumasia quadrangle of Mars, U.S. Geol. Survey.

Neukum, G., and Wise, D.U., 1976, Mars: A standard crater curve and possible new time scale, Science, v. 194, n. 4272, p. 1381-1387.

Wise, D.U., (in press), Geologic map and text for the Arcadia quadrangle of Mars, U.S. Geol. Survey.

Possible Intrusive Activity on Mars, P. Schultz, Lunar and Planetary Inst., 3303 NASA Road 1, Houston, TX 77058.

On the moon, impact craters provide significant conduits for volcanism via shock-induced fractures that immediately or -- more typically -- subsequently tap magma reservoirs. Such craters are clearly represented by unbreached mare-filled and floor-fractured craters. On Mars, lava-filled and floor-fractured craters also exist and prompt analogies with the eruptive style and sequence for the Moon (1, 2). Significant morphologic differences between many lunar and martain craters, however, suggest that other additional processes may be operative.

The global coverage of Mars by Mariner 9 revealed over 70 floor-fractured craters that exhibited concentrations both along the boundary between the plains of the norther hemisphere and in association with Vallis Marineris and the complexly modified terrains eastward (1). The placement along the margins of the plains is similar to the distribution of lunar floor-fractured craters (3). The identification of basalt-filled craters with exposed central peaks and structurally modified rims on Mars strengthen the analogy with the sequence of volcanic modification of lunar impact craters. Specifically, a tabular intrusion of fluid magma accumulates beneath the old impact crater within the zone of extensive fracturing and brecciation. As the intrusion grows, the old crater floor is uplifted as much as 2km, carrying with it the central peak complex. Lavas first extrude along the margins of the floor into an annular graben created by floor uplift. If extensive eruptions occur, the old, uplifted floor may be capped by a relatively thin (less than 1km) layer of lavas. The same sequence appears to be applicable to numerous martian craters, thereby strengthening the similiarity in their early eruptive histories.

However, martian craters with fractures exhibit several significant differences. From Mariner 9 imagery, both the polygonal fracture patterns and the development of wide moats between the floor and wall are more than twice as common as on the Moon. The characteristic concentric fracture pattern on the Moon probably reflects the effects of floor uplift with multiple periods of subsidence. The characteristic polygonal fracture pattern and wide moat on Mars is also probably related to intrusions beneath the crater floor but may be influenced by the presence of accumulated water/ice. Several examples exhibit little evidence for floor movement yet wide, deep discontinuous moats have developed. In several instances, such moats have been breached with braided channels extending down the rim. Such features could be understood if intrusions along ring fractures -- in a manner analogous to lunar floor-fractured craters -- melt and evaporate water/ice-rich sediments.

Magma/ice interactions may be expressed on a grand scale along Vallis Marineris where entire sections of craters are commonly removed with extensive and closely spaced polygonal fracturing of the old crater floor. Here, the polygonal fracture pattern probably develops as lateral fluid release removes support from beneath the crater and portions of the floor collapse or are rafted. Regardless of the specific style of modification, many of these craters correspond to sites of localized endogenism related to the development of Vallis Marineris and the chaotic terrains eastward. This is illustrated by clustering along the equatorial canyon system but exclusion along the north-trending channels that empty in Chryse(1).

The possible significance of endogenically modified craters on Mars are listed below.

1. Modification may provide a very sensitive indicator for the timing and distribution of the internal thermal activity of Mars.

2. The interaction between mafic intrusions and trapped water/ice deposits within craters may result in hydrothermally altered samples as interpreted from Viking Lander results (4).

3. The evolution of the old cratered uplands may provide significant clues to the evolution of terrestrial impact craters and in particular the ore concentrations in volcanically modified impact craters such as the Sudbury structure as interpreted by French (5).

REFERENCES

1. Schultz, P. H., W. D. Manley, Jr., and F. E. Ingerson, Comparison of lunar and martian crater floors (abs.) EOS 54, 1127, 1973.

2. Schultz, P. H., Floor-fractured craters on the Moon, Mars, and Mercury, NASA - TMX - 3364, 1976.

3. Schultz, P. H., Floor-fractured lunar craters. The Moon 15, 241-273, 1976.

4. Toulmin, P., A. K. Baird, B. C. Clark, K. Keil, H. J. Rose, Jr., R. P. Christian, P. H. Evans, and W. C. Kelliher, Geochemical and mineralogical interpretations of the Viking inorganic chemical results. Jour. Geophys. Res. 82, 4625-4634, 1977.

5. French, B., Possible relations between meteorite impact and igneous petrogenesis, as indicated by the Sudbury Structure, Ontario, Canada. Bull. Volcan. 34-2, 466-517, 1970.

The Yardangs at Rogers Playa, California, A. Wesley Ward, Department of Geological Sciences, University of Washington, Seattle, Washington 98195, John F. McCauley, U.S. Geological Survey, Flagstaff, Arizona 86001, Maurice J. Grolier, U.S. Geological Survey, Flagstaff, Arizona 86001

A series of wind-streamlined hills or yardangs occurs along the northeastern edge of Rogers Playa, Edwards Air Force Base, California. The yardangs, first described by Blackwelder (1934), are up to 8 m high, 300 m long, and spaced about 50 m apart. They have been sculptured by the wind in the strandline deposits of pluvial Lake Thompson, the ancestral Rogers Lake, which consist of loosely cemented quartz and alkali-feldspar sands and fine gravels in a matrix of clays. Granule ripples with grains up to 1 cm and lengths up to 10 m occur in the yardang troughs.

These yardangs show moderate to good aerodynamic shapes marred only by gullying of the flanks produced by infrequent rain storms. The yardangs have length versus width ratios which range from 16 to 1 to 2 to 1, with most forms at approximately 3 to 1 (this 3 to 1 ratio is also common to drumlins and streamlined fluvial features from the Channeled Scablands of Washington State). This tendency of Rogers Playa yardangs towards a common length versus width ratio may indicate that, even with episodic water erosion, these yardangs are in dynamic equilibrium with the wind. Yardang development probably was initiated by wind erosion of interfluves between the incised channels of small ephemeral streams entering Rogers Lake. The yardangs are shaped primarily by strong regional westerly and southwesterly winds. Deflation or aerodynamic plucking of loose grains on the yardangs themselves appears to be an important process in developing and maintaining their overall streamlined shape. Variations in nose geometry appear to be related to position in the yardang

cluster. Monitoring of the wind flow with a hot wire anemometer indicates acceleration near the bow, fall-off of velocity at the beam, and reacceleration near the stern. Comparisons of pictures in 1932, 1975, and 1977 suggest an average erosion rate on the yardangs of 2 cm per year at the bow and <1 cm per year laterally.

Reference

Blackwelder, Eliot, 1934, Yardangs: Geol. Soc. America Bull., v. 45, p. 159-166.

GARNET HILL EOLIAN STUDIES. R. S. Saunders and W. A. Hunter, Jet Propulsion Laboratory, Pasadena, CA. 91103

Garnet Hill, a few miles due north of Palm Springs, California is providing a remarkable natural laboratory for studies of transport and erosion by wind-borne sand. The small hill is an upwarped block of Pleistocene and Pliocene bouldery conglomerates. The boulders that have weathered out of the conglomerates display an intensity of pits, flutes, and grooves that is matched by few other localities. Detailed description of this process is found in Sharp (1949, 1964).

The purpose of the present studies is to extend earlier work in the area by Sharp and develop a better understanding of eolion transport and erosion. The source of the abrasive sand in the area is primarily the Whitewater River that drains the eastern end of the San Bernardino Mountains. This mountain stream descends more than 10,000 feet in a little over 10 miles carrying angular debris from the granitic rocks over which it flows. These coarse angular sands are then transported by strong winds that blow up through the San Gorgonio Pass. The sand is transported for at most four miles before it reaches Garnet Hill.

The current studies involve:

1. Documentation of the nature of wind erosion on Garnet Hill. The morphology of wind carved features are noted (pits, flutes, grooves) and their position and orientation and the lithology and orientation of the rock face is recorded. To date 80 stations have been studied. These include only those that appear not to have moved from their original position. Preliminary analysis of the directional data show that all ventifacted boulders formed in a wind regime consistent with the current wind (figure).

2. Samples have been taken along the outwash plain of the Whitewater river from the base of the mountains to points well past Garnet Hill. The purpose of these samples is to study the evolution of the sand population from an immature grus-like sand under conditions of eolian transport.

3. The rate of sand transport in sand driving winds is being measured. Many weeks of wind velocity records have been taken in the study area and are presently being analyzed and correlated with longer term records of the Palm Springs Airport five miles to the southeast. The Airport records cannot be used directly since they are just inside the wind shadow of the San Jacinto Mountains.

4. The wind test plot that was operated by R. P. Sharp for more than fifteen years until it was washed out by floods in 1969 has been re-established. This is a rather simple long-term experiment that seeks to determine rates of erosion on natural and manmade rock materials. We are attempting to relate actual sand flux measured or calculated from the wind

records to the rates of erosion.

The goal of these field studies is to help relate theoretical and laboratory work to wind abrasion under natural conditions. This will lead to a better evaluation of the importance and improve our ability to identify these processes on other planets with atmospheres, particularly Mars and Venus.

References

Sharp, R. P., 1949, Pleistocene Ventifacts East of the Big Horn Mountains, Wyoming: Jour. of Geology, Vol. 57, pp. 175-195.

Sharp, R. P., 1964, Wind-driven Sand in Coachella Valley, California: Bull. Geol. Soc. Am., Vol. 75, pp. 785-804.

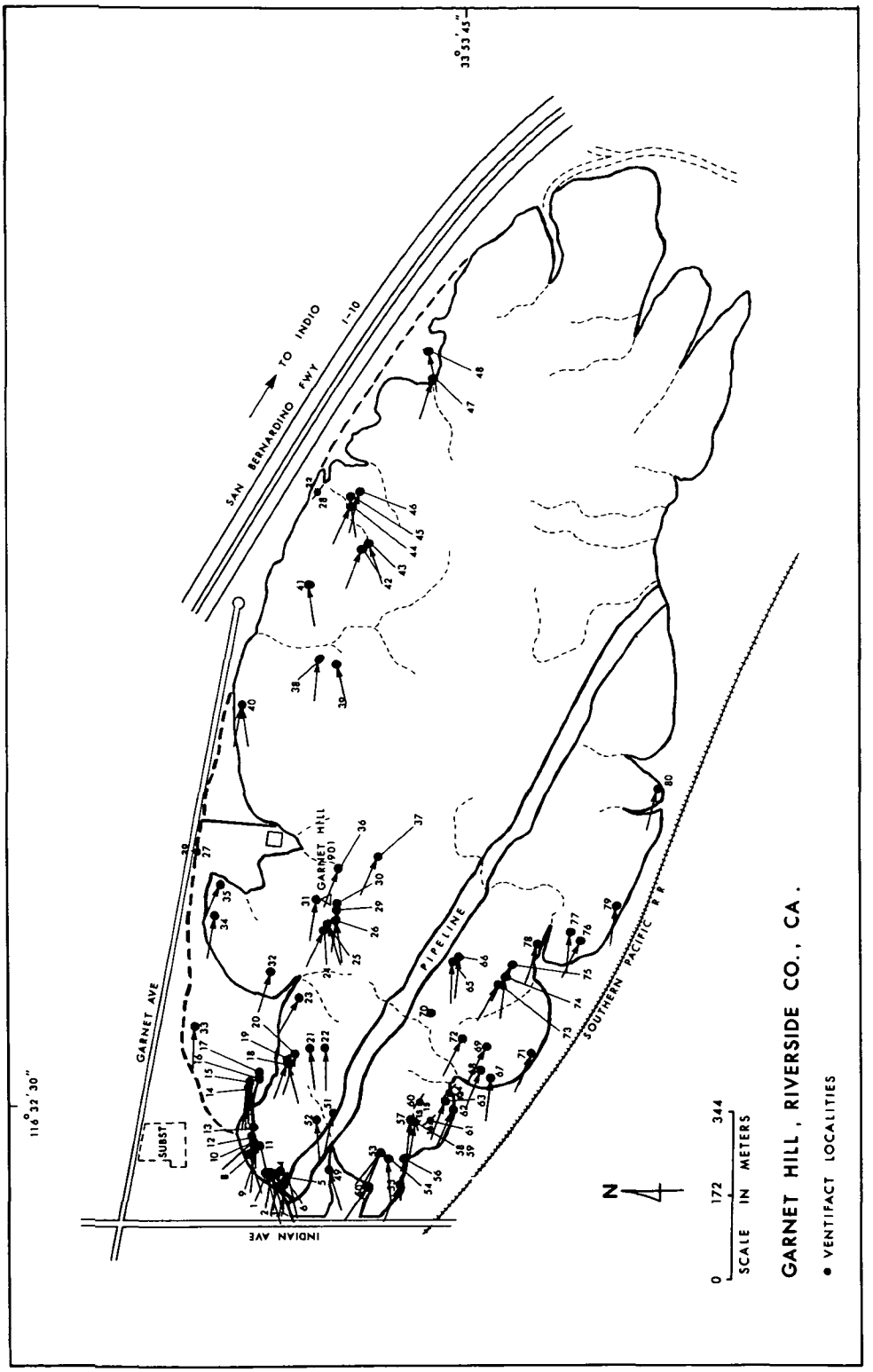
116°32'30"
33°33'45"
GARNET AVE
INDIAN AVE
SUBST
SAN BERNARDINO FWY
TO INDIO
I-10
GARNET HILL
PIPELINE
SOUTHERN PACIFIC R R
N
0
172
344
SCALE IN METERS
GARNET HILL, RIVERSIDE CO., CA.
• VENTIFACT LOCALITIES

Planetary Studies of Kilauea Volcano, Hawaii: Wind Action in the Kau Desert, Daniel Dzurisin, Hawaiian Volcano Observatory, Hawaii Volcanoes National Park, HI 96718

The Kau Desert on the island of Hawaii is a 350 km^2 wedge-shaped area bounded by the summit region of Kilauea Volcano on the northeast, the Kaoiki fault zone on the northwest, and Hawaii's coastline on the southeast. The area is cut by Kilauea's Southwest Rift Zone and by the southwestward extension of the Hilina fault system. Surface exposures consist primarily of thin basalt flows ranging in age from prehistoric to very young (December, 1974), and bedded accumulations of pyroclastic debris (primarily ash) produced by phreatic eruptions of Kilauea, the most recent in 1790 and 1924 A.D. Mean annual rainfall varies from roughly 130 cm/yr near the summit (1247 m elevation) to less than 30 cm/yr at the coast. Areas of intermediate to high elevation are occasionally subject to local torrential rains. High evaporation and percolation rates combine to inhibit vegetation growth in most areas. Prevailing tradewinds typically blow from the northeast at 15-35 km/hr, although short-duration winds in excess of 50 km/hr are not uncommon. Sub-freezing temperatures may occur for a few nights per year in the highest portions of the desert. The setting in a dynamic volcanic environment, easy accessibility, relatively unidirectional winds, and availability of wind-transportable fine materials in the form of primary ash and basalt-derived weathering products combine to make the Kau Desert a favorable site for planet-related studies of eolian processes.

Field work to date has been directed toward identifying major zones of deflation and accumulation, specifying the source and character of windblown materials, and describing the more prominent landforms and surface features produced by wind action. Five gradational zones have been mapped based on the degree and character of surface disturbance by wind. Zone A consists of a continuous deposit of 1790 and 1924 A.D. pyroclastic debris beginning at the rim of Kilauea Caldera and thinning southwestward. This deposit is locally mantled by thin basalt flows produced during the September, 1971 eruption along the upper Southwest Rift Zone. The pyroclastic blanket has suffered widespread fluvial erosion by ephemeral streams fed by occasional heavy rains, but nowhere has erosion proceeded to bedrock. Its surface is well-armored by pebbles and small cobbles embedded in a crust of fine-grained material a few millimeters thick.

Zone B is characterized by occasional surface exposures of basalt excavated by streams and wind, surrounded by primary pyroclastic deposits. The continuous surface crust of Zone A becomes patchy here, and wind erosion has therefore been relatively more effective than in Zone A. Roughly 1 cm has been removed

from the windward faces of some exposed boulders, presumably through abrasion by saltating sand-sized particles. Zone C consists of occasional remnants of primary, bedded pyroclastic materials generally occurring in swales on a primarily bedrock surface littered with small pebbles from the pyroclastic unit. The pahoehoe surface in Zone D has been completely stripped of primary pyroclastic materials, but exhibits wind-blown accumulations of ash and both glass and lithic fragments derived from weathering of nearby basalt flows. Finally, Zone E is an area of accumulation completely engulfed by wind-blown fine materials from the Kilauea summit region. An active field of poorly-formed dunes is currently migrating southwestward through sparse to moderate vegetation. Farther to the south of Kilauea Caldera, Zone E is characterized by marginal dunes 2-10 m high and enclosed, flat-lying deposits 0-2 m thick. In plan view, the contact between Zones D and E in this area consists of a series of lobes with snouts pointing northeastward into the prevailing tradewinds. Blowouts along dune crests indicate continuing movement of material locally, although much of the area has been stabilized by vegetation.

These observations suggest that large shield volcanoes on Mars may have been a significant source for wind-blown material in the form of primary ash and secondary weathering products derived from lava flows. Continuing work at Kilauea is intended to evaluate the relative importance of abrasion and accumulation in the production of large wind streaks on pahoehoe lavas south of Kilauea Caldera, and to better quantify the time-averaged rate of production of ash by Kilauea Volcano.

Field Studies of Sand-ridge Dunes in Central Australia and Northern Arizona. Carol S. Breed, U.S. Geological Survey, Flagstaff, AZ 86001 and William J. Breed, Museum of Northern Arizona, Flagstaff, AZ 86001

About half the total area of sand seas on Earth is occupied by dunes of the linear type, yet the wind processes that produce this type of dune are incompletely understood. Unlike barchanoid dunes, which are transverse to effective winds, linear dunes grow "longitudinally" along an axis that is parallel to the direction of the effective wind. Also unlike transverse or barchanoid dunes, linear dunes have slopes of approximately equal steepness on both sides of a long ridge, and they are either straight or irregularly sinuous in plan. Their lengths (measured in a downwind direction) are characteristically many times greater than their widths (measured cross-wind).

Theories of the origin and development of linear dunes are numerous, reflecting the high ratio of ideas to data (1,3,4,8,9,10,11, 12,13,15,18,19). Some workers propose that linear dunes are deposited in zones of low velocity between parallel, horizontal helical vortices which they believe develop in unimodal winds that blow along the interdune corridors (7,8,11). Other workers propose that linear dunes grow in a direction parallel to the resultant vector of opposing winds (1,3,4,13). The question of wind regime is complicated by the general acceptance of the "seif," a sinuous, sharp-crested linear dune, as typical of the entire "longitudinal" genre. Far more common, in deserts throughout the Southern Hemisphere, are dunes known as "sand-ridges." Sand-ridges are linear dunes that are extremely straight in plan view and have length-to-width ratios commonly in excess of 75:1.

Studies of internal structures, which usually preserve evidence of the processes that form dunes, have until recently been reported only for linear dunes of the "seif" variety, in the Wadi Zallaf, Libya (13), although a few photographs of seif dunes in southeastern Saudi Arabia are shown by Glennie (9). However, as long ago as 1950 W. A. Price (16) suggested that the seif dunes typical of North African deserts are distinctly different than the sand-ridge dunes typical of Central Australia. Morphological differences that would support Price's view were recently observed among linear dunes compared on Landsat pictures of various deserts on Earth. Field studies were than undertaken in Central Australia to obtain evidence of the internal structures and grain-size distributions in linear dunes at the type sand-ridge locality described by Madigan (14).

A consistent finding of the field investigations was that the internal structures of the observed sand-ridge dunes are mainly medium-scale, thin cross-beds or cross-laminae with dips commonly less than 20°. These layers occur in tabular and wedge-shaped sets bounded by planar erosion surfaces. The surfaces bounding the sets are commonly nearly horizontal. Steeply cross-cutting erosion surfaces, found in seif dunes in Libya (and thus generally thought to be typical of all "longitudinal" dunes) are rare. Furthermore, the sand-ridge dunes do not end in slip-faces but rather taper to a single layer of eolian sand on the desert floor.

Additional studies since 1975 of linear dunes in northeast Arizona have revealed internal structures that are more like those of the Australian sand-ridges than like those reported in seif dunes. The linear dunes in northern Arizona have morphologies (length, width, height, and spacing relationships) closely similar to those of the Australian sand-ridges, but are 6 times smaller in size. They extend over some 65,000 square kilometers (25,000 square miles) of the southern Colorado Plateau, including not only the Navajo and Hopi Indian Reservations of northeastern Arizona, but also parts of southern Utah, northwestern New Mexico, and southwestern Colorado (10,17). Thus they are the most widespread array of linear dunes in North America. Studies to date (3,4) suggest that the linear dunes in northern Arizona have formed in a wind regime that includes both seasonally bimodal components and a strong prevailing wind that coincides with, and reinforces, the resultant vector of the seasonally opposing winds. The axis of linear dune growth on the Moenkopi Plateau, Arizona closely coincides with the N62°E resultant direction of all effective winds recorded at Winslow.

Observations of changes in slipface orientations on an active segment of a linear dune on the Moenkopi Plateau indicates a seasonal shift of slipfaces from the north to the south slopes. However, strong prevailing winds from the west-southwest were also observed blowing sand directly east-northeastward along the length of the dune. At the time of this observation (June, 1977), neither the south nor the north slopes of the dune, though quite steep, included slipfaces. Rather, a series of small slipfaces had formed at intervals along the summit of the dune. These small avalanche slopes faced to the east-northeast, transverse to the long axis of the dune. It seems clear that the strong prevailing wind has a shepherding effect on the sand and is primarily responsible for the lengthwise growth and straight shape of the dune, whereas the seasonally shifting winds add to the height (and breadth) of the dune by depositing new layers of sand on one side of the dune during one season, and on the opposite side during another season. A strong prevailing wind, within a regime that has bimodal components, is characteristic of both northeastern Arizona and the Simpson Desert, Australia, where sand-ridge dunes are the predominant type (5). We postulate that the prevailing wind is an essential factor in the formation of very straight, very long linear dunes.

In contrast, the highly sinuous, relatively short seif dunes seem to form in regions subject to a simple bimodal wind regime, without the shepherding effect of a strong prevailing wind. The lengthwise growth of seif dunes in the Libyan locality was attributed by McKee and Tibbitts (13) to migration of sand in a direction parallel to the resultant vector of diurnally opposing winds, but the mechanism by which movement in that direction might take place was not explained. Recently, Haim Tsoar (18) has studied highly sinuous seif dunes in the Negev Desert, Israel. Tsoar (18) postulates that oblique components of two opposing winds provide sufficient impetus for lengthwise transport of sand along the dunes. A strong prevailing wind is thus apparently not necessary for the formation of this variety of linear dune.

The significance of these findings lies in the use of linear dune patterns to interpret wind patterns both in the less-known desert regions

on Earth and on Mars. On Viking pictures, linear dunes appear to be the second most abundant type, as they are on Earth. Proper interpretation of their patterns in relation to the martian wind regime requires that the numerous questions surrounding the origin and growth of linear dunes be answered. Further studies will include instrumentation of a test site on the Moenkopi Plateau, and wind-tunnel experiments to buiid linear dunes under various types of unimodal and bimodal wind regimes.

References

1. Bagnold, R. A., 1941, Methuen & Co., London, 265 p.
2. Breed, C. S., 1979, in McKee, E. D., (ed.), U.S. Geol. Survey Prof. Paper 1052 (in press).
3. Breed, C. S., and Breed, W. J., 1978, in El-Baz, Farouk (ed.), Scientific Results of the Apollo-Soyuz mission, NASA Spec. Paper (in press).
4. Breed, C. S., McCauley, J. F., Breed, W. J., Cotera, A. S., and McCauley, C. K., 1979, in Landscapes of Arizona: the geological story: Univ. of Arizona Press (in press).
5. Brookfield, Muriel, 1970, CSIRO, Div. of Land Res. Tech. Paper 30, 50 p.
6. Folk, R. L., 1968, Proc., v. 8, Rept. of the 23rd Internat'l Geol. Congr., Prague, Czechoslavakia, p. 9-32.
7. _____1971a, Sedimentology, v. 16, p. 5-54.
8. _____1971b, Geol. Soc. America Bull., v. 82, p. 3461-3468.
9. Glennie, K. W., 1970, Developments in Sedimentology 14, Elsevier Pub. Co., New York, 222 p.
10. Hack, J. T., 1941, Geogr. Rev., v. 31, no. 2, p. 240-263.
11. Hanna, S. R., 1969, Jour. Applied Meteorology, v. 8, p. 874-883.
12. King, D., 1960, Trans. Roy. Soc. South Australia, v. 83, p. 99-109.
13. McKee, E. D., and Tibbitts, G. C., Jr., 1964, Jour. Sed. Petrology, v. 34, no. 1, p. 5-17.
14. Madigan, C. T., 1946, Trans. Roy, Soc. South Australia, v. 70, no. 1, p. 45-63.
15. Melton, F. A., 1940, Jour. Geol., v. 48, no. 2, p. 113-145.
16. Price, W. A., 1950, Geogr. Rev., v. 40, no. 3, p. 462-465.
17. Stokes, W. L., 1964, Am. Jour. Sci., v. 262, p. 808-816.
18. Tsoar, Haim, 1978, Abs. for Planetary Geology Field Conf. on Aeolian Processes: NASA Tm-78,445 (addendum).
19. Twidale, C. R., 1972, Trans. Inst. British Geographers, v. 56, p. 77-109.

Eolian Erosion Studies. McCauley, John F., Breed, Carol. S., and Grolier, Maurice J., U.S. Geological Survey, Flagstaff, AZ 86001

The erosional effects of the wind in different types of deserts environments is becoming better understood as a result of recent field studies and laboratory work. These studies have provided new data on: a) the varieties of erosional land forms that can be produced by the wind, b) the kinds of rock that are susceptible to wind erosion and the role of inhomogenieties in these rocks on land form development, c) the relative roles of wind abrasion and deflation in landscape modification, and d) the conditions necessary for the wind to be an effective agent of removal and transport of fine debris. Two areas in the southwestern United States will be discussed here.

The area in the lee of the San Francisco Peaks and to the east of the Little Colorado River is the most windswept part of Arizona. Because of the presence of easily eroded rocks, a sparsity of vegetation and extremely strong prevailing winds, this area contains erosion features similar to those found in the even more arid parts of the world. The most prominent of the wind erosion forms are broad, roughly circular, flat floored deflation hollows, yardangs and wind fluted cliffs; small scale wind scour features are locally abundant (1).

The yardangs are cut into the relatively soft, reddish claystones and siltstones of the uppermost parts of the Chinle Formation (?), which when dry have loose, crumbly surfaces from which fine grains are readily picked up and carried away by deflation. Some of the former watercourses in the windward-facing cliffs in this area, which are now occupied by climbing dunes, have been modified into "U" shaped troughs

by a combination of abrasion and deflation of loose weathering detritus. Imperfectly shaped yardangs and irregular wind carved nubbins occur in the Navajo Sandstone, of Triassic age on the southern part of the Kaibito Plateau, northeast of Tuba City. This unit consists of now consolidated ancient dune sands which by virtue of earlier mechanical sorting have been pre-conditioned for subsequent eolian erosion.

Two years of drought in the western High Plains triggered on February 23, 1977, the greatest dust storm yet monitored by geostationary weather satellites (2). Two enormous dust plumes that spread over most of the southeastern states and out into the mid-Atlantic during a two day period, were tracked by the GOES-1 satellite. One of the point sources of the dust (the Clovis-Portales region, New Mexico) showed local wind scour effects as deep as 1 meter that produced myriads of small yardangs oriented parallel to the prevailing wind. This erosion was produced during less than a 12 hr period when northwesterly winds were blowing up to 100 km/hr. Lobate plumes of fine sand up to a meter thick and kilometers in length were deposited downwind from the scoured zones. The factors contributing to this event were: a) the prolonged western drought which dessicated the soils and exposed bedrock, b) the unusually strong winds but dry air associated with this first storm system to break through the prolonged Pacific atmospheric high. This high contributed to the drought by diverting storms northward during the winter of 1977, c) the local topography, particularly, the presence of the Llano Estacado escarpment which is about 200 meters high. This obstacle to the regional windflow undoubtedly created additional turbulence that contributed to the erosional capability of the wind on the flat erodible plains immediately downwind from the

escarpment, 3) the nature of the surficial units of Pleistocene or Holocene age exposed in the area. These consist of river sediments, old dunes and sand sheets that are especially susceptible to wind transport because of their prior eolian history, 3) land use practices such as the stripping away of the local range cover for farming on marginal sandy land.

Viking applications are: 1) lithology is a key factor in determining the intensity of wind erosion on the martian surface, only the weaker rocks with grains at or near the optimum for wind transport show intense erosion effects, 2) scarps locally intensify wind erosion and the redistribution of surface materials, 3) most of the wind erosion observed is probably episodic and the result of short-lived but intense windstorms that are widely spaced in time as on Earth.

References

1. Breed, C. S., McCauley, J. F., Breed, W. J., Cotera, A. S., and McCauley, C. K., Eolian landscapes, in Landscapes of Arizona, University of Arizona Press (Terah Smiley and others, eds.).

2. McCauley, J. F., Breed, C. S., and Grolier, M. J., The great U.S. dust storm of February 23-25, 1977: Geol. Soc. Am., 1977 Cordilleran Section Meeting, Tempe, AZ (abs.), in press.

Wind Tunnel and Field Experiments of Amboy Crater - A Terrestrial Analog to Martian Crater-Associated Dark Streaks, Iversen, J. D., Iowa State University, Ames, Iowa 50011 and Ronald Greeley, Arizona State University, Tempe, Arizona 85281.

Mariner 9 and Viking Orbiter images of the surface of Mars show streaks, associated with raised-rim craters, which are caused by strong surface winds and the resultant movement of surface particulate material. The Amboy lava field covers about 70 km^2 and is located in the Mojave desert of Southern California. The field contains a prominent cinder cone with an associated dark streak which is clearly visible from earth satellite, and thus is a possible terrestrial analog to some of the Martian streaks. The contrasting surface albedo is caused by sand which has been blown in from upwind alluvial sources to provide a thin light-colored cover over the much darker volcanic flow surface. The cinder cone is essentially a truncated cone which is 460m in diameter at the base and 240m at the top. The rim of the cratered cone is 75m higher in elevation than the immediate surrounding topography. The surrounding lava flow constitutes a relatively rough surface. The cinder cone is situated about 3500m downwind of the edge of the lava flow, which in turn lies downwind of a large relatively smooth alluvial plain.

Three 15m meteorological towers were erected at the Amboy crater site. One was placed 3300m upstream of the crater center in a relatively smooth-surfaced alluvial fan. The second was placed 400m upstream (but displaced laterally) in the middle of the relatively rough surfaced lava flow and the third tower was placed 600m downwind of the crater center. Of the 330 time periods for which data were taken over a 2-month period (Jan-Feb. 1976), 35 time-period runs were selected for final data reduction for which strong unidirectional winds were blowing from the northwest (streak direction).

Because the relative heights of the anemometers above the mean surface of the uneven terrain surrounding each tower are unknown, the wind velocity logarithmic profile is written including a zero-plane displacement height D as follows:

$$u = (u_*/0.4)\ \ln\ (\ (z+D)\ /z_o)$$

It is assumed in writing this equation, for the strong winds for which data were taken, that the atmosphere is neutral or very near neutral. Composite results for the 35 runs (total of about 100 hours) for which strong streak direction winds existed are listed in Table 1.

The average ratios of friction speed between towers for data taken simultaneously are $u_{*_2}/u_{*_1} = 1.2$ and $u_{*_3}/u_{*_1} = 2.1$. The rougher surface in the lava flow (Tower 2) resulted in a considerably larger roughness height and about a 20% larger surface

TABLE I Wind Speed Profile Data - Northwest Wind

Tower Number	z_o(m)	D(m)	u_*/U_∞ 15.24m	Number of runs
1	0.0017	-0.113	0.044	15
2	0.085	0.436	0.053	16
3	0.101	0	0.080	4

friction speed than in the smooth alluvial fan (Tower 1). The highest wind speeds and surface friction speeds, however, were recorded on Tower 3, located in the crater wake streak. In order to investigate in more detail the flow patterns near the crater a 1/1000 scale model of the crater area (representing an area 1200 x 3650m) was placed in the atmospheric boundary layer wind tunnel. The total fetch modeled in the wind tunnel upwind of the windward crater rim was 4500m (4.5m in the tunnel) for a fetch-length Reynolds number of $9(10)^6$. The wind tunnel turned out to be slightly rougher aerodynamically than the full scale topography (u_*/U at 15.24m at Tower 2 was 0.058, 9% higher than Tower 2 in the atmosphere). In addition to the Tower 2 and Tower 3 profile data, which compare well with the atmosphere, wind speed profiles were obtained at fifty additional locations near the crater. The wind tunnel and atmospheric velocity profiles for Towers 2 and 3 are shown in Figs. 1 and 2.

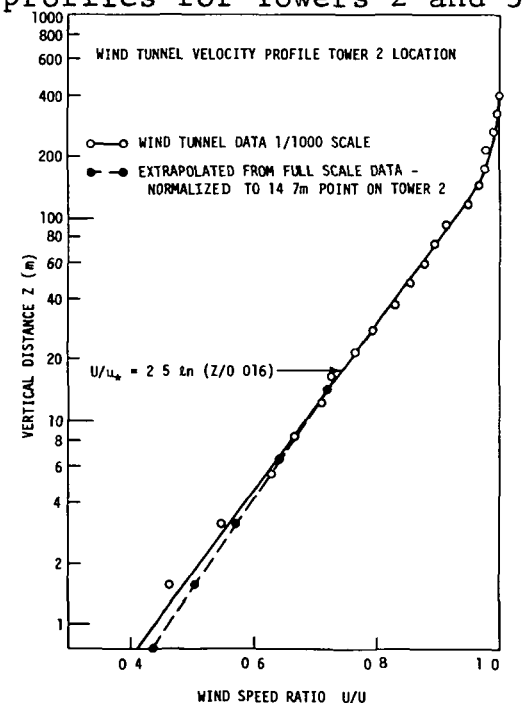

Fig. 1 Wind Tunnel - Field Data Comparison - Tower 2

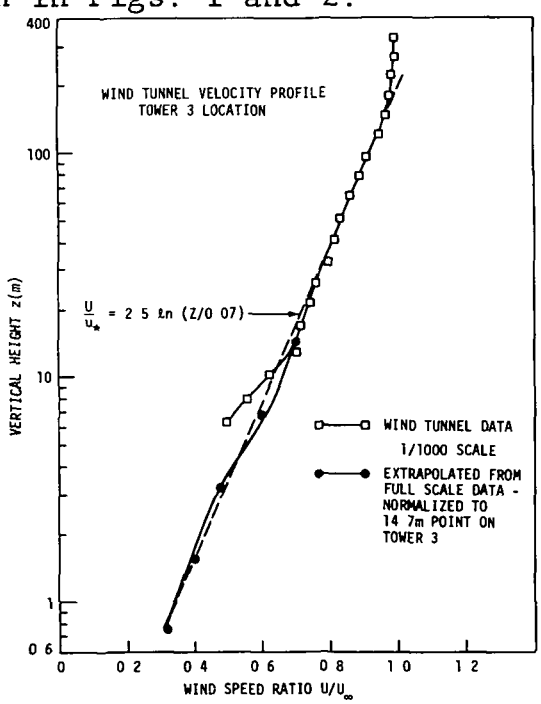

Fig. 2 Wind Tunnel - Field Data Comparison - Tower 3

The good agreement between wind tunnel and field experimental results is evidenced by the qualitative agreement of the profile shapes in Figs. 1 and 2 and by the quantitative results shown in Table II.

TABLE II Wind Tunnel-Field Comparison

		Tower 2	Tower 3
Roughness-Z_o(m)	Wind Tunnel	0.016	0.070
	Field	0.009	0.101
u_*/u_{15}	Wind Tunnel	0.058	0.074
	Field	0.053	0.080
u_{*3}/u_{*2}	Wind Tunnel	1.19	
	Field	1.73	

Results for the ratio of surface friction speed to tunnel free-stream speed for various locations near the crater are shown in Fig. 3. Of particular interest are the high values in the crater wake (locations 8A, 26A, Tower 3, 7A, 45A, 33A), the extremely high values on the lateral flanks of the cinder cone (11A, 12A), the low values just upwind (18A) and downwind (44A) of the cinder cone, and the relatively uniform values (average 0.040) everywhere else.

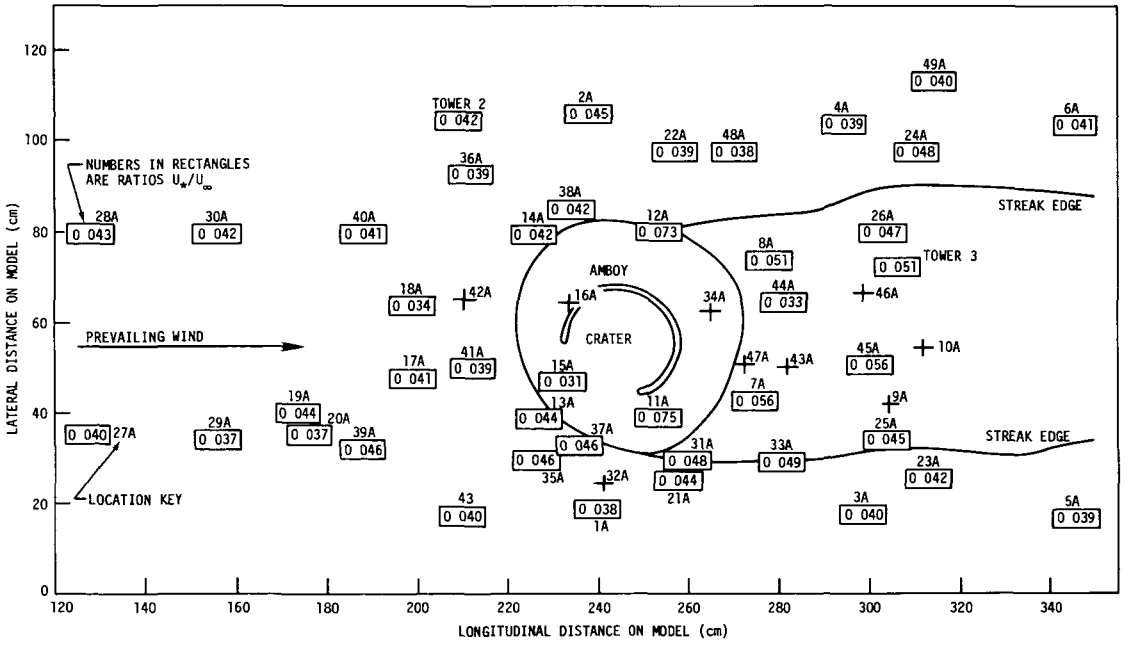

Fig. 3 Surface Friction Speed Distribution-Amboy Model Wind Tunnel Test

The wake streak characteristics are interpreted with the aid of the velocity data and with saltation experiments with glass spheres. Additional interesting wind caused albedo features of the Amboy lava flow exist in several places on the flow surface.

Surface Textures of Sand Sized Particles Abraded Under Earth and Martian Conditions, D. H. Krinsley and R. Greeley, Dept. of Geology, Arizona State Univ., Tempe AZ 85281.

Although very little is known concerning rates of aeolian erosion on the planet Mars as compared to those on Earth, very high velocity winds and low atmospheric pressures probably have considerable effect both on erosion rates and landforms created thereby. This problem has been studied by using techniques developed to analyze quartz sand surface textures.

Earth and martian aeolian abrasion of crushed quartz was simulated in wind tunnels and a laboratory erosion device at pressures corresponding to those on the two planets; the surface textures of the abraded materials were studied via scanning electron microscopy. Differences in aeolian abrasion on the two planets were indicated by differences in surface texture or roughness. Quartz was used as experimental material because a great deal of information is available on its surface characteristics; in particular, mechanical aeolian action on Earth has been studied in detail and a number of specific surface textures at various sand and silt sizes characteristic of large, hot deserts have been delineated (Krinsley et al., 1976). Subsequently, the same procedure was followed using basalt rather than quartz, since the surface and sediments of Mars likely include a great deal of the former material.

Laboratory Experiments

Samples of crushed Brazilian quartz (175-355 and 500-350μm) were examined and photographed with the scanning electron microscope. The samples were then abraded with particles at 8 meters per second under Earth (760 mm Hg) and martian (3mm Hg) pressures for periods of 20 minutes, one hour, three hours, four hours, and eight hours.

Fresh crushed Brazilian quartz contains a series of irregular fracture surfaces which are generally similar at grain diameters from 1 to 500μm; the grains are angular. During simulated mechanical (aeolian) abrasion at both high and low atmospheric pressures, mechanical action starts on grain edges and with time works its way over entire surfaces, thus rounding the grains. The textures produced are very similar to those found on quartz grains from hot deserts (Krinsley et al., 1976). However, under low atmospheric pressures the process appears to operate more rapidly even though impact velocities are the same; thus grains of the same size run at low atmospheric pressures are more abraded that those at high pressures.

The following textural differences between abrasion at low and high atmospheric pressures were noted:

1) A series of irregular fractures not noted previously occur on high and low atmospheric pressure abraded grains. These "popouts", about 5 to 10μm in diameter, apparently are the result of violent fracturing of grain surfaces; they probably represent very energetic, rare collisions. More of these features occur on grains abraded at low than high atmospheric pressures.

2) Other features that are rather rare and noticeable at high magnification

are irregular surface fractures; these features generally are 5 to 50μm long. Further abrasion of grains with cracks may lead to spalling of portions of grain surfaces. The few cracks that were observed were more common on the "low pressure" grains rather than the "high pressure" samples.

3) Rounding occurs much more rapidly in the low than the high atmospheric pressure environment on the smaller grains; no differences were noted on the larger group. The process of rounding is due to the abrasion of irregular fracture patterns on freshly crushed Brazilian quartz; upturned cleavage plates are formed which eventually cover the grains completely. Tiny rows of plates cover places where large angular areas were present, and at magnifications in which the entire grain is observed, the small plates create the appearance of rounding. Thus rounding simply corresponds to extensive "upturned plate" formation.

A number of other rather interesting observations were made which did not directly relate to the difference between abrasion at high and low atmospheric pressure:

1) After extended abrasion, the larger grains (at both pressures) were similar to modern aeolian dune sands in terms of degree of rounding and surface texture. The only major differences were those due to lack of solution and precipitation which occurs on Earth deserts. This suggested that the abrasion experiments at least roughly approximated aeolian desert abrasion.

2) The larger grains were better rounded after 3 hours than the smaller ones after 8 hours at both high and low atmospheric pressures, probably because of the increased momentum associated with the larger sizes.

3) Spacing of "upturned plates" on small grains abraded at low pressures appears to be closer than on those abraded at high pressures. This may have occurred because of the greater number of collisions and greater momentum generated at low pressures.

In sumary, abrasion under low atmospheric pressures appears to occur more rapidly, and creates somewhat more irregularities on grain surfaces than at high atmospheric pressures characteristic of Earth. The frequency of certain types of breakage textures appears to be more common in low than in high pressure environments. Thus the differences so far observed are mostly of degree rather than of kind and may be the result of decreased air cushions between grains at low pressures as suggested by McCauley (1973). However, it should be noted that wind velocities of only 8 meters per second were used in wind tunnel experiments, while maximum velocities presumed for wind storms on Mars may be as much as ten times that figure. A number of quartz particles, perhaps on the order of a micron in diameter or less, appear to have been partly melted. This was observed on grains that had been abraded at only 8 meters per second; the effect on quartz sand grains at velocities ten times as high is unknown. It may be that the "partly melted" material is a different phase than the

original quartz structure, perhaps more poorly crystalline.

Particles less than a micron in diameter are observed in great numbers adhering to the surfaces of large grains abraded at both high and low pressures; they are extremely difficult to remove. This phenomenon is not found on aeolian quartz grains in deserts; freshly broken surfaces on the experimental grains react differently than weathered material. Perhaps electrostatic forces are important here; if crystals are cleaved or split under a vacuum, electron energies of hundreds of kilovolts may be produced (Moore, 1973). It has been suggested that the martian dunes may be composed of aggregates and clods rather than mineral grains and rock fragments (Moore et al., 1977) and electric charging by mechanical fracture of materials could be involved.

In a series of preliminary experiments, glassy basalt from Hawaii was crushed to fine sand size and blown about in a wind device at pressures of 4 mm Hg and velocities of about 50 meters per second. The crushed, unabraded and the abraded materials of micron size ($\sim$1-2μm) were examined with transmission and scanning electron microscopy, and selected area diffraction. The abraded material was considerably more rounded and less ordered than the unabraded sample. This suggests that plastic deformation and/or melting may have taken place; if it can be shown that the experiments and results are a reasonable approximation of abrasion on Mars, our understanding of the weathering and abrasion characteristics of both large and small martian particles may have to be reconsidered.

References:

Krinsley, D., Friend, P., and Klimentidis, R., 1976. Eolian transport textures on the surfaces of sand grains of early Triassic age. Geol. Soc. America Bull., v. 87, p. 130-132.

McCauley, J. F., 1973. Mariner 9 evidence for wind erosion in the equatorial and mid-latitude regions of Mars. J. Geophys. Res., v. 78, p. 4123-4137.

Moore, A. D., 1973. Electrostatics and its applications. John Wiley and Sons, New York, p. 84.

Moore, H. J., Hutton, R. E., Scott, R. F., Spitzer, C. R., and Shorthill, R. W., 1977. Surface materials of the Viking landing sites. J. Geophys. Res., v. 82, p. 4497-4523.

Windform Patterns on Earth and on Mars: Implications for Similarities of Eolian Processes on Two Planets. Carol S. Breed, U.S. Geological Survey, Flagstaff, AZ 86001; Wesley A. Ward, Univ. of Washington, Seattle, WA 98195; and John F. McCauley, U.S. Geological Survey, Flagstaff, AZ 86001

Earth-like relationships of spacing, width, length, and height have been found among both dunes and yardangs on Mars. The close similarities to terrestrial wind-formed features suggest that the martian dunes and yardangs may be relics of a period of eolian activitv when the atmosphere of Mars may have been more like that of the Earth.

Dunes on Earth fall into several broad morphological categories that are recognized worldwide: crescentic, linear, star, dome, and parabolic types and numerous complex varieties. On a regional scale, certain dune types are associated with particular kinds of topographic settings and wind regimes. For example, the megabarchanoid ridges common to the sand seas of the Inner Gobi Desert, the Sahara, the eastern Rub al Khali, and the Karakum Desert of eastern U.S.S.R. occur mainly in extremely arid, inland basins subject to unimodal to unequally bimodal effective winds. These dunes are morphologically very similar to the most abundant type of dunes observed on Viking Orbiter pictures of the circumpolar sand seas and crater dune fields.

On Earth, the typical pattern of megabarchanoid dunes consists of wavy, subparallel sand ridges separated by a regular succession of interdune basins or hollows (the "fuljes" of Saudi Arabia, the "bahirs" of northern China). The interdune hollows and the dunes represent discrete environments in which different eolian processes operate. The dunes are built by saltation of sand that is well-sorted, having a characteristically homogeneous grain-size distribution, with a mean in the 1/8 - 1/2 mm range (fine to medium sand). The most common constituent of dunes on Earth is detrital quartz, but dunes are also built of sand-sized particles of gypsum and volcanic rocks. The quartz sand in most terrestrial sand seas is commonly coated with ferric oxide that imparts a red hue to the dunes. The intensity of the redness is in part a function of the age of dune formation.

In contrast, the interdune basins on Earth are built of clay- and sand-size particles, e.g., windblown dust deposited from suspension, and the surfaces of the basins are commonly veneered with a lag gravel of particles too large to be moved by saltation. The grain-size distribution of the interdune sediments is typically bimodal, with a deficiency in the sand-size range (e.g., the sizes of grains which are concentrated in the dunes). Thus the pattern of dunes alternating with interdune basins on Earth is a function of the distribution of grain sizes. On Mars, the occurrence of dune patterns that are morphologically like those just described on Earth suggests that a similar alternation of dunes and interdune basins may occur. If so, the grain-size distribution typical of Earth's sand seas may also be typical of Mars.

A detailed inventory of large-scale features, observed on approximately 1500 Mariner 9 and Viking Orbiter pictures of Mars, has been made to evaluate the dominant wind patterns and their interaction with materials on the dry, debris-mantled surface of Mars. Features which are considered indicative of past or present wind directions on Earth and on Mars include dunes, yardangs, and streaks. At present, the association of these features with certain types of wind regimes on Earth is known only in very broad, general terms. However, using similar features as indicators of the martian winds permits a broad categorization of regional wind directions.

This analysis indicates the following regional wind patterns on Mars. The north polar region includes dunes, light streaks, and yardangs that indicate westerly and southwesterly winds in a counter-clockwise circulation pattern; dark streaks are randomly distributed. The northern mid-latitude region includes streaks and dunes that indicate a trimodal wind regime, with dominant northeasterly winds and lesser components from the southeast and northwest. Both yardangs and structural trends have preferred northeast-southwest and northwest-southeast orientations. The northern equatorial region includes dunes and streaks that indicate a northeasterly wind regime, with lesser components from the southeast and southwest. Yardangs and structural features show preferred northeast-southwest and northwest-southeast orientation.

In the southern equatorial region, most light streaks indicate northwesterly winds whereas dark streaks indicate northwesterly and northeasterly winds. Structural features and yardangs show strong northeast-southwest and northwest-southeast trends. In the southern mid-latitude region, a few light streaks reflect a northwesterly wind. Abundant dark streaks and dune fields show strong easterly and southeasterly winds and a lesser northeasterly wind. In the south polar region no light streaks are recognized, but dark streaks show a southeasterly wind and the dunes show an easterly wind. Yardangs have preferred northwest-southeast and northeast-southwest trends.

An inventory of large-scale eolian features on Earth has been completed using Landsat, SKYLAB, and Apollo-Soyuz satellite pictures and aerial photographs. A global classification of these features, based on remote sensing, has been successfully applied to a ground-based inventory of eolian land forms in Arizona and adjacent states. Type areas of linear, star, dome, climbing and falling crescentic dunes, and yardangs eroded in two types of bedrock (sandstone and siltstone, with a variety of structural influences) have been identified. Because many of the martian yardangs seem to be structurally controlled, structural influence must be carefully evaluated if yardang orientations are used to interpret wind directions on Mars. The relationships of both depositional features (dunes of various types and compositions) and erosional features (deflation hollows and wind-fluted cliffs as well as yardangs) to wind regimes and local topography is currently under study.

Contrast Reversal on Mars. J. Veverka, P. Thomas, J. Burt*, Laboratory for Planetary Studies, Cornell University, Ithaca, N. Y. 14853 and T. Thorpe, Jet Propulsion Laboratory, 4800 Oak Grove Drive, Pasadena, California 91103.

Telescopic observations of Mars have suggested that "ultraviolet contrast reversal" may occur in localized areas of Mars. This is the phenomenon in which regions which are brighter than their surroundings in the visible (or red) appear darker than their surroundings in the ultraviolet. Since the apparent contrast of two adjacent areas can depend on many factors, including surface composition, particle size distribution, atmospheric conditions, amount of frost cover, etc., the correct explanation of the phenomenon was not evident.

High resolution color coverage of Mars by the Viking Orbiters has now demonstrated that such contrast reversal is not an uncommon localized surface phenomenon on the planet.

Contrast reversal appears to be associated most commonly with eolian features in localized areas of Mars. For example in the Cerberus region (near 12°N, 202°W) crater and hill-associated wind streaks have a "normal" appearance in the Red (about 0.58 μm) images, being brighter than their surroundings, while in the Violet (about 0.45 μm), they appear dark. Note, however, that the majority of bright streaks on Mars do not show contrast reversal.

Another locale where contrast reversal is conspicuous is Oxia Palus. Here, portions of many large mixed-tone streaks which appear dark in Red images, as well as some of the associated "dark" intracrater dunefields, appear brighter than their surroundings in Violet images.

Laboratory measurements indicate that such contrast reversal is a common property of relatively well-sorted, fine-grained samples of iron oxide minerals.

* Present address: Division of Geological Sciences
California Institute of Technology

Three Topics on the Mechanics of Dunes, Alan D. Howard, Dept. of Environmental Sciences, Univ. of Virginia, Charlottesville, VA. 22903

A. Origin of Longitudinal Dunes. The origin of longitudinal dunes is a highly contested issue in eolian geomorphology. The issue will not be resolved here, but a combination of experimental, field, and theoretical information limit the possible range of acceptable explanations. The two major themes of explanation are (A) longitudinal dunes form along the resultant of two strong seasonal winds which are at an acute angle to each other, and (B) longitudinal dunes form along a dominant wind direction as a result of helical vortices driven, presumably, by convective instabilities.

Evidence for hypothesis (A) includes documented bimodal wind regimes in some areas of longitudinal dunes and internal dune structures which indicate alternate deposition by winds from either side. The major difficulty with the hypothesis is the lack of a reasonable explanation for the regularity of spacing of the dunes. Evidence for hypothesis (B) is of several sorts. Longitudinal helicoidal vortices are observed in nature during strong winds, and they are of approximately the correct scale to account for the spacing of the draas dunes of the Mideast. A special type of longitudinal dune (lee dunes) occur behind topographic obstacles in unidirectional wind regimes as a result of convergent helicoidal eddies generated by the obstacle. Longitudinal ridge-crest dunes in a unidirectional wind regime in Peru occur as a result of convective slope winds. There is evidence that the process is self-accelerative, in that both lee dunes and ridge-crest dunes larger than a critical size may extend downwind indefinitely, and they mold their own topography. Winds over playa lakes that are elongated along the wind have an apparent secondary circulation off of the dry lake bed onto the adjacent dunes. Arguing against the hypothesis are the absence of longitudinal dunes in a unidirectional wind regime (Peru) in the absence of topographic controls (Barchanoid dunes are the prevalent form) and the existence of longitudinal dunes in the Southwestern U.S. and Australia that are too closely spaced to be due to convective eddies of atmospheric boundary layer scale (these dunes have the common feature of being vegetated on their lower flanks). In addition, wind measurements have never been made in the field with sufficient spatial and temporal density to evaluate the occurrence of helicoidal flow associated with dunes, and no mechanism has been proven to be able to "fix" the vortices to the surface, for they normally migrate over the landscape in the absence of topographic controls.

Recent numerical simulations of turbulent atmospheric boundary layer flow over low two-dimensional obstacles suggest why longitudinal ridges would be a stable form under bimodal wind regimes where both dominant winds arrive at an acute angle to the trend of the ridge. Stresses and, therefore, transport rates are much larger on the windward side than the lee side, ans the windward side flow is bent towards the crest. The lee side has much lower stresses, and the wind is deflected to a course more nearly parallel to the crestline. If the dune is steep enough that separation occurs, then the separated flow on the lee side has components towards the crest and downwind along the crestline (Allen, 1968, Current Ripples, North Holland), further enhancing the preservation of the dune. Thus little

sand arriving at the dune can escape. Entrapment by vegetation and reduced transport capacity on the loose dune sand may enhance the effect. Thus the longitudinal dune is an effective sand trap for winds of variable direction, and net sediment motion is along the crestline, so that the direction of an advancing longitudinal dune by hypothesis (A) would certainly lie along the direction of the resultant of sand-transporting winds.

The major problem with hypothesis (B) is tying the convective vortices to the surface, that is, finding some positive feedback mechanism between sand accumulation and convective instability. Three potential mechanisms have been postulated: (1) The influence of the topography upon the circulation, (2) the contrast in aerodynamic roughness between the dune and interdune flat, and (3) a difference in thermal characteristics between the dune and the inter-dune flat. The wavy topography itself does not seem to be a strong enough mechanism for affecting the wind fields to capture the vortices, particularly in the initial stages of growth; similarly, although sloping surfaces with crests parallel to the wind are excellent sites for development of upslope thermal winds and shedding of convective plumes, this mechanism can only act once sufficient sand has accumulated. Longitudinal dune surfaces are generally rougher than the inter-dune flats, either because of superimposed transverse dunes, a sinusoidal crestline, preferential growth of vegetation, or because of a greater quantity of sand in motion. However the sense of secondary circulation generated by a longitudinal roughness contrast is both weak and opposite in sense to the required circulation. Enhanced heat exchange between the sand surface and the lower atmosphere relative to the inter-dune flats is the most likely feedback mechanism. Unfortunately, there seems to be no outstanding or consistent contrast in either albedo or thermal inertia between dune sand and inter-dune flats, at least of the sense necessary to enchance thermal exchange over sand (darker albedo and a lower thermal inertia over sand). A different potential mechanism may exist during strong winds; sand-saturated winds over dunes may have enhanced thermal exchange in the lowest few tens of centimeters due to forced convective heat exchange between the saltating sand particles and the wind into which it is injected. Some scaling arguements will be discussed to estimate the potential magnitude of this effect. A critical need exists for detailed field observations of wind fields and the near-surface heat budget during saltation in areas of longitudinal dunes.

The actual mechanisms forming longitudinal dunes may be a combination of the two hypotheses: winds blowing nearly parallel to the axes of the dunes may tend to start accumulation of sand by localization of helicoidal vortices, also thereby defining the spacing of the dunes in accord with natural convective scales, while the stability of the longitudinal dune under winds arriving at an angle to the crest assures that such dunes, rather than transverse dunes, will be the stable form in areas of variable wind directions.

The absence of well-developed longitudinal dunes on Mars may either be due to deficiency of sand supply or to the lact of the interactive mechanism between vortices, if any, and the sand surface. If the latter is the case, understanding of saltation mechanics on Mars and the structure of its

boundary layer may be critical evidence for understanding the origin of terrestrial longitudinal dunes.

B. Relative Role of Bulk and Interdune Transport in Transverse Dune Fields. Lettau and Lettau have estimated the volume of sand transported by movement of the dunes themselves (Bulk transport). Recalculations of the relative transport rates due to dune movement on one hand and the combined transport by inter-dune and "streamer" transport (sand shed from dune wings) on the other suggest that for the low areal density of barchan dunes in their Peruvian field study the interdune transport is much greater than the bulk transport. However, if transverse dunes occupy an appreciable fraction of the total surface area, total transport rates may be enchanced by a factor of two or more above rates over a flat surface of loose sand. Thus development of transverse dunes may compensate for (1) lower transport rates over loose sand than over most desert surfaces and (2) downwind decreases in wind velocity or increases in sand supply.

C. Two Misconceptions about the Coriolis Effect and the Orientation of Eolian Features. It has been suggested that the difference in orientation of small (centimeter-scale) and large (meter-scale) wind drift features near the Viking I landing site are due to the Coriolic deflection of winds and associated secondary circulations associated with the larger features. But at any given time, near-surface wind over a generally flat surface blows in one direction, and local disturbances of the wind by obstacles or dunes of height much less than the thickness of the atmospheric boundary layer will not cause Coriolis deflections of secondary winds over and above the mean deflection of the surface wind as a whole. Thus the difference in orientation is more likely due to the most recent strong wind being at an angle to the prevailing wind regime (larger features have longer reconstitution times than smaller ones).

Differential Coriolis deflection of surface winds due to contrast in surface roughness has been postulated to account for differences between dune trends and the dominant direction of strong winds at nearby meteorological stations. However, the wind-turning effect of a downwind change in roughness is not felt until the adapted internal boundary layer is approximately as thick as the atmospheric boundary layer. Calculations suggest that the effect will not be felt until the airflow has penetrated a kilometer or more into the dune field. Thus only the most extensive dune fields are likely to show this effect, and then only deep within the dune field.

Wind-Deposited Sand atop Terrestrial Boulders: Possible Significance for the Viking Lander 1 Site on Mars, Roger S. U. Smith, Geology Department, University of Houston, Houston, TX 77004

Wind seems able to deposit sand atop terrestrial boulders by blowing it up their steep leeward faces, and may do likewise on Martian boulders. Such deposition was observed during December 1977 on Mustang Island, Texas, where artificially-broken granitic boulders one to two meters across have been placed 0 to 0.3 meters apart as riprap along a northwest-trending tidal channel. Boulders within the southwesternmost row rise as much as one meter above an apron of sand which slopes southwest. A south wind, estimated velocity 8-10m/s, excavated a horseshoe-shaped depression along the windward edge and flanks of each boulder and dusted sand onto its crest. This deposition was best observed on one boulder, 0.5m taller than the rest, whose 1.5m leeward face slopes roughly 90^{o}, 30^{o} and 60^{o}, respectively, over its bottom, middle and top thirds. Sand crept slowly up this surface, filling in surface irregularities like snow on a steep mountain peak, and finally came to rest on a gentle plateau leeward of the crest. Sand samples taken from the crest and from the upwind sand apron are both well- to very-well-sorted fine sand, median diameter 0.15mm.

The mechanism which lifted this sand to boulder crests is not clear. The observed creep suggests that the grains were moved by direct wind drag rather than by saltation, but it is not clear how either mechanism could move sand up slopes much steeper than the angle of repose. Although some grains may have saltated onto the boulder during earlier reversed winds, this mechanism cannot explain the observed upward creep of grains, and saltating grains tend to bounce off steep rock surfaces rather than cling to them. The interpretation which seems most consistent with preliminary field observations is that vortices generated by wind blowing around the boulder had an upward component large enough to suspend grains momentarily and lift them onto the boulder's leeward face. Although such vorticity might be enhanced by the close spacing of the boulders here, a similar sand deposit has been seen atop an isolated 1.5m boulder within the Salton Sea barchan field in California. Measurements of upward turbulent wind components behind boulders and the amount of sand (if any) suspended by them are planned to help determine how sand actually reaches boulder crests.

Patches of fine-grained sediment atop boulders have been observed at the Viking Lander 1 (VL-1) site in Chryse Planitia on Mars (Mutch et al, 1976a; Saunders, 1977). The most prominent cap is seen atop the southwest face of a two-meter boulder; this is the leeward face if winds which shaped the landscape have blown from the north to northeast as inferred by Mutch et al (1976a,b) and Sagan et al (1977). Mutch et al (1976a) suggested that these sediment caps might represent remnants of eolian sediment which partly buried the boulders but has since been deflated. Saunders (1977) suggested that the caps were deposited by dust storms but eroded from smaller boulders by subsequent impact of saltating grains. If wind can move sediment directly up leeward faces of boulders on Mars

(as seems to occur on Earth), then episodic accumulation followed by deflation is not required to produce these sediment caps, and no major episode of deflation is implied by their presence. These caps may well be in equilibrium with the occasional eolian forces which now act here.

References Cited

Mutch, T.A., R.E. Arvidson, A.B. Binder, F.O. Huck, E.C. Levinthal, S. Liebes, Jr., E.C. Morris, D. Nummedal, J.B. Pollack and C. Sagan, 1976a, Fine particles on Mars: Observations with the Viking 1 Lander cameras: Science, v. 194, p. 87-91.

Mutch, T.A., A.B. Binder, F.O. Huck, E.C. Levinthal, S. Liebes, Jr., E.C. Morris, W.R. Patterson, J.B. Pollack, C. Sagan and G.R. Taylor, 1976b, The surface of Mars: The view from the Viking 1 Lander: Science, v. 193, p. 791-801.

Sagan, C., D. Pieri, P.L. Fox, R.E. Arvidson and E.A. Guinness, 1977, Particle motion inferred from the Viking Lander cameras: Jour. Geophysical Research, v. 82, p. 4430-4438.

Saunders, R., 1977, Sedimentary regimes on Mars (abs): NASA Tech. Memorandum TM X-3511, p. 144-145.

A Preliminary Assessment of the Effects of Electrostatics on Aeolian Processes, Ronald Greeley and Rodman Leach*, Department of Geology and Center for Meteorite Studies, Arizona State Univ., Tempe AZ 85281 and *NASA-Ames Res. Ctr., 242-4, Moffett Field Ca 94035.

Interparticle forces have been shown to be important in affecting the behavior of wind-blown material (Iversen et al., 1976). Of the several forces that can be involved, one of the more important is that derived from electrostatic charges. Although some work has been done to determine the effects of electrostatics on Earth (e.g. Scheidegger, 1970), and consideration has been given to electrostatics on the Moon, neither of these cases apply to Mars because of the differences in atmospheric conditions. The electrical conductivity of gases is a function of density and composition; Paschen's curves of conductivity for CO_2 show maximum conductivity at about 1 mb pressure. Although data are not available for CO_2 with Ar, the general value for CO_2 suggests that on Mars the conductivity will be significantly higher than on Earth.

To determine the effects of electrostatics on aeolian processes in general, and on Mars in particular, a series of laboratory simulations and field studies have been initiated. Electrical charges on particles result primarily from: 1) friction between grains, 2) pressure (piezoelectric), 3) grain-to-grain contact, and 4) breaking of grains - all effects that occur within clouds of saltating particles. To determine the electric current generated under natural aeolian conditions, preliminary measurements were made in the field in Imperial Valley. A current of 1×10^{-9} amperes was measured for fine sand in saltation at a wind velocity slightly above threshold ($\sim$8 m/sec.). The current was measured with an electrometer using a copper probe 5 cm in diameter, oriented normal to the impinging grains. A sample of the same material was returned to the laboratory, placed in the wind tunnel, and the following results were obtained: at 6.9 m/sec wind velocity, the current of the saltating grains was 4.16×10^{-10}; at 8.4 m/sec (velocity comparable to the field measurement) the current was 1.5×10^{-9}; at 10.4 m/sec, the current was 4.15×10^{-9}. Thus, the wind tunnel appears to be suitable for conducting the experiments. Preliminary wind tunnel experiments indicate that higher currents occur under martian conditions than on Earth, which can be attributed at least partly to the higher velocities involved in saltation.

An additional result observed in the experiments (noted also by Gill, 1948) is that small particles may have one sign (e.g. negative) and particles of large size may have the opposite sign. The sign is partly a function of composition, relative humidity, and other factors; for quartz, our measurements have shown a negative charge for grains smaller than 60μm and a positive charge for grains larger than 60μm - however, the exact size for the cross-over is somewhat variable.

These preliminary results have several implications for aeolian processes on Mars: 1) laboratory experiments show that agglomeration of fine-grained material occurs under martian saltation conditions. This

agglomeration is attributed at least partly to electrostatic forces, and provides a means of producing large (sand-size) particles from smaller particles. 2) Erosion rates may be either enhanced or subdued by electrostatic charges: for example, for well-sorted homogeneous windblown materials, the charge may be of the same sign; thus, individual grains would be repulsed, reducing erosion within a saltating cloud. 3) Wind velocity threshold speeds for particle movement could be either raised or lowered depending on the net charge retained in an *in situ* particle bed.

Although these preliminary results are mostly qualitative, they show that electrostatic effects are important in aeolian processes. Quantitative studies are currently in progress to permit extrapolation to Mars.

References:

Gill, E. W. B., 1948. Frictional electrification of sand, Nature, v. 162, p. 568.

Iversen, J. D., R. Greeley, J. B. Pollack, and B. R. White, 1976. Saltation threshold on Mars: The effect of interparticle force, surface roughness, and low atmospheric density. Icarus, v. 29, p. 381-393.

Scheidegger, A. E., 1970. Theoretical Geomorphology, Springer-Verlag.

Viking Implications for Martian Aeolian Dynamics, R. Arvidson, McDonnell Center for the Space Sciences, Dept. of Earth and Planetary Sci., Washington University, St. Louis, Mo. 63130

The Viking Landers touched-down in the northern hemisphere during the onset of northern summer. The lander cameras have been monitoring the sky and surface on a regular basis since then, providing information on the nature and rate of aeolian processes that extends over nearly a full Martian year. Results that impact our understanding of aeolian dynamics on Mars are:

(1) Wind-blown drifts of soil at both landing sites extend from rocks and point in a southerly direction (Sagan et al, 1977). The southerly direction for the drifts is consistent with the direction of bright streaks seen from orbit at these latitudes and with the wind direction inferred from the Mariner 9 IR measurements near the end of the 1971 dust storm. However, Viking lander meteorology results suggest a much more complex distribution of winds. Two large "perihelion" dust storms occurred during Viking. Winds did not blow consistently from north to south at either site, during either storm (Ryan, pers. comm.).

(2) Viking Lander X-ray fluorescence results and Lander camera multispectral data (.4-1.1 μm) are consistent with the soils being composed of a mixture of weathering products derived from iron-rich igneous rocks (Toulmin et al, 1977; Huck et al, 1977). Similarities in composition and spectra at both landing sites imply that the soil has been homogenized by winds on a global scale. The lander camera spectra are also similar to spectra for large bright areas seen from Earth (McCord and Westphal, 1971). The spectral character of a given region on Mars probably depends on the extent of covering by bright wind-blown material and on the characteristics of in-situ materials.

(3) No obvious topographic changes have been found in comparing pictures of drifts and other undisturbed areas taken on various days with the lander cameras. Soil material within one of the footpads on VL1 has been significantly scoured by winds. The material in the footpad is loose, and in addition the footpad surface slopes some 30^{o}. Thus, the shear stress needed to entrain material will be lower than that needed to erode material on a flat surface that is dominated by the fairly cohesive soil found at the landing sites. Soil material dumped onto the lander deck has been considerably shaped by wind and by the action of subsequent dumps of soil, where the soil material impacted onto older deposits and reshaped them. Unfortunately, soil deliveries and dumps have continued throughout the mission, making it very difficult to tell if wind alone has done any of the reshaping.

(4) Reference gray patch charts mounted on the lander, used for calibration of multispectral imagery, have obtained a coating of red dust. Some of the dust was blown off the charts at the onset of high winds associated with the two perihelion dust storms. That is not too surprising since the chart surfaces slope at 79^{o} to the horizontal, and the grains must have been held largely by adhesive forces.

(5) In sum, the past year on Mars has been a relatively quiet one in terms of aeolian activity at the landing sites. With the exception of some wind induced redistribution of disturbed material, few obvious changes have been detected. It does appear, however, that the second landing site, and perhaps even the first landing site, were covered with a thin blanket of dust upon decay of the global dust storms.

(6) The soil at the landing sites has, in the past, been shaped in a significant way by winds. Either significant aeolian activity at the landing sites is a very rare event, connected to a very occasional storm with high velocity winds, or the deposits at the sites were last altered in a significant way when local climatic conditions were different. One possibility is that aeolian redistribution is strongly controlled by the location of the subsolar latitude at perihelion. At present that latitude is below the equator, while both landers are in the northern hemisphere. Arvidson, Goettel, and Hohenberg (1978) estimate that the present atmosphere must have exchanged with a much larger reservoir on a time scale of a few tens of millions of years in order to preserve the Earth-like oxygen isotopic ratios. Such a result is consistent in terms of time-scale with growth and decay cycles of the permanent polar layered deposits that are modulated by the 10^5 and 10^6 year spin axis obliquity changes found by Ward (1974). Clearly, aeolian dynamics on Mars would also vary in terms of intensity with the same periodicity.

(7) Viking lander 2 touched-down some 200 km southwest of the 100 km diameter crater Mie. From the lander view, the surface consists of discrete blocks sitting on and embedded in a fine-grained sediment. The areal distribution of the block population, together with the scarcity of small blocks ($\leq$.10 m in diameter) imparts an aspect to the scene that is reminiscent of the surfaces of terrestrial debris flows. Theoretical justification for a dominance of large blocks on debris flow surfaces has been provided by R.A. Bagnold, who suggested that larger blocks are forced toward the top of a debris flow because of vertical dispersive stresses within the flow that result from collisions between grains. Such stresses are proportional to the square of the block diameter. Lobate ejecta scarps from Mie are seen from orbit to extend to within a few kilometers of the most probable landing site. The proximity to the Mie ejecta, together with the appearance of the surface, suggests that Viking lander 2 is sitting on a subdued lobe of the ejecta deposit that was emplaced by a debris flow mechanism. A debris flow interpretation has some interesting consequences for aeolian erosion on Mars. Namely, debris flows provide a ready-made armored surface that will be resistant to wind erosion. For example, the formation of "pedestal" craters may be related to emplacement of ejecta as a debris flow. Subsequent deflation of the surrounding materials would then leave the crater and its ejecta standing above the intercrater terrain. A debris flow mode of ejecta

emplacement may also allow the ejecta to be transported to several crater diameters from the crater, thereby explaining the large ejecta/crater diameters for these peculiar craters relative to ballistically emplaced ejecta.

References

Arvidson, R., K. Goettel, C. Hohenberg, 1978. The Geology of Mars, Reviews of Geophysics and Space Physics, in press.

Huck, F.O., D.J. Jobson, S.K. Park, S.D. Wall, R.E. Arvidson, W.R. Patterson, W.D. Benton, 1977. Spectrophotometric and color estimates of the Viking lander sites. J. Geophysical Research, vol. 82, 4401-4411.

McCord, T.B. and J.A. Westphal, 1971. Mars: Narrow-band photometry, from 0.3 to 2.5 microns, of surface regions during the 1969 apparition. Astrophysical J., vol. 168, 141-153.

Sagan, C., D. Pieri, P. Fox, R.E. Arvidson, E.A. Guinness, 1977. Particle motion on Mars inferred from the Viking lander cameras. J. Geophysical Research, vol. 82, 4430-4438.

Toulmin, P.III, A.K. Baird, B.C. Clark, K. Keil, H.J. Rose, Jr., R.P. Christian, P.H. Evans, W.C. Kelliher, 1977. Geochemical and Mineralogic interpretation of the Viking inorganic chemical results. J. Geophysical Research, vol. 82, 4625-4634.

Ward, W.R., 1974. Large-scale variations in the obliquity of Mars. Science, vol. 181, 260-262.

Wind transport rates on Mars, B. White, Univ. Calif. Davis, Davis, CA 95616, and R. Greeley, Center for Meteorite Studies and Dept. of Geology, Arizona State Univ., Tempe AZ 85281.

The eolian transport of surface material on the planet Mars is determined from results of low-pressure wind-tunnel testing and theoretical considerations. A semi-empirical relation is developed that will estimate the total amount of surface material moving in eolian saltation, suspension, and surface traction. The estimated total mass movement of surface material q per unit width-time on the surface of Mars is

$$q = 2.61\ \rho(V_* - V_{*t})(V_* + V_{*t})^2/g$$

where ρ is the denisty of the atmospheric gas, g is the acceleration due to the gravity, V_* and V_{*t} are the friction speed and saltation threshold friction speed respectively. The units of q are grams per centimeter-second. The assumption of a flat surface composed of nearly uniform particle diameter size distribution is made. A change in the mean particle size is accounted for; and will change the threshold friction speed V_{*t}.

A series of wind-tunnel tests are designed to explore the relation between eolian movement of surface material between terrestrial atmospheric pressures and low pressures equivalent of Mars. (A discussion of the wind-tunnel test facility at NASA-Ames Research Center is available in Greeley et al. 1977.) Using the flux equation (White and Greeley, 1978) a comparison between Earth and Mars can be made. Assuming the same ratio of friction speed to threshold friction speed, V_*/V_{*t} is then the same for both Earth and Mars

$$\frac{q_E}{q_M} = \frac{\rho_E\ g_M\ (V_{*t})_E^3\ C_E}{\rho_M\ g_E\ (V_{*t})_M^3\ C_M}$$

To duplicate aerodynamic forces for typical conditions on Mars (i.e., temperature of 200°K and surface pressure of 0.75 kPa), the ambient pressure in the wind tunnel should be approximately 23 mb (2.3 kPa). At this value the gas density of the CO_2 on Mars is equal to the gas density of Earth air in the wind tunnel. This creates equivalent dynamic pressures and consequently aerodynamic forces on the particles. Interparticle force equivalence should exist since the ambient pressure is substantially reduced. The effects of gravity, not accounted in wind-tunnel tests, can be adjusted to Mars readily in the mass transport equation.

The wind-tunnel test consisted of spreading a 1 cm thick uniform layer of spherical glass bead particles (mean diameter of 0.208 mm) on the wind-tunnel floor. At the end of the test section a material trap was placed. It consisted of two uniform thin plates spaced 10 cm apart aligned parallel with the flow direction. The plates were from the floor to the ceiling of the wind tunnel. The front end (upstream side) was open to allow air flow to enter freely. The downstream end was sealed with #100 mesh wire to catch the particles yet still allow a sizeable amount of air to pass through so as not to alter the flow field streamlines around the trap. The length of the trap was

approximately 1 m long to prevent rebounding particles off the back screen from bouncing out of the trap. The flow field was carefully observed and no unusual flow anomallies were found due to the presence of the trap.

First the terrestrial case was tested and found to be in agreement with theory (figure 1). The test was repeated for martian surface conditions (0.75 kPa, 200 K) and the results are shown in figure 1 also. From the wind-tunnel data an empirical value of C_M can be determined with is, $C_M = 2.61$.

Figure 2 shows that q versus a function of friction speeds. Here both high- and low-pressure data collapse to a single line.

The flux of material on Mars is substantially higher than Earth. This increase is due to the existence of typically large pathlengths in the particle's trajectory and also to the reduction of gravity, which cannot be modeled in the wind tunnel. Moreover, the increase in q between the planets, assuming the ratio V_*/V_{*t} is equal, is

$$q_M = \frac{(V_{*t}^3)_M}{(V_{*t}^3)_E} \frac{q_E}{13.5}$$

For instance, the relationship between the movement on Earth compared to Mars, for equal ratios of V_*/V_{*t} of 1.47, would be $q_M/q_E = 6$ or 6 times as great on Mars for 0.2 mm particles.

Comparing the movement rates for similar dynamic conditions, equal ratios of V_*/V_{*t} on the two planets, yields,

$$\frac{q_{MARS}}{q_{EARTH}} = 0.94 \frac{\rho_M}{\rho_E} \frac{g_E}{g_{L_M}} \frac{V_{*t_M}^3}{V_{*t_E}^3}$$

A direct estimate of flux rates on Mars can be made by employing the obtained result.

REFERENCE CITED

Greeley, R., B. R. White, J. B. Pollack, J. D. Iversen, and R. N. Leach, 1977. "Dust storms of Mars: Considerations and simulations". *Proceedings of the Desert Dust Symposium*, (T.J.Péwé, ed.), American Association of Science, in press.

White, B. R., R. Greeley, 1978. "Wind transport rates on Mars". *Journal of Geophysical Research* (submitted to).

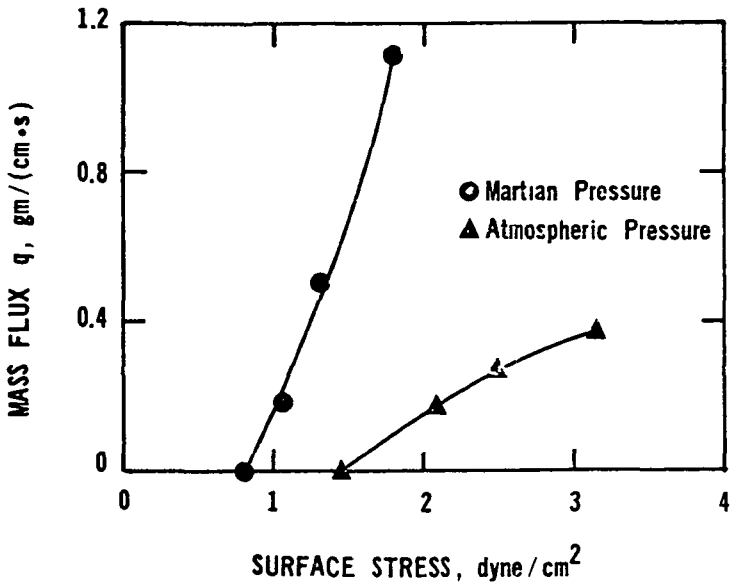

Figure 1 Mass flux q vs the surface stress for wind-tunnel tests. The circular symbols are at 1 atm and the triangular symbols are at 23 mb pressure. Tests were performed in the MARSWIT wind tunnel at NASA-Ames Research Center.

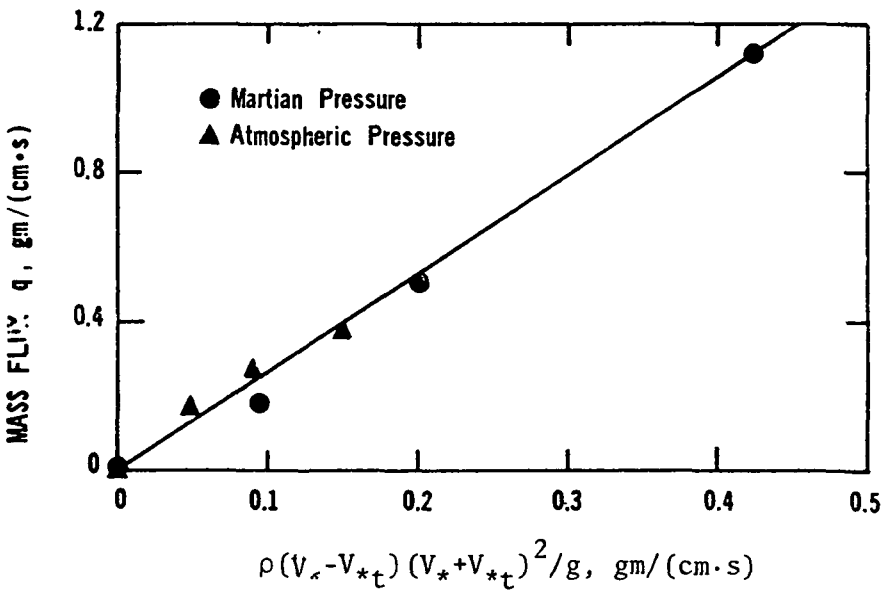

Figure 2 Mass flux q vs a friction speed parameter. Here atmospheric and low-pressure data collapse to a single curve.

Mars: A Model for the Formation of Dunes and Related Structures, Ronald Greeley, Dept. of Geology and Center for Meteorite Studies, Arizona State Univ., Tempe AZ 85281.

Knowledge of aeolian features and related processes on Mars has been advanced considerably by Viking Orbiter and Lander results. A problem, however, has arisen by two sets of observations that appear to be in conflict Features interpreted to be dunes are observed from orbit in many regions of Mars; deposits of presumed wind-blown particles are observed at Viking Lander sites to have bedding structures typical of dunes. Both of these observations suggest the presence of *sand-size* (.06 to 2.0mm) particles, because the physics of aeolian processes generally prohibits smaller and large particles from forming dunes, even under martian conditions. However, Viking observations also indicate the *lack* of sand particles at the lander sites and the prevalence of particles a few microns in diameter and smaller. This is partly attributed to the self-destructing, or "kamikaze" effect of saltating grains in the ∿150 mm size range (Sagan et al., 1977). Furthermore, grains in the atmosphere are estimated to be smaller than a micron or so in diameter (Pollack et al., 1977). Thus, the question arises as to how structures such as dunes originate that require sand-size particles for their formation. Several possibilities can be suggested: 1) The dunes are "fossil" features that formed some time in the history of Mars when sand-size particles were common, 2) the calculations for martian aeolian processes requiring sand-size particles for dune formation are incorrect, or 3) there is a mechanism of dune formation that does not require *individual* sand-size grains. Consideration of the electrostatic effects on grains (Greeley and Leach, 1978) and analysis of possible terrestrial analogs suggest the latter possibility, as follows: Electrostatic charges and other interparticle forces appear to be an effective means of holding aggregates of very fine particles together to form sand-size "particles"; in addition, nucleation around ice particles in the atmosphere may enable the formation of large particles (Pollack et al., 1977). These particles would then behave as "sand" in the aeolian environment to produce dunes and other typical sand structures as suggested by Moore et al., (1977). Although it is not known if the strength of the aggregates is sufficient to survive saltation on Mars, the presence of silt-clay dunes on Earth suggests an analog. These features, such as those in Clark Dry Lake in Southern California (Roth, 1960) involve aggregates of fine sediments that behave as sand-size particles and are emplaced as "sand" to form dune-like structures. Internal bedding characteristic of sand dunes also develops and is preserved. On Mars, after the aggregates are emplaned, the forces holding the tiny grains together may be lost (e.g. the electrostatic charges may be balanced or may "leak" to the highly conductive atmosphere), destroying the "clumps" and the grains would once again behave as very fine grained material. Thus, in this model, the observation of sand-like large scale features and the presence of fine grained materials are not in conflict.

Greeley, R., and R. Leach, 1978. A Preliminary Assessment of the Effects of Electrostatics on Aeolian Processes, in press, 9th Planetary Geology Principal Investigators Mtg.

Roth, E. S., 1960. The silt-clay dunes at Clark Dry Lake, California, Compass, v. 38, pp. 18-27.

Moore, H. J., R. E. Hutton, R. F. Scott, C. R. Spitzer and R. W. Shorthill, 1977. Surface Materials of the Viking Landing Sites, J. Geophys. Res. v. 82, pp. 4497-4528.

Mutch, T. A., R. E. Arvidson, A. B. Binder, E. A. Guinness, and E. C. Morris, 1977. The Geology of the Viking Lander 2 Site, J. Geophys. Res., v. 82, pp. 4452-4523.

Pollack, J. B., D. Colburn, R. Kahn, J. Hunter, W. Van Camp, C. E. Carlson, and M. R. Wolf, 1977. Properties of Aerosols in the Martian Atmosphere, as Inferred From Viking Lander Imaging Data, J. Geophys. Res., v. 82, pp. 4479-4496.

Eolian Activity in the Tharsis/Syria Planum Region of Mars: A summary of Viking and Mariner 9 results. J. Veverka, P. Thomas, S. Lee*, Laboratory for Planetary Studies, Cornell University, Ithaca, N. Y. 14853 and R. Greeley, Department of Geology, Arizona State University, Tempe, Arizona 85281.

Extensive observations of the Tharsis and Syria Planum regions of Mars have been carried out by the Viking Orbiters. The Viking coverage has now spanned the better part of a Martian year and has overlapped the seasonal coverage obtained by Mariner 9 during 1971/72. By comparing the Viking observations with those obtained by Mariner 9 at a comparable season it is becoming possible, for the first time, to assess the relative amplitudes of seasonal and secular changes in the albedo patterns in this area of Mars. Indications are that while the general pattern of activity repeats from year to year, the intensity of the variations as well as the local details do show considerable differences from year to year.

Although persistent eolian activity (inferred from time-variations in albedo markings) has been observed on the flanks of the three large Tharsis volcanoes (Arsia, Pavonis and Ascraeus Mons) throughout the Viking mission, this activity intensified markedly during southern summer — much as it did in 1971-72. The activity was most pronounced on the flanks of Arsia and Pavonis Mons. There is clear evidence of eolian activity on the very summits of these volcanos, suggesting very high winds ($\gtrsim$ 150 m/sec above the boundary layer). The observed variations in albedo markings are best explained in terms of the erosion of bright material by downslope winds. While the seasonal pattern of activity appears to be generally similar to that observed in 1971-72, the details are quite different. For example, although extensive dark patches appeared near the 25-26 km level on Arsia Mons during southern summer, much as they did in 1971-72 (cf. Fig. 6; Sagan et al., 1974), they differed both in location and extent from those observed by Mariner 9.

Spectacular albedo changes have also been documented in the adjacent Syria Planum region. Although the 1976-8 markings (light streaks, dark streaks and albedo boundaries) are generally similar to those seen in 1971-2, dramatic changes involving areas as large as 10^5 km^2 have occurred. Syria Planum is one of the few regions of Mars where individual bright streaks have changed conspicuously since 1971-2: some new ones have appeared, some old ones have completely disappeared, and many have changed both in outline and intensity. Yet the dominant wind pattern indicated by the bright streaks remains roughly the same: N to S close to the equator, swinging over to NW to SE near 15°S.

Following the 1977 duststorms, ragged dark streaks pointing E to W were observed to form (between L_S=325° and 360°) in the region immediately south of Syria Planum, duplicating a seasonal pattern first noticed during the Mariner 9 mission in 1972.

Sagan, C., Veverka, J., Steinbacher, R., Quam, L., Tucker, R., and Eross, B., Variable features on Mars. IV. Pavonis Mons. Icarus, 22, p. 24-47.

* Present address: Washington University, St. Louis, Missouri

CHAPTER 9 - FLUVIAL PROCESSES AND CHANNEL FORMATION

Hydrodynamics of Erosion by Catastrophic Floods. Victor R. Baker, Dept. Geological Sciences, Univ. Texas, Austin, TX 78712.

Catastrophic geomorphic response is dictated by the magnitude and frequency of process inputs and by the character of landscape resistance (1). In the catastrophic flood channels of eastern Washington (2) and in the outflow channels of Mars (3), the resistance is provided by layered rocks containing local defects in an overall simple structure. The responsible processes lie at the extreme ends of the magnitude and frequency scales (large and infrequent). In the Channeled Scabland we can reconstruct the responsible processes.

High-water mark evidence is used to reconstruct maximum flood stages and water-surface gradients. A variety of engineering hydraulic calculation procedures can then be used to estimate flood discharges and mean velocities. To check for consistency the estimated paleohydraulic conditions are then compared to the erosional and depositional phenomena of the Channeled Scabland.

The enormous flow velocities achieved in many scabland channels caused considerable reduction of absolute pressure, perhaps to the fluid vapor pressure. Shock waves produced by collapse of the air bubbles which form in such situations are recognized as intense erosional agents (4). For terrestrial conditions (5) we can reduce the equation for the critical cavitation velocity V_c (m/sec) to a simple function of flow depth (m):

$$V_c = 2.6 \sqrt{10 + d} .$$

This equation indicates that at very high flow depths, the velocity must rise to very high values in order to achieve cavitation (6). Several narrow constrictions permitted the Missoula flood flows to achieve sufficient velocity for cavitation. All these areas show intense bedrock erosion, which may, in addition, have been localized by separations and other macroturbulent phenomena.

A fundamental hydraulic characteristic of very deep, high gradient flood flows is the development of secondary circulation, flow separation, and the birth of decay of vorticity around obstacles and along irregular boundaries. The most important erosive form of macroturbulence is the "kolk", which designates intense energy dissipation by upward vortex action (7). The intense pressure and velocity gradients of the vortex produce a phenomenal hydraulic lift force along its filament. An alternative model for kolks (8) relates them to the oscillatory grow and breakup stages of the turbulent bursting phenomenon (9).

The dynamics of a turbulent separated flow at a downward step has been especially well studied. The maximum temporal mean fluid pressure measured on the bed reaches a maximum at the point of reattachment and gradually decays downstream (10). Throughout the separated region and downstream there are large fluctuations of instantaneous pressure at any given observation point. The bed experiences rapidly varying normal forces that alternately pull and push at it. Turbulent shear stresses developed in and downstream from separated regions are much greater than in the boundary layer. The greatest erosion by turbulent separated flows occurs at the points of flow reattachment. The actual erosion process may be cavitation, corrasion, fluid stressing, solution, or hydraulic plucking.

Both erosional and depositional bed forms in catastrophic flood channels exist in a hierarchical arrangement that relates to formative processes (Table 1). Recent fluid mechanics work (11) indicates that turbulent shear flows contain an inherent structure consisting of discrete secondary flows superimposed on the prevailing unidirectional mean flow. For the mesoscale, these structures consist of the bursting phenomenon, longitudinal vortices, in-phase waves, and possible transverse roller vortices. According to the passive bed theory, the fluid flows impart these properties on a passive bed through the hydraulic character of the responsible flow. The defect theory, in contrast, emphasizes defects or irregularities on the bed which disturb the flow to generate turbulent flow separations. Actually the two theories are difficult to resolve because the effects of one tend to enhance the operation of the other. In the basalt bedrock of the Channeled Scabland it is mainly the structural irregularity of the rock that provides defects which then perturb the flow hydrodynamics to create distinctive bed forms.

Scabland bed forms have evolved to present minimum resistance the catastrophic flood flows. Resistance on scabland bars and residual hills has two components: skin resistance and form resistance (pressure drag). Skin resistance is minimized for a given-size object by decreasing the surface area that it presents to the fluid. However, form resistance is minimized by increasing the elogation of a streamlined object so that less surface is presented transverse to the flow. The streamlined hills and bars are equilibrium forms, elongated sufficiently to reduce pressure drag, but not so long that they create excessive skin resistance. They owe their preservation in the high-velocity flood flows to this marvelous streamlining. Whereas the adjacent rock outcrops generated destructive macroturbulence, the loess hills and bars fostered a smooth bending of streamlines around them.

Some slight tendency for increased streamlining (increased K factors) appears to occur with increasing Reynold's number (fig. 1). The Reynold's numbers (R) used are the maximum values achieved in the flood flows and were computed from the expression

$$R = \frac{QR\rho}{A\mu}$$

where Q is the maximum discharge of a scabland reach computed by slope-area procedures (12), R is the hydraulic radius of the reach, ρ is the fluid density, A is the cross-sectional area, and μ is the dynamic viscosity. These maximum flow Reynold's numbers varied from 2×10^8 to 2×10^9 in most scabland reaches.

References: (1) Baker V. R. (1977) Geol. Soc. Amer. Bull. 88, 1057. (2) Baker V. R. (1973) Geol. Amer. Spec. Pap. 144. (3) Baker V. R. and Milton D. J. (1974) Icarus 23, 27. (4) Eisenberg P. and Tulin M. P. (1961) Handbook of Fluid Dynamics, McGraw-Hill N. Y., p. 12-1. (5) Barnes H. L. (1965) Amer. Jour. Sci. 254, 493. (6) Baker V. R.,(1973) Proc. 4th Ann. Geomorph. Symp., SUNY Binghamton, N. Y., p. 123-148. (7) Matthes G. H.(1947) Am. Geophys. Union Trans. 28, 255. (8) Jackson R. G. (1976) Jour. Fluid Mech. 77, 531. (9) Offen G. R. and Kline S. J. (1975) Jour. Fluid Mech. 70, 209. (10) Allen J. R. L. (1971) Sediment. Geol. 5, 167. (11) Jackson R. G. (1977) Program First Int. Symp. Fluvial Sedimentology, Calgary, Alberta, 15. (12) Baker V. R. (1977) Geol. Soc. Amer. Spec. Pap. 144.

Table 1. Important Beds Forms of the Channeled Scabland

	Scoured In Rock	Scoured In Sediment	Depositional
MACROFORMS (Scale Controlled by Channel Width)	Pool-and-Riffle Sequence Quadrilateral Residual Forms in Channel Anastomosis	Large-scale Streamlined Residual Forms	Longitudinal Bars (a) Pendant Bars (b) Alternate Bars (c) Expansion Bars Eddy Bars
MESOFORMS (Scale Controlled by Channel Depth	Longitudinal grooves Potholes Inner Channels Cataracts	Scour Marks	Large-scale transverse ripples ("Giant Current Ripples")

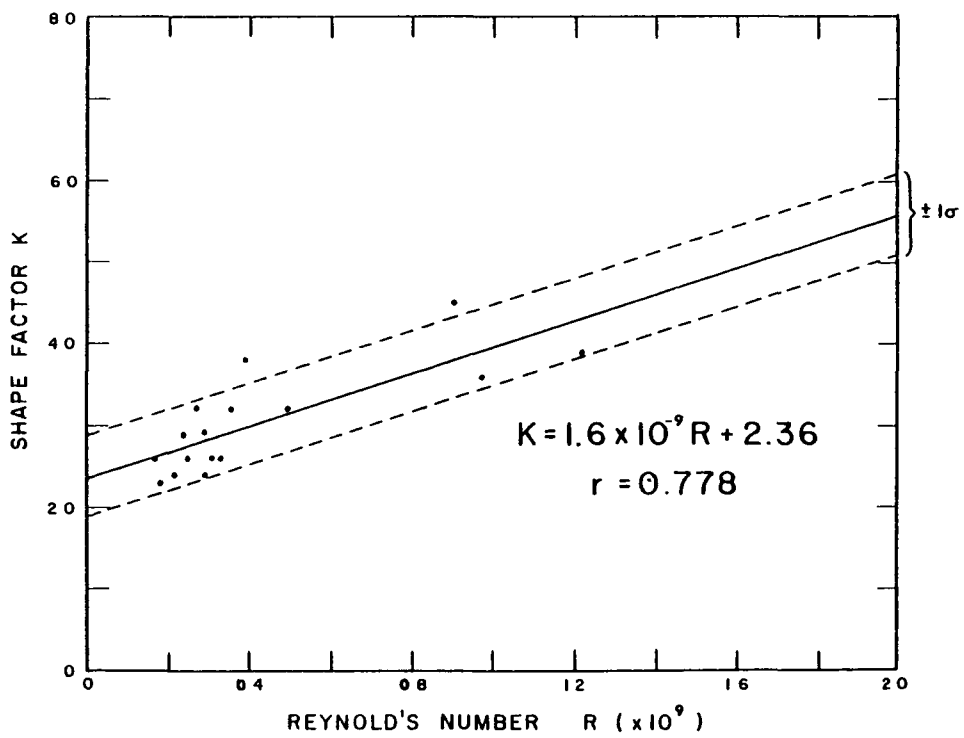

Fig. 1. - Streamlined shape factor K versus Reynold's number for maximum flood flows associated with scabland streamlined forms. The dashed lines indicate one standard error.

Morphometry of Streamlined Erosional Forms in Terrestrial and Martian Channels. Victor R. Baker and R. Craig Kochel, Department of Geological Sciences, The University of Texas at Austin, Austin, Texas 78712.

Streamlined uplands, or "teardrop-shaped islands," are among the most striking channel forms revealed by the Viking orbiter imagery (1, 2, 3). These residual landforms are characteristic of both Martian outflow channels and the flood-eroded Cheney-Palouse scabland tract of eastern Washington (4, 5). The streamlined uplands in both these regions commonly show the following: (a) flow obstacles that localized the resistant landform, (b) upstream crescent-like scour marks, (c) downstream tapering tails of residual material and/or deposition, (d) longitudinal grooves marking the flow streamlines on the adjacent channel floor, (e) oblique channels cutting through small divides at the crest of the streamlined form. Quantitative shape comparisons by Fourier analysis of residual erosional remnants in Martian channels and in the Channeled Scabland confirm the visual similarity of form (6).

In this report we compare streamlined erosional forms in the Channeled Scabland to streamlined features recognized in the region of Kasei Vallis on Mars. This analysis may be helpful in resolving the controversy over the origin of the Martian streamlined features. If the Martian forms were shaped by water, then very large floods are required.

Data for scabland features were derived from morphometric studies of large-scale topographic maps (7.5-minute quadrangles). Mars data were obtained by analysis of high resolution Viking photographs of Kasei Vallis and of areas in the vicinity of Chryse Planitia. Analysis of the streamlined shapes included three physical measurements: length (km) - measured parallel to suggested flow direction; width (km) - taken as the maximum width of the streamlined form measured perpendicular to the implied flow direction; and area (km^2) - measured with a grid emplaced over the feature. From these physical measurements a dimensionless parameter (K) can be calculated,

$$K = \frac{l^2 \pi}{4A} \qquad (1)$$

where l = length (km) and A = area (km^2). Chorley (7) used this parameter to show that drumlins have a close resemblence to airfoils. Through the use of the lemniscate loop equation,

$$P = l \cos K\Theta, \qquad (2)$$

where P and Θ are polar coordinates, an equation for the streamlined form can be derived and plotted on polar coordinates. These plots reveal that the streamlined loess hills in the Cheney-Palouse scabland were probably formed by rapidly flowing fluid (8). Although there is a wide range of streamlined forms in the Channeled Scabland and on Mars, the dimensionless K parameter allows ready comparison. One hundred thirty seven streamlined hills and bars were measured in the scablands and 47 streamlined forms were measured on Mars. Most of the scabland forms are located in the Cheney-Palouse tract, while most of the Martian forms are located in Kasei Vallis. K values in the scablands range from 0.9 to 8.3, with an average K = 3.2. Martian K values range

from 1.5 to 12.0 with an average K = 3.8. Although the forms on both planets are not identical, they are similar enough to probably have been produced by similar processes.

The width vs length relation serves as a measure of the Index of Elongation (Fig. 1). Greater values of the ratio l/w (more gentle slopes) imply greater elongation of the form. The curves fitted to the point scatter (via regression analysis) show that Martian and terrestrial streamlined forms exhibit nearly parallel relationships regardless of size. In addition, there is little change in the l/w ratio with increasing size. The elongation of streamlined features on Mars and earth approach the same value with decreasing size. For relatively large streamlined forms, Martian forms are slightly less elongate than terrestrial forms, but are similar toward smaller sizes. This may indicate a variance in velocities between the flow operating on Mars and earth, and that these differences become apparent only with larger obstacles to the flow.

The relationship of length to area (Fig. 2) measures the narrowness of streamlined forms. It is a measure of the relative percentage of the area contributed by the length component. Higher l/A values indicate increasing narrowness of streamlined forms. On Mars and earth the relationship between length and area (l/A) decreases with increasing form size. Mars has a slightly larger l/A at any given size of streamlined form; hence, the Martian forms appear to be slightly narrower than terrestrial forms. The relationship of area to length on both planets is parallel.

The relationship of width to area (Fig. 3) measures the degree of broadness, i.e. how much of the total area is contributed by the width component. As the w/A increases, the tendency toward broader forms will increase. On earth, at 100 km form lengths width accounts for 7% of the total area. The relation is virtually identical on both planets. Similarly, both planets exhibit forms whose area is dominated by length. The hydrodynamic implications of these results are currently under study.

References: (1) Carr M. H. et al. (1976) Science 193, 766. (2) Baker V. R. (1977) NASA Tech. Memo. X-3511, 169. (3) Masursky H. et al. (1977) J.G.R. 82, 4016. (4) Baker V. R. and Milton D. J. (1974) Icarus 23, 27. (5) Baker V. R. and Patton P. C. (1976) Geol. Soc. Amer. Abst. Prog. 8, 351. (6) Brown et al (1977) NASA Tech. Memo. X-3511, 166. (7) Chorley R. J. (1959) Jour. Glaciology 3, 339. (8) Baker V. R. (1973) Proc. 4th Ann. Geomorph. Symp., SUNY Binghamton, NY, p. 123-148.

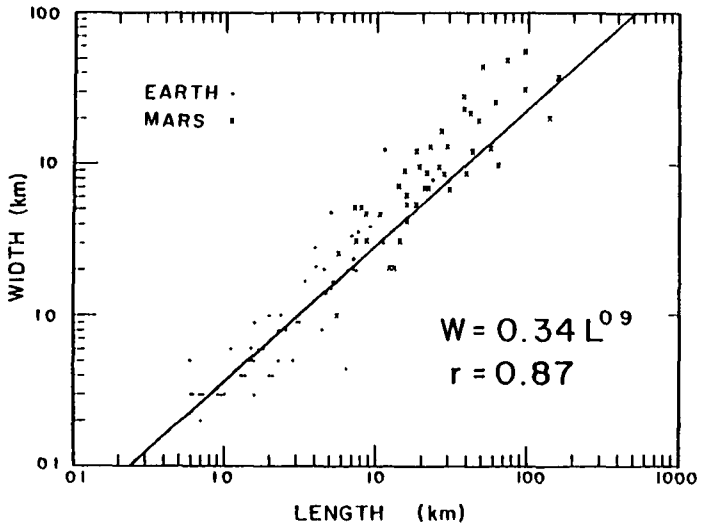

Figure 1

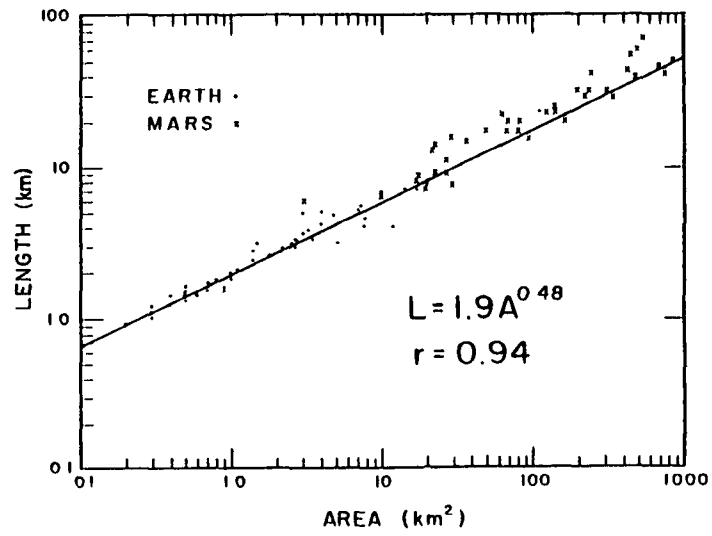

Figure 2

Figure 3

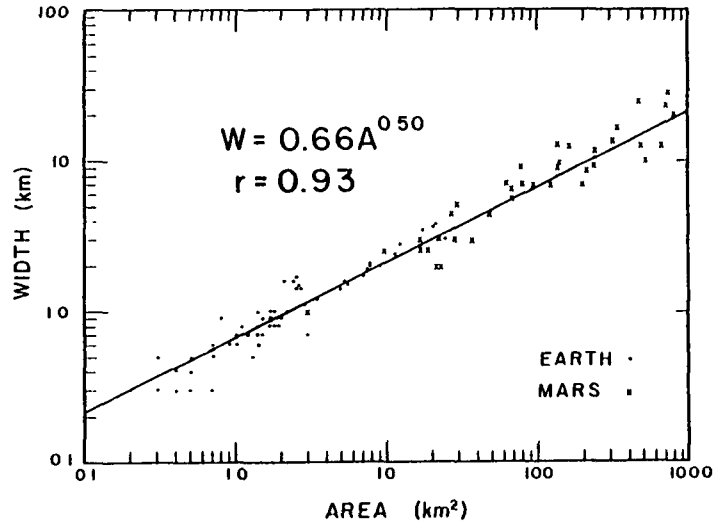

Landforms and Morphology of Selected Terrestrial River System, Jon C. Boothroyd and Thomas Donlon, Department of Geology, University of Rhode Island, Kingston, RI 02881.

A continuing study of bars, channel islands, erosional remnants, and general overall morphology of selected terrestrial river systems focused this year on cataloging island/remnant features and on preliminary comparisons by Fourier series analysis in closed form. In addition, some consideration was given to which 'total' river systems may be used as analogs to some of the Chryse debouchment channels. Parameters outlined in Boothroyd and others (1977) were used in this evaluation.

The two dimensional shapes of 135 terrestrial and Martian landforms were studied using a Fourier series analysis in order to compare landform shapes in a quantitative fashion. This work was done in conjunction with studies by Brown and others (1977). Landforms were divided into four groups:

1) Gravel erosional remnants on alluvial fans in Death Valley, California produced by Holocene degradation of fan surfaces by low discharge, flashy streams. These remnants range from 0.1 to 10 km in length.
2) Large channel islands from the Copper and Colville Rivers, Alaska; the Kosi River, India and the Amu Dar' ya River, USSR. These remnants are generally between 0.2 and 10 km in length.
3) Streamlined loess hills produced by catastrophic flows in the Channeled Scablands of eastern Washington. These remnants range in length from 0.3 to 40 km.
4) Streamlined erosional remnants of unknown composition on Chryse Planitia. These remnants range in length from 20 to 800 km.

The relative sizes of remnants studied are illustrated in Figure 1.

Results show that the high discharge, catastrophic flows of the Channeled Scablands produce remnants morphologically similar to Chryse remnants. Earlier work by Brown and others (1977) yielded similar results. This suggests that the Chryse remnants may have been subjected to catastrophic Scabland type flows as proposed by Baker and Milton (1974) and Baker (1977). The Fourier analysis of terrestrial river islands shows that the Kosi and Amu Dar'ya River also produce landforms morphologically similar to Chryse remnants, but of reduced size. These rivers have significantly lower discharges than those estimated for the Channeled Scablands (21,300,000 m^3/sec; Baker, 1973) and those proposed by Masursky and others (1977)for the Chryse channels (86,000,000 m^3/sec). This suggests that, while the Scabland remnants are good analogs for Chryse remnants, landforms of similar shape are produced in terrestrial rivers under lower discharge conditions. The scale problem is unresolved.

The Fourier results show that the Death Valley remnants and the channel islands from the Colville and Copper Rivers are clearly dissimilar from the Chryse remnants. These remnants were produced by the lowest discharges of the terrestrial study groups. Peak flood discharges in the Colville and Copper Rivers are 6,100 m^3/sec (Arnborg and others 1966) and

6,230 m^3/sec (USGS, 1975) respectively, versus discharges of 17,400 m^3/sec (UNESCO, 1976) and 8,800 m^3/sec (Lodina and Chalov, 1971) for the Kosi and Amu Dar' ya Rivers. This suggests that there is a lower limit on the magnitude of a flow that will produce a 'Chryse-like' remnant. However, remnants are found on the North Slope of Alaska where Holocene stream erosion has left topographic highs composed of material more resistant to erosion than the surrounding Arctic Coastal Plain. These remnants are up to 100 km in length and thus are similar in scale to Chryse remnants. Shape populations in the various categories are too few at present for good statistical comparisons.

A consideration of terrestrial river environments shows that large rivers in arid regions are able to maintain large discharges and high velocities downstream even though tributaries may be few or poorly developed, and much water is lost through evaporation and infiltration. This is a valuable observation in light of the fact that the Chryse channels lack well developed tributaries, and that evaporation rates on Mars may have been high due to low atmospheric pressures. Large rivers in arid regions, such as the the Amu Dar' ya, are known to transport large quantities of sediment suggesting that even if Chryse flows were considerably less than those proposed by Masursky and others (1977); the debouchment areas of the large Chryse channels may still be large areas of alluviation as proposed by Sharp and Malin (1975).

References:

(1) Arnborg, L., Walker, H.J. and Peippo. J. 1966. Water discharge in the Colville River. Geografiska Annaler. 48A/2:195-210.

(2) Baker, V.R. 1973. Paleohyrology and sedimentation of Lake Missoula flooding in eastern Washington. American Geological Society Special Paper No. 144, 79.

(3) Baker, V.R. and Milton, D.J. 1974. Erosion by catastrophic flood on Mars and Earth. Icarus 23/4:27-41.

(4) Baker, V.R. 1977. Viking-Slashing at the Martian Scabland problem. NASA TMX-3511, 169.

(5) Boothroyd, J.C, Donlon, T.J., Nummedal, D. 1977. Erosional and depositional features of some terrestrial channels. NASA TMX-3511,173-175.

(6) Brown, P.J., Nummedal, D., Eppler, D.T., Ehrlich, R. 1977. Characterization of erosional forms on Mars by Fourier analysis in closed form. NASA TMX-3511, 166-167.

(7) Lodina, R.V. and Chalov, R.S. 1971. Effects of tributaries on the composition of river sediments and on deformations of the main river channel. American Geological Institute Soviet Hydrology Selected Paper No. 4, 65-70.

(8) Masursky, H., Boyce, J.M., Dial, A.L., Schaber, G.G. and Strobell, M.E. 1977. Classification and time of formation of Martian channels based on Viking data. Journal of Geophysical Research 82/28:4016-4038.

(9) Sharp, R.P. and Malin, M.C. 1975. Channels on Mars. Geological Society of America Bulletin 86/5:593-609.

(10) UNESCO. 1976. World catalogue of very large floods. the UNESCO Press, 324.

(11) U.S. Geological Survey. 1975. Water Resources data for Alaska, water year 1975. U.S. Geological Survey Water Supply Report No AK 75-1, 410.

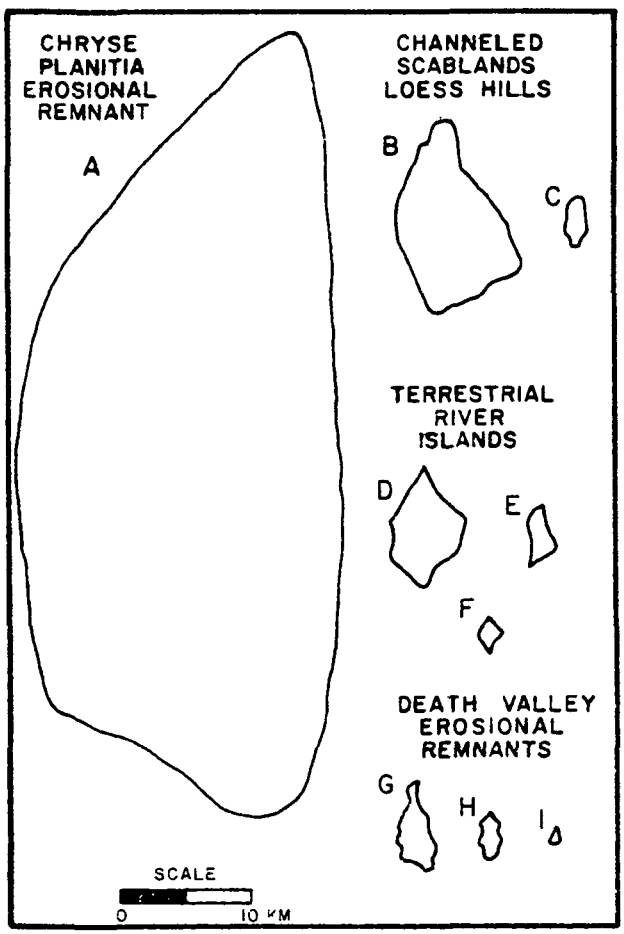

Figure 1 Representative shape and size of Martian and terrestrial landforms used in the Fourier analysis, shapes are all drawn to the same scale.

A Simud Vallis moderate size remnant
B Channeled Scabland large loess hill,
C Channeled Scabland small loess hill,
D,E Amu Dar'ya River, USSR channel islands,
F Colville River, Alaska channel island
G Hanaupah Canyon, Death Valley large remnant
H Trail Canyon, Death Valley moderate size remnant
I Trail Canyon, Death Valley small remnant

The Role of Liquefaction in Channel Development on Mars. Dag Nummedal, Dept. of Geology, University of South Carolina, Columbia, S. C. 29208

INTRODUCTION

The origin of the large channels on Mars is highly controversial, largely because their morphological attributes appear distinctively different from those of known terrestrial fluid erosion features. Sharp and Malin (1975) argued that at least runoff and outflow channels bore evidence of large-scale fluvial erosion, whereas Cutts and Blasius (1978) argue that channels across Luna Planum, which would be runoff channels in Sharp and Malin's terminology, might have been caused by lava erosion. Komar (1978) has added a quite interesting observation by pointing out the similarity between many large channels on Mars and terrestrial submarine fan channels.

Although no convincing model for Mars channel formation has yet been proposed, the above studies serve to demonstrate that one cannot force the morphological data on Mars to fit a model of conventional terrestrial fluvial erosion. Instead, an attempt must be made to explain the channels on Mars as well as their sources and sinks in terms of the physical properties of the proposed erosional medium. Such an approach is taken in this paper where it is proposed that the process of sediment liquefaction provides fluid properties consistent with the morphology generated in the chaotic terrains and the downstream channels. Furthermore, liquefaction provides a viable mechanism for the sudden release of large quantities of fluid, a commonly considered requisite for the formation of large-scale erosional remnants as observed near, for example, the mouth of Ares Vallis (Carr et al. 1976)

LIQUEFACTION

Sediments may behave as a liquid if the excess pore pressure resulting from high strains reach values approaching the effective overburden pressure. Under such conditions, sediment shear strength is reduced essentially to zero, allowing the sediment to flow down even gentle gradients. Andresen and Bjerrum (1968) differentiate between retrogressive flow slides and spontaneous liquefaction on the basis of the initial liquefaction pattern.

A retrogressive flow slide generally starts in the lower part of a slope as a result of local steepening by erosion or the effects of seepage pressures. Following the initial slip, the slide develops retrogressively inland, incorporating large areas of land slice by slice. The slide may propagate at a rate of thousands of meters per hour and will continue until a sediment unit which cannot be liquefied is encountered. Slides of this type are common in "quick" clays characteristic of Pleistocene marine sediment of Norway, Sweden and Canada (Bjerrum, 1954). Individual "quick" clay slides in Norway typically involve millions of cubic meters of material. The slide scar takes on the appearance of a bowl-shaped depression, usually floored by large flakes of the original dry surface soil layer which was not involved in the liquefaction process. The resulting down-valley liquefaction flow has a typical specific gravity of 1.9, can flow with very high velocities and is known to have caused localized severe erosion (Bjerrum, 1971).

Spontaneous liquefaction refers to the sudden loss of shear strength throughout a sedimentary deposit by a mechanism such as vibration or shock. Liquefaction may start at a single point and spread to adjacent sedimentary deposits possessing metastastable structures. The liquefaction wave may propagate over large areas at velocities up to 100 km/hour. The now-famous cable breaks on the Grand Banks off the shore of Newfoundland are thought to have been caused by spontaneous liquefaction of submarine sediment by an earthquake. While Heezen et al. (1954) argue that the cable breaks were caused by turbidity currents triggered by liquefaction, Terzaghi (quoted in Andresen and Bjerrum, 1968) contends that the cable breaks were due entirely to liquefaction. The possibility that initiation of flow in many large channels on Mars may have been due to liquefaction of susceptible metastable sediment in the areas of channel origin cannot be ruled out. Chaotic terrain near the "headwaters" of Ares, Tiu, Simud and Shalbatana Valles are perfect examples of liquefaction slide scars. Blocks of non-liquefied crust still can be seen littering the floors. Evidence of flowage of a large amount of liquefied sediment throug a relatively constricted outlet (the site of the initial slide of a retrogressive slide sequence) is widespread.

Komar (1978) points out that there is a striking similarity between terrestrial submarine fan channels and the large channels on Mars. However, this writer contends that the similarity is not due to the correspondence between the effective gravity on Mars and that in a terrestrial submarine setting, as Komar argues. Effective gravity has not been demonstrated to have any morphologic significance. If on the other hand, we accept the idea of flow initiation on Mars by sediment liquefaction, then the downstream channel characteristics will be those generated by the consequent mud flows. On submarine terrestrial fans, the turbidity current is initiated by slumping in the canyon. It flows from this point source down a gently sinuous deeply incised single channel with few or no tributaries. On Mars, by analogy, the turbidity current (or mud flow) is initiated by liquefaction in the chaotic terrain, and it flows from this point source down a very similar channel.

CONCLUSIONS

1. It is demonstrated that the physical properties of liquefied sediment would be consistent with the morphological characteristics of the chaotic terrain on Mars.

2. Mud flows resulting from the liquefaction of large areas of Martian crust might have been capable of producing the large channels draining the chaos.

REFERENCES

Andresen, A., and L. Bjerrum, 1968, Slides in sub queous slopes in loose sand and silt: Norwegian Geotechnical Institute, Publ. no. 81.

Bjerrum, L., 1954, Geotechnical properties of Norwegian marine clays: Norwegian Geotechnical Institute, Publ. no. 4.

Bjerrum, L., 1971, Kvikkleireskred; et studium av årsaksforhold og forbygningsmuligheter (in Norwegian): Norwegian Geotechnical Institute, Publ. no. 89.

Carr, M. H. et al., 1976, Preliminary results from the Viking Orbiter imaging experiment: Science, v. 193, p. 706-776.

Cutts, J. A., and K. Blasius, 1978, Icarus (manuscript in press).

Heezen, B. C., D. B. Ericson and M. Ewing, 1954, Further evidence for a turbidity current following the 1929 Grand Banks earthquake: Deep-Sea Research, v. 1, p. 193-202.

Komar, P. D., 1978, Deep-sea channels: Another earth-analog for Martian channels; (manuscript in preparation).

Sharp, R. P., and M. C. Malin, 1975, Channels on Mars: Geol. Soc. America Bull., v. 86, p. 593-609.

Formation of martian flood features by release of water from confined aquifers, Michael H. Carr, U.S. Geological Survey, Menlo Park, CA 94025

Many large martian channels arise full bore from discrete areas of chaotic terrain. It is proposed here that the channels were eroded by water, released rapidly under pressures close to the lithostatic pressure, from deeply buried aquifers. Peak discharges depend on the hydraulic head, the radius of the orifice to the surface, the thickness of the aquifer and its hydraulic conductivity. Plausible values for these parameters give discharges in the range of 10^5 to 10^8 m^3/sec which are consistent with the values computed from the dimensions of the flood features.

Chaotic terrain is commonly associated with large channels on Mars, especially around the Chryse basin. Channels emerge, full scale, from areas of chaotic terrain and continue downslope, maintaining their dimensions for great distances. The Chryse channels ultimately debouch onto the plains of Chryse Planitia where the flow diverged and cause extensive modification to the former surface. Tributaries are rare and catchment basins commensurate with the size of the channels are totally lacking. If the channels are formed by liquid flow then very high discharges must have been achieved almost instantaneously. Because of the difficulty of achieving such large instantaneous discharges of water, several alternatives have been proposed. It has been suggested that the chaotic terrain was a source of very fluid lava and that the channels were carved by lava (Schonfeld, 1977). The lack of associated volcanic landforms and the difficulty of achieving eruption rates of 10^6 to 10^8 m^3/sec, required by the scale of the channels however, render this hypothesis implausible. Wind action appears similarly improbable for a wide variety of reasons including the difficulty of confining wind action to a narrow linear zone, the close adherence of the channel direction to the regional slope and the difficulty of explaining the instantaneous emergence of the channels from chaos. Several workers (McCauley, et al, 1972, Masursky, et al, 1977), have suggested that the channels were indeed formed by water and that the high discharges result from melting of ground ice by subsurface volcanism. Such 'glacial bursts' in Iceland produce discharges as high as $10^5 m^3$/sec (Thorarinsson, 1957). On Mars however the huge areas of the chaos and the lack of volcanic features that are contemporaneous with the channels and chaos argue against the glacial burst hypothesis as a complete explanation for the floods, although such bursts may contribute to the more general mechanism being proposed here.

Fluvial action appears to have been widespread early in the planets history as evidenced by the extensive dissection of the old cratered terrain by fine dendritic channels (Masursky et al. 1977). Younger deposits are less dissected and most of the lava plains in the northern hemisphere and in the Tharsis and Elysium regions are totally undissected. Thus fluvial activity appears to have tapered off with time. Possible causes include a general global cooling and loss of an initially thick atmosphere. Much of the water required to form the channels may still be present as near surface ice, as liquid water

beneath the permanently frozen layer or as chemically bound water in the regolith. Evidence for near surface ice includes patterened ground, landslides, mass wasting features, possible thermokarst terrain, and the pattern of ejecta around impact craters (Carr and Schaber, 1977). The large flood features present possibly evidence of liquid water beneath the ice, at least for some part of the geologic history of the planet.

The specific mechanism for forming the large flood features is as follows. The rocks within several kilometers of the surface are probably volcanic origin or brecciated by impact and thus highly porous. Some of the water that initially outgassed from the planet or resided in a primitive atmosphere was lost to the ground water system. Other sinks include the polar terrain, the regolith and outer space. As the surface temperatures fell a permafrost layer developed and thickened with time. Ultimately the permafrost layer became so thick that it effectively sealed in the underlying ground water to form a system of confined aquifers. The pressure within the aquifer would be affected by surface relief, but in addition because of the volume increase of water upon freezing, any increase in the depth of the permafrost layer would cause an increase in pressure, and with progressive freezing the pressure will continue to rise. When the pressure within the aquifer builds up to the lithostatic pressure the system becomes unstable. Further freezing will result in uplift of the overlying terrain and possibly fracturing to allow breakout. Breakout could also be triggered by meteorite impact. Once access to the surface is achieved water will be forced out of the aquifer at rates dependent on the hydraulic head and the transmissivity. The highest known terrestrial transmissivities are from aquifers in regions of volcanic terrain. In Hawaii and the Snake River Plains aquifers occur with permeabilities in excess of 3000 Darcys. With such permeabilities and a hydraulic head equivalent to several hundred meters of overburden, extremely high flow rates will result. The flow rates may be so high as to disrupt the aquifer, undermine the overlying rocks and cause collapse to form the chaotic terrain. The disruption can thus propagate itself and affect large areas. If the affected region is 20 km in radius, and the aquifer is 1 km thick, and its upper surface 1 km below the ground surface then flow rates of 10^7 m^3/sec can be sustained for several days, depending on the areal extent of the aquifer. This discharge rate agrees well with those calculated from the channel dimensions. Withdrawal of water from the aquifer will result in drawdown of the piezometric surface around the chaotic region. The flow till terminate when the pressure around the breakout point is so reduced that the flow dwindles to the point where it freezes and the aquifer is resealed. This could result from depletion of the aquifer or drawdown such that the hydraulic head is insufficient to pump water to the surface. If the aquifer is recharged by planetary outgassing or by flow from adjacent regions, the cycle could be repeated.

References

Carr, M. H., and Schaber, G. G., 1977, Martian permafrost features; Journ. Geophys. Res., v. 82, p. 4039-4054.

Masursky, H., Boyce, J. M., Dial, A. L., Schaber, G. G., and Strobell, M. E., 1977, Classification and time of formation of Martian channels based on Viking data; Journ. Geophys. Res., v. 82, p. 4016-4038.

McCauley, J. F., et al, 1972, Preliminary Mariner 9 report on the geology of Mars: Icarus, v. 17, p. 289-327.

Schoenfeld, Ernest, 1974, Martian volcanism: in Abstracts, Eighth Lunar Science Conference, Part II p. 843-845, Lunar Science Inst., Houston, Tex.

Thorarinsson, Sigurdur, 1957, The jökulhlaup from the Katla Area in 1955 compared with other jökulhlaups in Iceland: Reykjavile Museum of Nat. Hist., Misc. Paper No. 18.

ANALYSIS OF SHAPE-FREQUENCY HISTOGRAMS OF TERRESTRIAL AND MARTIAN REMNANT LANDFORMS

Duane T. Eppler, P. Jeffrey Brown,
Robert Ehrlich, Dag Nummedal

Department of Geology,
University of South Carolina,
Columbia, South Carolina 29208

INTRODUCTION

The morphology of remnants formed by fluid erosion and deposition is dependent on the physical characteristics of the system in which they form. Factors such as fluid density, viscosity and velocity, sediment size, the degree to which eroded material is consolidated, and structural control in the eroding substrate will determine, to a large extent, the shape of resulting remnants. Thus, a quantitative study of the planimetric shape of features formed in different environments might permit identification of shape components that are characteristic of a given process or substrate characteristic. Subsequent comparison of such terrestrial analogue groups to erosional remnants in and adjacent to channels on Mars might permit general inferences to be made regarding the nature of processes that sculpted the Martian features.

METHODS

Discrete Fourier analysis in closed form (Ehrlich and Weinberg, 1970) is used to make quantitative comparisons between the shape of several types of terrestrial landforms, each representing a different environment and process, and a sample of erosional remnants from Mars. The terrestrial erosional features were selected so as to provide a sample that represents environments hypothesized to be similar to those in which the Martian channels may have formed. The sample consists of (1) well developed braided stream bars on the outwash fan of the Skeidra glacier in Iceland, traced from low-altitude aerial photographs, (2) wind eroded yardangs from the Rio Ica Valley of Peru, traced from high-altitude aerial photographs, and (3) erosional remnants carved by catastrophic floods in both Pleistocene loess and Yakima flood basalt of the Washington Scablands, traced from 1:62,500 topographic maps. The sample of Martian forms was traced from both Mariner and Viking imagery and consists of remnants located within Mangala, Kesai, and Chryse channels and on Chryse Planitia. All landform outlines then were digitized and the Fourier series of harmonic amplitudes describing each shape were computed.

COMPARISON OF TERRESTRIAL CANDIDATE ANALOGUES

Histograms showing frequency distributions of the second harmonic amplitude for landform groups studied are shown in Figure 1. Such histograms display graphically shape characteristics that are representative of a particular sample (Eppler, et al., 1978). The relationship between process of formation and land form shape is discussed below by making comparisons

between shape-frequency histograms of terrestrial features formed under different conditions.

Duration of Process: Braided stream-bars and yardangs are formed by long-term, ongoing processes. The unimodal nature of their histograms suggests that each group approaches a common shape that is in equilibrium with a particular formational process. In contrast, both types of scabland remnants formed in a short-lived, catastrophic flood. The polymodal nature of their histograms indicates that the formational process either was too violent or too brief to sculpt landforms of a common shape that was in equilibrium with the flood.

Structural Control in Eroded Substrate: Geologic structure of Yakima flood basalt into which scabland remnants have been carved is characterized by a rectangular joint pattern. Erosion of such joint controlled material should produce an abundance of equant shapes. The magnitude of second harmonic amplitudes is a direct measure of elongation. Highly elongate shapes have high second harmonic amplitudes; equant shapes have low amplitudes. Appearance of a strong mode at the left (low amplitude) tail of both the loess and basalt scabland distrubutions represents the effect of structural joints on remnant shape. These same modes are absent in both the braided stream-bar and yardang distributions where structural control is not a factor.

Erosional vs. Depositional Origin: Braided stream-bars are hybrid features formed by both erosional and depositional processes. They are formed by divergence of flow across the surface of the bar producing active erosion at the upstream end and deposition along the flanks. The shape of the resulting feature is characteristically short and squat. In contrast, a landform that is shaped exclusively by erosional processes along its flanks will become increasingly elongate as erosion procedes. Flow divergence around a remnant such as a yardang causes erosion to be most intense at the flanks. These fundamental differences are expressed in shape-frequency histograms as a shift in the position of the mode between the yardang and braided stream bar histograms (Fig. 1).

COMPARISON OF TERRESTRIAL ANALOGUES WITH MARTIAN FEATURES

Comparison between frequency distributions of terrestrial analogues and Martian remnants permits the following conclusions to be made:

1. Of all four groups of terrestrial landforms studied, the yardang distribution resembles the Martian distribution most closely. This does not necessarily mean that the Martian forms are yardangs. Rather, processes active in the Martian environment have produced forms that are similar in shape to terrestrial yardangs.

2. The absence of a large number of equant forms in the Martian population implies that:

    a. On the basis of planimetric shape, few if any of the Martian features can be considered to be true analogues to terrestrial bars;

b. Structural control in the form of rectangular jointing either is absent in regions where Martian remnants occur, or it is present but its influence on shape has been overridden by the magnitude of the process which carved the remnants.

3. The even spread of Martian remnants across the histogram corresponds well to neither the polymodal scabland histograms nor the unimodal nature of yardang and braided stream bar distributions. Lack of significant modes indicates that interaction between the Martian landforms and the process by which they are formed does not produce a preferred shape. Additional work is required to determine whether or not a terrestrial analogue to such a process exists. A distribution lacking modes also might result if the Martian sample contains landforms sculpted by several different processes, each producing one or more unique modes. The large number of diverse theories proposed to explain the origin of channels on Mars is evidence in itself that a single process may be inadequate to explain all that we see.

REFERENCES CITED

Ehrlich, R., and Weinberg, B., 1970, An exact method for characterization of grain shape: Jour. Sed. Petrology, v. 40, p. 205-212.

Eppler, D. T., Nummedal, D., and Ehrlich, R., 1978, Fourier analysis of lunar crater shape--possible guide to impact history and lunar geology: in Impact and Explosion Cratering (D. J. Roddy, R. O. Pepin, and R. B. Merrill eds.), Pergamon Press, N. Y.

FIGURE 1
HISTOGRAMS--SECOND HARMONIC

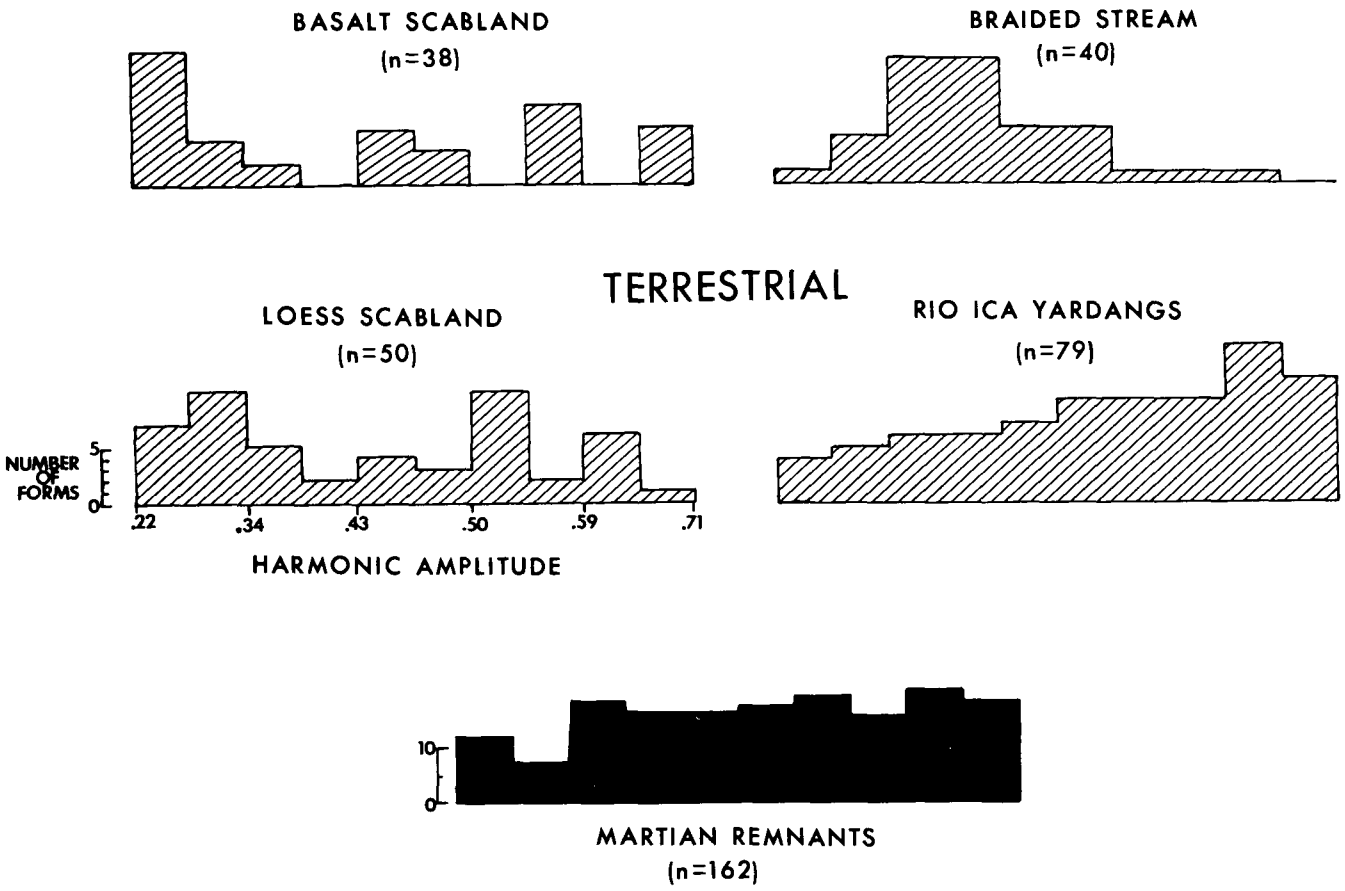

Small Channels on Mars from Viking Orbiter, David Pieri, Laboratory for Planetary Studies and Department of Geological Sciences, Cornell University Ithaca, NY 14853

Viking data show a rich heterogeneity of small channel morphology which may imply both a diversity of material response to the process which creates small channels and a diversity in the genetic processes themselves. Good quality imaging of channel systems in the Margaritifer Sinus region shows four distinct small channel morphology classes in that area (smooth and crenelated walled channels with V or U shaped cross sections), most likely related to differential erosion in varying lithology. Structural control varies systematically from strong (highly rectilinear graben controlled) to weak (dendritic in intercrater plains) and is likely evidence of heterogeneity of genetic processes. Interior talweg-like channel reaches have been discerned along with possible terracing. Ubiquitous flood lavas have buried the original terrain, although the higher, heavily cratered sub-regions have tended to preserve preexisting networks. Small channel networks are observed to occur in several planimetric geometries: (a) radially inward to shallow old basins, (b) radially inward and outward on the rims of some older basins, (c) dendritic-like in inter-cratered plains and (d) occasionally allogenous showing few or no tributaries away from "source" areas. Deposits concentric to the rim of Schiaparelli Basin correlate with the penetration of the rim by small channels and may be deltaic. Small channel networks occuring in northern high albedo terrains imaged by Viking show muting due to overlying debris blankets. Viking Orbiter images of Nirgal Vallis demonstrate that (1) slope processes are active on valley walls, including landsliding, (2) wall scalloping due to slope failure can produce alcoves which may mimic meandering, (3) debris accumulations on the valley floor indicate that any channel interior crater size-frequency distributions represent only a minimum bound and (4) headward branching valleys in the Nirgal system widen distally. Nirgal and the few other Nirgal-type channels (e.g., Neredi Vallis) may represent a unique combination of lithology and process which may not be entirely relevant to small channel formative processes generally. Although the small channels are probably the result of a spatially and temporally diverse (though ancient) erosion process in cratered terrain, they exhibit systematic branching networks extremely suggestive of either downhill overland flow of water or, perhaps more likely, subsurface erosion by wet or dry sapping.

Junction Angles of Martian Channels, David Pieri and Carl Sagan, Laboratory for Planetary Studies, Cornell University, Ithaca, NY 14853

Small channels on Mars exhibit stream branching ratios high by terrestrial standards (5-8) implying relative immaturity of system development. However, since Shreve (1966) predicts a branching ratio of 4 for any dendritic, non-reentrant network, little more can be accomplished in this manner with regard to genetic process. A general model for tributary junction angle as a function of Shreve link-magnitude has been developed for terrestrial river and arroyo systems and has been tested for a wide range of terrains and climatic regimes. At least 1500 junction angles have been measured in about 10 major terrestrial systems at scales varying from the small Perth Amboy badlands to Landsat images of the Rocky Mountains. The fit to predicted curves is quite good at all scales, although the scatter varies. Several martian systems have been analyzed so far, including Nirgal, 3 systems in Margaritifer Sinus, and the dendritic channel system in Thaumasia. Martian networks depart in two important ways from terrestrial systems analyzed in this fashion: (1) martian systems never exhibit, for a given tributary link magnitude, mean junction angles > 40° and (2) the standard deviation of martian tributary junction angles is about three times that of terrestrial networks. These data coupled with the remarkable incision of the martian channels imply, at least for some martian systems, basal flow sapping, either artesian or purely gravity-induced, or even dry sapping by sublimation, with little or no surface watershed development. The argument of generally shallow junction angles and inter-channel septum retention being the result of general overland flow on a very shallow surface is weakened by the lack of low magnitude tributary deflection into major trunk valleys, as is seen in terrestrial networks, even in the highly incised streams of the Colorado Plateau.

Simple scaling of the laws of flow for rivers on the Earth imply for Mars (1) that for turbulent flow the reduction in threshold velocity matches the reduction in available flow velocity due to gravity, (2) assuming that the variability of stream junction angles scales inversely as the ratio of inertial to tractive forces, that the variability of junctions angles for a given trunk-tributary magnitude ratio is gravity-independent and is both density- and, indirectly, viscosity-dependent (this should apply universally for tractive erosion by fluid flow), and (3) that cavitation should be a major force in hypothetical breakout flooding based on a simple consideration of Bernoulli's Law.

Channeling History of Maja Vallis, Eilene Theilig and Ronald Greeley, Dept. of Geology, Arizona State Univ., Tempe AZ 85281

Maja Vallis is a large channel extending from Juventae Chasma northward across Lunae Planum to Chryse Planitia. Masursky et al. (1977) and Carr (1978) included Maja Vallis in a class of channels they consider to have been formed by catastrophic floods of water released from chaotic terrain. Maja Vallis is about 1200 km long and ranges from 25 to 100 km wide. This study is restricted to the section of Maja Vallis from about 17°N, 57°W eastward to Chryse Planitia. This area was chosen for study because at least two periods of channeling can be demonstrated. In addition, because the channel passes from Lunae Planum through hilly and cratered terrain to Chryse Planitia, information on the stratigraphy of the area may provide clues to the age and origin of the northern plains.

Three major types of erosional features occur within Maja Vallis: 1) large, erosional remnant "islands", 2) widespread scoured surfaces, and 3) channels. 1. Remnant "islands" (fig. 1,a) are topographically high features that dominate the western part of Maja Vallis; they range from small, streamlined features to larger tear-drop shaped "islands" formed by flow from the west. Scarps and alternating light and dark bands oriented along the sides of some remnants may indicate stratigraphic layers. Most of these remnant islands do not have craters on the upstream end as is common farther west on the plains and at the mouths of the channels entering Chryse Planitia from the south. In these areas, craters are commonly considered to have been the obstacles behind which the "islands" formed. Since this is not the case here, resistant lithologic zones or structural controls are probably responsible. The plains unit between the remnants is an erosional surface and exhibits small scour features oriented with the inferred flow direction and narrow ridges parallel to the edges of the remnants. 2. Scoured areas (fig. 1,b) are defined by numerous closely spaced ridges and mounds that are parallel or subparallel to the trend of the channel. They become prominent where the broad channels from the west and south merge and become deeper and more restricted. This surface forms the major part of the floor of Maja Vallis and extends up the northern bank to the upper level of the channel. At the entrance to the major channel the ridges and mounds are more subdued with small scale channeling being more prominent. Elsewhere the ridges and mounds are steep and are often rough and irregular. This erosional scouring pattern may be a characteristic erosion form of the remnant material when the upper surface has been stripped away and the material subjected to a flow regime associated with the narrower, deeper channel, or it may represent a layer of different composition below the material comprising the remnants. 3. Small U-shaped channels (fig. 1,c) may be divided into two morphological types. The first type includes flat-floored, steepsided channels incised into the scoured areas and forms the lowest erosional surface within Maja Vallis. The second type has less distinct walls and occurs at a higher level than the incised channels. Three major incised channels in the west merge toward the east and form the canyon through the mountainous material where Maja Vallis

debouches into Chryse Planitia. Most of the incised channels merge with the surrounding materials at their upstream ends; however, one channel ends in a "box" canyon.

Maja Vallis has been formed by at least two, and possibly three episodes of channeling. The first episode is indicated by a tributary (fig. 1,e) to the south. The relative age of this channel has been determined by superposition. This channel occurs in the older, heavily cratered terrain which extends along eastern Lunae Planum; although it is distinct near Maja Vallis it becomes subdued southward where it is overlain by ejecta from a large crater. The ejecta on the other side of the crater, however, has been eroded by a channel representing a second episode of channel formation. The fact that most of this channel is more heavily modified than the rest of the system is also an indication of greater age. The lower reaches were reoccupied by fluids flowing above the main bank of Maja, resulting in the fresher appearance of that section. Channels of similar appearance and age occur to the south.

The second channel episode produced the features seen in the major Maja Vallis channel. This flow originated in the chaotic terrain of Juventae Chasma and moved northward across Lunae Planum to the section of the channel where two branches merged, creating erosional features in both the west and the south. The flow eroded large volumes of material leaving the remnant "islands" surrounded by an erosional surface. As the channel increased in depth and became restricted in the hilly and cratered terrain, prominent scouring within the channel occurred. The material removed from Lunae Planum was deposited on the western slope of Chryse Planitia as the fluid flowed into the basin. During the later stages of the flood, small channels were incised into the floor of Maja Vallis and part of the deposits at the mouth of the canyon were eroded as the floor of the channeling activity was lowered. This could also have been related to a second discharge episode from Juventae Chasma or a third independent channel event.

References:

Carr, M. H., 1978. Martian Channels, in press, Scientific American.

Masursky, H., Boyce, J. M., Dial, A. L., Schaber, G. G., and M. E. Strobell, 1977. Classification and time of formation of martian channels based on Viking data. Jour. Geophys. Res., Vol. 82, No. 28, pp. 4016-4038.

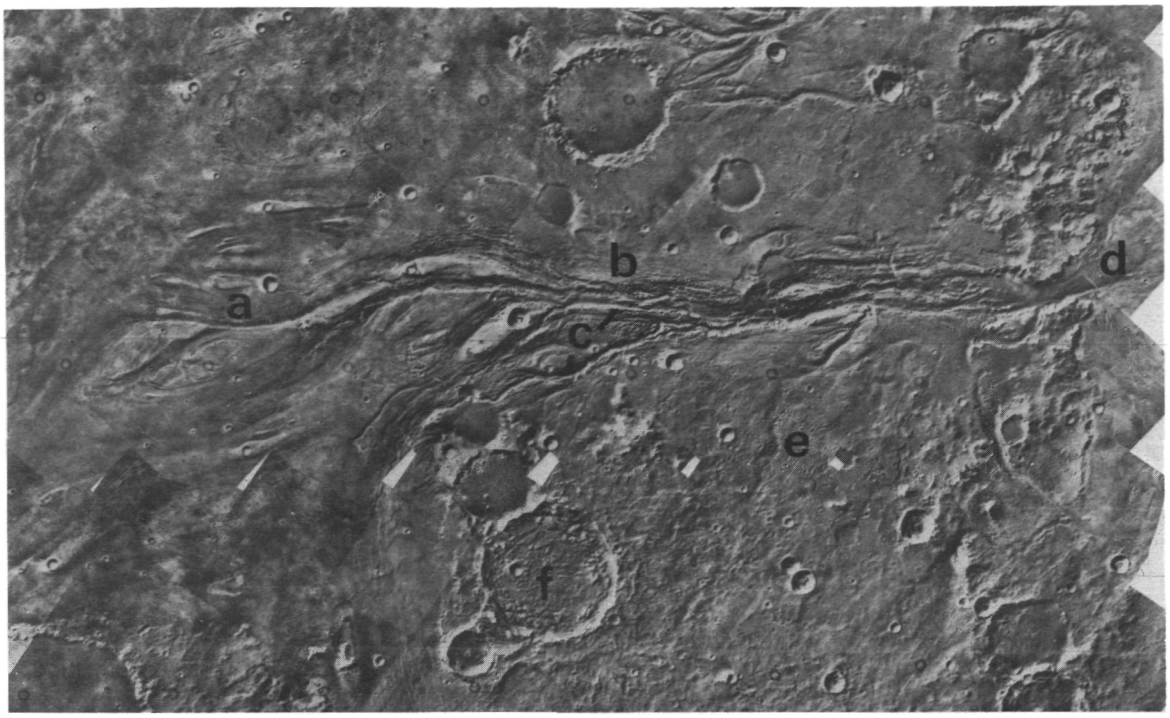

Figure 1: Viking mosaic of Maja Vallis; a. "island" remnants, b. scoured areas, c. incised channel, d. mouth of Maja Vallis, e. older degraded channel of first channeling event, f. crater used for determination of relative ages of the channels. North is to the top of the figure, Chryse Planitia is to the right. The area shown is approximately 100 km by 170 km.

Stability Analysis for the Origin of Martian Fluvial Features, David E. Thompson, Jet Propulsion Laboratory, Pasadena, CA 91103

The origin of major fluvial features and channel bed forms is an important unresolved question in Martian geomorphology. Earth analog/descriptive studies tend to indicate that many of the large Martian channels originated from catastrophic flooding events akin to the Pleistocene debouching of glacial Lake Missoula (Baker and Milton, 1974). Presumably some form of mobilization of water from subsurface permafrost is the most reasonable explanation for the source of such Martian flooding. However, considering the wide range of channel sizes and complexities in drainage patterns, it is not necessary that water alone be considered as the prime erosive agent. Most fluvial features observed in the Viking images are suggestive of formation by rather low viscosity fluids. Nevertheless, given that fluvial-type features can be found on Earth which are very similar in morphology but which originate under radically different environmental conditions (for example, extensive longitudinal grooving found in major dry river channels as well as the ubiquitous longitudinal grooving of the land surface in glaciated regions of Canada and elsewhere), it is reasonable to allow for the possibility that any of several types of fluids or fluid-debris mixtures (water, mudflows, debris flows, slush-debris flows, lava flows, or more viscous or visco-plastic surges) may be responsible for the formation of the surface channel features observed.

The fluvial features themselves provide a mechanism by which one may decipher the types of fluids responsible for creating the observed bed forms. By studying analytically the stability of fluids of various rheological properties against basal perturbations which correspond in aspect to the size and form of the observed Mars features, and by constraining the form of the perturbation to these data while varying the rheological properties, the rheology of those fluids which allow stable secondary flow to arise of an aspect characteristic to the observed features can be ascertained. In this sense, a class of fluids, defined by their rheological properties, is being determined which have the potential of creating the observed Martian features. These fluids then can be related to selected types of fluids, debris flows, or ice-rock-debris fluids known on Earth which have these corresponding rheological properties.

Much recent theoretical analysis has been carried out on the stability of river channels, on the cause of meandering or braiding in channels, and on the stability or evolution of fluid or fluid-sediment flow itself (Callander, 1969; Grishanin, 1972; Engelund and Skovgaard, 1973; Engelund, 1975; Eagles and Weissman, 1975; Parker, 1976; Smith, 1977). These studies provide guidance for the perturbation analysis described here, but here variations in rheology or in specific gravity or density are included in both the equations and the stability criteria.

Fluvial features arising from channel bed instability or from stable secondary currents within a fluid can develop from two basic types of perturbations. First, disturbances which are characterized by wavelengths of the size of or greater than the stream width give rise to large scale features such as channel bars, extensive longitudinal grooving or deposition, or mid-stream islands. These features are intimately connected with the meandering or braiding nature of the stream. Second, disturbances with wavelengths on the order of the fluid depth are responsible for small scale channel bed features such as ripples, dunes, or various cross-current deposits related to local bed morphology and small scale secondary flow. Because of the dichotomy in length scales appropriate to types of features, and hence to each type of perturbation, a given fluvial system may be regarded as, for example, stable against long wavelength perturbations but still contain any number of features which arise directly in response to small-scale instability in either the fluid itself or the channel bed. Similarly, a highly meandering or multiple-braided reach of a channel may be comparatively uniform along its bed. Fluid instability analysis which intends to delineate the feature-forming potential of various fluids must include this length scale dichotomy either in terms of the perturbation expansion parameter involving the appropriate disturbance wavenumbers (i.e., by carrying out a different perturbation scheme for each length-scale problem) or in terms of some similarity transformation which remains invariant in the stability analysis irrespective of whether the perturbation is imposed on a deep-narrow channel fluid (the small-scale feature problem) or on a shallow-broad channel fluid (the large-scale feature problem). Either approach should yield similar results and stability criteria, and both approaches are applicable to fluids of various rheology, specific gravity, or density variations.

It has been found expedient, however, to restrict the class of basal perturbations to either 1) doubly-periodic disturbances imposed as changes in channel bed elevation h

$$h = h_o \cos(k_2 x_2) e^{ik_1 x_1}$$

where x_1 and x_2 are the longitudinal and transverse coordinate directions, and k_1 and k_2 are wavenumbers, or 2) full solenoidal disturbances which immediately give rise to longitudinal, helicoidal disturbances at the channel bed. The doubly-periodic disturbance is required for meander/braiding analysis and is, in a sense, a subset of the solenoidal disturbance class. Furthermore, either type of perturbation is applicable to generation of small scale features by secondary currents, and the doubly-periodic disturbance can initiate standing-wave distributions in the flow. The solenoidal or helicoidal perturbations allow development of extensive longitudinal grooving as well as lateral migration or transport of bed material. Other perturbation classes such as simple-longitudinal or simple-transverse are not being considered because they do not relate independently to the full category of large- and small-scale feature development. They will be more important

when the analysis requires a more detailed study of specific channel features. Thus, it is felt that the above-defined restricted class of perturbations are complete and applicable to the main problems of interest for the origin of both the large scale and small scale features.

The stability analysis being carried out on fluids of various rheologies yields results in the form of a class of perturbation wavenumbers which grow when imposed on certain initial primary flow fields. The growth or decay of disturbances depends on the rheology or specific gravity of the primary-state fluid. It is important to recognize that it is not this class of wavenumbers, arising from linear theory, which must correspond to the observed fluvial features. Rather, it is the stable secondary flow patterns which develop in this fluid from these initial, unstable perturbations that actually must form the surface features observed. Although the secondary flow is not necessarily of the same wavelength as the unstable disturbances, the two wavelengths are related and can be separated by energy considerations in finite amplitude analysis.

The Viking Orbiter images are not of high enough resolution in many cases to decipher what are here termed the small-scale bed features. Large scale features are evident. Despite the dichotomy in length scale stability considerations discussed above, this instability analysis will nevertheless provide a detailed classification of potential channel bed forms associated with the small scale instability for various types of fluids. Even if these features cannot be observed presently, environmental considerations derived from whole-channel stability analysis should allow reasonable speculation as to their actual presence on Mars.

REFERENCES

Baker, V. R. and Milton, D. J., 1974, Icarus, 23(1), p. 27-41.

Callander, R. A., 1969, Jour. Fluid Mech., 36. p. 465-480.

Eagles, P. M., and Weissman, M. A., 1975, Jour. Fluid Mech., 69, p. 241-262.

Engelund, F., and Skovgaard, O., 1973, Jour. Fluid Mech., 57, p. 289-302.

Engelund, F., 1975, Jour. Fluid Mech., 72, p. 145-160.

Grishanin, K. V., 1972, Soviet Hydrology, selected papers no. 5, p. 382-389.

Parker, G., 1976, Jour. Fluid Mech., 76, p. 457-480.

Smith, F. T., 1977, Jour. Fluid Mech., 79, p. 631-655.

Large Scale Erosive Flows Associated With Chryse Planitia, Mars: Source and Sink Relationships, K.R. Blasius, J.A. Cutts, and W.J. Roberts, Planetary Science Institute, 283 S. Lake Ave., Ste. 218, Pasadena, CA 91101

Enormous channels 500 to 3000 km long associated with the Chryse Planitia lowland have a total area of at least $2 \times 10^6 km^2$ but their apparent source regions (mostly chaotic terrain) total less than $1 \times 10^6 km^2$. The occurrence along these channels of evidence of fluid erosion - primarily anastomatic reaches, streamlined bedforms, and islands, and the topographically depressed character of chaotic terrain led previous investigators (1,2,3,4) to hypothesize catastrophic release of liquid water from the areas of chaos as they subsided. A reassessment of this hypothesis here is based upon stratigraphic and topographic relationships seen in Viking Orbiter images:

a. Fluid erosional forms of substantial relief occur on central and northern Chryse Planitia, far beyond the presumed sink for flood debris.

b. The channels or zones of fluid erosion generally broaden downslope, contrary to their appearance in poorer quality pre-Viking images.

c. Where channel heads join chaotic terrain the streamlined erosional forms are truncated abruptly, often along a scarp facing the chaos interior. No drainage networks are seen within the chaos.

Fluid erosion by large scale flows extends greater distances (up to at least 3000 km) and eroded far greater areas ($> 2 \times 10^6 km^2$) than previously inferred. The total estimated volume deficience in source regions and the estimated volume of downstream erosion are approximately the same ($5 \times 10^5 km^3$) and by terrestrial standards are inconsistent with the catastrophic one-time release of water from chaos.

Zones eroded by large scale flows broaden downslope as if the mechanism of incision gathered power. In the hostile (cold and low pressure) environment of Mars surface evaporation, freezing, and absorption into the regolith would be expected to diminish the erosive power fo flood waters away from their source. Apparently, the fluid involved or an erosive bedload were incremented significantly downstream from the chaotic terrain.

Chaotic terrain development appears to have been prolonged beyond the period of channel incision to enlarge the area of chaos at the expense of both the surrounding ancient cratered terrain and the channels. Thus, patches of chaos cannot generally be considered representative of the original morphology of channel source regions. Additionally, the present areal extent of chaos connected to large scale flow channels is

an overestimate of the possible source area for catastrophic water outflow; the discrepency cited above between estimated erosion and water outflow is thus enhanced.

The features formed by large scale channelized flows onto Chryse Planitia are better explained by repeated atmospheric flows than by one-time emptying of several water reservoirs. The chaotic terrain is envisioned to have been the source of an erosive saltating bedload for the flow rather than the source of fluid. The apparent increase in erosion downstream may be the consequence of the building up of both suspended load and bedload in the flow.

During the search for a landing site for Viking 1 much of Chryse Planitia was photographed at high resolution (40 to 50 m per picture element) in a vain attempt to locate the sediment dumped by the hypothetical great floods. The evidence found recently indicating erosive flow out of Chryse Planitia to the north, and the proposal here that the flows were atmospheric in origin allows one to conceive of spreading more widely the debris scoured from channels. The suspended load may have been spread around the planet over the north polar region and the vast northern plains (Vastitas Borealis) while the saltating bedload probably accumulated more locally, perhaps forming the plains and mesa units observed in patches in eastern Acidalia Planitia at the proposed Cydonia landing site for Viking 2 (5).

REFERENCES: (1) Milton, D.J., 1973, J. Geophys. Res., 78, 4037-4047; (2) Baker, V.R. and Milton, D.J., 1974, Icarus 23, 27-41; (3) Sharp, R.P. and Malin, M.C., 1975, GSA Bull., 86, 593-609; (4) Masursky, H., et al., 1977, J. Geophys. Res., 82, 4016-4038; (5) Guest, J.E., et al., 1977, J. Geophys. Res., 82 4111-4120.

CHAOTIC TERRAIN AND CHANNELS ASSOCIATED WITH CHRYSE PLANITIA, MARS: AN ALTERNATIVE EROSIONAL MODEL

J.A. Cutts, K.R. Blasius, W.J. Roberts, Planetary Science Institute, 283 S. Lake Ave., Ste. 218, Pasadena, CA 91101

In a companion paper (1) we cited certain quantitative and qualitative evidence from surface morphology and topography to argue that catastrophic release of water from chaotic terrain was inadequate to cause the extensive erosion observed in channels and on Chryse Planitia. Instead we proposed that atmospheric flows moving both suspended and saltating loads could more adequately explain the features observed.

Here we compare in detail the erosional characteristics of martian outflow channels and source areas with those of terrestrial catastrophic floods and with a mathematical formulation of the alternative aeolian hypothesis.

Disturbing inconsistencies between the erosional consequences of terrestrial catastrophic floods and hypothesized martian counterparts first emerge when we examine the relationships between gross volumes of erosion and source volume (Fig. 1a). The ratios of volumes of erosion to source volume cluster independently for the earth and Mars separated by three orders of magnitude. For some channels, it appears that the flood-waters must have excavated and transported several times their own mass from the martian terrain.

The relationship between the amount of erosion and distance from the source Fig. 1b, is also revealing (Fig. 1b). Whereas terrestrial floods tend to lose their erosive power with distance from the source as the transporting capacity of the waters becomes saturated with moving debris, it appears that the appetite of the martian floods is enhanced. Clearly, the generally accepted catastrophic flooding model for channel formation is inadequate and there is some question that any fluvial model can explain the data of Figs. 1a and 1b.

Our theoretical aeolian model designed to account for the relationship between chaotic terrain and outflow channels and the erosional characteristics of Figs. 1a and 1b has the following elements. The model involves a type of avalanche effect in which saltating particles drawn from the chaotic terrain impact particles of comparable size causing them to participate in a ground hugging sand blast. Significant erosion takes place when this sand blast injects finer particles into atmospheric suspension.

We consider the source-channel geometry of Fig. 2 in which a flux (F_o) of saltating (bounding) particles is released into a channel width w_o km with an angular divergence of Q. The maximum transport capacity of the wind (F_1) is considered to be uniform throughout the channel and larger than F_o. We assume that the rate of erosion is not limited by the rate of production of small sand and dust sized particles by weathering but rather by this transport capacity for saltating particles and by the efficiency with which even finer particles of dust can be injected into suspension. In this circumstance it can be shown that the ratio (R) of the amount of erosion performed within the channel up to distance x from the source to the total mass flow from the source that was ultimately responsible for that erosion is:

$$R(x) = (1 + \ell_1/\ell_2)\ (e^{x1/\ell_1} - 1)$$

$$+ F_1/F_0\ (x-x')\ \{\theta/w_0 + \frac{1}{\ell_2}\ \ 1 + \frac{(x + x')}{2}\frac{\theta}{w_0}\ \} \qquad (1)$$

where F_1, F_0, w_0 and θ have already been defined, x' is the solution of

$$e^{x1/\ell_1} = \frac{F_1}{F_0}\ (1 + x'\ \theta/w) \qquad (2)$$

ℓ_1 is the e-folding distance for the increase in the flux of sand grains within the channel and ℓ_2 is the distance a saltating (bouncing) grain must travel in order to inject its own mass into atmospheric suspension. The essential physical process determining ℓ_1 and ℓ_2 is illustrated in Fig. 2b and ℓ_1 and ℓ_2 can also be expressed in terms of the mean saltation length (ℓ), diameters ad and as of dust and sand grains respectively and other parameters p and n defined in Fig. 2b as

$$\ell_1 = \ell/p \quad ; \quad \ell_2 = \frac{\ell}{n}\ (\frac{as}{ad})^3 \qquad (3)$$

In Fig. 3 theoretical and observed values of erosion ratio R(x) are compared. Approximate agreement with the form of the observed R-x curves can be achieved with at least two different choices of parameters for the theoretical curves. If ℓ_1 is on the order of the length of the channel and $F_1/F_0 = 10$, then the observed rapid increase of R with x can be duplicated (Curve A). This is the situation where the sand supply is extremely limited. On the other hand, in a situation where both the sand concentration on the channel floor and F_0 are high (F_1/F_0 is small 1, $\ell_1 <$ 50 km) then the transport capacity of the wind is saturated. In these circumstances, then the observed R-x relationships can be approximately reproduced (Curve C) although the fit to the slope of the observed R-x relationship is not very satisfactory.

Observations of several of the channel floors suggest a lack of dune cover compared to the situation in many other areas on Mars. This indicates the sand supply limited situation of Curve A may be the more appropriate model for these channels. A much more detailed study of the channel geometry and a more exact treatment of the aeolian processes is needed to confirm this.

In summary, we have developed a model of outflow channel formation which accounts for the intimate physical relationships of these channels to chaotic terrain, for the large sizes of these erosional features with respect to the source areas, and for the increase in size with distance from the source. The model involves a type of avalanche effect in which saltating particles emerging from the chaotic terrain impact particles of comparable size causing them to participate in the ground hugging sand blast. Significant erosion is contributed when this sand blast injects finer particles into atmospheric suspension.

REFERENCES: (1) Blasius, K.R. et al. 1978.

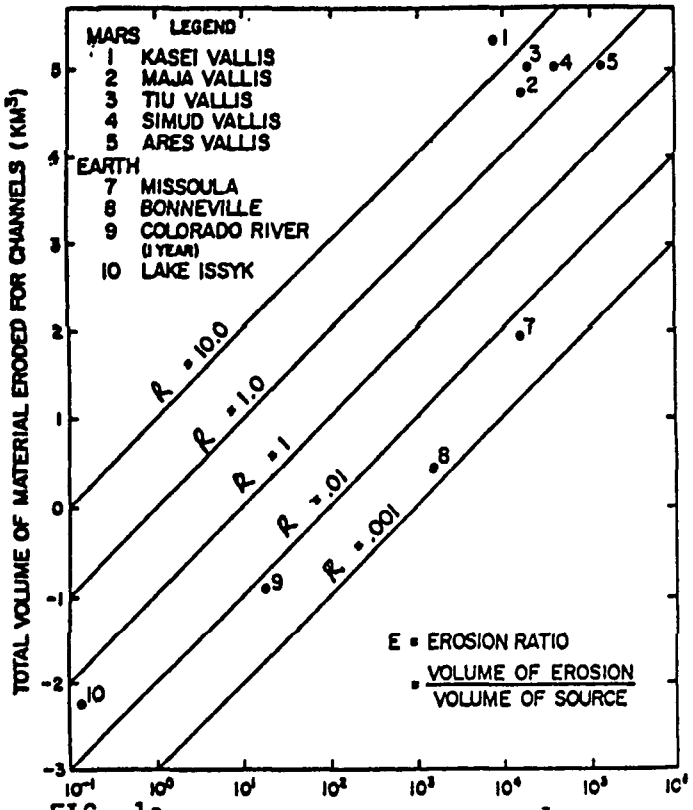

FIG. 1a

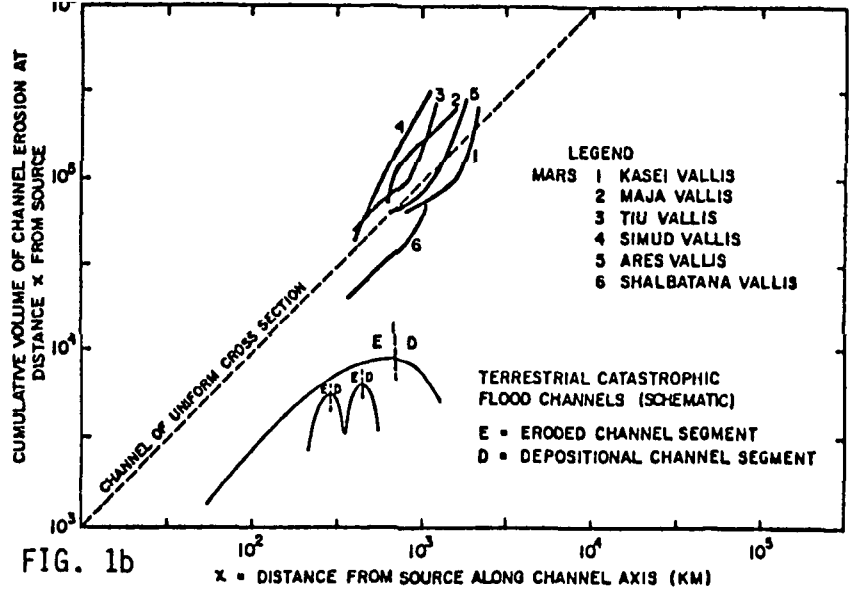

FIG. 1b

$\omega = \omega_0 + x\theta$

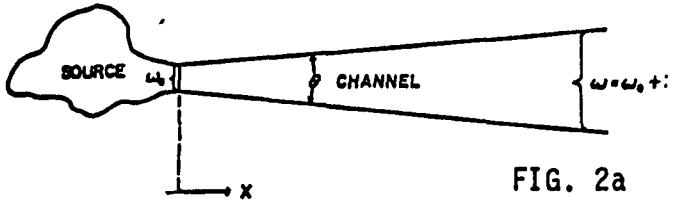

FIG. 2a

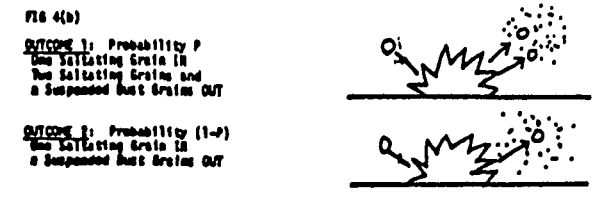

FIG. 2b

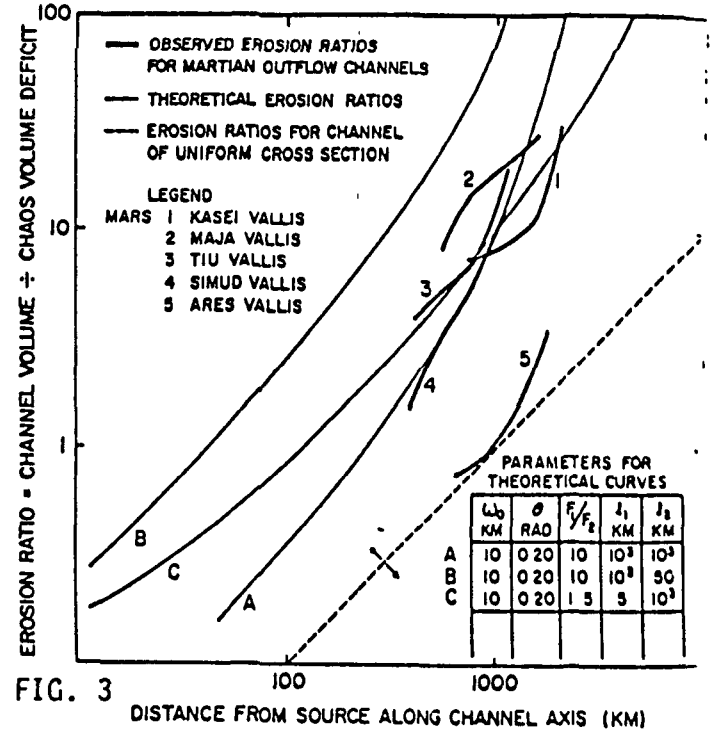

FIG. 3

The Flow Mechanics and Resulting Erosional and Depositional Features of Explosive Volcanic Density Currents on Earth and Mars.

Clare E. Reimers and Paul D. Komar, School of Oceanography, Oregon State University, Corvallis, Oregon 97331.

At the northeast margin of the Tharsis volcanic province of Mars are clustered three volcanic domes, Ceraunius Tholus, Uranius Tholus, and Uranius Patera. A similar dome, Hecates Tholus, is located in north Elysium. Important differences between these smaller domes and the four great Tharsis shields include: (1) slope angles, (2) caldera morphologies, (3) the presence on the domes but not on the shields of numerous radial channels which extend from just below the rim toward the base of the cone, and (4) apparent blanketing (ash?) on the lower flanks of the domes but not on the shields.

A possible explanation for the morphological features associated with the domes is that they were formed by explosive volcanic density currents. Such eruptions would be expected on Mars where a volcanic conduit came in contact with a thick layer of ground ice generating a base surge flow, or after a Volcanian explosion of a separate gas phase producing a nuée ardente.

A model to explain the physical processes of explosive volcanic density current transport, erosion and deposition is developed from the equations governing turbidity currents and debris flows, similar species of sediment gravity flows. The model reasonably illustrates the mechanisms which create erosional and depositional features associated with many tuff rings and composite volcanoes on Earth, and implies formation of comparable features on Mars.

Corroborating evidence is the remarkable similarities in summit and flank morphologies shown between Ceraunius Tholus on Mars and Barcena Volcano on Earth. Barcena Volcano, Isla San Benedicto, Mexico, is a tuff cone which was sculptured by base surge density currents during a shallow phreatic eruption in 1952 (1). Photogeologic observations of erosional and depositional forms point strongly to an analogous presence of copious ground water or ice during the time of the formation of Ceraunius Tholus and the other mentioned martian domes. Crater age data indicate these volcanic constructs probably represent an intermediate period of martian volcanism (0.5 to 2 billion years), older than the quietly erupted flank surfaces of the giant Tharsis shields and the basal plains. This is consistent with the view that martian atmospheric conditions in the past may have been more favorable for abundant water to condense and percolate downward in the vicinity of volcanic conduits.

(1) Richards, A.F., Bull. Volcanology, 22, 73-123 (1959).

The Mechanics of Transport of Gravity-Driven Debris Flows.

Paul D. Komar, School of Oceanography, Oregon State University, Corvallis, Oregon 97331.

Landslides, debris flows and turbidity currents form a range of mass transport processes that involve gravity-driven flows consisting of mixtures of sediment and water. Landslides do not entirely destroy the original fabric of the sedimentary material forming the flow. In contrast, within debris flows all of the material actively participates in the flow process and flow shearing completely destroys the initial fabric. Debris flows are characterized by high concentrations of sediments (mud plus rock clasts) such that flow turbulence is prevented, the flow instead being laminar or pseudo-laminar. This differs from the low-concentration turbidity currents with their turbulent flow.

In spite of their high sediment concentrations, which should lead to high internal drags (apparent viscosities), debris flows can be surprisingly mobile. Another significant observation is that the clasts within the flows are sorted into an inverse grading, the largest clasts moving to the top of the flow with progressively smaller clasts toward the flow base.

Such flows are being analyzed through considerations of the apparent viscosity of suspensions and the forces produced by the interactions between clasts during flow. A number of equations have been proposed to evaluate the apparent viscosity of a fluid-granular mixture under shear, relating the apparent viscosity to the concentration and size of the grains and to the rate of shear. These equations have been

reviewed with the existing laboratory measurements of apparent viscosity.

Considerations of the clast interactions during flow involve the fundamental work of Bagnold (1) on the grain dispersive pressure produced when a granular suspension is sheared. At high stages of grain interaction, Bagnold showed that this dispersive pressure P_i is given by the relationship

$$P_i = a_i \rho_s (\Lambda D)^2 \left(\frac{dU}{dy} \right)^2$$

where ρ_s and D are respectively the density and diameter of the grains, Λ is the linear concentration of grains, dU/dy is the local velocity gradient, and a_i is a dimensionless coefficient. In a flow the velocity gradient dU/dy is a maximum at the base of the flow, decreasing upward until it becomes zero at the flow surface. If D and Λ are initially constant throughout the flow thickness, it is apparent that P_i will be a maximum at the flow base, decreasing upward. As pointed out by Bagnold, this vertical gradient in P_i will cause grains (clasts) to migrate upward toward the flow's surface, the larger clast sizes migrating preferentially. This migration will continue until there is a vertical balance between this upward dispersive pressure gradient and the downward force of gravity.

The present analysis of debris flows is an attempt to include both the dispersive pressure considerations of Bagnold (1) together with a satisfactory inclusion of the internal drag on the flow due to the apparent viscosity of the granular flow. Such a model explains both the vertical sorting of clasts within a flow and the observed mobility. The analysis

is analogous to my earlier work on the flow of magmas containing solid phenocrysts into dikes and sills; similar sorting of the phenocrysts by size and concentration are produced (2, 3, 4).

The results of this study have application to the large landslides or debris flows observed on Mars (5) as well as on Earth. With modifications, the analysis also applies to crater ejecta emplaced at high concentrations.

(1) Bagnold, R.A., Proc. Royal Society London, ser. A, 225, 49-63 (1954).
(2) Komar, P.D., Geol. Soc. Amer. Bull., 83, 973-988 (1972).
(3) Komar, P.D., Geol. Soc. Amer. Bull., 83, 3443-3448 (1972).
(4) Komar, P.D., Geol. Soc. Amer. Bull., 87, 1336-1342 (1976).
(5) Lucchitta, B.K., Reports of Planetary Geology Program, NASA TM X-3511, 178-179 (1977).

Martian Landslides -- Classification and Genesis, E. H. Christiansen and J. W. Head, Department of Geological Sciences, Brown University, Providence, RI 02912.

A large number of variables affect the morphology of landslide deposits including the nature of the rupture surface, physical properties of the failed mass (lithology, stratification, strength), the volume of the slide, height of fall, surface gravity, adjacent topography, and the nature and efficiency of any lubricating mechanisms. Study of Viking images has revealed the presence of numerous landslide scars and deposits on the walls and floors of Valles Marineris (1). Over 20 large landslides (volume $\geq$10 billion m^3) are located in Ius and Tithonium Chasmas alone. A variety of landslide morphologies exists. Schroder (2) defined the surface of rupture (A in Figure 1) as the surface along which the rock mass becomes unattached, the foot line (FL) as the line of intersection between the lower part of the surface of rupture and the original ground surface, and the surface of translation (B) as the surface below the foot line over which the slide has moved. The position of the landslide deposit relative to the surface of rupture can be used to classify three types of landslide features. Those landslide deposits which lie predominantly upon the surface of rupture, topographically higher than the foot line are herein called Class I landslides. Class II landslides have substantial areas above the surface of rupture and the surface of translation. Class III deposits lie entirely over the surface of translation, essentially all of the material has been transported away from the surface of rupture. This geomorphic classification is preferred for martian landslides because it is simple, does not depend on the composition of the slide mass and is nongenetic, but still allows comparisons that give insight into slide development.

Class I landslides typically involve the largest volumes of material. They are marked by chaotic masses of landslide debris with toreva blocks and transverse ridges as the main surface features (Figure 2). Several occur near the west end of Ius Chasma where the narrow canyon prohibited production of a large debris tongue. The major factor in the development of this class is the geometry of the rupture surface which in some cases extends below the surface of the canyon floor. Most of the scars parallel the canyon; rupture surfaces have been initiated along faults that parallel the canyon wall.

The most spectacular landslides have long fan-shaped debris lobes and are headed by a series of slump blocks (Figure 3). Most of the debris tongues have grooves and ridges that parallel the direction of movement. These ridges probably formed by shear between substreams of debris with slightly different

velocities (3). A few lobes have transverse ridges at their distal ends caused by backing up against topographic obstructions. In general the debris lobes have smooth, non-digitate fronts and may be a few 10's of meters thick. Lobes often override one another but the extent of older slides is visible beneath the younger ones. Slump blocks partly override the flow deposits indicating their development was late in the event. The rupture surface of Class II slides rarely excavates canyon floor material and in some cases the foot line is well above the canyon floor.

Class III deposits (Figure 4) are numerous on the canyon floors. These deposits are generally much smaller and develop complexly overriding sequences; similar deposits are found on the walls of some craters (4). Few extend far from the canyon walls or develop well-defined longitudinal grooves. Some emanate from gullies in the canyon wall much the same as terrestrial mudflows, but most fall from over-steepened walls. Other Class III landslides are similar to terrestrial debris avalanches involving wholesale removal of portions of the lower walls.

All three classes have very low effective coefficients of friction (maximum height/maximum length, H/L), some much lower than terrestrial slides for which air cushion sliding (3) or wet, steam bouyancy (5,6) have been proposed. It is unlikely that these mechanisms were effective on Mars. It is impossible under present atmospheric conditions for martian landslides to have trapped sufficient volumes of air beneath them to produce even a thin, 25 cm, cushion. Launching mechanisms are lacking as well in most cases. Lateral levees or imbricate terminations, features associated with air cushioning, are not evident on Class II deposits where topographic constraints are not present. Morphologically most martian landslides do not resemble wet landslides that develop swirl surface textures and multiply digitate toe structures (6,7). Large martian slides may not involve water as a lubricating mechanism as postulated earlier (1,8). Even many large terrestrial landslides are deposited with significant amounts of unmelted snow and ice, even though kinetic energy considerations predict melting or vaporization (8). Certain small Class III deposits with raised rims, undulatory surface features or digitate margins may have involved water but most larger Class III and Class II deposits were more likely produced by thixotropic flow as suggested by Hsü (9) for terrestrial landslides.

(1) B. K. Lucchitta, GSA Abstracts with Programs, 1077 (1977).
(2) J. F. Schroder, Utah Geol. and Mineral. Survey Bull., 90 (1971).
(3) R. L. Shreve, GSA Special Paper, 108 (1968).
(4) J. Veverka and T. Liang, Icarus, 24, 47-50 (1975).
(5) B. K. Lucchitta, NASA TMX-3511, 178 (1977).
(6) A. Pautre, F. Saborly and B. Schneider, Int. Soc. Rock Mechanics, Proc. 2, pt. B, 1859-64 (1974).
(7) A. Post, USGS Prof. Paper 544-D (1967).
(8) M. H. Carr and G. G. Schaber, Jour. Geophys. Res., 82, 4039-4049 (1977).
(9) K. J. Hsu, GSA Bull., 86, 129-140 (1975).

TABLE 1: Comparison of Typical Landslides

	A/B	Volume (m^3)	Energy (J)	L/H
I	3.70	1.3×10^{12}	1.9×10^{19}	13.1
	2.00	6.4×10^{11}	1.9×10^{18}	11.8
	----	6.0×10^{11}	9.0×10^{18}	6.6
II	0.13	1.2×10^{11}	2.4×10^{17}	30.0
	0.25	8.8×10^{10}	1.0×10^{18}	15.0
	0.25	4.5×10^{10}	5.0×10^{16}	17.8
III	0.00	2.0×10^{9}	4.5×10^{12}	32.0
	0.10	3.7×10^{10}	2.8×10^{17}	50.0
	0.10	6.0×10^{8} (4)	1.8×10^{15}	5.8

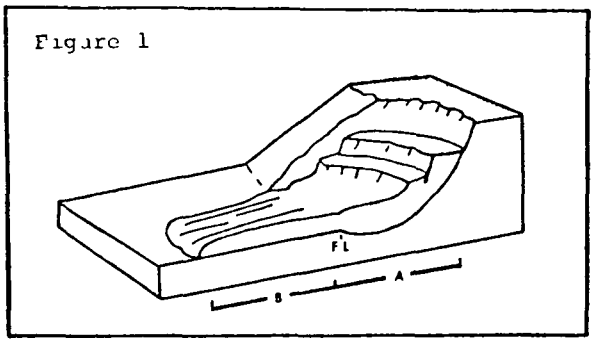

Figure 1

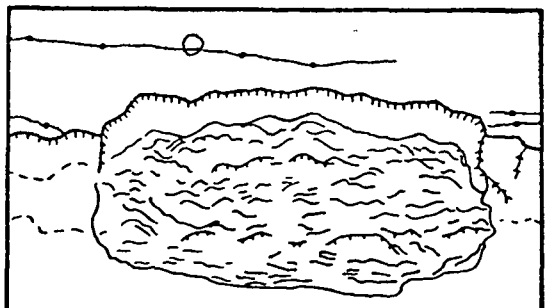

Figure 2: Class I

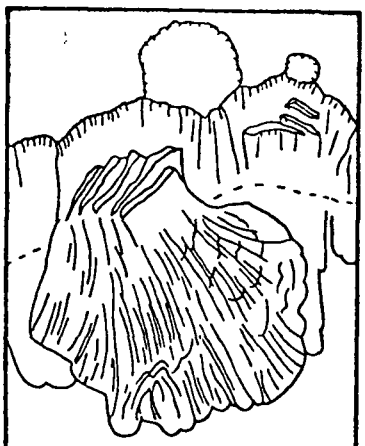

Figure 3

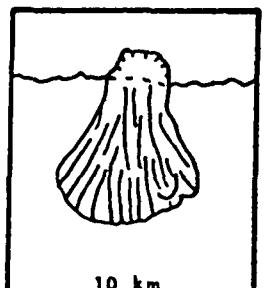

Figure 4

Landslides in the Valles Marineris, Mars, B.K. Lucchitta, U. S. Geological Survey, Flagstaff, Arizona 86001.

About 25 landslides in the martian troughs were studied on Viking images in order to shed light on the time and mechanism of their emplacement. The landslide deposits cover a total area of 31400 km^2 of the trough floors. Individual deposits range from 40 km^2 to 7500 km^2 in area; 65 percent of these measure less than 1000 km^2, 19 percent between 1000 and 2000 km^2, and 16 percent more than 2000 km^2. Many of the deposits have mountainous slump blocks at the head, and smooth or longitudinally grooved aprons towards the toe. The longest distance, about 100 km, was traveled by a landslide in eastern Ius Chasma; the largest scar, about 100 km wide and 30 km deep, occurs on a slide in the middle of Ius Chasma. Several of the landslides have volumes in excess of 1000 km^3. Elevation differences of as much as 7000 m from the top of the scar to the lowest point on the landslide deposit occur locally (Wu et al., in prep.) and, after collapse, precipitous, unsupported scarps were left standing with slope angles of 30 degrees, and towering 5000 to 6000 m above the trough floor.

The age of the landslides is difficult to establish with certainty; crater counts are unreliable because craters are obscured by the rough topography on the slump blocks and crater-like, curved, re-entrants within them. From the counts that were made it appears that the age of individual landslides varies, as some slide deposits are relatively heavily cratered, whereas others are not. A plot of the number of superposed craters versus area of the individual deposits is highly scattered and does not show a trend of increasing crater number with increasing area, as would be expected if the slides occurred nearly simultaneously. A cumulative crater curve was constructed for the combined deposits, and includes craters ranging in size from 500 m to 3.8 km. A crater density of 570 + 130 craters/$10^6 km^2$ area was calculated from these data and indicates that the time of emplacement of the landslides roughly coincided with the late eruptive activity of Arsia Mons (Schaber et al., in press). This age also coincides with the formation of some of the channels (Masursky et al., 1977).

When comparing large terrestrial landslides with some of the martian ones by plotting their weight versus the coefficient of friction (tan of slope from top of scar to tip of slide) it becomes apparent that most of the martian slides are larger and heavier. However, the plot is as scattered for the martian landslides as for the terrestrial ones, indicating that factors other than weight and coefficient of friction account for the variability in the relation. An obvious factor is the variation in width of the troughs and the detailed topography of their floors; but other factors may be important, such as rock type,

cementation, and presence of ground ice or water.

The landslides occurred on the trough walls, which Blasius et al. (1977) showed to be mostly fault scarps, and the scars of the slides in many places occupy fault and joint planes. Elsewhere the slide deposits appear to be cut by faults, which indicates that tectonism pre-dated and post-dated the sliding and suggests that the landslides may have been triggered by quakes. The apparent concurrence of sliding activity with Tharsis volcanic events further supports this contention.

The fault scarps, on which the landslides developed, are very high and unstable. On Mars, in the absence of vigorous pluvial erosion, the fault scarps apparently rose to several thousands of meters in height, thus forming free, unsupported faces with considerable shear stresses in the wall rock. Furthermore, liquid water may be present in the rock materials only a few hundred meters behind the scarp faces and further weaken the walls: Fanale (1976) calculated that liquid water may be present in the equatorial belt on Mars at a depth of as little as 1 km beneath the surface; this water-ice interface would be located high above the bottom of the troughs, and would intersect the walls if projected. Even if the interface were bent down towards the trough floor near the free face, water would be present a short distance behind the face in the wall rock. Also, higher heatflow along the faults paralleling the trough walls may melt ground ice there and contribute to the instability of the walls [melting along faults in permafrost terrain was noticed by Dobrovol'skiy (1974)]. It is apparent that landslides could be easily triggered on these fault scarps and this may explain the abundance of slides. Their enormous size, on the other hand, may result from the great height of the scarps.

A sliding event may have involved a minor quake, ensued by collapse of the wall along planes of weakness along faults. The cap rock, probably lava, fell as slump blocks; the lower material of the wall squeezed out together with liberated pore water and some water converted from ground ice, and streamed over the valley floor as tremendous mudflows. That mudflows rather than debris flows on air cushions were involved is supported by the observations (1) that locally the slide deposits appear to have flowed, seeking low topographic gaps for their passage; (2) that the martian atmosphere most likely never was dense enough to support an air cushion (Anders and Owen, 1977) and (3) that longitudinal ridges like those in the martian landslides are locally found on terrestrial mudflows (Johnson, 1970; Shelton, 1966, Fig. 121).

References:

Anders, E., and Owen, T., 1977, Mars and Earth: Origin and abundance of volatiles. Science, v.198, no. 4316, p. 453-465.

Blasius, K. B., Cutts, J. A., Guest, J. E., and Masursky, H., 1977, Geology of the Valles Marineris: First analysis of imaging from the Viking I Orbiter Primary Mission. Jour. Geophys. Res., v.82, no. 28, p. 4067-4091.

Dobrovol'skiy, 1974, Effect of tectonics and subsurface waters on development of permafrost. Internat. Geol. Review, v.16, no. 7, p. 690-697.

Fanale, F. P., 1976, Martian volatiles: Their degassing history and geochemical fate. ICARUS, v.28, p. 179-202.

Johnson, A. M., 1970, Physical Processes in Geology. Freeman Cooper and Co., San Francisco, California, 577 p.

Masursky, H., Boyce, J.M., Dial, A.L., Schaber, G.G., and Strobell, M.E., 1977, Classification and time of formation of martian channels based on Viking data. Jour. Geophys. Res., v.82, no. 28, p. 4016-4038.

Schaber, G. G., Horstmann, K.C., and Dial, A.L., The distributi and eruptive history of lava flow materials-Tharsis regior of Mars. In Lunar Science IX, The Lunar Science Institute Houston, Texas, in press.

Shelton, J. S., 1966, Geology Illustrated, W. H. Freeman and Co., San Francisco, California, 434 p.

Wu, S.S.C., Schafer, F.J., and Barcus, Loretta, Topographic mapping of the canyonlands from Viking photographs. In preparation.

CHAPTER 10 - VOLATILES AND REGOLITH

Volatile Evolution, Fraser P. Fanale, Jet Propulsion Laboratory, California Institute of Technology, Pasadena, California 91103

Martian Volatile Evolution: We completed a study of the role of Mars' regolith as a storehouse for adsorbed CO_2 and an exchanger of CO_2 with the atmosphere and caps [1]. The model was based on determination of isotherms for CO_2 adsorption on ground rock for all likely Mars subsurface regolith temperatures (158°K-231°K) and equilibrium CO_2 pressures from 1.0 to 60 torr. We modeled the anticipated response of the Mars system to (a) long-term changes in surface insolation, (b) increases or decreases in the number of exchangeable CO_2 molecules, (c) changes in the CO_2 pressure. We concluded: (1) The regolith is a CO_2 capacitor which can buffer the amount of CO_2 in the atmosphere-plus-cap system. For example, if all the CO_2 in the atmosphere-plus-cap system were removed episodically, it would be replaced - over a period of 10^5-10^6 years - by regolith adsorbed CO_2 and the final atmospheric pressure would be the same or only slightly lower than the initial pressure. (2) Exchange of adsorbed CO_2 between the regolith and the atmosphere-plus-cap system has helped to prevent an ^{18}O enrichment relative to ^{16}O which would otherwise be comparable to that observed for ^{15}N relative to ^{14}N. Carbon dioxide exchange is important because orders of magnitude more CO_2 can be "pumped" into the atmosphere than can H_2O owing to vapor pressure limitations. The CO_2 can serve directly as an oxygen capacitor or as a messenger which promotes exchange between regolith H_2O and the atmosphere. (3) Changes in surface insolation which last long enough to penetrate the deep regolith (10^5-10^6 years) will seriously involve the regolith in modifying the CO_2 pressure changes which would otherwise result if Mars had no regolith but only a two part atmosphere-plus-cap system. Serious obstacles to predicting the response of the regolith are lack of knowledge concerning latitudinal dependence of regolith mass and the cause of the change of surface insolation (hence its latitudinal dependence). Knowledge of precise mineralogy and surface area per gram of regolith is a lesser source of uncertainty than it might intuitively seem (see below). We might expect pressure variations of tens of bars to occur as the result of major insolation changes even if the CO_2 caps, which do not now appear to be of vastly greater mass than the atmosphere itself, "run out" of CO_2. Up until the point when the caps might "run out" of CO_2, the effect of the regolith would be to act as a buffer and blunt what might otherwise be a more dramatic increase in atmospheric pressure because the slopes of CO_2 isoteres are lower than the vapor pressure curve of dry ice. Thus phenomena that could be accounted for by simple periodic increases in aeolian transport such as the layered terrain could and would be produced by superimposition of long-term temperature (obliquity) variations regardless of the mass of any postulated surface CO_2 reservoir. But pressure changes required to institute major climate change ($\geqslant$ 300 mb?) involving abundant surface liquid H_2O would require the additional postulated presence of reduced species [2] which might have been present only in early Martian history [3], or a much smaller early regolith, or much higher surface insolation than is postulated. We are conducting CO_2 adsorption experiments on montmorillonite which has been postulated as a major regolith constituent and is known to have a much higher surface area than the ground basalt

we studied. We found that the montmorillonite exhibits an effective surface area for CO_2 adsorption which is only about a factor of 10 greater than the ground basalt rather than the factor of ~100 we expected. Presumably this is because of H_2O molecules preventing full use of the interlayer surfaces by CO_2 molecules. This factor of ten provides for 10x the CO_2 storage for any given "regolith" dimension or allows for a 10x thinner regolith to provide the same CO_2 storage. In the latter case, the response to surface insolation changes may be more rapid and hence of greater amplitude for short-term insolation variation. However, for any given degree of regolith warming the predicted pressure variations are found to be about the same as for basalt (or even less!) because the amplitude of the response depends on heat of adsorption, not surface area. We also modeled rare gas [4] and H_2O adsorption on the regolith. We are also studying mixed-layer adsorption effects to determine how the presence of any member of the "CO_2 - H_2O - rare gas" triad on a surface affects the isotherms for adsorption of the other members.

Studies of Earth Degassing History: As a member of the Basaltic Volcanism Project, the PI has undertaken a reinvestigation of the degassing history of the Earth and its implications for Earth differentiation, following on an earlier study of this problem undertaken under this task [5]. The focus of the current investigation is to analyze the implications for early Earth degassing of some recent constraints on the abundances of various isotopic components of Xe in Earth's atmosphere and deep interior [6]. Some of the constraints (with assumptions concerning the bulk composition of Earth and the overall efficiency of Earth degassing) have been used to calculate the formation interval of the Earth. The underlying thesis of our current study is that the presently available array of such constraints is now sufficient to allow construction of a "simple" analytical model which yields constraints on both the formation interval of the Earth and a function describing transfer of Earth rare gas from the Earth's interior to its atmosphere in terms of degassing intensity vs. time. So far, we have found that the equations which describe the simultaneous solution for an Earth degassed according to a first order law yield discordant formation intervals. (Still, it seems likely that the formation interval of the Earth is 60 my $\leqslant \Delta t \leqslant$ 200 my). Moreover, we have determined that neither varying the I or U (Pu) concentration of the bulk Earth within reasonable limits nor allowing for Xe readsorption onto sediments can remedy the situation [7]. We devised another "compound" analytical model which allows for stepwise or episodic degassing of unspecified efficiency at some point in early Earth history which is then followed by first order degassing. Using this model, we have so far still been unable to produce a concordant solution for all Xe systems. However we have made some limited progress with these "compound" models and have by no means exhausted even the major possibilities yet.

Galilean Satellite Studies: We suggested earlier: (1) That Io's surface is not covered with silicates or ices/frosts, as the surfaces of the myriad other solid planetary bodies of the solar system appear to be, but is instead largely covered with an anhydrous mix of S and salts. This conclusion was based on the optical properties of Io's surface. (2) That the Na in the Io-surrounding extended cloud is sputtered off Io by Jovian

magnetospheric particles, and (3) That line emission from the cloud is excited by resonant scattering of sunlight [8,9,10].

We completed and published a study which suggests that more recent observations of the cloud emission, which have resulted in the identification of K and S^+ and setting of significant upper limits on other atomic species in the cloud are supportive of our surface compositional model [11]. We also recently published a study showing that mixtures of S and salts simulating our model match well the reflectance spectrum of Io in the 0.3-2.5 μm range [12]. Unfortunately, only very subtle features are discernible in Io's spectrum in that range. More diagnostic features have recently been observed in the 2.5-5.0 μm range by investigators at Ames Research Laboratory using the Kuiper airborne observatory [13] and by investigators at the Institute for Astronomy in Hawaii [14]. These groups both conclude that the observed bands tend to support our compositional hypothesis, indicating the possible presence of nitrates [13] or a mixture of nitrates and carbonates [14] on the surface. However other interpretations are still possible [13]. Our current efforts involve laboratory and theoretical studies. The experimental effort (conducted with D. B. Nash and R. Nelson at JPL) is an attempt to measure and interpret the reflectance spectrum of candidate mixtures of satellite surface materials all the way from 0.2 μm to 5.0 μm at appropriate low temperatures (~140°K) and in a radiation environment roughly simulating that in the Jovian magnetosphere. We are also attempting to explain some of the peculiar features of Io's reflectance spectrum - including broadness of some of the bands and the almost complete absence of a 3.0 μm H_2O band - in terms of exogenic effects, i.e. in terms of the peculiar history of the optical surface in the particle bombardment environment. Using results of both the laboratory and theoretical study, an effort will be made to identify key future observations which can be made of all the Galilean satellites not only from the ground, but from Earth-orbiting spacecraft and spacecraft in the vicinity of Jupiter. [The principal investigator on this task is a member of the Near Infrared Mapping Team on the Galileo project, which will map the mineral distribution on the Galilean Satellites surfaces, and Interdisciplinary Scientist and Chairman of the Satellite Working Group on the mission. Thus, immediate synergism exists between current laboratory and theoretical studies and planning of studies of the Galilean satellite surfaces from spacecraft.]

References: [1] Fanale, F.P. and Cannon, W.A., J. Geophys. Res., in press, 1978. [2] Pollack, J.B., NASA TM X-3511, 187-188, 1977. [3] Fanale, F.P. Icarus, 15, 270-303, 1971. [4] Fanale, F.P. et al., Geophys. Res. Lett., in press, 1978. [5] Fanale, F.P., Chem. Geol., 8, 79-105, 1971. [6] Pepin, R.O., Proc. 7th Lun. Sci. Conf., 682, 1976. [7] Fanale, F.P. and Banerdt, W.B., EOS (abs.), in press, 1978. [8] Fanale, F.P. et al., Science, 186, 922-925, 1974. [9] Fanale, F.P. et al., in Planetary Satellites, J. Burns, ed., U. Ariz. press, 1977. [10] Matson, D.L. et al., Astrophys. J., 192, L43-L46, 1974. [11] Fanale, F.P. et al., Geophys. Res. Lett., 4, 303-306, 1977. [12] Nash, D.B. and Fanale, F.P., Icarus, 31, 40-80, 1977. [13] Pollack, J.B. et al., Icarus, in press, 1978. [14] Cruickshank, D.P. et al., Ast. J., in press, 1978.

Amorphous Ice on Saturn's Rings, R. Smoluchowski, Princeton University, Princeton, N.J. 08540.

(after Sep. 1, 1978: Dept. of Astronomy, U. of Texas, Austin, TX. 78712)

The fact that amorphous ice is formed during slow deposition of H_2O vapor at temperatures below about 150°K makes its properties of great interest for the rings of Saturn which are very likely covered with amorphous ice. This could be verified by observations from fly-by spacecraft. The existence of amorphous ice on the rings of Saturn depends on the temperature at which the ice was or is being formed and on its stability. Using the analyses of Pollack (1) and of Lewis (2) one concludes that once the temperature during the formation period of the rings dropped below 150°K there was plenty of time during which the newly deposited ice was not contaminated with other ices and was amorphous. Clathrate ices, like crystalline and amorphous ices, are tetrahedrally coordinated and it is quite likely that if they were formed at the same time they were amorphous and contained foreign molecules supporting their basically metastable structure.

Another possible source of amorphous ice is the sputtering of the outside edge of the rings by high energy protons as discussed recently by Cheng and Lanzerotti (3). The molecules thus formed are redistributed over the inner rings and because of the low temperature the ice should be amorphous and it should grow at the rate of the order of 1000 Å per year.

A similar process has been suggested by Banfi (4) and Tang (5) who considered the possibility that H_2O molecules evaporate from the innermost rings, are ionized and are deposited on the cooler parts of the rings. This process has not as yet been quantitatively evaluated.

The most important factors affecting the stability of amorphous ice on Saturn's rings are the radiation belts and spontaneous crystallization. According to Van Allen (6) no particles are accelerated to high energies because this would require multiple crossings of the quite opaque rings. The remaining thermal plasma plays essentially no role. Spontaneous crystallization of pure amorphous ice can be estimated and it is probably not significant. On the other hand one does not know how impurities would affect this process.

Since there seems to be no simple spectroscopic terrestrial observation for distinguishing between crystalline and amorphous ice on Saturnian rings one has to rely on thermal conductivity K which is known to be very sensitive to the perfection of the crystalline lattice at low temperatures. One expects that at the temperature of the rings for the amorphous ice $K = 2$ to 5×10^{-4} cal cm^{-1} sec^{-1} deg^{-1} thus a factor between 50 and 100 lower than for crystalline ice. Aumann and Kieffer (7) were first to analyse the cooling and heating of particles in the Saturnian rings upon their entry into and emergence from the planet's shadow. For sufficiently long times the thus calculated change in temperature is strongly dependent on the radius R of the particle and essentially independent of K. It turns out that for times shorter

than $t' = R^2\rho c/4K$ (where ρ is the particle density and c is the specific heat) after the entry into the shadow $T/T_0=1-(t/\rho cK)^{\frac{1}{2}}\varepsilon\sigma\beta$ (here T_0 is the brightness temperature before entry into the shadow, ε is the emissivity, σ is the Stefan-Boltzmann constant and β is that fraction of solid angle seen by the particle which is not obstructed by the rest of the ring). As expected this drop in temperature depends on K but not on R and the rate of temperature drop dT/dt for a given t should be 7 to 10 times slower for the amorphous ice. For crystalline ice time t' would be 50 to 100 times shorter. The portion of the planet's shadow which is visible from earth is too narrow and too close to the bright disc of the planet to permit accurate terrestrial measurements at sufficiently short times. The situation is, however, favorable for observations from a fly-by spacecraft. Such measurements would also help answer the question whether or not the external layer of the particles is ice while their interior is rocky or metallic as suggested by radar reflectivity measurements.

It is known (8) that there is significant azimuthal asymmetry of brightness in the ring A but not in the ring B and several models to account for this effect have been proposed (9,10). It appears that the steady diffusion of water molecules from the outer towards the inner rings may be the reason for these observations because of the differences in the circular components of the Keplerian orbits. The molecules would preferentially form fresh ice on the leading outward and on the trailing inward quarters of large particles which rarely collide among themselves and are facing the planet in a synchronous motion. Small particles on the other hand undergo too many collisions among themselves to be synchronous. They are however covered with fresh ice and would be similarly deposited and stick to the particular areas of the larger particles contributing to the same brightness anisotropy. The sticking of small particles is caused primarily by the gravitational attraction of smaller particles to the big ones and the probability of sticking is highest near a direction which forms an angle of 55-60° to the orbital velocity vector in the leading-outward direction and the same angle in the trailing-inward direction. These effects would lead to a progressive increase of non-sphericity and of albedo asymmetry of the large particles just at the right orientation to explain the observations. The albedo asymmetry would enhance the effect of forward and backward wakes (9,10). The absence of a similar brightness asymmetry in the B ring could be then a direct consequence of a much narrower range of particle sizes which through collisions would destroy any tendency to synchronism and disturb their regular motion.

REFERENCES

1. J. B. Pollack, A. S. Grossman and R. Moore, Icarus 29, 35 (1976).

2. J. S. Lewis, Icarus 16, 241 (1972).

3. A. F. Cheng and L. J. Lanzerotti (to appear in J. Geoph. Res.).

4. V. Banfi, Mem. Soc. Astr. Ital. 53, 247 (1972).

C. C. H. Tang, JPL Report 76-134 (1975).

J. A. Van Allen in Highlights of Astronomy, E. A. Müller (ed), Vol 4, p. 195, (D. Reidel, Dordrecht, Holland 1978) and private communication.

7. H. H. Aumann and H. H. Kieffer, Astroph. J. 136, 305 (1973).

8. H. J. Reitsema, R. F. Beebe and R. A. Smith, Astro. J. 81, 209, (1976).

9. G. Colombo, P. Goldreich and A. W. Harris, Nature, 264, 344 (1976).

10. F. A. Franklin and G. Colombo, to be published.

Viking Soil: Chemical Activity from Surface Frosts? R. L. Huguenin, Planetary Chemistry Lab., U. Mass. Dept. of Physics and Astronomy, Amherst, MA 01003, and Brown U. Dept. of Geological Sciences, Providence, RI 02912.

One of the most important discoveries of the Viking mission was the unusual chemical activity of Martian soil during the biology experiments. The Gas Exchange (GEx) and Labeled Release (LR) experiments revealed the presence of strong oxidants in the soil: O_2 gas rapidly evolved from samples exposed to liquid H_2O or humidified, and nutrients (e.g., formate or lactate) were oxidized to CO_2. This activity has not been observed with conventional terrestrial soil samples, and the question arises as to what makes the Martian soil so active.

One major difference between terrestrial and Martian soils is that Martian soils are never exposed to liquid H_2O, and interactions with the atmosphere do not occur via solution mediums as they do on Earth. Instead, interactions occur with adsorbed gases (1,2), and it has been proposed that this can lead to the formation of several chemisorbed complexes that should be quite chemically active (3). In this paper we report the first results of an experiment designed to determine whether these complexes could produce the kinds of soil activity observed during the LR and GEx experiments.

Theory. One of the proposed complexes is adsorbed OH^- derived from surface frosts. Primary basaltic minerals (e.g., olivine and pyroxene) are unstable in the presence of H_2O, and H_2O dissociates to H^+ and OH^- at the the crystal surface. A fraction of the H^+ is drawn into the crystal by the attractive potential of negatively charged lattice defects, δ^-. For olivine, and other basaltic silicates, the most common δ^- is Al^{3+} substituted for Si^{4+} on tetrahedral sites, with Al^{3+}/Si^{4+} for olivine usually exceeding .002. At δ^- the H^+ combines with lattice O^{2-} to form lattice hydroxyl, $\delta^-.\ OH_o^-$. The loss of H^+ from the frost produces an excess of OH^- (relative to H^+) at the surface. Energetically, the reaction is favored:

$H_2O_{(g)} \rightarrow H^+_{(g)} + OH^-_{(g)}$	+16.9eV
$H^+_{(g)} + \delta^-.O_o^{2-} \rightarrow \delta^-\cdot OH_o^-$	-8.1eV + Δ_1
$OH^-_{(g)} \quad OH^-_{(ads)}$	-6eV
$H_2O_{(g)} + \delta^-\cdot O_o^{2-} \rightarrow OH^-_{(ads)} + \delta^-\cdot OH_o^-$	+2.8eV + Δ_1

where Δ_1 is the energy required to convert $Al^{3+}\cdot O_o^{2-}$ to $Al^{3+}\cdot OH_o^-$, or $\Delta_1 \simeq \Delta GAl(OH)_3 - \Delta GAl_2O_3 = -4.1$eV (4).

During conventional weathering in liquid H_2O, the excess OH^- go into solution. This not only raises the pH of the solution, but the charge imbalance created (H^+ in mineral, OH^- in solution) causes the ejection of metal ions into solution. In solution, the metal ions react with excess OH^- and dissolved atmospheric gases to form phases that are in equilibrium with the atmosphere (e.g., FeOOH, $CaCO_3$, and clays). When the H_2O occurs as a frost rather than liquid, the excess OH^- and metal ions cannot go into solution. They are restricted to the crystal surface, and thereby form high potential

energy surface layers that are charge-separated and unstable (particularly in the presence of liquid H_2O) (3). The charge separation tends to relax through release of electrons from OH^- to positively charged lattice defects δ^+ in the crystal. For olivine and other basaltic silicates the most common δ^+ are Fe^{3+}, Cr^{3+}, and/or Ti^{4+} substituted for Fe^{2+} in octahedral sites. The potential exerted on OH^- by δ^+ can be approximated by $V = ne^2/kr$, where n is the excess charge of the defect (n=1 for Fe^{3+} and Cr^{3+} and n=2 for Ti^{4+}), e is electronic charge, k is the dielectric constant, and r is the δ^+ - OH^- separation. For olivine, k ranges from 6.2 (forsterite) to 3.3 - 3.5 (fayalite), and V should thus exceed the electron affinity of OH^- (1.8eV) for r between 1.3 and 4.8Å; thus OH^- should lose its electron to δ^+ at surface sites. Most of the δ^+ should be in surface sites following H^+ incorporation: the crystal becomes net positive and δ^+ is attracted to the excess surface OH^-. δ^+ migrates to the surface via efficient $Fe^{2+} \rightarrow \delta^+$charge transfer in basaltic minerals (3). Transfer of electrons from OH^- to δ^+ represents a reduction of the crystal and restoration of charge balance.

Exposure of the hydroxylated minerals to humidification or liquid H_2O, as during Viking, should release the OH to solution. Since hydroxyls cannot desorb as isolated radicals or ions, it was proposed that adjacent adsorbed OH combine and desorb as H_2O_2 and/or H_2O and $\frac{1}{2}O_2$ (3). Metal ions should also be released from the surface layer, catalyzing the decomposition of H_2O_2 to $H_2O + \frac{1}{2}O_{2(g)}$. H_2O_2 can also efficiently oxidize any formate present to H_2O + $CO_{2(g)}$ in the presence of metal ions.

Experimental. To determine whether frost-treated soil can in fact evolve O_2 upon wetting, a 2g sample of Jackson Co. olivine (FeO/MgO = .17; Al_2O_3/SiO_2 = .003; $Fe_2O_3 + Cr_2O_3 + TiO_2/FeO$ = .004) was evacuated for 48 hours at 20°C in 2×10^{-4}torr atm. H_2O vapor was introduced into the 2 1 environmental chamber, where it formed a frost on a cold block held at 0 to -20°C. After allowing 10 minutes for the frost to form, the chamber was evacuated to 1×10^{-3}torr. The sample was then slowly cooled to -22°C, and the frost storage block was slowly warmed to +10°C. The chamber pressure was held at $<10^{-2}$torr, and frost was allowed to form on the sample as it cooled from -11°C to -22°C. During this interval (15 min) the sample was pulverized using a rotary vacuum feedthrough pestel. This insured that frost formed on freshly cleaved crystal faces at temperatures cold enough for only solid H_2O to exist. After reaching -22°C, the coolant was turned off and the sample was allowed to warm. The frost storage block was cooled again to -30°C to trap H_2O vapor from the warming sample. After about 30 minutes the frost on the sample began to melt and the chamber pressure rose rapidly to 9×10^{-2}torr. The gas was analyzed using a 300 cm x .6 (O.D.) SS gas chromatograph column packed with 100/120 mesh Porapak Q and a thermocouple detector. The chromatogram registered a single peak corresponding to the production of 4×10^{18} O_2 molecules and less than 1×10^{18} molecules of N_2. The experiment was repeated, yielding the same results. It was followed by a series of control experiments. In one of these, the same procedure was followed without using an olivine sample. In another, a sample was pulverized at low temperatures without frost. In another a sample was pulverized in the presence of 1×10^{-2}torr H_2O vapor at +10°C. For each of the controls, no detectable gas evolved.

The amount of O_2 produced (2×10^{18} molecules g^{-1}) is in the range predicted for frost-treated olivine (10^{18} -10^{21} molecules g^{-1}) by Huguenin et al. (3). It was, however, about an order of magnitude higher than the largest amount evolved during the GEx experiments, although the kinetics were very similar.

To determine whether frost-treated soil could oxidize aqueous nutrients (such as formate) to CO_2, another 2 gram olivine sample was again pulverized in the presence of H_2O vapor for 15 minutes at -11°C to -22°C, as in Experiment 1.

After reaching -22°C the coolant was turned off, and again after ∿30 minutes the frost on the sample began to melt. At this point 5 ml of 0.1 M HCOONa solution was injected into the sample (remotely) and the gas pressure rose to 1.8 torr in ∿1 hr. The gas chromatogram registered two peaks, one corresponding to $O_2/N_2$and the other corresponding to 1.8 torr of CO_2. The experiment was repeated with the same results. As a control, 5 ml of 0.1 M formate solution was injected into the chamber without a sample present. The chamber pressure slowly rose to 2×10^{-1} torr, but the chromatogram showed no measurable peaks. Presumably the chamber filled with H_2O vapor. As a second control, 5 ml of 0.1 M formate solution was injected into an olivine sample that was pulverized in the absence of H_2O vapor. The chamber pressure raised to 1×10^{-1} torr, and again there were no measurable peaks.

The amount of CO_2 produced (6.5×10^{19} CO_2 molecules g^{-1}) was very close to the number of formate ions available for oxidation (3×10^{20} molecules), and it represented nearly complete (43%) conversion to CO_2 in ∿1 hr. This is very similar to the findings of the LR experiments, although much weaker nutrient solutions were used in the Viking experiments.

These experiments are only the first in a series of experiments to determine the origin of the Viking soil activity. Clearly many more tests are needed before any conclusions can be drawn. The results do, however, raise the possibility that $OH^-_{(ads)}$ and H_2O_2 produced by surface frosts may have been partly responsible for the unusual chemical activity of the Martian soil.

Acknowledgment. Contribution No. 3 of the Planetary Chemistry Laboratory.

References

1. Huguenen, R. L. (1974) J. Geophys. Res., 79, p. 3895-3905.
2. Huguenin, R. L. (1976) Icarus, 28, p. 203-212.
3. Huguenin, R. L., Prinn, R. G., and Maderazzo, M. (1977) Icarus, 32, p. 270-297.
4. Tardy, Y. and Garrels, R. (1976) Geochim. et Cosmochim. Acta, 40, p. 1051-1055.

Surface Materials of the Viking Landing Sites-Extended Mission, H. J. Moore, U.S. Geol. Survey, Menlo Park, CA 94025; C. R. Spitzer, NASA Langley Research Ctr., Hampton, VA 23665; P. Cates, Bionetics Corp.1800 Research Dr., Hampton, VA 23666; K. Bradford, Martin Marietta Aerospace, Denver, CO 80201; R. F. Scott, Dept. Engineering and Applied Sciences, Calif. Inst. Tech., Pasadena, CA 91125; R. E. Hutton, 1501 Palos Verde Dr., Harbor City, CA 90710; and R. W. Shorthill, Univ. of Utah Research Inst., Salt Lake City, UT 84108.

Since the primary Viking Mission, the surface samplers and cameras of landers 1 (VL-1) and 2 (VL-2) have continued to operate. Major accomplishments of the Extended Mission include: (1) excavation of two deep trenches by VL-1 and one by VL-2, (2) acquisition of pictures of surface sampler backhoe penetrations into the surface materials, (3) acquisition of pictures of small impact craters produced by fragments dropped from known heights, (4) construction of conical piles of soil on rocks and between the rocks using the surface sampler, (5) excavation of trenches by plowing with concomitant acquisition of surface-sampler motor currents which can be interpreted in terms of forces exerted during plowing, (6) acquisition of pictures of temperature sensors on footpads 2 of both landers using mirrors mounted on the surface sampler boom housings, (7) acquisition of pictures of the surfaces beneath retroengines 2 of both landers using mirrors mounted on the surface sampler boom housings, (8) attempts to move, scratch, chip, and break rocks with the surface samplers, and (9) measurements of temperatures throughout an entire martian day (Sol) using the thermal sensors on the surface sampler collector heads while inserted in the soil. Additional surface sampler activities will be completed by early May.

The first deep trench was excavated by VL-1 in the drift material of "Sandy Flats" (Moore and others, 1977) to a depth of 23 cm without difficulty. This depth when combined with the local topography indicates that drift material extends well below the 16.5 cm penetrated by footpad 2. Analyses of footpad penetration, backhoe penetrations, and fragment impacts are consistent with a material that has a density near 1400 kg/m^3. Slope stability analyses of the deep trench reaffirm that the cohesion of the drift material is near 10 to 10^2 N/m^2.

The second deep trench was excavated by VL-1 in "Rocky Flats" (Moore and others, 1977) to a depth of 12 to 14 cm with difficulty. Subsequently the surface sampler failed to attain the commanded extensions during sampling from the deep trench. This shows that forces near 200 N were exerted on the materials of "Rocky Flats" at 12 to 14 cm and that the cohesion is larger than about 10 kN/m^2. Such a large cohesion is consistent with the small penetration of footpad 3 into "rocky" material (Moore and others, 1977).

A single deep trench was excavated with difficulty by VL-2 to a depth of 8 to 10 cm, judging from achieved surface sampler elevation angles. Surface sampler commanded extensions were achieved during sample acquisitions from the trench. In a separate trenching operation, forces of 75 to 100 N were exerted by the surface sampler as it plowed to a depth of 3 cm, indicating that the surface material at the trench site has a cohesion of 7 to 9 kN/m^2. Such a large cohesion is consistent with a small backhoe penetration of about 1 cm at the same site.

At this time, winds, which have gusted to 34 m/s, have not altered the shapes of the conical piles of soil constructed by the surface samplers. The temperature sensors on footpad 2 of VL-1 are buried by drift material, and those on VL-2 are unburied and exposed to the atmosphere. The surfaces beneath the retroengines have small craters that were produced by exhaust gases from individual engine nozzles during landing. Rocks that have been moved by the surface sampler have not chipped, scratched, or spalled.

Surface sampler temperatures have not been fully analyzed. The lowest temperatures measured by VL-2 were about 171°K from 0700 to 0800 hours on Sol 406, and highest temperatures were constant and about 217°K from 1500-1800 hours on Sol 405; on the following day they were constant and about 218°K from 1330 to 1500 hours, at which time the experiment ended. The constant temperatures may be the result of a phase change of some constituent in the soil. There is evidence that remnant ground frost was present in shadows near VL-2 on Sols 405 and 406 (Kenneth L. Jones, personal comm., 1978).

Analyses of desorbed gases in "Sandy Flats" samples in the Gas Exchange Instrument of the Biology Experiment indicate that the surface area of the grains is near 17 m^2/g (Ballou and others, 1978), corresponding to a grain size near 0.07 μm.

References:

Moore, H. J., and others, 1977, Surface materials of the Viking landing sites: Jour. Geophys. Res., v. 28, p. 4497-4523.

Ballou, E. Vernon, and others, 1978, Chemical interpretation of Viking Lander 1 life detection experiment: Nature (in press).

Geochemical Studies Within Simulated Martian Environments, Michael C. Booth and Hugh H. Kieffer, Department of Earth and Space Sciences, University of California, Los Angeles, CA 90024.

Studies are presently underway examining the chemical interactions of atmospheric volatiles with rock material under simulated Martian environments. These studies seek to determine the nature of chemical weathering phenomena currently active on the Martian surface and measure their rates of reaction as a function of pCO_2, H_2O abundance, UV irradiation, soil temperature and composition, pO_2, and the rate of diurnal cycling. Carbonate formation under nonaqueous conditions, and the generation of an active oxygen-bearing surface chemistry, are the processes receiving primary attention; a preliminary study of the possible nonaqueous formation of sulfate minerals is also being undertaken.

An improved environmental simulation system now in use is capable of providing the temperatures, atmospheric pressures and compositions, and UV flux rates present at the Martian surface. Experimental soil temperatures can be controlled to $\pm$ 1 K within the range 150 - 297 K to simulate any temperature environment existing on Mars. Mars-like diurnal temperature variations can also be produced in experimental samples. Atmospheric pressures and compositions within the environmental chamber are controlled throughout experiments of extended duration (114 hours). Water in the environment is controlled so as to provide the desired humidity during simulated 'day' periods, frosts on soil samples during 'night' modes and an absence of liquid water throughout the experiments. The ultraviolet illumination system is capable of providing direct UV irradiation of soil sample surfaces up to 100 times the expected solar flux at the Martian surface, with a cutoff at ~2200Å.

Recent work in which pulverized tholeiitic basalt was subjected to nonaqueous, low pressure, environments for 66 hours (5½ simulated diurnal cycles) have provided insight into the mechanism for carbonate growth previously reported[1]. First, the complete absence of UV irradiation from the simulated Martian environment causes a significant reduction in the amount of carbonate growth in pulverized basalt versus that in irradiated samples. These results support the involvement of the photochemistry of water and photochemical H_2O_2 in surface chemistry as proposed in earlier work. Experiments in which samples were either partially or totally shielded from direct UV irradiation, but received UV irradiation into the chamber environment, did not show this reduction in growth. In addition, experiments lacking diurnal cycling (perpetual 'day') resulted in no measureable carbonate growth. The involvement of H_2O frost in the surface chemistry is strongly suggested here since frosts normally sublime from samples during the beginning of each 'day' period. Also, in experiments now completed down to pCO_2 levels of 50 mbar and 20 precip. μm H_2O, rates of carbonate growth were observed to be essentially the same in samples of pulverized glassy Mauna Ulu tholeiite as in the highly, crystalline, magnetite-rich andesitic basalt of initial studies. Rates of growth of recent low pCO_2 experiments (50 mbar) are $1 - 4 \times 10^{12}$ cm^{-3} sec^{-1}. Experiments using fine-grained glass beads as samples, however, have shown no measurable degree of CO_2 fixation. These latter results are most easily explained as being due to the absence of metallic cation sites on glass beads and the site selectivity of carbonate formation.

[1]Booth, M. C. and H. H. Kieffer, J. Geophys. Res., 83, in press, 1978.

Solar Wind Sputtering: An Ineffective Weathering Process of Airless Bodies, R.E. Scott (R.L. Huguenin, P.I.), Planetary Chemistry Laboratory, Dept. of Physics and Astronomy, U. of Massachusetts, Amherst, MA 01003.

The apparent absence of metal coatings, produced by solar-wind sputtering, on returned lunar samples indicates that the solar wind does not modify the soils to the extent predicted by laboratory studies. The reason for this discrepancy is that in laboratory models of the solar wind plasma-lunar surface interaction, the interaction of the solar wind plasma with electric fields, created in the plasma-magnetic field interaction, at the lunar surface were neglected.

Theories of sputtering. There are two major theories of sputtering. The sputtering yields of metal targets for ions at normal incidence is given by the following expression,

$$S(M) = \frac{0.0420 \cdot \alpha(\varepsilon) \cdot 4\pi \cdot Z_1 Z_2 e^2 a_{12} \{M_1/(M_1+M_2)\} s_n(\varepsilon)}{U_o \text{Å}^2} \qquad (1)$$

where M_1 and M_2 are the mass numbers of the ion and target, Z_1 and Z_2 are the atomic numbers of the ion and target, U_o is the surface binding energy of the target, a_{12} is defined by $a_{12} = 0.8853 \cdot (Z_1^{2/3} + Z_2^{2/3})^{-\frac{1}{2}}$, $s_n(\varepsilon)$ is a universal function, a_o is the Bohr radius, ε is defined by $\varepsilon = \{M_2 E_i/(M_1+M_2)\} \{Z_1 Z_2 e^2/a_{12}\}^{-1}$ where E_i is the energy of the incident ion {1}.

Eq. (1) holds only for $M_1 \gtrsim M_2$. In the case of proton sputtering we have $M_1 << M_2$. This implies that a problem enters if Eq. (1) is used to predict the sputtering yield values of metal targets for protons at normal incidence. Instead we made the following approximations. (1) In order to improve Eq. (1), we scaled the quantity $\alpha(\varepsilon)$ to the experimentally determined value of Ag for normally incident protons at 2keV {2}. We found that a better estimate of $\alpha(\varepsilon)$ is given by $\alpha'(\varepsilon) = \alpha(\varepsilon)/2$. (2) For metals the surface binding energy, U_o, is equated with the measured sublimation energy.

The sputtering behavior of oxides is different from that of metals. {3}. The sputtering behavior of oxides in some cases follow the collisional theory for metals but in other cases the collisional theory is supplemented by thermal sputtering and/or by oxygen sputtering; therefore the sputtering of oxides cannot be explained by the collisional theory for metals. Instead, an approximation was used. The approximation is to use Eq. (1) in a form which is weighted for the mole fractions of metal and oxygen,

$$S_{oxide} = X_{metal} S(M_{metal}) + X_{oxygen} S(M_{oxygen}) \qquad (2)$$

where $X = \{(A/E)\}/\{(A/E)+(100-A)/B\}$ and A ≡ weight % of metal ions, B ≡ molecular weight of oxide lattice, and E≡ molecular weight of metal ions. The predicted sputtering yields of various oxide targets in comparison with experimental yield values turn out to differ by about a factor of 2-3 for most oxides. For example the predicted yield for Al_2O_3 and Fe_2O_3 at 7.0 keV are 0.010 and 0.013, respectively, and the experimantal values are 0.006 and 0.005, respectively (4).

We found that the sputtering yield values of various oxide targets fall off precipitously with reductions in incident proton energies. A minimum energy of 20-50eV is required for sputtering to occur {5}. By simple momentum transfer theory minimum incident proton energies for the various oxide targets are: Al_2O_3, 1-1.3keV; CaO, 0.6-1.4keV; FeO, 0.7-1.8keV; Mgo, 0.4-1.1keV; MnO, 0.7-1.8keV; and TiO_2, 0.8-2keV. Reductions in the incident energies of the

solar-wind protons can have a substantial effect on their sputtering efficiency.

Deceleration of the solar-wind protons at the lunar surface. When the solar wind enters the inhomogeneous lunar magnetic field, the solar-wind protons and electrons separate. The lunar surface absorbs the particles and thus charges up. The resulting electric currents that are created tend to accelerate the electrons and decelerate the protons {6}.

The Apollo-12 ALSEP solar wind spectrometer experiment shows evidence of proton deceleration at the Apollo-12 site. The proton velocity at the Apollo-12 ALSEP-site was found to be less than or equal to the velocity in the free stream solar wind, measured by OGO and Vela. This large a deceleration of the solar wind protons is attributed to the interaction of the solar wind plasma with the local remanent field, since it is unlikely that such a large decelaration of the solar-wind protons is the result of the positive electric potential of the lunar surface {7}.

Assuming (1) a locally uniform magnetic field, (2) cold solar wind, nearly electrically neutral hydrogen plasma and (3) solar wind particles are completely absorbed, the decrease in the velocity of the solar-wind protons is given by the following expression:

$$\Delta V = \frac{B_{\parallel}^2 - B_{\parallel o}^2}{8\pi m_p n_o V_o} \qquad (3)$$

where $\perp$ and $\parallel$ define the components of velocity and magnetic field perpendicular and parallel to the lunar surface, respectively, and the subscript o defines the upstream solar wind values. Utilizing the data obtained by the ALSEP magnetometer, ARC magnetometer aboard Explorer 35, OGO 5 and Vela 5 spectrometer, the predicted $\Delta V_{\perp}$ (0705 UT March 27, 1970) at ALSEP site is 127 km/sec, while the measured $\Delta V_{\perp}$ = 50 km/sec (18.5% reduction).

The reason for this descrepancy is that the assumption of local magnetic field uniformity over distances comparable to the thickness of the region of interaction is invalid {7}.

The Apollo-12 ALSEP solar wind spectrometer experiment recorded solar wind-proton velocities ranging from 298-589 km/sec for the period 26 Nov. - 1 Dec. 1969 and from 210-362 km/sec {8} corresponding to solar-wind-proton energies ranging from 0.5-2keV and 0.2-0.7keV, respectively. Since sputtering of most oxides requires proton energies greater than 0.6-2keV, we predict the sputtering efficiency of the solar wind protons at the Apollo-16 site should be lower than their sputtering efficiency at Apollo-12 since the local magnetic field is stronger. Sputtering efficiencies at other regions of the moon will similarly be low; therefore the unexpected low abundances of metal surface coatings predicted to have been produced by sputtering can now be possible explained. It is expected that hydrogen ion implantation is a more important alteration process on the lunar surface.

Laboratory work is clearly needed to determine the dependence of sputtering yield on incident proton energies in lunar-like magnetic fields.

Acknowledgement. Contribution No. 1 of the Planetary Chemistry Laboratory.

References.

(1) Sigmund, P. (1969) Physical Review 184, p. 383-416.
(2) Gronlund, F. and Moore, W.J. (1960) The Journal of Chemical Physics 32, p. 1540-1545.
(3) Kelly, R. and Lam, N.Q. (1973) Radiation Effects 19, p. 39-47.
(4) Webner, G.K., Rosenberg, D.L., and Ken Knight, D.E. (1964) General Mills Third Quarterly Status Report.
(5) Wehner, G.K. (1957) Physical Review 108, p. 35.
(6) Siscoe, G.L. and Goldstein, B. (1973) Journal of Geophysical Research 78, p. 6741-6748.
(7) Neugebauer, M., Snyder, C.W., and Goldstein, B.E. (1972) Planet. Space Sci. 20, p. 1577-1591.
(8) Dyal, P., Parkin C.W., and Cassen, P. (1972) Proc. Lunar Sci. Conf. 3rd, p. 2287-2307.

Photometric Analyses of Spacecraft Planetary Images. B. Hapke, Dept. of Earth & Planetary Sci., U. of Pittsburgh, Pittsburgh, PA. 15260

This abstract summarizes results of several activities involving photometric analyses of spacecraft images and supporting theoretical and ground-based observational activities.

1. Photometric Theory: The main result of the present year is the completion of a new, analytic photometric function for light-scattering from particulate surfaces. The new expression includes the opposition effect and multiple scattering, so that it is applicable to virtually any body in the solar system, particularly outer planet satellites. Using this theory the following may be estimated from planetary photometry: average single-scattering albedo, average single-particle phase function, average macroscopic slopes, and porosity of the surface. An expression for the scattering efficiency Q_S of a large, irregular particle has been derived which relates Q_S to the size D, refractive index, and true absorption coefficient α. A good approximation is $Q_S \approx (1 + \alpha De)^{-1}$, for $\alpha De \lesssim 3$, where De is about twice the average particle size. Reflectance spectra of mixtures may be calculated. This result is useful for measuring $\alpha(\lambda)$ from reflectance spectra, and for calculating theoretical planetary spectra from laboratory measurements for comparison with observations.

2. Spacecraft Image Analysis: (A) Mercury Color Ratio Map: All Mariner 10 images of Mercury and the moon were surveyed for possible use in constructing color ratio images for studying color differences on the surfaces of the planets. These images were then processed by the Image Processing Laboratory of JPL to produce ORANGE/UV color ratio images. This processing has been completed and color ratio maps of Mercury are currently being constructed. Unfortunately, it appears that the camera calibration is sufficiently sensitive to temperature that reliable color differences cannot be measured on frames taken when the cameras were not at the design temperature. Thus the lunar and Mercury III frames cannot be used for colorimetry, although they are still useful for photometry.

(B) Mercury Albedo Map: The correction to the photometric function due to roughness is nearly completed and is being incorporated into the computer program for calculation of normal albedos. The other poorly-known parameter in the photometric function is the single-particle scattering function. In order to better evaluate this function we have requested several more frames from IPL, which we have just received, but not yet reduced. Work on the albedo map was delayed because we decided to concentrate our efforts on the astronomical observations of Mercury, which yielded the new absorption band (see below).

(C) Viking Lander Photometry: The data from the special photometric sequence taken by Viking Lander I was finally received from IPL in the Spring of 1977, but due to lack of a graduate student assistant, reduction was not begun until this Fall. Six-color images of a number of rock and soil areas under various lighting angles have been reduced and are currently being analyzed with the objective of determining the properties listed in Section 1 above.

(D) Venus Cloud Photometry: Early reductions of Mariner 10 Venus images at small phase angles implied that the brightness profiles are consistent with isotropic scatterers. Portions of several other frames taken by Mariner 10 at

a variety of phase angles were analyzed.

It was found that the scattering particles are not isotropic but have properties consistent with those of spheres of the type deduced by Hansen and his colleagues from polarization measurements.

3. Astronomical Observations: (A) Mercury: Using a new technique of daytime observations of Mercury and the sun at McDonald, the relative reflectance spectrum of the planet between about 6000-12,000Å was measured at 20Å resolution. A previously-unreported, weak, absorption band at 10,300Å was discovered (Figure 1). This band is provisionally identified as due to Fe^{+2} in diopside. It's weakness compared to a similar lunar band confirms the low abundance of FeO in the crust (Hapke, et al, 1975, J. Geophys. Res., 80, 2431). If the identification of diopside is correct this implies that the crust of Mercury is basaltic in nature, like the moon's crust. However, the band may possibly be due to forsterite, which would imply an ultrabasic crust with a considerably different differentiation history than the moon. We are planning observations at 20,000Å, where diopside has a band but forsterite does not.

(B) Venus: The UV reflectance spectrum of Venus was measured. A drop in the spectrum at about 3300Å was found, confirming a previous discovery of the feature on Venus by Barker et al (1975, J. Atmos. Sci., 32, 1205). A similar feature was also found by us on Io (see below). It has been suggested that the Venus clouds are a mixture of sulfuric acid and elemental sulfur, while the crust of Io is sulfur plus various salts. The discovery of a common feature on both bodies makes it likely that this drop is due to S also, probably a metastable isomer.

(C) Outer Planet Satellites: Since telescope time was available at McDonald when the Mercury and Venus observations described above were being taken, spectra of the Galilean satellites of Jupiter and Titan were also made at 20Å resolution between 3000 - 8600Å. The moon was used as a primary spectral standard. In general, the observations confirm the results obtained by previous workers, with the following new results (Figure 2). (1.) There is a drop in Io's reflectance spectrum at 3300Å. (2.) We found no evidence for the band at 8000Å reported by Johnson for Io. (3.) The depths of the methane bands on Titan do not vary with time.

(D) Sun-Io Correlation: A survey of the controversial post-eclipse brightening reported on Io lead to the discovery that every observation of brightening, except one, has been preceeded by a major solar flare near the sub-Jovian meridian on the sun. We have suggested that the post-eclipse brightening is due to flare-enhanced radiation fluxes in the Jovian magnetosphere causing thermoluminescence on Io.

4. Papers:

B. Hapke, 1977, Interpretations of Optical Observations of Mercury and the Moon, Phys. Earth Planet, Interiors, 15, 264.

L. Tepper and B. Hapke, 1978, Mercury: Detection of a 1000 nm Ferrous Band, submitted to Science.

R. Nelson and B. Hapke, 1978, Possible Correlation of Io's Post-Eclipse Brightening with Major Solar Flares, Icarus, 33, 203.

R. Nelson and B. Hapke, 1978, Spectral Reflectivities of the Galilean Satellites and Titan 0.32-0.86 Micrometers, submitted to Icarus.

B. Hapke, 1978, Bi-Directional Reflectance Spectroscopy. I. Theory, submitted to Rev. Geophys. Space Sci.

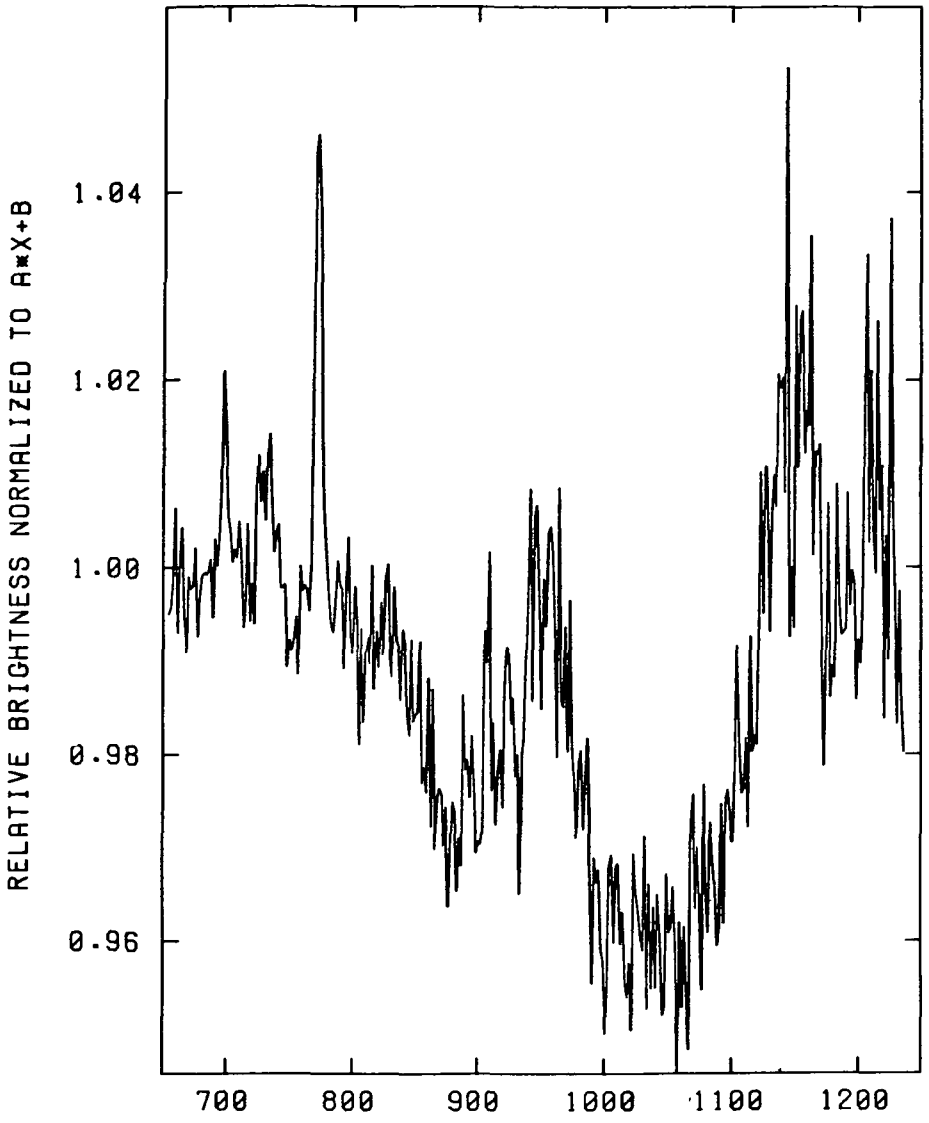

Figure 1
Mercury

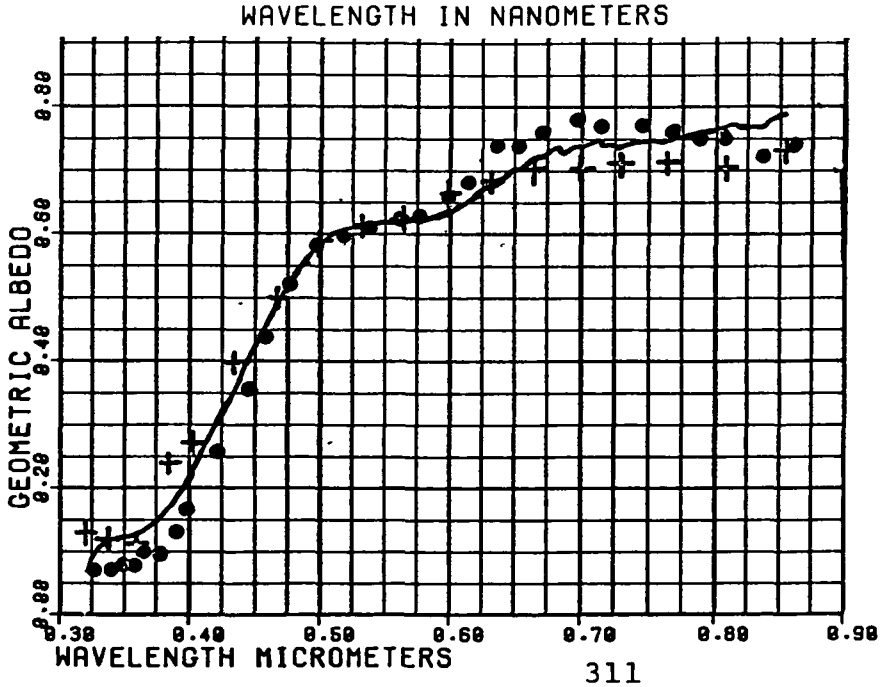

Figure 2
Io

Use of the Edge Enhancer in Geologic Analysis of Planetary Surfaces, James R. Underwood, Jr., Dept. Geology, Kansas State Univ., Manhattan, KS 66506

Preliminary use of the edge enhancer to study images of the surfaces of Mars and Mercury and to study terrestrial air photographs has shown this device to facilitate the identification of subtle, otherwise difficult to recognize, linear features. It is particularly useful in discriminating structural grain that is obscured by "busy" topography or that is reflected weakly through a blanket of overlying material. For example, the region in which two large (2.8 km diameter and 11.5 km diameter) impact structures occur in southeast Libya is characterized by a series of prominent northwest trending ridges 100 m high. There, along northwest trending fractures the Nubian Sandstone was so hardened by secondary mineralization that the rock adjacent to the fractures became much more resistant to erosion than the intervening, less mineralized areas. These ridges thus have been interpreted to be erosional remnants, produced by differential erosion as the land surface was lowered, and they give to the region a pronounced northwest-southeast structural grain. Use of the edge enhancer, however, has revealed a finely textured northeast-southwest structural trend that was not recognized earlier.

In the instrument used, the film, transparency, or photograph of interest, up to 35 cm x 45 cm, is placed on an adjustable mask easel overlying a uniform-brightness light box. A vidicon scanner, with a 25 mm f1.4 lens is mounted vertically and converts the photograph or film to electronic signals suitable for processing in the edge enhancer.

There, the object edges or margins on the film or photograph being studied are enhanced by emphasizing, electronically, changes along the X direction of the vidicon image, which can be rotated. The enhancement of changes at edges and margins is achieved by electronic differentiation of the vidicon signal, i.e. the original signal (image) is delayed and is subtracted from in order to highlight changes at boundaries and edges. A delay control enables the operator to vary the ratio of the normal to the delayed signal and thus to enhance image anomalies. Additionally varied perspective can be achieved by switching between a positive and a negative image. The enhanced image is displayed on a 43-cm solid state black and white TV monitor from which photographs may be made for a permanent record of the enhanced images.

Optional features include a high-brightness light box and a "3-d electronic package" which converts a conventional, two-dimensional image into a three-dimensional isometric model displayed on the TV monitor. The isometric model can be rotated so that it may be studied from varied perspectives.

Mars Water Instrument Study, James B. Stephens, Jet Propulsion Laboratory, California Institute of Technology, Pasadena, California 91103.

Experiment Purpose: The evidence for abundant and diverse forms of water in the regolith of Mars is well documented by others. The primary observational objectives of this experiment are to identify mineralogical sites of H_2O and OH^- in samples of the Martian regolith in situ, and to measure the quantity of H_2O and OH^- in each mineralogical site. The secondary objectives are to determine the temporal and spatial variations in H_2O and OH^- occurence, and to obtain supportive information on soil minerology. The ultimate purpose of this experiment is to allow us to understand the implications of the regolith H_2O and OH^- occurences for the physical and chemical history of the regolith material and its interaction with Martian atmospheric and surface volatiles.

Instrument Development Task: During the previous period, soil water instrumentation suitable for use on penetrators was developed and some feasibility demonstration tests were performed with critical elements of the instrument.[1] During this current period (FY78) and the next period (FY79) soil water instrumentation will be developed which will be suitable for use on rover type vehicles (roligons and airplanes as well as conventional crawlers).

Soil Water Analysis Instrument Functional Description: The flight instrument will be based upon differential scanning calorimeter technology as is commonly practiced in the laboratory. The flight instrument's sensitivity will be similar to the present laboratory instrument (Perkin Elmer DSC II). As such it will have the following sensivitity for various forms of water: 0.1% H_2O ice in sample, 0.1% bound H_2O in hydrated iron oxides and clays, and 0.1% bound H_2O in hydrated "evaporite" minerals. It will also be capable of detecting the following mineral forms calorimetrically: anhydrous "evaporite" minerals that melt at less than 700°C (including KNO_3 and $NaNO_3$, at 1% level), goethite and limonite at 3% level, and clay minerals (kaolinite, montmorillonite) at 5% levels. The principal functional difference it will have from laboratory DSC instruments, other than its conversion into space flight hardware, are an ability to handle a large number of soil samples sequentially, and to feed the volatile gases outgased from the sample in the oven into a mass spectrometer. As an adjunct to the DSC an electrolytic (P_2O_5) water sensor instrument will be used to provide an absolute measure of the amount of H_2O evolved from the DSC oven during each thermal cycle.

The Mars Soil Water Experiment Science Requirements that are Imposed upon the Soil Sample Acquisition System: The soil acquisition manipulations may modify the volatile content of the sample by causing evaporation or melting. It may also cause the volatile form to change by migration from one phase to another. Therefore, the soil water experiment must impose some science requirements upon the soil acquisition systems.

Soil Acquisition Systems Functional Description: It is assumed that the soil sample will be extracted by an auger (from soil) or a drill (from rock). A manipulator arm will transport and distribute samples (delivered by the drill or auger) to the processing system which will crush and sieve it to proper size. The sample will then be delivered to the various analytical instruments (probably by gravity or by the manipulator).

Mars Water Experiment Science Requirements Imposed Upon Soil Acquisition Systems: The drill or auger shall be capable of driving a hole into a vertical as well as a horizontal surface a distance of 10 cm in

unaltered rock (drill) and at least one meter in soil (auger). A sample must be obtainable from the drill or auger which is not mixed with soil from other hole depths. The auger shall be capable of driving a hole into soil and extracting a sample during the halt portion of travel cycle in autonomous mode during night time as well as day time. The soil processor shall be capable of comminuting (crushing) and size separating (sieving) rock and soil to grain size. The extraction, processing, transporting and distribution functions shall be performed without disturbing the volatile content or volatile form of the sample by more than 0.1% of total sample. The soil acquisition system shall be capable of obtaining hundreds of samples.

Progress for this FY: The science requirements, functional requirements and rover interface requirements have been defined for the soil water instruments (DSC and P_2O_5). The science requirements for the soil sample acquisition system, pertinant to the soil water experiment have been defined. No insurmountable problems have been discovered. Two difficult problems have, however, been recognized: (1) how best to implement the multiple sampling requirement for the DSC and (2) how to avoid redistributing or evaporating the volatiles in the soil sample during the acquisition and processing operations. Several alternative solutions are under study for both problems at present.

Plan for this FY: The relationship between the various analytical instruments and the soil acquisition system will be studied in more detail and a conceptual design of their functional interrelationships will be developed. A nominal time-line for a typical acquisition and analysis period will be developed in order to analyze the logistical problems inherent in such complex and interrelated elements. In the laboratory, resources permitting, a DSC instrument will be integrated with a spare Viking GCMS instrument. It is anticipated that, as a first step, the existing GCMS ovens can be adapted as crude DSC ovens. Flight quality ovens designed for multiple loading and unloading would be developed later. The Viking hardware for this purpose is presently in our possession. This preliminary integration of instruments will provide considerable hands-on-experience that will prove invaluable in the ultimate design of the instrumentation compliments for the mission.

Reference: [1] Anderson, D. M., et al, "Mars Soil-Water Analyzer Instrument Description and Status", Proceedings of the Colloquium on Water in Planetary Regoliths, Oct. 1976, Pub. by U. S. Army Cold Regions Research and Engineering Laboratory, Hanover, N. H., 03755.

Laboratory Infrared Reflectance Studies, Larry A. Lebofsky, Lunar and Planetary Lab., Univ. of Arizona, Tucson, AZ 85721 and Jet Propulsion Lab., Pasadena, CA 91103.

An extensive study of the infrared (1-5μm) reflectance spectra of various materials is being carried out. We are attempting to build up a data base for the interpretation of telescopic spectra observations of the surfaces of solar system objects for the determination of their surface composition.

These infrared (1-5μm) reflectance studies can be broken down into three categories:

1) Silicates and hydrated silicates. These studies have a direct bearing on studies of the infrared spectra of asteroids and the Galilean satellites of Jupiter. Unpublished work of Salisbury and our own laboratory studies have shown that the spectra of dark hydrated material (e.g. carbonaceous chondritic material) show a water absorption band (due to water of hydration) in the 3 to 4μm region, but that the water absorption bands shortward of 3μm are suppressed by the presence of dark material. This band is found in both Type I and Type II carbonaceous chondrites, but not in Type III or Type IV carbonaceous chondrites. The band can thus be used to distinguish among different types of carbonaceous asteroids. This has already been used to identify water of hydration on the asteroid 1 Ceres (Lebofsky, 1978). This is also important to our understanding of the surface composition of Callisto (JIV) which has a surface

composed primarily of hydrated minerals (Pollack et al., 1978), but may also contain some water frost (Lebofsky, 1977).

2) Frosts. The visible surfaces of outer solar system satellites appear to be frost covered. For some of the satellites of Saturn infrared observations have shown the presence of water frost, but for the other Saturn, Uranus, and Neptune, no positive identification of their surface compositions has been made. In the case of Pluto, a probable identification of CH_4 frost has been made, but other frost seem to be present. Laboratory studies of various frosts (CH_4, NH_3, H_2O and mixtures) are being conducted to comparison with telescope infrared observations of the satellites that are now being carried out, in an attempt to determine their surface compositions.

3) Salts. Recent observations of Io in the 1-5μm spectral region have shown the presence of several absorption bands in the 3-5μm region. Preliminary results seem to indicate that these bands may be due to evaporite salts as has been hypothesized by Fanale, et al. (1974) (Pollack et al., 1978, Cruickshank et al., 1978). Based on these results we have been studying in the laboratory a large number of salts in order to make an identification of the bands that have been

observed in Io's spectrum. We are also cooling the salts and mixtures to the temperature expected on the surface of Io to see what effect Io's low temperature environment will have on the band centers and shapes.

The overall goal of our program is to produce spectra in the laboratory that can be used along with the data now being taken at the telescope to help us in our understanding of the surfaces of the carbonaceous asteroids and the satellites of the outer solar system.

References

Cruikshank, D.P., Jones, T. and Pilcher, C.B. (1978) in preparation.

Lebofsky, L.A. (1977) Nature, 269, 785-787.

Lebofsky, L.A. (1978) MNRAS, in press.

Pollack, J.B., Witteborn, F.C., Erickson, E.F., Strecker, D.W., Baldwin, B.J., and Bunch, T.E., in preparation.

Diffuse Reflectance Spectra of Azurite, Malachite, and Chrysocolla, K.L. Andersen (R.L. Huguenin, P.I.), Planetary Chemistry Laboratory, Dept. of Physics and Astronomy, U. of Mass., Amherst, MA 01003, and Dept. of Earth and Planetary Sciences, MIT, Cambridge, MA 02139.

Lab reflectance spectra (0.35mμ →2.50mμ) of suites of azurite, malachite, and chrysocolla samples are analyzed as part of the background research for development of a remote sensing regime for copper and other sulfide-derived ore deposits on Mars and other planetary objects. Features appearing in the reflectance spectra are correlated with crystal structure: electronic transitions are assigned using ligand field theory and vibrational features are determined from the ligand fundamentals.

Crystal structures. Malachite, $Cu_3CO_3(OH)_2$, belongs to the space group $P2_1/a = C_{2h}^5$ with Z=4. Cu^{2+} occupies two sites both of which are axially elongated octahedra with the ligands in trans-positions. The site population is 1:1. Azurite, $Cu_3(CO_3)_2(OH)_2$, belongs to the space group $P2_1/c = C_{2h}^5$ with Z=2. Cu^{2+} occupies two very distorted sites - one site is essentially square planar with the ligands in trans-positions, and the other site is a square pyramid with the ligands in cis-positions. The site population is 1:2. The crystal structure of chrysocolla, $CuSiO_3 \cdot nH_2O$, has not been reported.

Reflectance spectra of malachite. In Figure 1, the reflectance spectra of five malachite samples show 3 electronic transitions centered near 9200cm^{-1} ($^2B_{1g} \rightarrow {}^2A_{1g}$), 13,000cm^{-1} ($^2B_{1g} \rightarrow {}^2B_{2g}$), and 22,400cm^{-1} ($^2B_{1g} \rightarrow {}^2E_g$). The reflectance peak near 19,100cm^{-1} gives malachite its green color. The band assignments are based on Figure 3, with the $^2B_{1g} \rightarrow {}^2B_{2g}$ equal to 10Dq (1). The D_{4h} distortion of the octahedral sites is not great so that the tetragonal field splitting parameters can be calculated to give Ds=-2660cm^{-1} and Dt=245cm^{-1}. All malachite transitions are spin allowed, and all are vibronically allowed except for the $^2B_{1g} \rightarrow {}^2B_{2g}$ which is forbidden in the z-direction. This might explain the band's apparent asymmetry, although it could also arise from the superposition of transition energies due to Cu^{2+} in two different structural sites. Effective symmetry coupling or intensity borrowing from the $^2B_{1g} \rightarrow {}^2A_{1g}$ might explain the $^2B_{1g} \rightarrow {}^2B_{2g}$ transition's high absorption intensity relative to the others. The broadness of the $^2B_{1g} \rightarrow {}^2E_g$ suggests a removal of the term degeneracy. The first derivative of each spectrum was calculated which resolved the positions of the split components - the energy difference between them was found to range between 1000 and 1800cm^{-1}. The strong absorption at the high energy end of the spectrum (>29,000cm^{-1}) is probably due to the

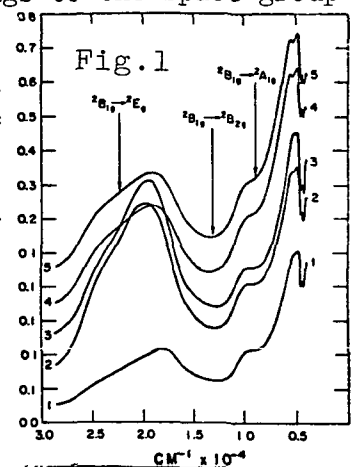

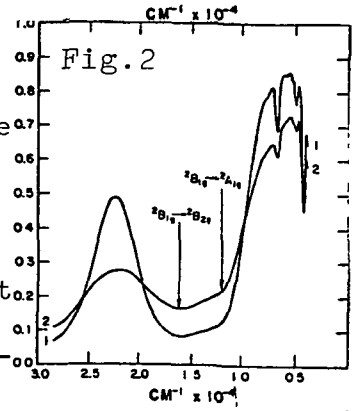

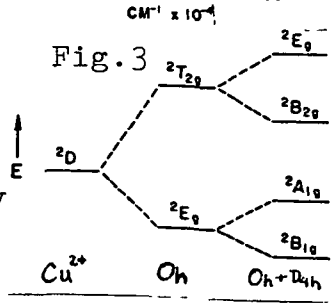

edge of the $O^{2-} \rightarrow Cu^{2+}$ charge transfer transitions which generally occur at energies just above the ligand field transitions and may extend far into the ultraviolet region. The electronic transitions in the spectra of samples 4&5 occur at higher energies than the others and seems to be related to structural disorder (2).

Reflectance spectra of azurite. In Figure 2, the reflectance spectra of two azurite samples show two electronic transitions centered near 13,000cm^{-1} ($^2B_{1g} \rightarrow {}^2A_{1g}$) and 16,000cm^{-1} ($^2B_{1g} \rightarrow {}^2B_{2g}$). The reflectance peak near 22,300cm^{-1} gives the mineral its azure color. The band assignments are based on Figure 3, but it should be noted that the azurite sites are much more distorted than the malachite sites and thus Ds and Dt have little meaning. Because of the gross site distortion, one might expect the $^2A_{1g}$ term to be higher in energy than the $^2B_{2g}$ term. However, the energy separation between the $^2B_{2g}$ and $^2B_{1g}$ terms would still be equal to 10Dq resulting in Dq = -1300cm^{-1}, the same as the malachite value. Since Cu^{2+} occupies similar ligand environments in both minerals, it is more reasonable to expect Dq to be higher for azurite than for malachite since the azurite sites are more distorted and the average Cu^{2+} - ligand bond lengths are comparatively shorter. Therefore, the ordering of the transitions in azurite is assumed to be the same as in malachite (Fig.3) giving Dq = -1610cm^{-1} for azurite. The azurite transitions are relatively broader and more intense than those in malachite. Greater site distortions most likely account for the broadness of the azurite bands. The intensity of the transitions arise mainly from site 2 not only because it occurs twice as often in the azurite structure as site 1, but because the cis-symmetry of site 2 precludes an INVERSION CENTER, meaning the vibronic interactions will greatly intensify transitions arising from it. The two malachite sites are evenly distributed throughout the crystal structure so that they may be expected to contribute equally to the observed transitions, assuming similar symmetry coupling in both sites. Although the energy of the $^2B_{1g} \rightarrow {}^2E_g$ is too high to be observed (>29,000cm^{-1}) in the azurite spectra, this band may be predicted to be non-degenerate as in malachite, and the arguments for its non-degeneracy can be extended to the azurite case.

The absorption features in the near IR region of the azurite and malachite spectra arise from combinations and overtones of the OH and CO_3 fundamentals and are discussed in detail in (2).

Reflectance spectra of chrysocolla. Chrysocolla is a blue to green mineral usually associated with azurite and malachite. Spectra of representative blue (BC) and green (GC) samples (taken from a suite of three each) are shown in Figures 4A and 4B respectively. In BC, the sharp IR features arise from H_2O vibrations, while the IR bands in GC are very similar to CO_3 and OH bands in the malachite spectrum. Further, the Cu^{2+} transitions in GC occur at the same energies as those in malachite. The Cu^{2+} transitions in BC occur near 11,800cm^{-1}, 14,000cm^{-1}, and 23,800cm^{-1}. It can be concluded that BC is truly a hydrous copper silicate while GC seems to be a mixture of malachite and silica.

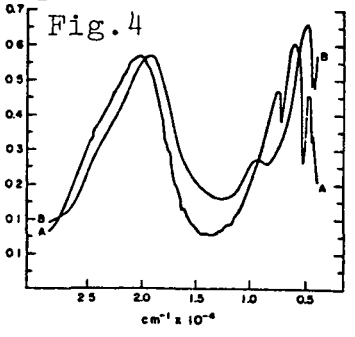

Acknowledgement. Contribution No. 5 of the Planetary Chemistry Laboratory.

References.

(1) Lever, A.B.P. (1968). Inorganic Electronic Spectroscopy, American Elsevier, New York, P. 78.

(2) Andersen, K.L. (1978). "Diffuse Reflectance Spectra of Azurite and Malachite," (unpublished manuscript).

Tests of a Miniaturized Chemical Analysis System, T. E. Economou and A. L. Turkevich, Fermi Institute, University of Chicago, Chicago, IL 60637, and E. J. Franzgrote, Jet Propolsion Laboratory.

A miniaturized chemical analysis system, incorporating scattered alpha, alpha-proton, and X-ray production modes, has been assembled and tested. The system is designed to provide chemical analyses of samples of about 1 cm^2 area using an instrument head of less than 300 cm^3 volume. Such a system should be able to identify and determine the amounts of more than 99% of the atoms (other than H) in a sample, as well as many minor and trace elements. It would thus be suitable for use on Penetrator type missions, as a survey-type instrument for sample selection, as well as for analyses of collected samples on board a planetary Rover or on a cometary mission.

The geometrical relations of source-sample- detectors are those of "Micro-Alpha", with an alpha source in the center of two silicon ring detectors.[1] The front detector is a thin (~25 micron) surface barrier detector for the alpha mode of the instrument; the back detector is a thicker lithium drifted silicon detector for the proton mode. The two are operated in appropriate electronic coincidence-anticoincidence. Two X-ray detectors have been used: a cooled, intrinsic germanium detector system of a type that has been demonstrated to be operable with a Joule-Thomsen cryostat,[2,3] and a room temperature HgI_2 crystal detector[4] with a Peltier-cooled FET first stage of amplification[5].

The system has been tested at a Tandem van de Graaf accelerator[6] with monochromatic alpha particles of 6.1 MeV (corresponding to those available from a ^{242}Cm alpha source) in order to check on the design parameters of the alpha and proton mode geometries. Data have also been obtained on the angular and energy dependencies of the response in these modes.

The performance in the alpha mode has been very good, comparable to that of the larger Mini-Alpha system.[3] The proton mode performance has been good for low energy proton emitters (e.g. Mg, Si) but less satisfactory for elements emitting higher energy protons(e.g. Al) due to less than optimum proton detector characteristics. Better detectors of this type have been available in the past and so this should be no problem.

The X-ray detectors have operated with a resolution (at 5.9 KeV) of less than 200 eV for the cooled intrinsic germanium, and 400 eV for the room temperature HgI_2 detector. The satisfactory performance of the latter detector is a very promising development for compact, low weight and power instruments for extra-terrestrial in-situ chemical analyses.

1. A. L. Turkevich and T. E. Economou (1977) Planetary Principal Investigators Meeting, St. Louis, MO, May 23-25.

2. E. J. Franzgrote and L. Wang (unpublished).

3. T. E. Economou and A. L. Turkevich (1976) Nucl. Instr. Meth. 134 391-400.

4. W. Seibt, M. Slapa and G.C. Huth (1976) Nucl. Instr. Meth. 135 573-576.

5. A. Dabrowski and G. C. Huth (1978) To be published. We acknowledge the cooperation of A. Dabrowski and G. C. Huth in providing the HgI_2 detector and assisting in the tests.

6. Courtesy of T. Tombrello, California Institute of Technology. We acknowledge the cooperation of the C.I.T. Tandem staff in the performance of these tests.

Planetary Cartography, R. Batson, U.S. Geological Survey, Flagstaff, Arizona 86001

During fiscal year 1977 the Planetary Cartography project performed work on six major tasks. Although most of this work was completed during fiscal 1977, delays were incurred in some phases and modifications were required in other areas due to advancing technology. This is a status report for each of the tasks.

Mars 1:5,000,000 Topographic Series:

All but eight 1:5,000,000 Mars sheets remained to be compiled in 1977. Six of those eight were started after receipt of high quality Viking images in their areas. Initially the determination was made to allow airbrushing to incorporate data visible on Viking pictures where such extra detail actually speeded up compilation by clarifying Mariner 9 data. Once work was begun in the southern intermediate latitudes of Mars, it was found that information on Viking pictures was comprehensive and detailed compared to totally inadequate information on Mariner 9 pictures. Compilation was therefore much slower than originally planned. A second evaluation was then made of the Mars mapping effort. Prior to that time, overlays were made showing albedo markings for each shaded relief sheet. Discussion with many members of the Viking team revealed that in nearly all the areas where albedo markings had not yet been compiled with the airbrush, the Mariner 9 data is virtually useless, even in the limited and restricted mode that was used in the mapping. It was therefore decided to invest the extra effort required in drawing a reasonable level of relief detail from Viking images, rather than in the compilation of meaningless albedo pattern mapping.

1:25,000,000 Shaded Relief Map of Mercury:

A shaded relief map of Mercury was compiled at 1:15,000,000 for publication at 1:25,000,000. The bases for this map were the three 1:5,000,000 Mercator projections of the equatorial region, the two 1:5,000,000 Mercator projections of the Polar region, and the four 1:5,000,000 Lambert conics of the intermediate reductions. The latter were digitized on an optical mechanical scanner and put through a geometric transformation to the Mercator projection. The digitized sheets were distorted where possible to make them match better control point positions than were available when they were originally compiled.

Mercury Digital Data Base:

The objective of this task was the compilation of a low resolution computer mosaic of all of Mercury visible to Mariner 10. This data base is to provide basic geometric control for future mapping of Mercury. Approximately 50 percent of this data base was complete by the end of fiscal year 1977. Modifications to this project include the digital encoding of all shaded relief maps so that they can be reformatted to the latest Mercury control net.

Mars Digital Data Base:

This project was designed to develop procedures for the routine compilation of cleaned up computer mosaics of unenhanced black and white Viking orbitor pictures. These are required in the compilation of controlled base mosaics for topographic mapping and geologic investigations. All basic technology for this project has been developed previously. The only requirement was to standardize and streamline procedures by compiling digital data bases of two areas covered by Viking pictures. This task is complete and the technology and techniques are available for future work.

Experimental Mapping of Satellites:

The objective of this task is the compilation of a map of Phobos with Mariner 9 data to evaluate techniques for compiling maps of Jovian and Saturnian satellites or of other irregular bodies. All basic software for this project has been written and techniques have been developed. The extremely low quality of the Mariner 9 images and the extremely high qualify of the Viking data resulted in restarting the compilation phase of this work near the end of the fiscal year. The project was continued into fiscal 78 and expanded to include Deimos as well. The work will be done by methods developed under this project but with Viking pictures rather than Mariner 9 pictures of the satellites.

Gazeteer of Planetary Nomenclature:

The objective of this task was to compile and maintain a gazeteer of names of features on the Moon and planets exclusive of the earth. The gazeteer is required for lunar and planetary cartography. Owing to funding cutbacks at the beginning of the fiscal year, the lunar part of the gazeteer was dropped. A gazeteer of names appearing on 1:250,000 and smaller scale maps of Mars and Mercury was compiled. It is encoded in computer readable form and is updated as necessary for cartographic work on those two planets.

Mercury Geologic Mapping
Holt, H. E.

Mercury Geologic Mapping, H. E. Holt, U. S. Geological Survey, Flagstaff, Arizona, 86001.

The NASA Mercury Geologic Mapping program is based on the photographic data returned by Mariner 10 during three flybys of the planet in 1974-1975. About 45 percent of the surface of Mercury was photographed during the three flybys. Geologic maps of nine quadrangles at a scale of 1:5,000,000 and one geologic map at a scale of 1:25,000,000 are being prepared from the available data. Four of the quadrangles are in technical review which include: Kuiper Quadrangle (H-6); Tolstoi Quadrangle (H-8); Discovery Quadrangle (H-11) and Bach Quadrangle (H-15).

Preliminary results from the Mercury Geologic Mapping program have already provided information about mercurian geologic history and the geological processes that have affected and controlled this history. For example, the extensive ejecta blanket that surrounds the Caloris basin is used as a stratigraphic marker in recognizing pre- and post-Caloris events over much of the surface of Mercury. Correlations, based on crater frequencies between plains units and larger crater degradation sequences, provide means of establishing relative chronologies and relating most of the remaining surface of Mercury to the Caloris event. The Caloris event occurred after the intense cratering period and smooth plains materials postdate the formation of the Caloris basin. The widely distributed, but localized, occurrence of smooth plains materials show large spatial separation from possible impact sources and imply local volcanic origins.

The Control Net of Mars. Merton E. Davies, The Rand Corporation, Santa Monica, California, 90406

A new control net of Mars, containing 4138 points, was computed in February 1978.[1] Measurements of these points on 1009 Mariner 9 and 204 Viking pictures were used in the photogrammetric solution; horizontal coordinates of the points and the camera orientation angles of the pictures were determined. The radii at the control points came from three sources: 3146 were interpolated from Mariner 9 radio occultation measurements,[2] 22 were computed photogrammetrically,[3] and 970 were derived from the USGS 1:5,000,000 series topographic maps of Mars.[4] The JPL navigation team furnished the spacecraft positions when the pictures were taken.

Like the May 1977 net, this computation used the rotation rate and spin axis of Mars determined by the Viking lander radio science team.[5] However, the areocentric right ascension and latitude of the Viking 1 lander site as identified by Elliot Morris and Ken Jones on Viking orbiter picture 452B11 were held at values determined by the Viking team.[5] Longitude of the Viking landers was measured photogrammetrically from Airy-0. The Viking 1 lander site identified by Morris and Jones was about 12 km from the location expected by the May 1977 net.

In the February 1978 control net, the areocentric right ascension of the prime meridian, V, is given by

$$V = 148.516^\circ + 350.891986^\circ \ (J.D. - 2433282.5)$$

and the coordinates of the Viking landers are

V1	ϕ	= 22.272° areocentric	V2	ϕ	= 47.670° areocentric
	ϕ'	= 22.482° areographic		ϕ'	= 47.966° areographic
	λ	= 47.968°		λ	= 225.736°
	R	= 3389.38 km		R	= 3381.91 km

Work on the control net of Mars started soon after Mariner 9 went into orbit, and many versions have been published. The reason, of course, was to furnish the latest data for the mapping program being carried out simultaneously with this work. The following table summarizes the computational parameters of the published control nets over the years. It is a pleasure to see the overdetermination finally exceed 2 with the introduction of Viking pictures.

HISTORY OF CONTROL NET OF MARS

Date	Points	Pictures	Observation equations	Normal equations	Overdetermination factor	Standard error of measurement
August 1972	809	407				
November 1972	1205	598				
April 1973	1340	613	8002	4519	1.77	0.0163 mm
June 1973	1645	660	9804	5270	1.86	0.0144 mm
May 1974	2061	762	11678	6408	1.82	0.0155 mm
May 1977	3037	928	17224	8858	1.94	0.0167 mm
February 1978	4138	1213	27582	11915	2.31	0.0207 mm

References

(1) Davies, M. E., F. Y. Katayama, and J. A. Roth, Control Net of Mars: February 1978, The Rand Corporation, R-2309-NASA, February 1978.

(2) Davies, M. E., Mariner 9 Control Net of Mars: June 1973, The Rand Corporation, R-1309-JPL, June 1973.

(3) Davies, M. E., "Photogrammetric Measurements of Olympus Mon on Mars," Icarus, Vol. 21, No. 3, March 1974, p. 230.

(4) Wu, S. C., "Topographic Mapping of Mars," U.S. Geological Survey, Interagency Report: Astrogeology 63, December 1975.

(5) Mayo, A. P., et al., "Lander Locations, Mars Physical Ephemeris, and Solar System Parameters: Determination from Viking Lander Tracking Data," J. Geophys. Res., Vol. 82, No. 28, September 30, 1977, p. 4297.

Mars Geologic Mapping, D. H. Scott, U. S. Geological Survey, Flagstaff, Arizona 86001.

The systematic geologic mapping program of Mars using Mariner-9 photographs is nearing completion. Mapping was started in 1972 and involved 30 quadrangles covering the planet at a scal of 1:5,000,000. In addition, a geologic map of the planet at 1:25,000,000 scale and representing a compilation with revisions of the larger scale efforts was completed and is in press.

During 1977 (Figure 1), eight maps were processed through technical review stages; seven completed maps were submitted to the editorial unit for Director's approval, and six maps were transmitted to the U.S.G.S. Branch of Map Reproduction (BMR) for publication. By the first quarter of 1978, ten maps had been published and 12 maps were in press.

Among the more interesting disclosures of the recent mapping were the concepts of chasma capture (higher ones by lower ones) and the existence of large, long enduring lakes along the Valles Marineria system. These ideas were advanced (1) to explai the interconnections between Ophir, Candor, and Melas chasmas as well as the rhythmically stratified deposits in the canyon floors Complex fault systems in Thaumasia (2) and Arcadia (3) quadrangle have revealed a long history of crustal deformation peripheral to the Tharsis region. Ring structures in Sabaeus Sinus (4) are indicated by faults concentric to Hellas and are some 3000 km from the basin center. Studies (5) of the Argyre basin

suggest that this large relatively fresh appearing basin has few elements for comparison with lunar counterparts such as Orientale where processes for basin development might be inferred from structural and morphological details. Multiple episodes of volcanism in the Phoenicis Lacus quadrangle (6) separated by periods of erosion were recognized around the shields of Arsia and Pavonis Mons. Mountain materials form massive ridges in the Memnonia quadrangle (7) that do not resemble the angular peaks surrounding martian impact craters such as Isidis. They are assigned to a period of structural deformation early in the formation of the Tharsis uplift. Similarly, the Phlegra mountains in the Cebrenia quadrangle (8) are not associated with any known basin ring and are considered to be of possible tectonic origin.

References:

(1) McCauley, J.F., 1978, Geologic Map of the Coprates quadrangle of Mars: U.S. Geol. Survey, Misc. Geol. Inv. Map I-897.
(2) McGill, G. E., 1978, Geologic Map of the Thaumasia quadrangle of Mars: U.S. Geol. Survey, Misc. Geol. Inv. Map I-1077.
(3) Wise, D. U., 1978, Geologic Map of the Arcadia quadrangle of Mars; U.S. Geol. Survey, Misc. Geol. Inv. Map (in press).
(4) Moore, H.J., 1978, Geologic Map of the Sabaeus Sinus quadrangle of Mars: U.S. Geol. Survey, Misc. Geol. Inv. Map (in press).
(5) Hodges, C.A., 1978, Geologic Map of the Argyre quadrangle of Mars: U.S. Geol. Survey, Misc. Geol. Inv. Map (in press).
(6) Masursky, H., Strobell, M.E., Dial, A. L., 1978, Geologic Map of the Phoenicis Lacus quadrangle of Mars: U.S. Geol. Survey, Misc. Geol. Inv. Map I-896.
(7) Mutch, T.A., and Morris, E.C., 1978, Geologic Map of the Memnonia quadrangle of Mars: U.S. Geol. Survey, Misc. Geol. Inv. Map (in press).
(8) Elston, W.E., 1978, Geologic Map of the Cebrenia quadrangle of Mars: U.S. Geol. Survey, Misc. Geol. Inv. Map (in press).

MARS GEOLOGIC MAPS

Status – First Quarter, 1978

MC	Quadrangle	Technicial Reviews	Editorial Review (TRU)	In Press	Published
1	M. Boreum				
2	Diacria				
3	Arcadia				
4	M. Acidalium				
5	Ismenius Lacus				
6	Casius				
7	Cebrenia				
8	Amazonis				
9	Tharsis				
10	Lunae Palus				
11	Oxia Palus				
12	Arabia				
13	Syrtis Major				
14	Amenthes				
15	Elysium				
16	Memnonia				
17	Phoenicis Lacus				
18	Coprates				
19	Margaritifer Sinus				
20	Sabaeus Sinus				
21	Iapygia				
22	M. Tyrrhenum				
23	Aeolis				
24	Phaethontis				
25	Thaumasia				
26	Argyre				
27	Noachis				
28	Hellas				
29	Eridania				
30	M. Australe				
Mars Geol Map 1 25M					

Figure 1

CHAPTER 13 - COMMITTEE AND WORKSHOP REPORTS

Report on the Tharsis Workshop, R. J. Phillips, Jet Propulsion Laboratory, California Institute of Technology, Pasadena, California 91103

INTRODUCTION: On September 5th through 9th, 1977 a workshop was convened in Vail, Colorado to discuss the origin, evolution, and present state of the Tharsis volcano/tectonic province of Mars. Workshop participants were Karl Blasius (PSI), Michael Carr (USGS), Gordon Eaton (USGS), Charles Gilbert (VPI), Michael Malin (JPL), Thomas McGetchin (LPI), Roger Phillips (JPL), Steve Saunders (JPL), Norman Sleep (Northwestern U.), Sean Solomon (MIT), and Donald Wise (U. Mass.). The goals of the workshop were: (1) to thoroughly review observational and theoretical constraints regarding Tharsis, (2) to outline multiple working hypotheses regarding the origin of Tharsis, (3) to test, in a preliminary fashion, the hypotheses against the constraints, and (4) to define areas of research to further constrain the hypotheses. To carry out the above-mentioned goals, the workshop was structured in the following manner: The first two days were used for individual tutorial presentations on the present state of knowledge of the geological, geophysical, and petrological constraints regarding Tharsis. From that point, a series of constraints were formulated that any hypothesis must satisfy. The third and fourth days of the workshop were devoted to formulating hypotheses and preliminary testing of these hypotheses against the specified constraints. The final day was devoted to defining crucial research necessary to help distinguish among the hypotheses.

THE HYPOTHESES FOR THARSIS: 1. Chemical Plume - Description: Mars formed by "classical" inhomogeneous accretion. In this model the primitive lower mantle is less dense (higher Mg/Fe ratio) and carries more radiogenics than the primitive upper mantle. The arrangement is unstable and becomes more unstable as the lower mantle is heated preferentially. The instability breaks out in a "chemical plume" that rises to the base of the lithosphere. The plume heats the local mantle relative to its surroundings and provides buoyant, thermoelastic, and possibly viscous stresses for the uplift of Tharsis. Difficulties: The hypothesis specifically requires inhomogeneous accretion with a nebular temperature at the start of accretion in excess of 1600°K. The temperature must drop some 1200° during the accretion interval. This seems implausible at the Mars distance. It is furthermore difficult to imagine this type of accretion in view of contemporary theories which require an intermediate stage of planetesimal formation. Testable Questions: Can the plume maintain volcanism for several billion years? There may be chemical differences among lavas at different places on the surface, testable by spectral differences or differences in flow morphology.

2. Homogeneous Accretion and Whole Mantle Convection - Description: The primitive mantle is homogeneous; after core formation whole mantle convection begins. Tharsis is the result of first harmonic convection. Lighter material separates at the top of the ascending limb and carries most of the radiogenic material. Difficulties: Where is the antipodal effect for the first harmonic? If the harmonic mode of convection is actually higher, where are the other contemporaneous volcanic centers? Testable Questions:

Can the convecting system produce the gravity anomalies and topography?

3. Compressional Arching - Description: This model suggests that the uplift of Tharsis and adjacent depressions of Chryse and Amazonis result from lateral compression and crustal warping. A possible mechanism could be global shrinking as a result of overall cooling. Difficulties: The model does not satisfy the volcanism requirement without an additional local source. The gravity data are not satisfied unless the crust can be thickened under Tharsis and thinned under the adjacent basins. The observed structural features are not consistent with such a model since no compressional features are observed in the basins.

4. Hellas Antipode - Description: Tharsis and Elysium are approximately antipodal to the large impact basins Hellas, Syrtis Major, and Isidis, and to Argyre, respectively, and may be connected in origin to them. On both the Moon and Mercury, tectonic effects antipodal to the largest basins may be present. Theoretical calculations indicate that for a large impact into a sphere much of the shock energy is focused in the antipodal region. Dissipation of shock energy in the antipodal regions will raise subsurface temperatures and could create a sizable thermal anomaly which in turn could cause updoming. Reflection of the shock waves from the surface will also create fracturing of the lithosphere. If mantle temperatures are close to the solidus previous to impact, then the effect of the impact may be to raise the temperatures above the solidus. Difficulties: The Tharsis and Elysium uplifts are not exactly antipodal to the largest impacts. As a mechanism in itself, it could not sustain long-term volcanism. This mechanism might be effective as a triggering device, such as pushing near-solidus temperatures just to solidus.

5. Primordial Inhomogeneity - Description: The model supposes that during either formation of the planet or during differentiation of its crust, compositional inhomogeneities developed in the martian mantle and that some parts of the mantle are relatively less depleted in radiogenic elements than others; then these predetermine the locations and areal extents of the martian volcanic provinces. Heating of these mantle regions gives rise to mass transfer of heat to the base of the lithosphere accompanied by injection, thermal doming, and fracturing. Difficulties: This model may not have an adequate life span to account for the longevity of the Tharsis activity. Testable Questions: Can the inhomogeneity sustain volcanism for several billion years? Are there chemical differences in surface lavas?

6. Core Formation - Description: Some years ago Elsasser proposed that the thermal gradient in an evolving planet would rise into the iron/iron sulfide melting curve at some intermediate depth in the mantle. The result would be a gravitationally unstable layer of liquid collecting at that intermediate depth, which would finally dimple and drain downward to form a core. Applied to Mars this process would provide an asymmetric deep heat source through the gravitational energy given up by the sinking fluid. Core formation on Mars is a slow process unlike the catastrophic runaway

envisaged for the Earth.) This heat pulse would then power localized convection and/or conduction in the overlying mantle to cause the Tharsis bulging and expansion. Other variations involving convective motion in an already formed molten core might be suggested for the heat asymmetry under Tharsis, but suffer from problems in maintaining an adequate temperature difference in one location to maintain convection in that spot. Difficulties: There seem to be no major difficulties with this model providing it is quantitatively reasonable. It has the potential to provide a localized heat source of long duration. Testable Questions: What is the heat budget and mass transfer as a function of time? What are the instability relationships and probable size of instabilities?

7. De-Sulfidization of the Lithosphere - Description: About 20% of the mass of Mars is in the core. If the lithosphere of Mars was cool during the time of main core formation, the Fe-FeS present in the lithosphere would remain there. During the time of core formation or thereafter, the sulfide layer (or disseminated sulfide) was lost from the Tharsis region and replaced by ordinary mantle of much lower density. This lower density causes permanent updoming and fracturing. A positive free-air gravity anomaly results from second order isostatic effects. Volcanism is concentrated by edifice effects on stress. Other possible chemistries include hydration and scapolitization. For these mechanisms the density difference between depleted and undepleted mantle is about 1%, insufficient to produce the Tharsis uplift. Difficulties: This process requires a mechanism to preferentially deplete Fe-FeS from one geographic region of the lithosphere or to initially concentrate Fe-FeS at some other region of the lithosphere. Testable Questions: Since this mechanism leads to a permanent density change and buoyancy, the same gravity anomaly, albeit scaled, ought to exist for Elysium. This can be tested with the low altitude Viking data now being collected. The Pratt isostatic mechansim implied here for Tharsis can be tested specifically against the gravimetric and topographic observables.

8. Mantle Lithosphere Overturn - Description: The mantle part of the lithosphere is colder and more dense than the underlying asthenosphere. If tensional deviatoric stresses occur, the lithospheric mantle may sink toward the center of the planet. The hotter material which replaces the sunken material is less dense and will produce uplift by isostasy and free-air gravity anomalies by second order isostatic effects. Slope reversals and recent faults are expected from this process and the uplift will decay in 300-400 M.Y. unless reactivated. Alternatively, desulfidization of the mantle may lead to a permanent density anomaly after the first overturn. Volcanism is concentrated in this mechanism by edifice effects on stress. Difficulties: This mechanism may require continual reactivation to explain the long duration of Tharsis volcanism. This would require periodic fracturing, which does not seem to be observed. Testable Questions: Are there, in fact, extremely young fractures?

Planetary Geology Field Conference on Aeolian Processes, Ronald Greeley, Dept. of Geology and Center for Meteorite Studies, Arizona State Univ., Tempe AZ 85281

A comparative geology field conference was held in Palm Desert, California, January 10-14, 1978 in order to establish a dialogue between geoscientists interested in aeolian processes on Earth and planetary geologists studying aeolian processes on the planets. Approximately sixty-five participants attended the technical sessions and field trips. Invited participants included R. A. Bagnold, E. D. McKee, and R. P. Sharp; field trip leaders included R. P. Sharp, J. Shelton, R. Saunders, R. S. U. Smith, and T. Pewe. Field trips included Garnet Hill (a well-known ventifact locality), Salton Sea dune field, Algodones dune field, Amboy Crater, Kelso dunes, and general geology of the southern Mojave Desert and Imperial Valley.

A comparative geology field guide covering the area was published as a NASA publication and copies are available on request from R. Greeley.

Standard Techniques for Presentation and Analysis of Crater Size-Frequency Data - A Report of the Crater Analysis Techniques Working Group*

A committee composed of twelve scientists deeply involved with the collection and analysis of crater statistics met in Flagstaff on September 8 and 9, 1977, to make recommendations for standards of crater measurements and statistical analysis methods. The committee recommended the following:

Graphs:

1. Display data on both a "Cumulative Size-Frequency Plot" and a "Relative Size-Frequency Plot".
2. Make the abscissas and ordinates both base 10 logarithmic.
3. Use consistent units on both axes.
4. Use the same scale for both axes.
5. Plot the 1σ confidence intervals for the data points.

Tables:

1. Give all of the data in tabular form.
2. Bin the data in $\sqrt{2}$-factor or finer bins.
3. Give the number of craters in each bin.
4. Specify the amount of surface area on which the data were measured.
5. Deposit the data tables with LPI.

Supporting Information:

1. Specify the source and kind of materials on which the measurements were made.
2. Specify the measuring technique used and assess its accuracy.
3. Give the exact location of the area studied.
4. Give all other pertinent information such as the assumed scale of the photographs and the corrections, if any, made to the raw measurements.

Regression Analyses:

1. Give the 1σ confidence intervals on the regression coefficients.
2. Report the results of a goodness-of-fit test of the data to the regression.

Morphologic Analyses:

1. A quanitative measure is preferable to a qualitative measure.
2. Specify the exact criteria used for making qualitative assignments or measurements.

All of the recommendations were made unanimously by the committee and have been endorsed by the group 8 of the planetary basaltic consortium. A summary of the results and recommendations of this meeting are being drafted and will be published in the open lit rature as well as a NASA document. A second meeting, which will also include several new committee members, is tentatively scheduled for the spring to discuss standards for crater morphology statistical studies.

---

*(Alphabetically) R. Arvidson, Washington Univ.; J. Boyce (Co-chairperson), USGS/NASA Hdqt; C. Chapman, Planetary Sciences Inst.; M. Cintala, Brown Univ.; M. Fulchignoni, Lab Astrofiscia Spacial CRN; H. Moore, USGS; G. Neukum, Univ Munich; P. Schultz, Lunar and Planetary Inst.; L. Soderblom, USGS; R. Strom, Univ. Arizona; A. Woronow (Chairperson), Univ. Arizona; R. Young, SUNY.

1 Report No	2 Government Accession No	3 Recipient's Catalog No
NASA TM 79729		

4 Title and Subtitle	5 Report Date
Reports of Planetary Geology Program, 1977-1978	May 1978
	6 Performing Organization Code: SL-4

7 Author(s)	8 Performing Organization Report No
Compiled by Robert Strom and Joseph Boyce	
	10 Work Unit No

9 Performing Organization Name and Address	11 Contract or Grant No
Office of Space Science Planetary Division Planetary Geology Program	
	13 Type of Report and Period Covered

12 Sponsoring Agency Name and Address	14 Sponsoring Agency Code
National Aeronautics and Space Administration Washington, DC 20546	

15 Supplementary Notes

16 Abstract

A compilation of abstracts of reports which summarizes work conducted by Planetary Geology Principal Investigators and their associates. Full reports of these abstracts were presented to the annual meeting of Planetary Geology Principal Investigators and their associates at the University of Arizona, Tucson, Arizona, May 31, June 1 and 2, 1978.

17 Key Words (Suggested by Author(s))	18 Distribution Statement
Planetary Geology Solar System Evolution Planetary Geologic Mapping Instrument Development	Unclassified - Unlimited

19 Security Classif (of this report)	20 Security Classif (of this page)	21 No of Pages	22 Price*
Unclassified	Unclassified	356	

*For sale by the National Technical Information Service, Springfield, Virginia 22161

NASA-Langley, 1978

National Aeronautics and Space Administration

Washington, D.C.
20546

Official Business
Penalty for Private Use, $300

SPECIAL FOURTH CLASS MAIL
BOOK

Postage and Fees Paid
National Aeronautics and Space Administration
NASA-451

U.S. MAIL

25 2 1U,J, 040878 S90844HU
MCDONNELL DOUGLAS CORP
ATTN: PUBLICATIONS GROUP PR 15246-A
P O BOX 516
ST LOUIS MO 63166

NASA

POSTMASTER: If Undeliverable (Section 1
Postal Manual) Do Not Ret